Fabrication and Characterisation of Nickel Manganite Thin Films by Pulsed Laser Deposition

By

Shaun Dorey

UNIVERSITY OF BIRMINGHAM

A thesis submitted to The University of Birmingham for the degree of

DOCTOR OF PHILOSOPHY

School of Metallurgy and Materials

The University of Birmingham

April 2016

Abstract

Nickel Manganite ($NiMn_2O_4$) thin films (~3μm thickness) have been deposited on polycrystalline alumina substrates using pulsed laser deposition (PLD). The influence of deposition conditions, including substrate temperature and oxygen pressure, on the structure and properties of the films has been investigated. The effect of post – deposition annealing at 800 °C in oxygen has also been studied.

The starting materials of nickel manganite including nickel oxide (NiO) and manganese oxide (Mn_2O_3) were analysed by X – Ray Powder Diffraction (XRD) and Scanning Electron Microscopy (SEM), to allow for a comparison with the thin film produced. Different substrates were examined and their suitability for deposition of Nickel Manganite (NMO) was determined. An investigation into the resistance measurement techniques was conducted with the NMO sintered material to determine which technique would produce reliable and repeatable measurements. Measurement of a known resistor was conducted to see if any changes in the resistance were noticed to establish the reliability of the four wire resistance measurement technique.

The structure and microstructure of the films were characterised by XRD, profilometry, optical microscopy and scanning electron microscopy SEM. A four – wire resistance measurement technique was also carried out to measure the resistance and to calculate the films electrical parameters. Optimisation of the deposition parameters enabled films to be produced which exhibit characteristic negative temperature coefficient of resistance (NTC) thermistor behaviour. The dependence of the structure and properties of the films on deposition conditions will be presented and discussed. The reproducibility of the films was investigated by producing repeats and comparing them with each other analytically by their structure, microstructure and

electrical properties. This study has demonstrated that PLD is a promising technique for fabricating high quality $NiMn_2O_4$ thin films suitable for use as NTC thermistors.

Acknowledgements

Firstly, I would like to express my sincere gratitude to my advisor Prof. Tim Button, for his continuous support throughout my Ph.D. studies, for his patience, motivation, and immense knowledge. I appreciate all his contributions of time, ideas, and funding to make my Ph.D. experience productive and stimulating.

Secondly, I would like to thank all those at Amphenol, in particularly Dr. Deborah Desimone Silva, for her time, discussions, suggestions and direction.

I would like to express my sincere gratitude and thanks to Mr Andy Bradshaw for his technical help and expertise on the PLD system throughout its many breakdowns and for his ideas on improving my project.

I would also like to particularly thank Mr. Carl Meggs for being one of the best technicians I have ever worked with. His ingenuity, technical knowhow, friendship and comedy kept me going throughout my studies and time at Birmingham.

Additionally, I would like to thank all my friends and colleagues I have made at Birmingham for their support, it has been a pleasure to have worked with you all.

Lastly a very special thank you goes to my Family for their encouragement, drive and ambition to believe in myself that a Ph.D. was possible.

List of Publications

Shaun Dorey, Deborah Desimone, Xin Gu and Tim W Button, Fabrication and Characterisation of Nickel Manganite Thin Films by Pulsed Laser Deposition, accepted for oral presentation at the Electroceramics 14 Conference, Bucharest, Romania, 16 – 20 June 2014.

Shaun Dorey, Deborah Desimone, Xin Gu and Tim W Button, Fabrication and Characterisation of Nickel Manganite Thin Films by Pulsed Laser Deposition, Journal of the European Ceramic Society, *'in preparation'*.

Abbreviations

A	Annealed
AC	Alternating Current
AD	Aerosol Deposition
AFM	Atomic Force Microscopy
Ag	Silver
Ag_2S	Silver Sulphide
Al_2O_3	Alumina
Al	Aluminium
Ar	Argon
ArF	Argon Fluorine
Au	Gold
atm	Atmospheric pressure
a	Localisation Length
Ba	Barium
$BaTiO_3$	Barium Titanate
C	Thermal Energy Storage Capacity
Co	Cobalt
CO_2	Carbon Dioxide
Co_3O_4	Cobalt (III) Oxide
Cu	Copper
CRT	Cathode Ray Tube
Cr	Chromium
CSD	Chemical Solution Deposition
cm	Centimetre
D	Temperature Independent Contribution to Conductivity
DC	Direct Current
d	*interplaner distance*
E	Voltage Source
E_a	Activation Energy
EBE	Electron Beam Evaporation
EBSD	Electron Backscatter Diffraction
EDX	Energy Dispersive X – Ray Spectroscopy
E_F	Fermi Level
E_T	Static Thermistor Voltage
e	Thickness Of Lamella
e^-	Electron
eV	Electron Volt
Fe	Iron
Fe_2O_3	Iron (III) Oxide
GΩ	Giga Ohm
g	Gram
H_A	Heat Absorbed
H_L	Energy Loss

HP	Hewlett Packard
H_S	Energy Absorbed
H.V.	High Vacuum
hr	Hour
Hz	Hertz
I	Current
IC	Integrated Circuit
I_T	Steady State Current
J	Joules
JCPDS	Joint Committee On Powder Diffraction Standards
K	Kelvin
kN	Kilo Newton
KrF	Krypton Fluorine
kV	Kilo Volts
k_B	Boltzmann Constant
l	Thickness Of Material
$LiMn_2O$	Lithium Manganate
ln	Natural Log
$MgAl_2O_4$	Magnesium Aluminate
Mn	Manganese
Mn_3O_4	Manganese (III) Oxide
Mn_2O_3	Manganese Oxide
Mo	Molybdenum
MOD	Metal Organic Deposition
MS	Magnetron Sputtering
m	Mass
min	Minute
mTorr	Millitorr
mm	Millimetre
N	Newton
N_2	Nitrogen
Nb:STO	Niobium Doped Strontium Titanate
Nd:YAG	Neodymium – Doped Yttrium Aluminium Garnet
Ni	Nickel
$NiAlMn_2O_4$	Nickel Aluminium Manganite
$NiMnO_3$	Ilemite Nickel Manganite
Ni_6MnO_8	Cubic Nickel Manganite
$NiMgMnO_4$	Nickel Magnesium Manganite
NiO	Nickel Oxide
NMO	Nickel Manganite ($NiMn_2O_4$)
NTC	Negative Temperature Coefficient Of Resistance
n	Order Of Diffraction
nm	Nanometer
O	Oxygen
O_2	Oxygen
P	Power dissipation

P_c	Power Applied To A Circuit
PLD	Pulsed Laser Deposition
P_L	Thermal Power
PTC	Positive Temperature Coefficient of Resistance
Pt	Platinum
PVA	Polyvinyl Alcohol
PVD	Physical Vapour Deposition
P_w	Electric Power
p	Exponential Power Law Dependance
R	Resistance
R_0	Resistance at 20 K
RF	Radio Frequency
RTD	Resistance Temperature Detector
R_T	Thermistor
R_{T0}	Resistance At A Specified Temperature
rpm	Revolutions Per Minute
S	Probe Spacing
SEM	Scanning Electron Microscopy
Si	Silicon
SiO_2	Silicon Dioxide
$SrTiO_3$ / STO	Strontium Titanate
s	Second
T	Temperature
TCR / α	Temperature Coefficient of Resistance
TEM	Transmission Electron Microscopy
TOF	Time Of Flight
t	Time
T_A	Surrounding Temperature
T_c	Curie Point
T_0	A Specified Temperature
T_s	Specific Heat
UO_2	Uranium Oxide
UoB	University Of Birmingham
UV	Ultraviolet
V	Volt
V_2O_4	Vanadium Oxide
VDP	Van Der Pauw
W	Watt
W_a	Activation Energy Of The Hopping Mechanism
XeCl	Xenon Chlorine
XRD	X – Ray Diffraction
YSZ	Yttria – Stabilized Zirconia
β	Thermistor Constant
°	Degree
°C	Degrees Celcius
δ	Dissipation Constant

$\boldsymbol{\tau}$	Thermal Time Constant
ρ	Resistivity
ρ_0	Resistivity At Infinite Temperature
σ	Conductivity
π	Pi
θ	Diffraction Angle
σ_0	Temperature Independent Constant
σ_{DC}	Small Polaron DC Hopping Conductivity
γ	Pre – Exponential Temperature Dependance
Ω	Ohm
ξ_C	Percolation Threshold Parameter
r_c	Critical Radius
λ	wavelength
r_{ij}	Separation In Real Space
ε_{ij}	Separation Of Energy Space Of The i And j Electron States
ε_3	Average Activation Energy
μA	Micro Amp
μm	micrometer
3Y – TZP	Tetragonal Zirconia Polycrystalline

Contents

Chapter 1

Introduction

This work is about the production and characterisation of thin films of $NiMn_2O_4$ (NMO) with negative temperature coefficient (NTC) of resistance properties, for their possible use as thermistors. The word thermistor is derived from *thermally – sensitive – resistor*, and is used to describe a resistive material that possesses a large temperature coefficient of resistance (TCR) over a large temperature range [1, 2]. There are two forms of thermistors which are categorised in accordance with their TCR. They can either possess a negative (NTC) or a positive temperature coefficient of resistance (PTC). A NTC thermistor's resistance will decrease with an increase of its body temperature while a PTC thermistor's resistance will increase with an increase of its temperature. NTC thermistors are made from semiconducting materials consisting usually of a sintered ceramic which has been fabricated in a variety of shapes and sizes from a mixture of oxides such as Mn, Ni, Co, Cu and Fe [2-4]. They ususally exhibit a spinel type crystal structure, which has a cubic close packing of oxygen anions where the cations are located on the tetrahedral and octahedral sites [5]. It is possible to tailor the thermistor for specific devices by varying the composition of these materials and their size to

get resistance values between 10^0 and 10^6 Ω. Currently NTC thermistors are available in a wide variety of shapes consisting of beads, discs and washers. These can be encapsulated either in solid glass, glass envelopes or transistor cans and they can then be further mounted inside metal or plastic housings to suit particular applications.

NTC thermistors have become the most widely used temperature sensors because of their low cost and high sensitivity [6] and are generally suitable for mass production in industry. Their resistance vs. temperature is characteristic over a wide temperature range (-200 °C – 350 °C) allowing them to be applicable for many different temperature measurement applcations. NTC thermistors are used as temperature sensors and temperature compensation devices. NTC thermistors are generally used where high accuracy is important, examples include in the medical field where a localised or general body temperature measurement is required, in the car industry as engine temperature controllers and in meterology for weather forcasting. Commercial NTC thermistors are generally based on transition metal oxides, such as NiO, Mn_3O_4, Co_3O_4 and Fe_2O_3 with a general spinel composition of AB_2O_4. Nickel and manganese oxides spinels have attracted the most attention because of their low room temperature resistivity ($\rho < 100$ Ω.cm), so therefore as a result are used widely in devices that operate at room temperature and their composition and processing conditions have a huge effect on their electrical properties by affecting the distribution of the cations and oxidation states in the spinel structure [7, 8].

The trend in the electronics industry today is to produce smaller and more reliable devices. This has led to the increasing popularity of the use of thin films techniques to achieve this. The sponsoring company for this project (Amphenol) currently produce thermistors in bulk form and are currently interested in producing small thermistor devices with a small thermal signature which maintain the same NTC properties as their bulk material. The advantages of using NTC thin films include a faster response time, a lower operating voltage and a moderate

annealing temperature. Pulsed laser deposition (PLD) is a good technique for the production of trial components due to its simplicity of use. The main advantage of PLD is its ability to preserve the same chemical structure and stoichiometry of the target material, also its deposition parameters can be easily controlled and manipulated. Currently past work on the production of NTC thin films has been achieved using polished substrates to produce epitaxial films using single crystal substrates. The main focus of this work was not to produce epitaxial films but to instead see if bulk NTC properties could be reproduced in thin film form using cheap polycrystalline substrates, giving the project a more commercial focus.

The structure of the thesis is as follows, Chapter 2 consists of the literature review. The first part consists of an introduction to temperature measurement and its history. The second part consists of the crystal chemistry of the NMO including the electrical and thermal properties of the material.

Chapter 3 is a further literature review summarising the different thin film growth techniques that have been used to deposit thin films of NMO. Also included is review of past papers that have involved the deposition of thin films of NMO.

Chapter 4 describes the experimental methods used including the PLD technique used in this investigation to produce the thin films. The preparation of the substrates and targets for the PLD process and a decription of the analytical techniques used.

The intial results are given in Chapter 5 which involved the investigation of the starting materials. The bulk material was analysed microstructurally and its electrical properties analysed. An initial set of NMO films were produced using past conditions for films produced using $LiMn_2O$. Different resistance measurement techniques were employed and were analysed and compared.

A set of films using an optimised deposition technique was analysed and the effect of changing the oxygen pressure and substrate temperature and is discussed in Chapter 6.

The reproducibility of the films is investigated and analysed in Chapter 7, including changes in resistivity and microstructure. Also how changing the electrodes has an effect on the resistance measurements.

The main findings and conclusions of this investigation are summarised in Chapter 8 along with suggestions for future work to further understand the effects of changing the PLD conditions on the thin films.

References

1. Macklen, E.D., *Thermistors,* 1979, Glasgow, Scotland: Electrochemical Publications Ltd.
2. Parlak, M., et al., *Effect of heat treatment on nickel manganite thin film thermistors deposited by electron beam evaporation.* Thin Solid Films, 1999. **345**(2): p. 307-311.
3. Parlak, M., et al., *Electron beam evaporation of nickel manganite thin-film negative temperature coefficient thermistors.* Journal of Materials Science Letters, 1998. **17**(23): p. 1995-1997.
4. Fau, P., et al., *Thin-films of nickel manganese oxide for NTC thermistor applications.* Applied Surface Science, 1993. **65-6**: p. 319-324.
5. Schmidt R., B.A.W., *Electrical properties of screen-printed $NiMn_2O_{4+delta}$.* Journal of the European Ceramic Society, 2005. **25**(12): p. 3027-3031.
6. Schmidt, R., *Production and performance of thin and thick film NTCR thermistors based on $NiMn_{(2)}O_{(4)+}$*, 2003, University of Durham: Durham.
7. Park K. and B. D.Y., *Electrical properties of Ni-Mn-Co-(Fe) oxide thick-film NTC thermistors prepared by screen printing.* Journal of Materials Science-Materials in Electronics, 2003. **14**(2): p. 81-87.
8. Varghese, J.M., Seema, A. and Dayas, A.R. *Microstructural, electrical and reliability aspects of chromium doped Ni–Mn–Fe–O NTC thermistor materials.* Materials Science and Engineering: B, 2008. **149**(1): p. 47-52.

Chapter 2

Literature Review

2.1. Introduction

In this chapter the background of NMO is presented with its role in temperature measurement and other applications. A brief history is also given from its discovery to its mass production and inclusion in many of today's appliances. The crystal chemistry is then presented with details of its cation distribution and the close relationship between crystal structure and the conductivity of the NMO material. A detailed review of the thermal properties of NMO is then described from the thermally activated hopping process [1] to the nearest neighbor hopping mechanism [2]. A review of different studies conducted on the aging of NMO is given along with the effects several different dopants can have on the aging process.

2.2. Introduction to Temperature Measurement

The simplest and most widely used method of temperature measurement is thermal expansion, which is the phenomenon employed in liquid – glass – thermometers. The electrical

measurement of temperature on the other hand uses different methods of sensing, such as resistive, thermoelectric, semi conductive, optical, acoustic and piezoelectric detectors [3].

There are four main types of electrical temperature measurement sensors which are used for domestic, medical and industrial purposes. These are called thermocouples, resistance temperature detectors (RTDs), integrated circuits (IC) sensors and thermistors. Each different type of temperature sensors offers their own specific advantages and disadvantages, as shown in Table 1, allowing them to be used for a specific application.

Thermocouples, for example, consist of two dissimilar electrically conductive materials which are joined together at two junctions to form a circuit. A voltage is generated by the Seebeck Effect when the two junctions are at different temperatures the heated electrons will flow towards the cooler conductor and the potential difference is measured as a function of temperature. Thermocouples are widely used due to their small size, durability, ease of use and cover a wide temperature range, they are however prone to corrosion from the environment and liquids. They consist mainly of combinations of copper / constantan, chromel / constantan, iron / constantan, chromel / alumel, platinum / rhodium, tungsten / rhenium [4]. In comparison to thermistors they have a wider temperature range and are especially useful at measuring at very high temperatures (up to +2300°C) [4], but they have a lower sensitivity (microvolts per degree) and accuracy and have a need for a reference temperature. They are characterised as having a larger linearity than thermistors, but smaller in comparison to RTDs.

RTDs are metal sensors which are produced either in the form of a wire or thin film. The resistivity of the metal allows them to be used in temperature sensing, platinum (Pt) is used almost exclusively in RTDs because of its extremely predictable response, durability and long term stability [3]. When compared with NTC thermistors, Pt RTDs are much less sensitive to small temperature changes and have a much slower response time [4].

Silicon and germanium based semiconductors are integrated into ICs but only offer reasonably accuracy in the temperature range of -55°C to 150°C.

Table 2.1. Characteristics of Temperature Sensors (After Feteira [4]).

Characteristics	**Thermocouple**	**RTD**	**Thermistor**	**Integrated Circuit**
Active material	Two dissimilar metals	Platinum	Ceramic	Si or Ge
Changing parameter	Voltage	Resistance	Resistance	Voltage or current
Temperature range [°C]	-270 to +2300	-200 to +650	-50 to +1000	-55 to +150
Additional circuitry	Reference junction	Lead compensation	Linearization	Linearization
Sensitivity	~ 1-80 μV/°C	~ 0.4% / °C	-2%/° to -6%/°C	-7.3%/°C (Si) -5%/°C (Ge)
Accuracy [± °C]	0.5-5	0.001-1	0.001-1	1
Response time	Fast, 0.1-10s	Slow, 1-50s	Fast, 0.1-10s	Fast, <0.1s
Stability	Moderate	Excellent	Moderate	High
Cost	Low	Moderate to high	Low to moderate	Low
Advantages	Wide operating temperature range, Low cost, Rugged	Linearity, Wide operating temperature range, Highest stability	Fast response time, Low cost, Small size, Large changes in resistance versus temperature	Highly linear, Low cost
Disadvantages	Nonlinear, Low sensitivity, Reference junction compensation required, Subject to electrical noise	Slow response time, Expensive, Current source required, Sensitive to shock	Nonlinear, Current source required, Currently, limited temperature range	Very limited temperature range, Power source required

2.3. Introduction to Thermistors

Thermistors are defined as electronic components which exhibit a large change in resistance with a change in their body temperature. The majority of commercial thermistors are comprised of ceramic semiconductor oxides such as manganese, cobalt, copper and nickel [4] due to their stability and high sensitivity to temperature [5]. A large temperature coefficient of resistivity can arise in ceramic oxides due to one of two phenomena. One being a large increase in resistivity with temperature over small temperature ranges (a PTC thermistor), directly related to the interaction between the grain boundary acceptor states formed during processing and the

ferroelectric to paraelectric phase change at the Curie temperature. This effect is characterised by a large increase of resistivity of up to six orders of magnitude.

Changing the dielectric properties of the ferroelectric ceramic affects the electronic properties in the grain boundary giving rise to the positive temperature coefficient [5]. The second is an exponential decrease in resistivity over a wide temperature range (a NTC thermistor) which is characteristic of a semiconductor. NTC thermistors tend to show a more gradual change in their resistance over a much broader range of temperatures in comparison to PTC thermistors.

The materials used in NTC's and PTC's are different, with ceramic NTC's composed of metal oxides such as manganese, nickel, cobalt, iron, copper and titanium. PTC's fall into two categories, the first consist of thermally sensitive silicon resistors, sometimes referred to as "silistors". The second are ceramic PTC's which are referred to as switching PTC thermistors and are mostly made up of barium, lead and strontium titanates with additives such as yttrium, manganese, tantalum and silica. Both types of thermistors (NTC and PTC) possess specific properties which make them perfect for particular sensor applications.

A comparison of the different resistance versus temperature characteristics in various different types of thermistors is shown in Figure 2.1.

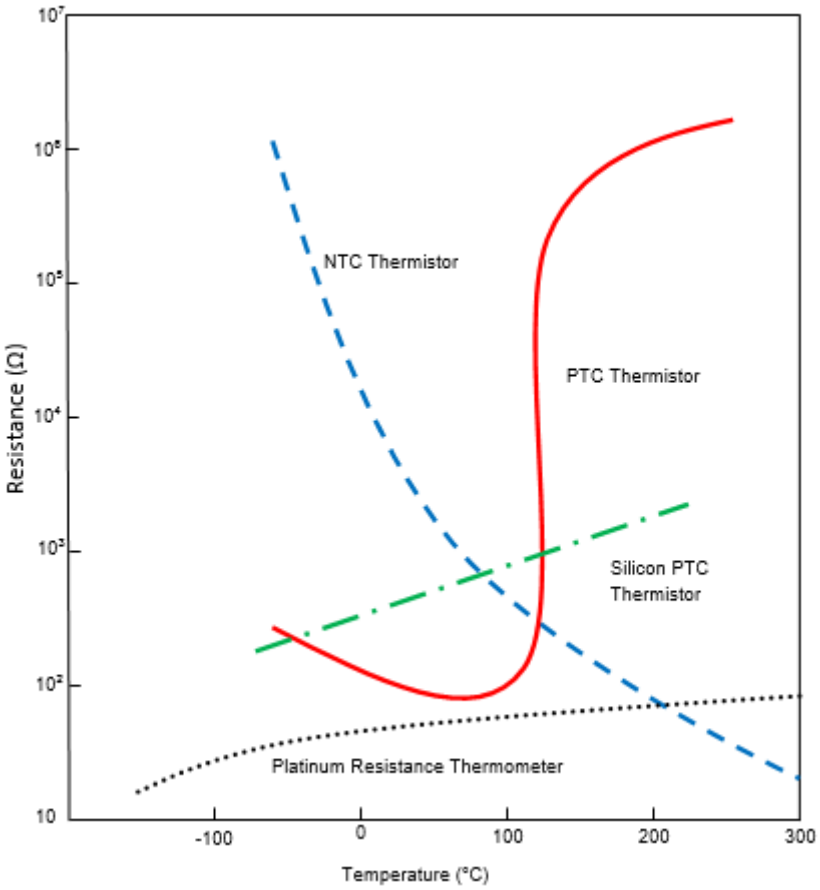

Figure 2.1. Resistance versus temperature characteristics of several different types of thermistor [5].

The change in resistance per Kelvin is called the Temperature Coefficient of Resistance (TCR) which is represented by the Greek lower case letter 'alpha' (α). TCR is measured in % / K and is defined in equation 2-1 as variation of resistance per degree rise of temperature to its original temperature [6].

$$TCR = \alpha = \frac{1}{R} \times \frac{dR}{dT} \tag{2-1}$$

The most common application of thermistors is in temperature measurement, gas flow meters and attenuators. In these applications a negligible amount of power is applied and the

resistance change monitored. These characteristics are used in applications such as automotive engines, air – conditioning units, hair dryers, heart catheters, fever thermometers, television receivers, and resistive bolometers [7].

2.4. History and Brief Introduction to PTC Thermistors

The PTC resistance effect was first exploited in the 1950s in the Philips Research Laboratories in the Netherlands [8]. Diverse applications have prompted research efforts to understand the structural and compositional issues which rule the electrical properties of PTC thermistors. A PTC thermistor's resistivity will increase up to six order of magnitudes suddenly at its transition temperature where it is much higher in comparison to its room temperature resistivity value [9]. A typical PTC characteristic is shown in Figure 2.2. At low temperatures of up to about 100°C (A – B) the PTC thermistor displays a NTC characteristic as well as at higher temperatures above 200°C (C – D). Between these temperatures however (B – C) there is a sudden increase of the order of several magnitudes in resistivity. As a result, PTC thermistors are generally used as circuit temperature overload protectors, other uses include temperature and liquid level sensors, automatic electric chokes, hair dryers, television degaussers, early fuel evaporation devices and food warmers.

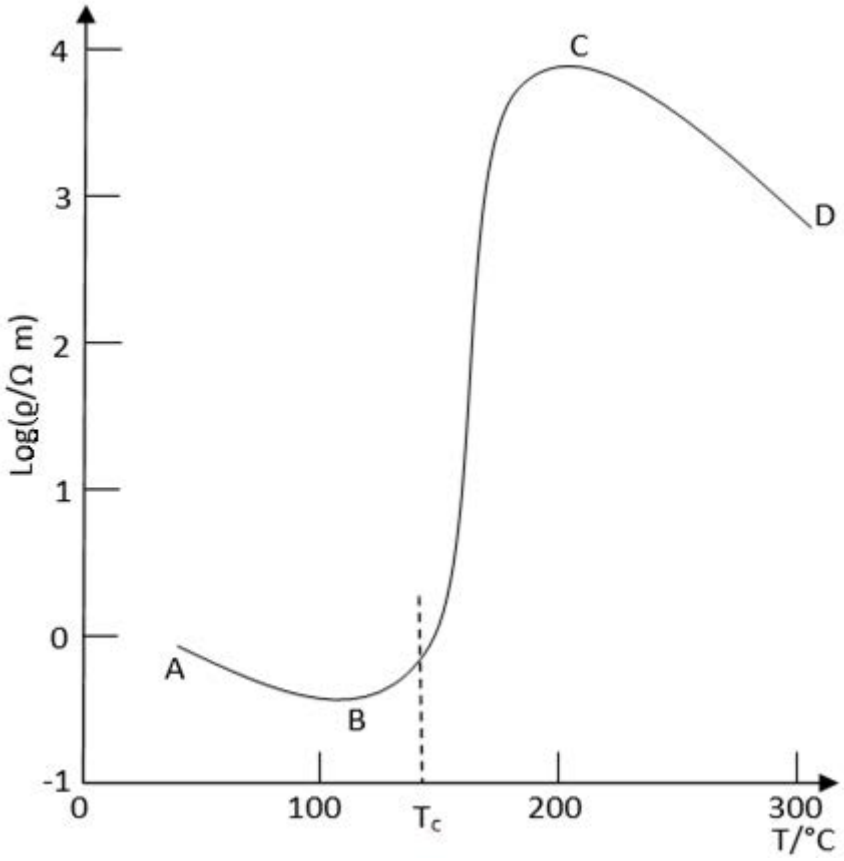

Figure 2.2. Characteristics of a PTC thermistor [7]

The PTC effect is found in semiconducting ferroelectric titanate ceramics, it is related to the grain – boundary acceptor states which are formed during their processing and the ferroelectric – paraelectric phase transition at the Curie temperature. There are four main material groups associated with PTC: $BaTiO_3$ based or quasi $BaTiO_3$ based ternary perovskite compounds, ceramic composites, polymer composites and V_2O_4 based compounds [8].

The size of the jump of resistivity is determined by the composition and fabrication conditions of the PTC material. The cooling rate and post atmospheric oxidising annealing conditions have a huge impact on the PTC's resistivity. Oxygen is chemisorbed at the PTC's grain boundary with the aid of counter – dopants such as Mn, Fe and Cu, this depletes electrons from the grain near the grain boundary region [7]. The depletion of oxygen causes the formation of a grain boundary potential barrier, this is shown in Figure 2.3.

The sudden increase in the resistivity is attributed to an increase in the potential barrier at the grain boundaries. This is inversely related to the dielectric constant of the material by the Curie – Weiss law above T_c [9].

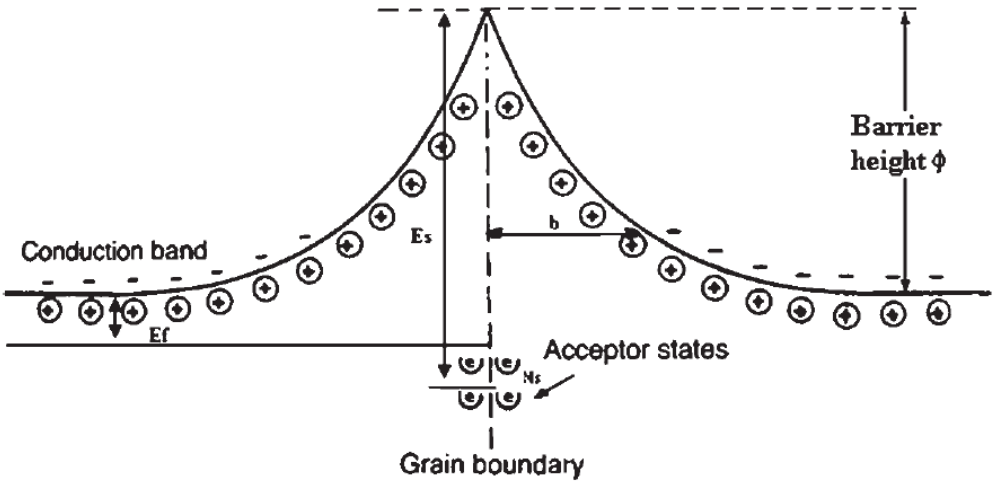

Figure 2.3. Grain Boundary of a PTC thermistor [7]

The electrical characteristics of PTC thermistors are mainly attributed to microstructural aspects such as the grain size, phase profile and porosity. Decreasing the grain size and adding dopants is a useful way to enhance their electrical properties.

2.5. NTC Thermistors a Brief History

NTC ceramic thermistors are found in almost all modern electronics, where they are used for temperature measurement, control and compensation [4]. They make up an important business segment in most electroceramic manufacturers and it is therefore not surprising that historically most of the research on NTC thermistors was led by this industry.

The NTC phenomenon was first noticed by natural philosopher Michael Faraday on February 21 1833, who observed that the resistance of silver sulphide, Ag_2S, would decrease with increasing temperature. This phenomenon remained a scientific curiosity for nearly 100 years until it was noticed again in transition – metal oxides such as NiO, which led to the design

of novel instruments which were based on NTC behaviour, such as an electrical pyrometer device by Samuel Ruben in 1930 [4].

The first commercial thermistors were made of uranium oxide (UO_2) in Germany in 1932 by Osram [10]. In the late 1930's Bell laboratories decided to start mass producing commercial spinel structured ceramics based on mixtures of oxides, such as manganese and iron or nickel and manganese, which exhibited NTC behaviour. Their major application was in telecommunication and temperature measurement [11]. It was soon discovered however that the resistivity of some of these ceramics could vary by 3 – 6 orders of magnitude, depending on the preparative heat treatment [4]. Most of the work therefore carried out in Bell laboratories attempted to overcome these shortcomings by changing the materials and processing procedures leading to improved stability and reproducibility. These improvements led to an increase of the number of American and European manufacturers which would use the NMO system.

In the late 1940's, thermistors could be found in various important and large scale uses, such as military equipment where some of their functions were as device protection, time delay and voltage regulation. The most influential work carried out at this time was done by Verwey and his colleagues from the Phillips Research Laboratories [12], where they carried out research into the structure – composition – property relationship of the spinel-based ceramics.

From 1950/60 there was an increase in sophisticated applications as aerospace and cryogenic devices were introduced. Further research into the cation arrangement and physical properties was undertaken by Romeijn from the Phillips Laboratories by an exhaustive characterisation of the physical and crystallographic properties of spinels [4].

In the 1970's interest in NTC ceramics had spread to companies such as Ford Motor Corporation, Matsushita Electric Industrial Co. Ltd and Siemens. By the 1980's interest had evolved into use of high temperature thermistors (400 – 800°C). Then in 1990's, several

University based research groups became active in the field of NTC ceramics [4]. From 2000 onwards, most research had been devoted to the controlling factors of the stability of NTC ceramics, improved cost effectiveness, high accuracy, stability and reliability [11]. Figure 2.4. gives a number of examples of bulk NTC thermistors that are currently available.

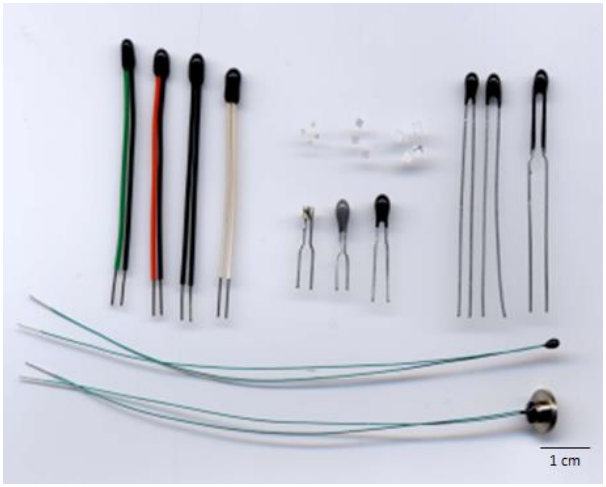

Figure 2.4. A range of different NTC thermistors [13]

To fulfil requirements imposed by different applications, thermistors components are provided by many electroceramics manufacturers in a wide variety of designs, which range from surface mounted to radial or axial leaded packages. Commercial NTC thermistors can be classified into two major groups, bead type thermistors and thermistors with metallized surface contacts. These groups can also be subdivided into various types of thermistors where each type is then categorised by their differences in geometry, packaging and / or their processing techniques.

Bead type thermistors all have platinum alloy leadwires which are directly sintered into the ceramic body. Bead types include bare beads, glass coated beads, ruggedized beads, miniature glass probes, glass probes, glass rods and bead in glass enclosures. Thermistors which have metallised surface contacts can have radial or axial leads as well as without leads for surface

mounting. Metallized surface contact thermistors include disks, chips (wafers), surface mounts, flakes, rods and washers. NTC thermistors are available in a wide variety of configurations and protective coatings. Thermistors that are hermetically sealed in glass are the most stable and accurate thermistors. The hermetically sealed thermistors are used almost exclusively, for applications which are continuously exposed to temperatures above 150 °C.

2.6. The Crystal Chemistry of NTC $NiMn_2O_4$ Spinel Ceramics

NMO exhibits a spinel type structure. The term spinel refers to the mineral $MgAl_2O_4$, but the term is also used to identify a group of minerals with the general formula $A(B_2)O_4$, [4, 14] where A is a divalent and B is a trivalent cation [2]. The crystal structure of spinels has long been known and was first determined by Bragg [15, 16] to be in the cubic space group *Fd3m*. The crystal structure of spinel is illustrated in Figure 2.5. showing the basic cubic unit cell and eight slices taken in the (100) crystal direction [17].

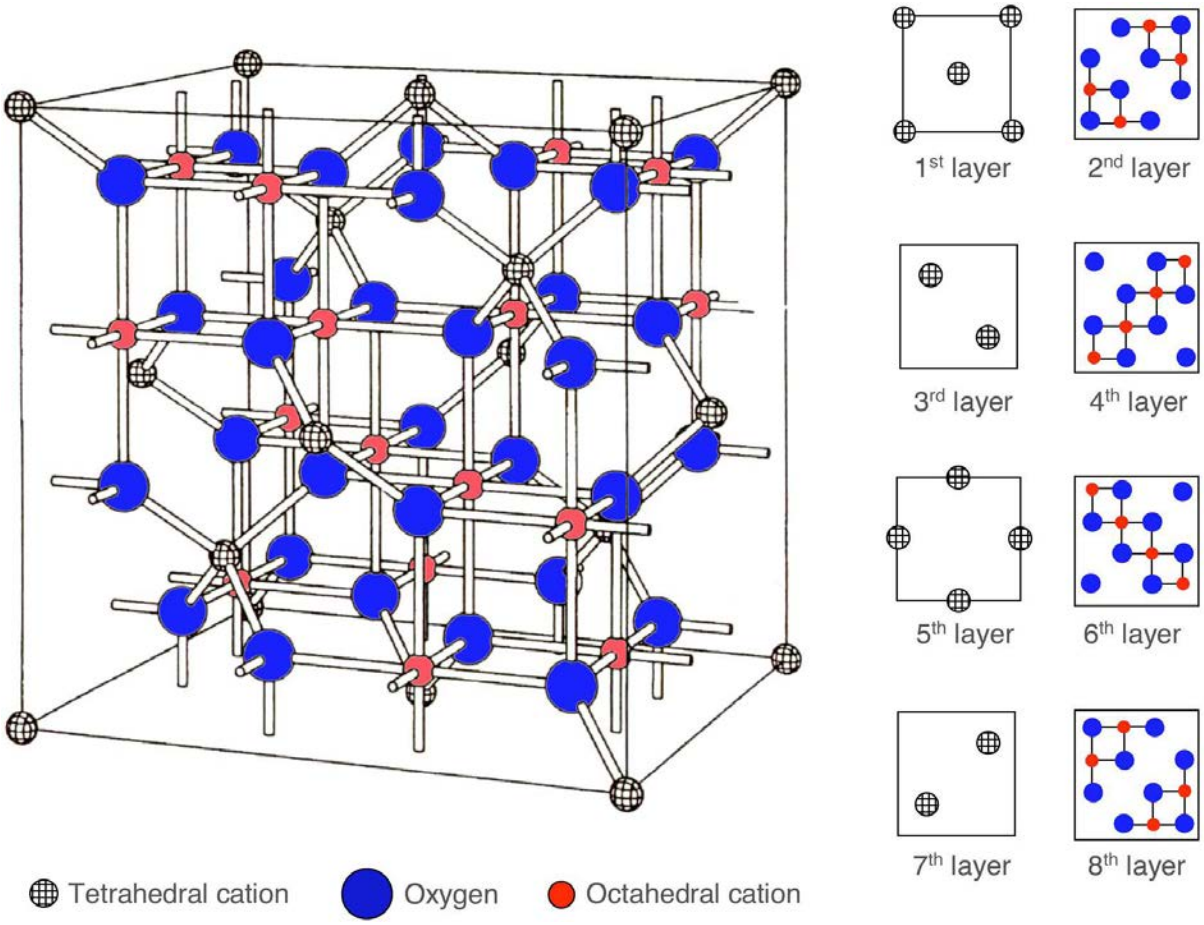

Figure 2.5. Basic cubic unit cell of the Spinel structure and in eight slices taken in the [100] crystal direction [17]

The spinel structure consists of two types of cubic building blocks housed within a unit cell, these being diamond – like and rocksalt – like. This allows for cation occupancy in both the tetrahedral (AO_4) and octahedral sites (BO_6) sites, this can be seen more clearly in Figure 2.6.

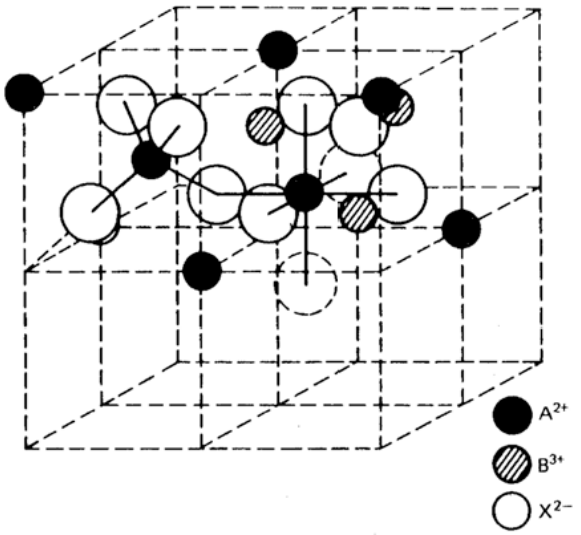

Figure 2.6. Cubic spinel crystal structure [13]

The spinel structure in a material may be normal, inverse or disordered, this is determined by its cation occupancy. In a normal spinel, 2^+ ions (A) are found on the tetrahedral sites and 3^+ ions (B) are located on the octahedral sites. However, in an inverse spinel structure, there is the same amount of 2^+ and 3^+ ions found in the octahedral sites, whilst the remaining 3^+ ions occupy the tetrahedral sites.

Spinel type manganates are known as high technology electroceramic materials. Spinel $Ni_{1-x}Mn_{2+x}O_4$, where x denotes the deviation from the stoichiometric 1:1 $NiO:Mn_2O_3$ ratio, is a mixed – valent oxide which possesses an unusual range of electrical properties which allows it to be useful in temperature sensing applications [1]. NMO is a strongly correlated system, where the crystal structure and its electrical properties are closely linked [17]. At room temperature it exhibits a cubic symmetry which is very different from the regular tetragonal symmetry present in normal spinel type structures [18]. NMO is actually a partially inverse spinel type ceramic semiconductor [19-21]. NMO unit cell contains 64 tetrahedral and 32 octahedral interstices, 8 (12.5%) of the tetrahedral and 16 (50%) of the octahedral interstices sites are occupied. 32 oxygen anions, 16 manganese and 8 nickel cations, make up the cell [2].

Despite $NiMn_2O_4$ adopting a partially inverse spinel structure and simple chemical formula it is a surprising complex material, the reason for this is the variability of the nickel and manganese lattice positions [20]. The metal cations (nickel and manganese) are located on both the tetrahedral (A) and octahedral (B) sites [22-24], a tetragonal distortion is caused by the Jahn – Teller effect of the Mn^{3+} ions located on the octahedral sites [25]. The Jahn – Teller effect is often encountered in octahedral complexes of transition metals and states "any non – linear molecular system in a degenerate electronic state will be unstable and will undergo distortion to form a system of lower symmetry and lower energy, thereby removing the degeneracy" [26]. In an octahedral complex the five d atomic orbitals are split into two degenerate sets when constructing a molecular orbital diagram which are represented by the sets symmetry labels: t_{2g} (d_{xz}, d_{yz}, d_{xy}) and e_g (d_{z^2} and $d_{x^2-y^2}$). When the molecule possesses a degenerative electronic ground state, it will distort due to the Jahn – Teller effect in order to remove the degeneracy and form a lower energy and also consequently have lower symmetry. The octahedral complex will then either elongate or compress the z ligand bonds as shown in the figure below.

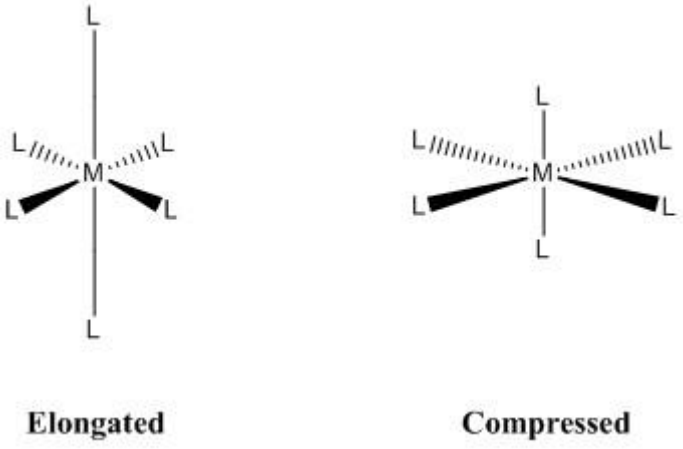

Figure 2.7. Jahn – Teller distortions in an octahedral complex [27]

When the octahedral complex exhibits elongation, the axial bonds are longer than the equatorial bonds. In a compression the reverse occurs where the equatorial bonds are longer than the axial bonds. These distortions are dictated by the amount of overlap that occurs between the metal and ligand orbitals. The stronger the metal – ligand interactions are, the greater the chance the Jahn – Teller effect will occur [27].

The defining feature of NMO which separates it from other spinel structures is Ni^{2+} ion's strong octahedral site preference, which forces a cation arrangement, this leads to its partially inverse structure, [25] which can be written as follows, determined by X – ray photoelectron spectroscopy:

$$Ni_{1-x}^{2+}Mn_{x}^{2+}\left[Ni_{x}^{2+}Mn_{2-2x-2\delta}^{3+}Mn_{x+2\delta}^{4+}\right]O_{4+\delta}^{2-} \quad (2\text{-}2)$$

The cations not in the square brackets are located in the tetrahedral (A) sites, cations found within the square brackets means they are located at octahedral (B) sites and *x* indicates the inversion parameter. A fraction *x* of the Ni^{2+} cations are displaced from the tetrahedral to the octahedral sites of the oxygen fcc sublattice. δ is the stoichiometric excess (δ > 0) or loss (δ <

0) of oxygen [2]. A corresponding proportion of 2x trivalent Mn cations disproportionate to Mn^{2+} and Mn^{4+}, and Mn^{2+} cations will consequently move to the tetrahedral sites to compensate for the Ni^{2+} vacancies [17, 28]. The inversion parameter $x \leq 1$ decreases with increasing temperature. The electrical conductivity depends on the concentration of donor (Mn^{3+}) and acceptor (Mn^{4+}) electron pairs (i.e. conductivity will reach its maximum when there is exactly the same amount of Mn^{3+} to Mn^{4+}). The oxidation states of the Ni and Mn cations depend greatly upon the temperature and atmosphere during their synthesis. The inversion parameter (x) is dependent on how it has been sintered [28, 29]. How the sample is sintered can also influence the oxygen stoichiometry, which again in turn affects the number of Mn^{3+} and Mn^{4+} pairs. NMO sensitivity to how it is produced is what allows it to have such a range of different resistance versus temperature properties.

The cation distribution of NMO has been a controversial matter as Larson et al [30] has suggested that x = 1 with both Mn^{2+} and Mn^{3+} found on tetrahedral sites and $\delta = 0.65$. Also Macklen [31] and Gillot et al [32] have proposed x = 0.60 and $\delta = 0.65$. However confirmation by Brabers et al [33] and Hashemi and Brinkman [34] of 3 different valencies of manganese by X – ray photoelectron spectroscopy (XPS) which is consistent with equation (2-2) has been made.

Neutron diffraction has also been used to determine the cation distribution in spinels by Fritsch *et al* [23]. They discovered that the conditions of cooling the samples after sintering affected the Ni site occupancy. With slow cooling (-5°C/min) only a small fraction of the Ni cations would be found on the tetrahedral sites due to their strong preference for the octahedral sites. However, when NMO was quenched from 1160°C to 900°C more Ni cations were present on the tetrahedral sites. This therefore supported the theory that the degree of inversion will decrease at high temperatures. Boucher *et al* [35] measured the degree of inversion and confirmed that this was the case.

2.7. Nickel Manganite Phase Stability

When analysing the resistivity and conductivity in NMO ensuring its phase purity is imperative. A bulk phase diagram was mapped out by Wickham for the NiO – Mn_2O_3 – O_2 system for temperatures between 500°C and 1200°C [36]. The electrical conductivity of NMO at high temperatures is due to a change in the cation distribution, it also is not as stable at higher temperatures and it's conductivity may be affected by a second phase [2].

The Ni / Mn ratio (R) is defined as:

$$R = [Mn]/\{[Ni] + [Mn]\} \quad (2\text{-}3)$$

where the ions in the square brackets denote normal concentrations.

This phase diagram indicates that at temperatures between 750°C and 900°C the cubic NMO spinel phase is stable in air. To the left of this region there is a rock salt structure and dual phase region of a spinel and NiO. At temperatures lower than 750°C it will dissociate to the ilmenite structure $NiMnO_3$ and another cubic phase Ni_6MnO_8 in air or an oxygen rich atmosphere. At even lower temperatures the bixbyite structure Mn_2O_3 is formed. If heat treated above 400°C in an inert environment, a cation deficient spinel is produced up until 600°C [18].

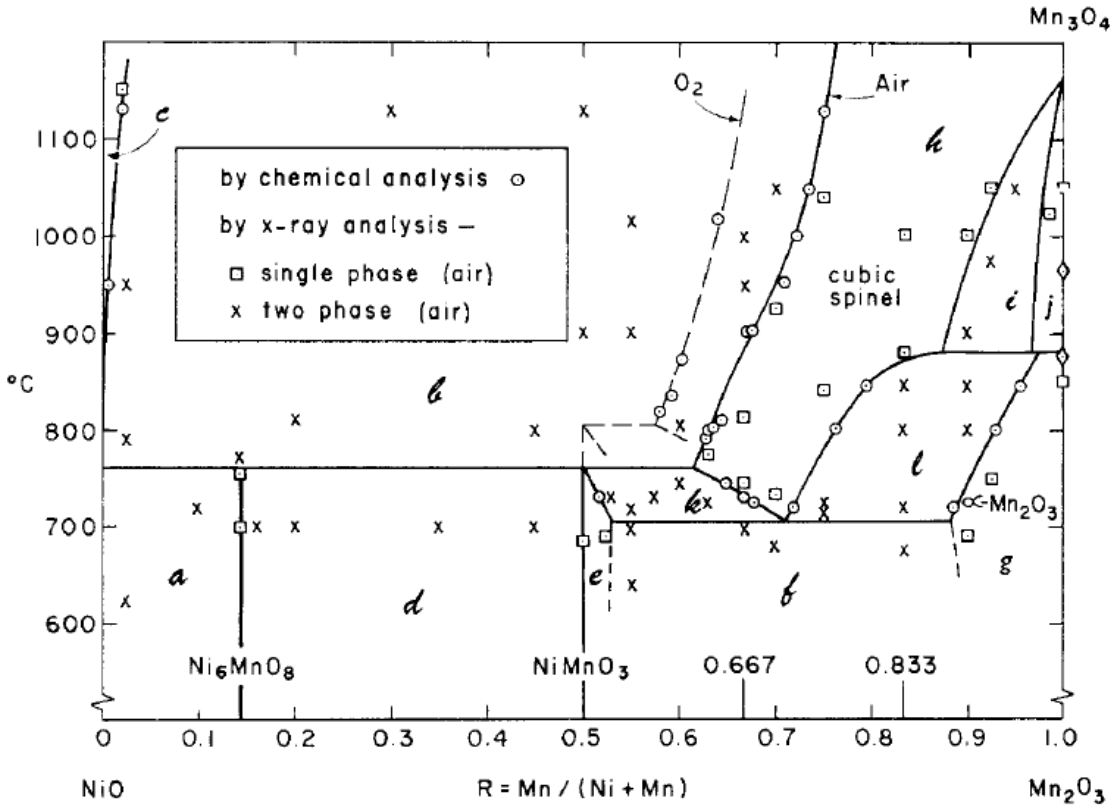

Figure 2.8. Phase diagram for the NiO – Mn_2O_3 – O_2 [36]

At higher temperatures i.e. > 900°C, NiO and O_2 loss was reported [36]. A tetragonal spinel Mn_3O_4 forms at temperatures > 1200°C. An extended phase diagram has more recently been reported by Tang *et al* in 1989 [18] for the lower temperatures (Figure 2.9.). During the preparation of the materials a slight change was implemented to prevent manganese acetate remaining in the solution after precipitation by adding a slight excess of oxalic acid 1M solution to the mixture of Ni and Mn acetates.

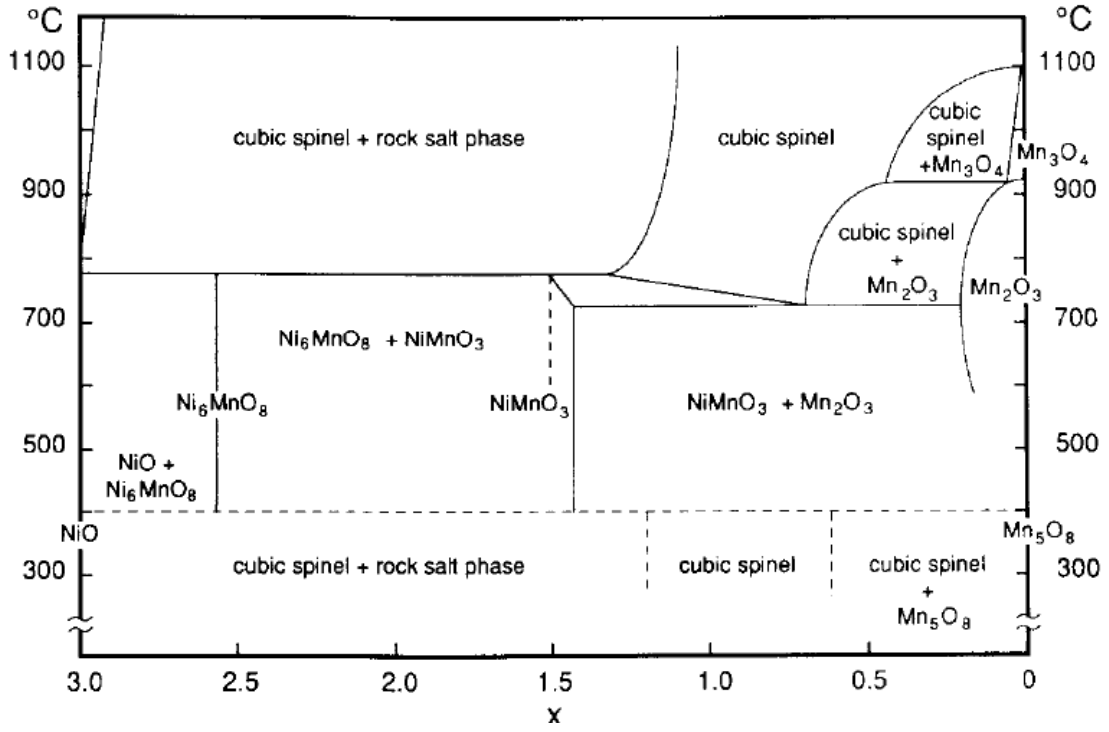

Figure 2.9. Phase diagram for the thermal decomposition of $Mn_{3-x}Ni_x(C_2O_4)_3 \cdot 6H_2O$ as mapped by Tang *et al* in 1989 [18]

At temperatures below 400°C it was found that a cubic spinel phase and Mn_5O_8 exists with a composition of $R > 0.8$. However, with a composition $R < 0.8$ a cubic spinel and a rock salt phase forms. Tang also verified that with a composition $0.6 < x < 1.2$ a metastable single – phase cubic spinel would be present.

At temperatures lower than 200°C a tetragonal spinel is witnessed and at 300°C the beginning of the formation of the cubic spinel is observed.

2.8. Properties of NTC Thermistors

NTC thermistors possess interesting thermal and electrical properties, these properties are of great importance when selecting them for a specific application. These properties are based on the geometry of the thermistor, the composition of metal oxides that are being used in the system and other additional materials (such as electrodes, inks, solders, leadwire, etc.) that are applied [37].

2.8.1. Thermal Properties

As thermistors are active systems, i.e. an electrical current is required for them to operate. The electrical current that is applied to a thermistor can be either DC or AC and the power is dissipated as heat causing the thermistor to Joule heat, this results in its body temperature rising above the temperature of its environment. The self heating effect is dependent not only on the applied power but also on the thermal dissipation factor δ_{th} and the geometry of the thermistor [4]. It can be expressed as:

$$\delta_{th} = dP/dT \tag{2-4}$$

This expresses the relationship between the power dissipation (P) and the thermistor's body temperature (T) increase. The thermal dissipation factor depends on the sensor design, thermal conductivity and motion of the medium where the thermistor is located. It is also dependant on heat transfer from the thermistor to its surroundings by conduction through its leads, by free convection in the medium, the length and thickness of the lead wires, and by radiation from the thermistor's surface [37]. The dissipation constant varies slightly due to changes in the thermistor's temperature, it is therefore measured typically at equilibrium conditions.

This will consequently be a source of error which will result in a flawed determination of the temperature of a considered object. Despite this, the self heating effect can sometimes be put to good use, for example in applications for sensing thermal radiation, fluid flow, and other stimuli [3].

Figure 2.10. shows the thermal events that take place when an electric current is applied to a NTC thermistor.

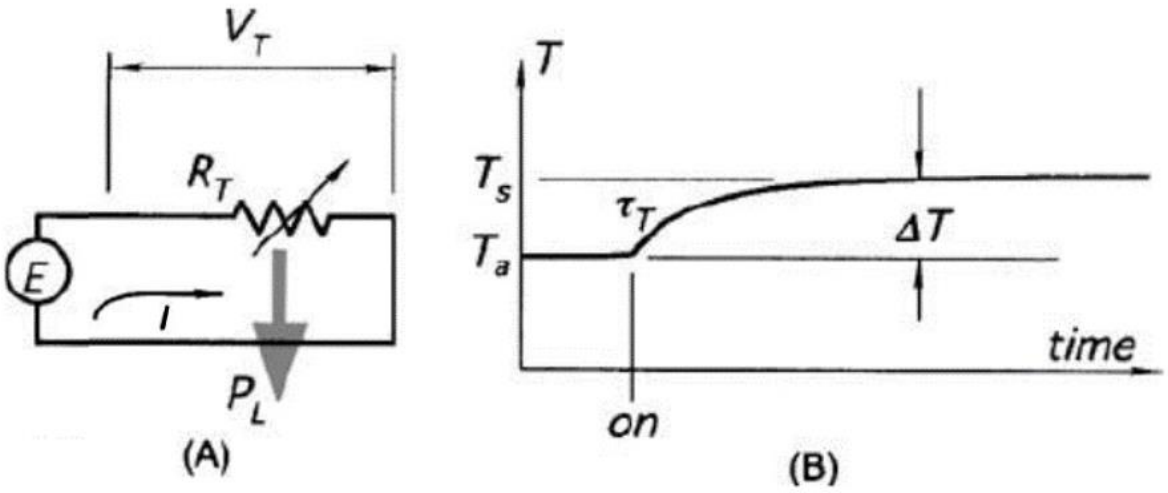

Figure 2.10. Representation of the self heating of a thermistor. (A) A current passes through the thermistor which causes self-heating; (B) the temperature of the thermistor rises with the thermal time constant ($\boldsymbol{\tau}$), P_L is the thermal power that is lost to the surroundings [3]

A voltage source (E) is connected to a thermistor (R_T), power (P_c) is applied to the circuit, the rate at which energy is supplied to the thermistor must be equal to the rate at which energy (H_L) is lost plus the rate at which energy (H_S) is absorbed by the thermistor, this is the thermal energy storage capacity (C) of the thermistor [3].

$$\frac{dH}{dt} = \frac{dH_L}{dt} + \frac{dH_S}{dt} \tag{2-5}$$

In accordance with the law of conservation of energy, the rate at which thermal energy is supplied to the thermistor in an electrical circuit must equal to the amount of power that is dissipated within the thermistor.

$$\frac{dH}{dt} = P_c = I^2 R_T = EI \tag{2-6}$$

Thermal energy that is lost by the thermistor to the environment is proportional to the temperature gradient rise (ΔT) between the thermistor and the surrounding temperature (T_A).

$$P_L = \frac{dH_L}{dt} = \delta\Delta T = \delta(T - T_A) \tag{2-7}$$

Thermal energy is absorbed by the thermistor producing a specific rise in temperature. The rate of heat absorption by the thermistor is proportional to the thermal capacity of the sensor assembly [3]. This is expressed as:

$$\frac{d\,H_A}{dt} = Tsm\frac{dT}{dt} = C\frac{dT}{dt} \tag{2-8}$$

where (Ts) is the specific heat, (m) is the mass of the thermistor, (H_A) is the heat absorbed and (C) is the heat capacity of the thermistor which is dependent on the materials that the thermistor is made from. The rate of heat absorption causes the thermistor's body temperature *T* to rise above that of its environment. The heat transfer equation after power has been applied at any time to the circuit is:

$$\frac{dH}{dt} = P_w = I^2R_T = \delta(T - T_A) + C\frac{dT}{dt} \tag{2-9}$$

This is a differential equation which describes the thermal behaviour of a thermistor [3]. When electric power (P_w) is supplied to the circuit constantly the solution to the differential equation is:

$$\Delta T = (T - T_A) = \frac{P_w}{\delta}\left[1 - exp\left\{\frac{-\delta}{C}t\right\}\right] \tag{2-10}$$

This equation demonstrates that when a significant amount of power is applied to the thermistor, its body temperature will rise higher than the environment temperature as a function of time. The transient conditions at "turn on" and all the applications that are based on the current – time characteristics are based upon this equation.

When an equilibrium is reached after waiting for a sufficient amount of time, the rate of change of temperature with respect to time is equal to zero (dT/dt = 0). The heat loss rate is equal to the supplied power.

$$\delta(T - T_A) = \delta\Delta T = P_w = E_T I_T \tag{2-11}$$

where (E_T) is the static thermistor voltage and (I_T) is the steady state current.

When a low voltage power is supplied to a thermistor with a high resistance, the current is extremely low resulting in the self-heating effect being reduced to a point where it is considered unimportant. The heat transfer equation is then:

$$\frac{dT}{dt} = \frac{-\delta}{C}(T - T_A) \tag{2-12}$$

Equation 2-13 is a mathematical statement of Newton's Law of Cooling.

$$T = T_A + (T_I - T_A)exp\left\{\frac{-t}{\tau}\right\} \tag{2-13}$$

where T_I is the initial body temperature, (T_A) is the ambient temperature and ($\boldsymbol{\tau}$) is the thermal time constant.

The thermal time constant is the amount of time it takes for a thermistor to reach 63.2% temperature difference of its final (asymptotic) value when it is subjected to a step function change in temperature under negligible power conditions [37].

2.8.2. Resistance – Versus – Temperature Characteristics

The resistance – temperature characteristics of thermistors allow them to be used in many applications of thermometry, temperature control and temperature compensation. In these applications the self-heating effect that is observed is undesirable, so the power supplied to the thermistor is kept as close to zero as possible. The zero – power of resistance of a thermistor (R_T) at a specified temperature (T) is when the power dissipation of the thermistor is considered negligible. The power is considered as negligible when any further reduction of power to the thermistor results in no more than 0.1 percent change in its resistance [37].

There are a number of equations that can be used to describe the resistance – versus – temperature characteristics of thermistors. Resistance versus temperature characteristics are often plotted with the logarithm of a specific resistance that is expressed as a function of the reciprocal of absolute temperature. Over any specified temperature range where the slope of a given material system is considered to have a straight line relationship between ln R_T and 1/T, the resistance of the device can be determined using equation 2-14.

$$R_T = R_{T0} exp\left[\frac{\beta(T_0 - T)}{TT_0}\right] \quad (2\text{-}14)$$

where R_T is the resistance at temperature T (measured in K), β is the "beta" or "material constant" which is the slope of the thermistor's R – T characteristics over a specified temperature range, and R_{T0} is the resistance at a specified temperature T0 (measured in K).

Thermistor manufacturers provide "beta" information for the thermistor materials they offer. Equation 2-14 can be rearranged to solve for beta (K) or temperature (°C) as follows:

$$\beta = \frac{TT_0}{T_0 - T} ln\left[\frac{R_T}{RT_0}\right] \tag{2-15}$$

$$T = \left[\frac{1}{\beta} ln\left[\frac{R_T}{R_{T0}}\right] + \frac{1}{T_0}\right]^{-1} - 273.15 \tag{2-16}$$

2.8.3. Electrical Properties of Nickel Manganite

Electrical conductivity in metals occurs due to movement of free electrons, which are always present. While in non – metallic, the conductivity is due to either the movement of electrons (electronic conductivity), valence holes or the movement of ions (ionic conductivity), it is common therefore for both of these movements to take place at the same time [4]. In semiconductors conduction occurs through the movement of free electrons and "holes", known collectively as charge carriers. When a semiconductor contains mainly mostly free holes it is known as a p – type and then it contains mostly free electrons it is known as n – type.

NMO is a semiconductor and its conduction is due to the same movement of electrons that occurs in metals, however the phenomenon of the mechanism is different as it is based on a thermally activated hopping mechanism [1, 38-41]. We can visualise conduction in insulators, conductors and semiconductors by plotting the available energy states of their electrons into a valence and conduction band. These bands in solid state physics are the bands closest to the Fermi level (E_F) which is the total chemical or electrochemical potential for electrons and consequently determine the electrical conductivity of the solid. The conduction process is dependent on whether there are electrons available in the conduction band. The valence band

is the highest range of electrons in which electrons are present at absolute zero temperature and the conduction band is the lowest range of vacant electronic states. In insulators, the electrons in the valence band are separated by a large gap from the conduction band, while in conductors (metals) the valence band overlaps the conduction band. In semiconductors the gap between the valence and conduction band is very small, which allows for thermal or other excitations to bridge this gap. Also the presence of a doping material can increase the conductivity dramatically because of the small gap.

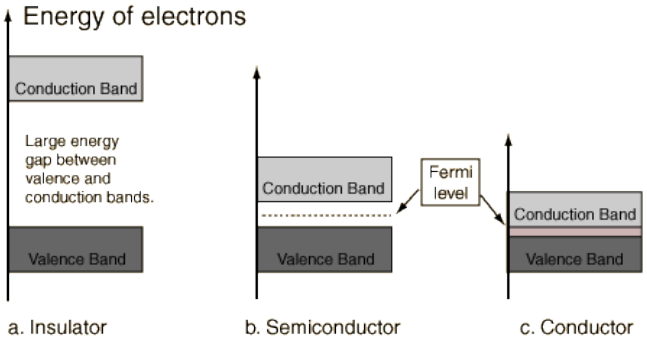

Figure 2.11. Band structure of insulators, semiconductors and conductors.

The electrons transfer themselves between manganese cations Mn^{3+} and Mn^{4+} with the different valance states causing a lattice distortion on the octahedral sites. As the hopping mechanism is thermally activated the conductivity has an inverse exponential dependence on temperature, whereby its resistance will decrease with an increase of temperature, thus giving NTC behaviour.

In NMO, the Ni^{2+} ions are substituted for Mn^{3+} ions which in turn leads to the formation of Mn^{4+} ions in its octahedral sites [42]. The electrical conductivity in NMO is as a result dependent on the concentration of Mn^{3+} donor and Mn^{4+} acceptor electron states, where electrons are transferred between the different valence states [43, 44]. Maximum conductivity

is theoretically achieved when the Mn^{3+} / Mn^{4+} ratio is 1:1 with an inversion parameter of x = 2 / 3.

Schmidt has suggested that there are possible jumps also between the Mn^{2+} and Mn^{3+} cations on tetrahedral and octahedral interstices respectively. Cations located on octahedral and tetrahedral sites are approximately the same distance from each other in comparison to two octahedral cations (~ 3.0Å). Electrons in Mn^{2+} may have weaker bonding than in Mn^{3+} which could possibly result in hopping between the two cations [2]. On the other hand tetrahedral Mn^{2+} cations may not contribute to the hopping, because donation of an electron from the Mn^{3+} cation to the Mn^{2+} cation would mean there are Mn^{3+} cations on the tetrahedral sites, which is undesirable [19]. The charge transfer and lattice distortion between the manganese cations is referred to as small polaron conduction [2, 45].

2.8.3.1. Resistivity of $NiMn_2O_4$

The resistivity of NTC NMO semiconductors follows the classical law of semiconductors [14, 46-49] (i.e. the Arrhenius equation) which is dependent on the temperature where the resistivity decreases exponentially with an increase in temperature:

$$\rho = \rho_0 \exp(\beta/T) \tag{2-17}$$

where ρ is the resistivity and ρ_o is the resistivity at infinite temperature. T is the temperature and β is the thermistor constant which is defined as the ratio between the activation energy for electrical conduction. The resistivity at infinite temperature is determined by the total number of 'B' lattice sites that are available to take part in the hopping process [50].

With

$$\beta = (W_a/k_B) \tag{2-18}$$

where W_a is the activation energy of the hopping mechanism and k_B is the Boltzmann constant.

2.8.3.2 The Small Polaron Conduction Hopping Mechanism in Nickel Manganite

The small polaron model can be used to describe the conductivity in ionic semiconductors, where a strong interaction between the electron and lattice is found. This strong interaction causes the mobility of the electron to be extremely small, becoming "self – trapped" in its own polarization fields [6, 51]. When the local charge distributions are rearranged it causes a slight displacement with the participating ions, this is known as a lattice distortion. The orbital of the electron which causes this distortion is small, the polaron transfer is therefore referred to as "small polaron hopping" [2, 17, 28].

In ionic or highly polar crystals such as semiconductors, Coulomb interactions between conduction electrons and lattice ions results in strong electron – phonon coupling. The electron in this case is always surrounded by a cloud of virtual phonons which corresponds to the electron pulling nearby positive ions towards it and pushing negative ions away. The electron and its virtual phonons together can be treated as a new composite particle, called a polaron. In a polaron, the electron sits in a potential well because of the ion displacements it has created. The potential wells' shape and strength is such that the electron can be confined to a volume of approximately one unit cell or less. In this case, the polaron is called a small polaron.

Several authors have successfully described the electrical conductivity of $NiMn_2O_4$ as a thermally activated "hopping" mechanism between the Mn^{3+} and Mn^{4+} cations present on the octahedral sites [17, 19, 20, 24, 28, 43, 52-60], which results in a small polaron.

The hopping of small polarons between lattice sites is thermally activated [30], therefore conductivity can be expressed by the following equation:

$$\sigma = \sigma_o \exp(-\frac{E_a}{k_B T}) \quad (2\text{-}19)$$

where σ_o is the temperature independent constant, k_B is Boltzmann's constant, E_a the activation energy and T is the temperature.

Localised Mn^{3+} states are associated with a strong electron – phonon coupling and a strongly Jahn – Teller distorted Mn^{3+} O_6 octahedra. The Jahn – Teller distortion of the Mn^{3+} cations leads to a formation of polarons, whereby electrons are thought to be localised due to the strong ionic character of the bonding in spinel crystals [28]. Electrons are self – trapped in the localised states, causing the surrounding positive ions to move closer resulting in the negative ions being repelled which causes a lattice distortion. The electrons cannot move unless the distortion they caused moves with it. The distortion of the lattice is also caused by the size differences associated with cation valence [6]. When the electron becomes self – trapped, it is considered to be in a potential well and activation energy is required to be met to enable the electron to be freed, this is shown in equation 2-19.

A polaron is the lattice distortion, which is the result of the reconfiguration of the electron distributions, which is what takes place when an electron is transferred from a donor ion (e.g. Mn^{3+}) to an acceptor ion (e.g. Mn^{4+}) [6].

The charge transport is thought to be achieved by small polaron dc hopping, this is best understood from a simple real – space picture, which is in contrast to classical semiconductors (CS) where their charge carriers are delocalised and can best be described in momentum space.

Small polaron DC hopping conductivity σ_{DC} can be expressed by the following generalised equation.

$$\sigma_{DC} = DT^{\gamma} exp\left(-\frac{T_0}{T}\right)^{p} \quad (2\text{-}20)$$

where D is the temperature independent contribution to the conductivity, T_0 characteristic temperature, γ describes the pre – exponential temperature dependence, and p the exponential power law dependence [52]. For conventional variable range hopping $0.25<p = \gamma/2<0.5$, for nearest neighbour polaron hopping in the quantum tunnelling regime $p=\gamma=1$, and for the Boltzmann's thermally activated transport $p=1$ and $\gamma=0$ Figure 2.12. shows the jump of an electron from a Mn^{3+} cation to a Mn^{4+} ion, which are both located in the octahedral sites.

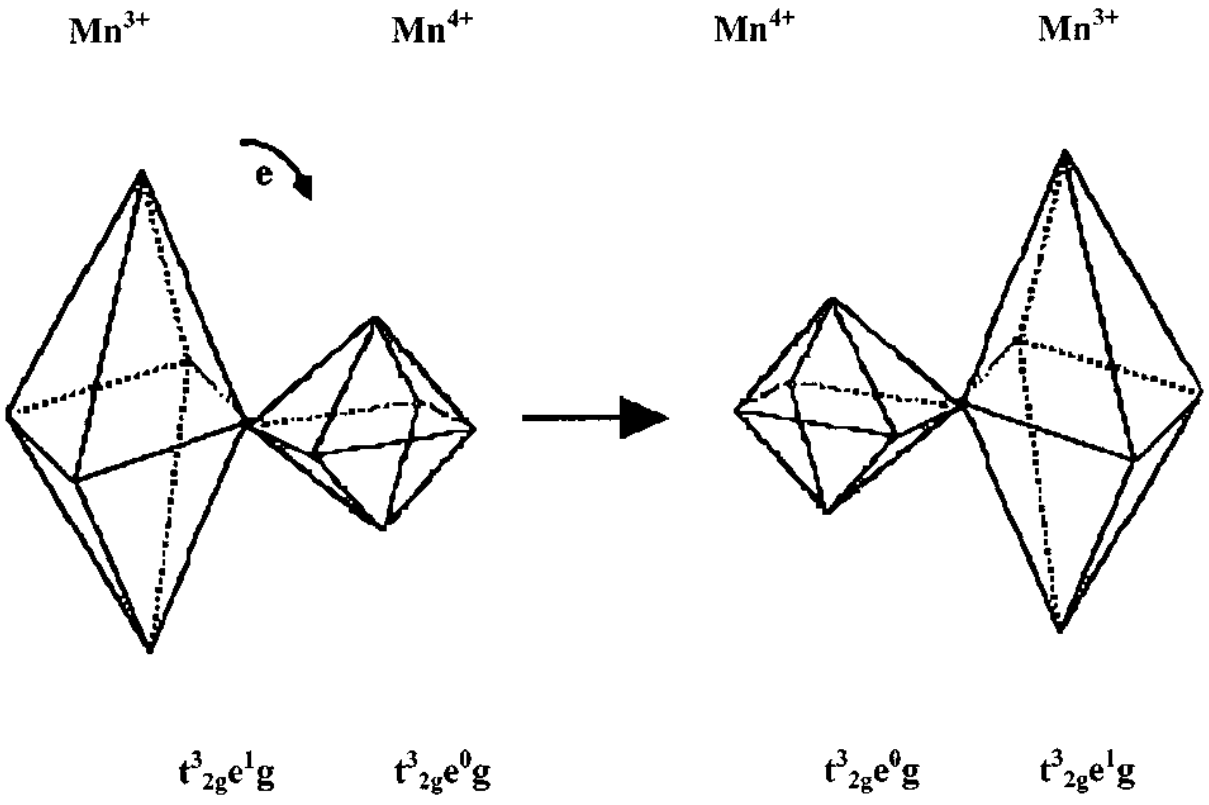

Figure 2.12. Electron jump between two manganese ions (after Metz [42]).

The localisation of donor Mn^{3+} and acceptor Mn^{4+} states arise from random crystal field fluctuations, internal degrees of freedom and inhomogeneous lattice strain.

2.8.3.3. Review of Other Conductivity Models

It has been shown that decreasing the oxygen content in NMO will decrease the Mn^{4+} concentration, causing the conductivity to decrease. Also a maximum in conductivity in NMO was not achieved with an even ratio of Mn^{3+} and Mn^{4+} which suggests that the conduction may not rely completely on hopping mechanisms [31].

Changes in oxygen content are a major contributor to changing the cationic arrangement, and consequently the conductivity, but it is also possible that the change in the cationic distribution may not be the only important factor.

2.8.3.3.1. Localised Electron Hopping

At very low temperatures electron hopping between localised impurity states can occur and are able to dominate other electrical transport systems. This is achieved either by ionisation of a donor or acceptor level or by the excitation of electrons from the valance to the conduction band.

Electron hopping also occurs in amorphous and highly disordered materials, which exhibit large energy ranges of localised electron states. In NMO it is possible that localised electron hopping occurs, because the manganese cations which participate in electron hopping can be regarded as localised electron states [2].

2.8.3.3.2. Percolation Theory

Conducting electrons will travel through a sample via the most conductive path. The most conducting path is generally a randomly distributed sequence of sites, where the average

distance between them is low. A percolation problem arises when the electrons try to find the most conductive path through a sample. This is best illustrated in Figure 2.13.

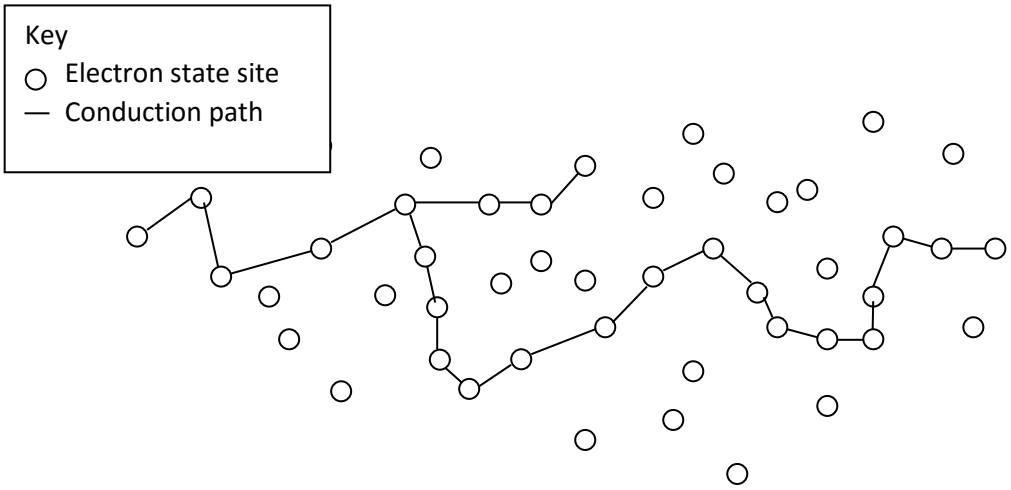

Figure 2.13. Percolation pathway through randomly distributed electron states.

On each of the most conducting paths there is a certain critical radius r_c, this is the largest distance between two sites. Hopping conduction is dominated by electrons propagating via several of these most conducting paths, hopping along these paths is dominated by the critical radius r_c.

Connectivity does not wholly depend on spatial distribution, but also on their separation in energy space. A percolation problem arises macroscopically with the percolation threshold parameter ξ_C, affecting both the energy and spatial contributions.

$$\xi_C \geq \frac{2r_{ij}}{a} + \frac{\varepsilon_{ij}}{k_B T} \tag{2-21}$$

where r_{ij} and ε_{ij} are the separation in real and energy space of the i and j electron states and *a* is a localisation length [43]. Resistivity is a hopping process with a ξ_{ij} value that is close to the threshold value. Macroscopic resistivity is expressed as:

$$\rho = \rho_o \exp(\xi_c) \tag{2-22}$$

where ρ is resistivity and ρ_o is resistivity at infinite temperature.

2.8.3.3.3. Nearest Neighbour Hopping

Nearest neighbour hopping (NNH) is based on the equation of the percolation value (equation 2-21).

NNH only occurs when $\frac{\varepsilon_{ij}}{k_B T}$ much larger in comparison to the $\frac{2r_{ij}}{a}$, which occurs at high temperatures. If the second term is significantly smaller it will contribute slightly to the overall resistance. The overall resistance is reduced considerably if electrons only transfer to their nearest neighbour, resulting in a small value for r_{ij}. Having a low value for ξ_{ij} is favourable in hopping processes. $\frac{\varepsilon_{ij}}{k_B T}$ in the above equation is independent of temperature, therefore resistivity is:

$$\rho = \rho_0 \exp(\frac{\varepsilon_3}{k_B T}) \tag{2-23}$$

where ε_3 is the average activation energy between the nearest neighbour donors and acceptors which is constant at all temperatures [2].

2.9. Aging of the Electrical Characteristics of NTC Thermistors

In sophisticated equipment in areas such as medicine, aerospace and cryogenics, NTC thermistors are required to be highly reliable in extreme operating environments. However, over time and under thermal stress i.e. above 150°C [61], the resistivity of NTC ceramics increases, this is generally referred to as aging [23, 39, 42, 62-64], which can eventually lead to failure of the device as resistivity further increases. The first detailed case of aging was reported by Becker *et al* [65] in 1946 where the resistance rose with time [64, 66]. In this case two three quarter inches diameter disks were made of two materials with silver contacts and soldered leads. Material one was composed of manganese and nickel oxides and material two was composed of oxides of manganese, nickel and cobalt. The materials were aged in an oven at 105°C and tested periodically at 24°C for 3 years. A percentage change in resistance over its initial value was plotted versus the logarithm of the time in the oven, shown in Figure 2.13. It was found that most of the aging took place in the first day or week of the test. This discover led to the determination that if the disks were pre-aged for a week or a month, with the subsequent change in the resistance after referred to as the resistance after pre-aging, they would only age 0.2% in one year which corresponded to a temperature change of 0.05°C. If the thermistors were mounted in an evacuated tube or coated with a thin layer of glass, they would age even less.

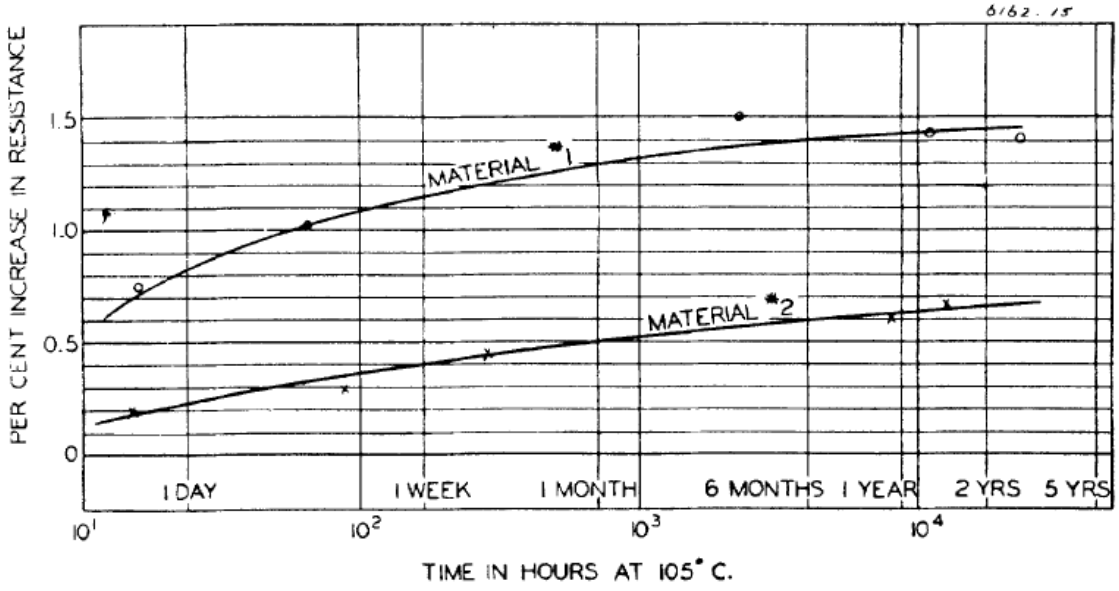

Figure 2.14. The aging characteristics of thermistors made of manganese and nickel oxides (material 1) and manganese, nickel and cobalt oxides (material 2)

Due to the demand for NTC thermistors to be in advanced applications, the need for their reliability at extreme temperatures is high, their aging characteristics therefore have to be minimised.

The aging coefficient of NTC thermistors is characterised by:

$$(R - R_0)/R_0 \times 100\% \tag{2-24}$$

where R_0 is the resistance value at 20K before aging and R is the resistance value at 20K after aging [47]. The aging coefficient indicates the long term stability of the electrical characteristics of NTC thermistors.

There are a few models which have been reported to explain how aging occurs [61]. Fang et al [67] and Castelan *et al* [68] found that aging of NMO depends upon their thermal history and compositions. For example, an increase in the Ni content will lead to an increase in the

aging coefficient but it was discovered that with a Ni content of less than or equal to 0.7 the thermistor showed remarkable electrical stability with an aging coefficient of less than 0.5%.

Macklen has suggested a number of factors that can influence the aging process. These include contact degradation, the degree of inversion and the distribution of the cations between the octahedral and tetrahedral sites without changing the overall chemical composition [44]. Ni will diffuse locally between lattice sites, which will slowly change the carrier concentration. Also another suggestion for the instability of NMO electrical properties was due to a possible change in its oxygen content. However experiments performed in different oxygen atmospheres resulted in little influence in the aging behaviour [44]. The author also suggested that aging could be due to a change in the carrier concentration and mobility that are associated with the electronic states on the crystallite surfaces [6, 44].

It is generally accepted that aging is due to the exchange of cations between the sublattice tetrahedral sites and octahedral sites [57]. Mossbauer Spectroscopy has been used to show that the migration of Mn^{3+} occurs between the octahedral and tetrahedral sites by Groen et al. [61]. The authors also suggested that aging is also strongly dependant on the atmosphere during cooling after sintering of the material. As result a model was suggesting stating that during aging a cationic vacancy migration occurs from grain boundary to bulk. A cation vacancy assisted migration of cations and cationic vacancies occurs to thermodynamically more stable sites [61]. These processes result in an increase of metal vacancies on the B-sites in the spinel inside the grains, resistivity therefore increases as the hole conduction is over the B-sites in the spinel. Some studies have also shown that aging also occurs due to the migration of cation vacancies from the grain boundary to the interior [57].

2.9.1. Effect of Dopants on $NiMn_2O_4$ Aging Process and its Conductivity

Aging has been reported to be improved by changing the composition of the thermistor. In thermistors with the composition $Cu_{0.3}Ni_{0.66}Mn_{2.04}O_4$ Gao *et al* found that aging was reduced

and electrical resistivity was improved with a lower concentration of Cu^{+} [69]. A sintered ceramic was obtained through solid state coordination reaction by milling a mixture of copper acetate, nickel acetate and oxalic acid at room temperature. The spinel structured oxide powder was attained by calcining the mixed oxalate in air at 800°C for 2 hr. The oxide powder compact was sintered at a relatively low temperature of 1100°C for 2.5 hr where it attained a relative density of around 98%. The electrical resistances of the sintered ceramic were measured at 25°C and 50°C with an average specific electrical resistivity ρ25 of 63.3Ω.cm and $B_{25/50}$ of 2740K. A lower shift in the electrical resistivity upon aging at 150°C for 500 hr of 5.4% was observed which was lower than previously reported by Metz et al [42] with around a 15% shift. They suggested the reason behind this was due to a fine grained microstructure and a lower sintering temperature. Since a lower sintering temperature was used the concentration of Cu^{2+} ions in the as – obtained ceramic is increased and less Cu^{+} is present. The higher Cu^{2+} concentration causes a lower concentration of Mn^{4+} and consequently a decrease in the Mn^{4+} : Mn^{3+} ratio resulting in a decrease in the electrical conductivity of the sample. The aging of the ceramic which is caused by the oxidation of Cu^{+} to Cu^{2+}, is inhibited because of the lower concentration of Cu^{+} and Cu^{2+} in the sample.

Increase in Co leads to increased conduction and decrease in resistivity [70, 71]. Balitska *et al* produced Ni enriched ($Cu_{0.1}Ni_{0.8}Co_{0.2}Mn_{1.9}O_4$), Cu enriched ($Cu_{0.8}Ni_{0.1}Co_{0.2}Mn_{1.9}O_4$) and Co enriched ($Cu_{0.1}Ni_{0.1}Co_{1.6}Mn_{1.2}O_4$) ceramic samples and found that their cobalt enriched samples had a lower ageing coefficient [66]. The samples were each measured at 25°C after certain hours of degradation at an aging temperature of 125°C (24,72, 144, 288, 500, 740 and 1000 hr). The electrical resistance measurements of the prepared NTC samples were performed using a digital multimeter. The greatest degradation was observed in the early hours of aging followed by the longer saturation effect. In the Co – enriched NTC sample the saturation effect

was quickly achieved after just 100 hr of thermal exposure, while the Ni enriched sample took 500 – 600 hr of aging to achieve saturation.

Addition of Cu to the NMO improves the conductivity of the thermistor however it becomes unstable with time [68, 72]. Castelan *et al* [73] produced samples from powders from oxalic precursor with two different compositions, one doped with Barium the other without, $Mn_{1.93}NiO_{0.66}Cu_{0.41}O_4$ and $Mn_{1.87}Ni_{0.66}Cu_{0.46}O_4$ with 3.6% Ba. The samples were made into small blocks 2.5cm long and fired at 126°C and sintered for 1 ½ hr. The resistivity of the samples was measured systematically at 25°C. It was found that the addition of Cu did not reduce the resistivity of the thermistor, however when a small amount of Cu is added to the NMO aging would be greatly increased. Yet when more Cu is added the aging was found to be disproportional to the quantity added. When Ba is added to the Ni – Cu – Mn – O system an increase in the thermistor's stability and resistivity is observed [68]. It was concluded that the instability of the resistivity of the materials was linked to the modification of the equilibrium between the Mn^{3+} and Mn^{4+} ions in the octahedral sites.

Several authors [64, 70, 74] have combined both Cu and Co into the NMO system to successfully produce a highly stable and conductive thermistor, which benefits from both the Co and the Cu additions characteristics.

An increase in the thermistor's stability and resistivity was found by Sarrion *et al* and Topfer *et al* when Li was added to the NMO system [75, 76], with similar results found with the addition of Mg [77].

The substitution of Indium for Mn in the NMO system leads to increased resistivity, this is due to the formation of single phase spinel compounds. The reduction in aging is possibly due to the fact In has only one oxidation state (3+) under the conditions it is to be used in [78].

The conditions of the NTC ceramics can have a huge effect on the thermistor's conductivity behaviour. For example if the sintering temperature of the NTC ceramic is changed, it can lead

to a change in the cation rearrangement thus influencing the electrical conductivity [74]. Vakiv *et al* found that in a sample with composition $Cu_{0.4}Ni_{0.4}Co_{0.4}Mn_{1.8}O_4$ a change in sintering temperature from 1100 to 1200 and 1300°C caused the sample conductivity to change from 3.64, 1.83 and 2.64$\Omega^{-1}m^{-1}$ respectively [74]. Annealing NMO at 1050°C resulted in good electrical stability with an aging coefficient of less than 1%. However, when annealed at 850°C, and especially with an increase in Ni, the aging coefficient could increase up to 3.8% [67].

Liang *et al* studied the effect ball milling had on the electrical stability of $Ni_{0.6}Si_{0.2}Al_{1.6}O_4$ and found that increased milling time led to a decrease in the resistance drift along with a decrease in the particle size and $B_{25/85}$ constant and activation energy [57]. Raw materials of NiO, SiO_2, Mn_2O_2 and Al_2O_3 were mixed and milled for 12 hr with alcohol and agate balls, the resultant slurry was then dried at 80°C in an oven for 12 hr. The prepared powder was then calcined at 950°C for 2 hr and then further milled for 6, 12, 24, and 48 hr respectively. The dried powders were ground in mortar and passed through a 200 – mesh sieve. Polyvinyl alcohol (PVA) solution was then added and the mixture ground in mortar and ball milled for 2 hr in a plastic jar using agate balls. The powders were then pressed and sintered at 1280°C for 4 hr in an air furnace. The activation energy of the samples increased with a decrease of the density of the compounds and a resistance drift of 0.02% was achieved when ball milling reached 48 hr. With a long ball milling time (48 hr) a well refined powder could be obtained and the electrical reliability of NTC thermistors were therefore improved using these powders.

2.10. Summary

In this chapter the general properties of NMO were presented with detailed descriptions of the thermal and electrical properties. The importance of cationic distribution in the system was stressed and its effects on the conductivity and resistivity on NMO.

Details of the phase stability of the NMO system were also given, which is essential in explaining the required composition and temperature required in producing the desired spinel structure.

The undesirable effects of aging were discussed along with the effect dopants can have on improving aging along with the resistivity of NMO.

References

1. de Gyorgyfalva, G., A.N. Nolte, and I.M. Reaney, *Correlation between microstructure and conductance in NTC thermistors produced from oxide powders.* Journal of the European Ceramic Society, 1999. **19**(6-7): p. 857-860.
2. Schmidt, R., *Production and performance of thin and thick film NTCR thermistors based on $NiMn_{(2)}O_{(4)}$ +.* 2003, University of Durham: Durham.
3. Fraden, J., *Handbook of Modern Sensors - Physics, Designs and Applications (3rd Edition)*. Springer - Verlag.
4. Feteira, A., *Negative Temperature Coefficient Resistance (NTCR) Ceramic Thermistors: An Industrial Perspective.* Journal of the American Ceramic Society, 2009. **92**(5): p. 967-983.
5. Vasantha R.W. Amarakoon, B.C.L., Hernandez, O, Fagan, J. G. Pietras, J. and Peterson, J. L. *Thermistors - Fundamentals and Manufacturing Issues*. 10/12/2007 ed. 1995: American Ceramic Society. 12.
6. Schulze, H.M., *Synthesis and characterization of nickel manganite thin films for application in uncooled microbolometers*, in *Materials Science and Engineering*. 2008, The Pennsylvania State University. p. 184.
7. Moulson, A.J. and Herbert, J.M. *Electroceramics: materials, properties, applications*. 2003: Wiley.
8. Chen, Y.L. and S.F. Yang, *PTCR effect in donor doped barium titanate: review of compositions, microstructures, processing and properties.* Advances in Applied Ceramics, 2011. **110**(5): p. 257-269.
9. Aga, Z.B.H. and S.R. Ramanan, *Electrical and structural characterization of PTCR pure $BaTiO_3$ nanopowders synthesized by sol-gel emulsion technique.* Journal of Electroceramics, 2012. **28**(2-3): p. 109-117.
10. Sachse, H., *Semiconducting temperature sensors and their applications*. 1975: Wiley.
11. Fagan, J.G. and V.R.W. Amarakoon, *Reliability and reproducibility of ceramic sensors .1. ntc thermistors.* American Ceramic Society Bulletin, 1993. **72**(1): p. 70-79.
12. Verwey, E.J.W. and E.L. Heilmann, *Physical properties and cation arrangement of oxides with spinel structures.* Journal of Chemical Physics, 1947. **15**(4): p. 174-180.
13. Buchanan, R.C., *Ceramic Materials for Electronics, Third Edition*. 2004: Taylor & Francis.
14. Barrk K. and B. D.Y., *Electrical properties of Ni-Mn-Co-(Fe) oxide thick-film NTC thermistors prepared by screen printing.* Journal of Materials Science-Materials in Electronics, 2003. **14**(2): p. 81-87.
15. Bragg, W.H., *On the structure of the spinel group of crystals.* Philosophical Magazine, 1916. **31**(181-86): p. 88-88.
16. Bragg, W.H., *The structure of the spinel group of crystals.* Philosophical Magazine, 1915. **30**(175-80): p. 305-315.
17. Schmidt, R., A. Basu, and A.W. Brinkman, *Small polaron hopping in spinel manganates.* Physical Review B, 2005. **72**(11).
18. Tang, X.X., A. Manthiram, and J.B. Goodenough, *$NiMn_2O_4$ revisited.* Journal of the Less-Common Metals, 1989. **156**: p. 357-368.
19. Ryu, J., D.S. Park, and R. Schmidt, *In-plane impedance spectroscopy in aerosol deposited $NiMn_{(2)}O_{(4)}$ negative temperature coefficient thermistor films.* Journal of Applied Physics, 2011. **109**(11).
20. Diez, A., et al., *Structure and physical properties of nickel manganite $NiMn_{(2)}O_{(4)}$ obtained from nickel permanganate precursor.* Journal of the European Ceramic Society, 2010. **30**(12): p. 2617-2624.

21. Ashcroft, G., I. Terry, and R. Gover, *Study of the preparation conditions for $NiMn_2O_4$ grown from hydroxide precursors.* Journal of the European Ceramic Society, 2006. **26**(6): p. 901-908.
22. Schmidt, R., A. Basu, and A.W. Brinkman, *Production of NTCR thermistor devices based on $NiMn_2O_{4+delta}$.* Journal of the European Ceramic Society, 2004. **24**(6): p. 1233-1236.
23. Fritsch, S., et al., *Correlation between the structure, the microstructure and the electrical properties of nickel manganite negative temperature coefficient (NTC) thermistors.* Solid State Ionics, 1998. **109**(3-4): p. 229-237.
24. Jadhav, R.N. and V. Puri, *Influence of copper substitution on structural, electrical and dielectric properties of $Ni_{((1-x))}Cu_{(x)}Mn_{(2)}O_{(4)\ (0 <= x <= 1)}$ ceramics.* Journal of Alloys and Compounds, 2010. **507**(1): p. 151-156.
25. Topfer, J., et al., *Cation valencies and distribution in the spinels $NiMn_2O_4$ and $MzNiMn_2$-Zo_4 (m = li, cu) studied by xps.* Physica Status Solidi a-Applied Research, 1992. **134**(2): p. 405-415.
26. Housecroft, C.E. and A.G. Sharpe, *Inorganic Chemistry*. 2008: Pearson Prentice Hall.
27. K. G. Ghiassi, R.J.L.; Available from: http://chemwiki.ucdavis.edu/Inorganic_Chemistry/Coordination_Chemistry/Basics_of_Coordination_Chemistry/Coordination_Numbers_and_Geometry/Jahn-Teller_Distortions.
28. Schmidt, R., et al., *Electron-hopping modes in $NiMn_2O_{4+delta}$ materials.* Applied Physics Letters, 2005. **86**(7).
29. Gillot, B., et al., *Electrical-conductivity of copper and nickel manganites in relation with the simultaneous presence of Mn_{3+}-ions and Mn_{4+}-ions on octahedral sites of the spinel structure.* Solid State Ionics, 1992. **51**(1-2): p. 7-9.
30. Larson, E.G., R.J. Arnott, and D.G. Wickham, *Preparation, semiconduction and low-temperature magnetization of system $Ni_{1-x}Mn_{2+x}O_4$.* Journal of Physics and Chemistry of Solids, 1962. **23**(DEC): p. 1771-&.
31. Macklen, E.D., *Electrical-conductivity and cation distribution in nickel manganite.* Journal of Physics and Chemistry of Solids, 1986. **47**(11): p. 1073-1079.
32. Gillot, B., et al., *Electrical-properties and cationic distribution in cubic nickel manganite spinels $Ni_xMn_{3-x}O_4$, 0.57-less-than-x-less-than-1.* Solid State Ionics, 1991. **44**(3-4): p. 275-280.
33. Brabers, V.A.M., F.M. Vansetten, and P.S.A. Knapen, *X-ray photoelectron-spectroscopy study of the cation valencies in nickel manganite.* Journal of Solid State Chemistry, 1983. **49**(1): p. 93-98.
34. Hashemi, T. and A.W. Brinkman, *X-ray photoelectron-spectroscopy of nickel manganese oxide thermistors.* Journal of Materials Research, 1992. **7**(5): p. 1278-1282.
35. Boucher, B., *Structure magnetique du manganite de nickel.* Comptes Rendus Hebdomadaires Des Seances De L Academie Des Sciences, 1959. **249**(4): p. 514-516.
36. Wickham, D.G., *Solid-phase equilibria in the system NiO-Mn_2O_3-O_2.* Journal of Inorganic & Nuclear Chemistry, 1964. **26**(8): p. 1369-1377.
37. GE, *NTC Thermistors.*
38. Savic, S.M., et al., *Electrical and transport properties of nickel manganite obtained by Hall effect measurements.* Journal of Materials Science-Materials in Electronics, 2009. **20**(3): p. 242-247.
39. Kukuruznyak, D.A., J.G. Moyer, and F.S. Ohuchi, *Improved aging characteristics of NTC thermistor thin films fabricated by a hybrid sol-gel-MOD process.* Journal of the American Ceramic Society, 2006. **89**(1): p. 189-192.

40. Muralidharan, M.N., et al., *Effect of Cu and Fe addition on electrical properties of Ni-Mn-Co-O NTC thermistor compositions.* Ceramics International, 2012. **38**(8): p. 6481-6486.
41. Nikolic, M.V., et al., *Far infrared reflectance of sintered nickel manganite samples for negative temperature coefficient thermistors.* Materials Research Bulletin, 2007. **42**(8): p. 1492-1498.
42. Metz, R., *Electrical properties of NTC thermistors made of manganite ceramics of general spinel structure: $Mn_{3-x-x'}M_xN_{x'}O_4$ (0 <= x plus x ' <= 1; M and N being Ni, Co or Cu). Aging phenomenon study.* Journal of Materials Science, 2000. **35**(18): p. 4705-4711.
43. Schmidt R., B.A.W., *Electrical properties of screen-printed $NiMn_2O_{4+delta}$.* Journal of the European Ceramic Society, 2005. **25**(12): p. 3027-3031.
44. Macklen, E.D., *Thermistors*. 1979, Glasgow, Scotland: Electrochemical Publications Ltd.
45. Goodenough, J.B. and A.L. Loeb, *Theory of ionic ordering, crystal distortion, and magnetic exchange due to covalent forces in spinels.* Physical Review, 1955. **98**(2): p. 391-408.
46. Luo, W., et al., *Negative Temperature Coefficient Material with Low Thermal Constant and High Resistivity for Low-Temperature Thermistor Applications.* Journal of the American Ceramic Society, 2009. **92**(11): p. 2682-2686.
47. Lan, Y.Q., et al., *Construction and Characterization of NTC Thermistors at Low Temperature.* International Journal of Thermophysics, 2010. **31**(8-9): p. 1456-1465.
48. Hrovat, M., et al., *Thick-film strain and temperature sensors on LTCC substrates.* Microelectronics International, 2006. **23**(3): p. 33-41.
49. Park, K., *Fabrication and electrical properties of Mn-Ni-Co-Cu-Si oxides negative temperature coefficient thermistors.* Journal of the American Ceramic Society, 2005. **88**(4): p. 862-866.
50. Jagtap, S., et al., *'Lead Free' thick film thermistors: a study of variation in glass frit concentration and organics composition.* Journal of Materials Science-Materials in Electronics, 2010. **21**(9): p. 861-867.
51. Böttger, H. and V.V. Bryksin, *Hopping Conduction in Solids*. 1985: VCH.
52. Schmidt, R. and A.W. Brinkman, *ac hopping admittance in spinel manganate negative temperature coefficient thermistor electroceramics.* Journal of Applied Physics, 2008. **103**(11).
53. Schmidt, R., M. Parlak, and A. Brinkman, *Control of the thickness distribution of evaporated functional electroceramic NTC thermistor thin films.* Journal of Materials Processing Technology, 2008. **199**(1-3): p. 412-416.
54. Schmidt, R. and A.W. Brinkman, *Studies of the temperature and frequency dependent impedance of an electroceramic functional oxide NTC thermistor.* Advanced Functional Materials, 2007. **17**(16): p. 3170-3174.
55. Kukuruznyak, D.A., et al., *Electrical screening of ternary NiO-Mn_2O_3-Co_3O_4 composition spreads.* Applied Surface Science, 2006. **252**(10): p. 3828-3832.
56. Schmidt, R., et al., *Screen printing of co-precipitated $NiMn_2O_{4+delta}$ for production of NTCR thermistors.* Journal of the European Ceramic Society, 2003. **23**(10): p. 1549-1558.
57. Liang, S., et al., *An efficient way to improve the electrical stability of $Ni_{(0.6)}Si_{(0.2)}Al_{(0.6)}Mn_{(1.6)}O_{(4)}$ NTC thermistor.* Ceramics International, 2011. **37**(7): p. 2537-2541.

58. Basu, A., et al., *A study of the electronic states of NixMn3-xO4+delta thin films using scanning tunneling microscopy and current imaging tunneling spectroscopy.* Journal of the European Ceramic Society, 2004. **24**(6): p. 1149-1152.
59. Schmidt, R., et al., *An investigation into the surface topology and thickness profile of functional ceramic spinel manganate sputtered, evaporated and screen-printed layers.* Applied Surface Science, 2006. **252**(24): p. 8760-8767.
60. Park, K., *Structural and electrical properties of FeMg0.7Cr0.6Co0.7-xAlxO4 (0 <= x <= 0.3) thick film NTC thermistors.* Journal of the European Ceramic Society, 2006. **26**(6): p. 909-914.
61. Groen, W.A., et al., *Aging of NTC ceramics in the system Mn-Ni-Fe-O.* Journal of the European Ceramic Society, 2001. **21**(10-11): p. 1793-1796.
62. de Gyorgyfalva, G. and I.M. Reaney, *Decomposition of NiMn2O4 spinel: an NTC thermistor material.* Journal of the European Ceramic Society, 2001. **21**(10-11): p. 2145-2148.
63. Shpotyuk, O., et al., *Aging phenomena in Cu0.1Ni0.8Co0.2Mn1.9O4 NTC ceramics*, in *Euro Ceramics Vii, Pt 1-3*. 2002, Trans Tech Publications Ltd: Zurich-Uetikon. p. 1317-1320.
64. Vakiv, M.M., et al., *Ageing behavior of electrical resistance in manganite NTC ceramics.* Journal of the European Ceramic Society, 2004. **24**(6): p. 1243-1246.
65. Becker, J.A., C.B. Green, and G.L. Pearson, *Properties and uses of thermistors - thermally sensitive resistors.* Bell System Technical Journal, 1947. **26**(1): p. 170-212.
66. Balitska, V.O., et al., *On the analytical description of ageing kinetics in ceramic manganite-based NTC thermistors.* Microelectronics Reliability, 2002. **42**(12): p. 2003-2007.
67. Fang, D.L., et al., *Aging of nickel manganite NTC ceramics.* Journal of Electroceramics, 2009. **22**(4): p. 421-427.
68. Castelan, P., et al., *Aging study of nickel-copper-manganite negative temperature-coefficient thermistors by thermopower measurements.* Journal of Applied Physics, 1992. **72**(10): p. 4705-4709.
69. Gao, J.F., et al., *Preparation and electrical properties of copper-nickel manganite ceramic derived from mixed oxalate.* Sensors and Actuators a-Physical, 2007. **135**(2): p. 472-475.
70. De Vidales, J.L.M., et al., *Preparation and characterization of spinel-type Mn Ni Co O negative temperature coefficient ceramic thermistors.* Journal of Materials Science, 1998. **33**(6): p. 1491-1496.
71. Zheng, C.H. and D.L. Fang, *Preparation of ultra-fine cobalt-nickel manganite powders and ceramics derived from mixed oxalate.* Materials Research Bulletin, 2008. **43**(7): p. 1877-1882.
72. Baliga, S. and A.L. Jain, *Electrical-conduction and ordering in CuxNi1-xMn2O4 spinels.* Materials Letters, 1990. **9**(5-6): p. 180-184.
73. Castelan, P., et al., *Aging study of ntc thermistors by thermopower measurements.* Sensors and Actuators a-Physical, 1992. **33**(1-2): p. 119-122.
74. Vakiv, M., et al., *Controlled thermistor effect in the system CuxNi1-x-yCo2yMn2-yO4.* Journal of the European Ceramic Society, 2001. **21**(10-11): p. 1783-1785.
75. Sarrion, M.L.M. and M. Morales, *Preparation and characterization of ntc thermistors - nickel manganites doped with lithium.* Journal of the American Ceramic Society, 1995. **78**(4): p. 915-921.
76. Topfer, J., et al., *Thermopower analysis of substituted nickel manganite spinels.* Materials Research Bulletin, 1994. **29**(3): p. 225-232.

77. Feltz, A. and B. Neidnicht, *Investigations on electronically conducting oxide systems .20. $MgNiMnO_4$ and properties of Mg_ZNiMn_{2-zO4} spinelS.* Journal of Alloys and Compounds, 1991. **177**(1): p. 149-158.
78. Metzmacher, C., R. Mikkenie, and W.A. Groen, *Indium-containing ceramics with negative temperature coefficient characteristics.* Journal of the European Ceramic Society, 2000. **20**(7): p. 997-1002.

Chapter 3

Thin Film Growth Techniques

3.1 Introduction

There are various thin film growth techniques that are available and have been used to deposit NTC NMO thermistors. These techniques can be divided up into two main categories, chemical and physical methods.

Chemical methods consist of techniques such as chemical solution deposition (CSD), metal – organic deposition (MOD), sol – gel and spin coating. The physical methods consist of magnetron sputtering (MS), electron beam evaporation (EBE), and pulsed laser deposition (PLD).

3.2. Chemical Methods

3.2.1. Chemical Solution Deposition

Chemical Solution Deposition (CSD) was first developed in the 1980's, it is a common processing method for the deposition of thin films. It is a simple and inexpensive technique due to there being no vacuum system or deposition chamber required. Deposition can be achieved at low temperatures and it has the advantage that large areas can be deposited, CSD has been known to produce high quality films with good homogeneity [1, 2].

CSD allows the user to control the composition on a molecular level and allow multiple elements into the solution [1]. CSD consists of three steps, synthesis of the precursor solution, deposition of the solution on the substrate followed by heat treatment which is used to remove any organics present in the chemical solution and to crystallize the film to the desired phase [3].

CSD can be separated into two categories, these are metal – organic decomposition (MOD) and sol – gel. These processes have been used to successfully produce NMO thin films [4-6].

3.2.2. Metal – Organic Deposition

MOD is another popular method to produce thin films. Involving the coating of an organic precursor solution onto a substrate and then heat treated to decompose to the desired compound [7]. It has been used to successfully deposit thin films of $Ni_{0.48}Co_{0.24}Cu_{0.6}Mn_{1.68}O_4$ [8-10].

Metal organics are carboxylate compounds or beta – dikeytonates that are dissolved in non – polar solvents such as xylene. For NMO manganese (III) 2,4 – pentanedionate (acetylacetonate), Mn $(C_5H_7O_2)_3$, (designated as $Mn(acac)_3$), $Ni(acac)_2$ are used for the production of thin films of NMO. A chemical solution of the precursor materials are deposited on a substrate either by dipping, spraying or spinning methods. MOD advantages include its

low cost as no vacuum equipment is necessary, an easily controllable starting metal composition, and it is able to coat a wide variety of different shapes [11].

The precursors are physically condensed onto the substrate through rapid solvent evaporation [3]. This liquid film is then heat – treated to allow for thermal decomposition onto the substrate by pyrolysis, any organic in the film is removed during this stage usually in the form of CO_2 or water. If the film is subjected to prolonged heat treatment biaxial tensile stresses occur which can cause the film to crack [1].

3.2.3. Sol – Gel

Sol – gel is a wet chemical technique that can be used to produce ceramic materials in thin film form. A liquid is deposited onto a substrate and then transformed into a solid through hydrolysis and polycondensation reactions [1, 3]. Sol – gel has been used to produce thin films of $NiMn_2O_4$ [12], $NiAlMnO_4$ [13], $NiMgMnO_4$ [14].

Sol is a colloidal or a molecular suspension of solid particles of ions in a solvent, the gel is a semi – rigid mass which forms when the sol's solvent evaporates. The ions and particles left behind join together in a continuous network [3]. The sol consists of metal alkoxides such as aluminium butoxide or titanium isopropoxide, or metal salts (e.g. nitrates and acetates) [3]. The metal alkoxides are dissolved in an alcohol – based solvent to form the stable sol, it also encourages miscibility in the alkoxide and water, the water is used for hydrolysis. Metal – oxide – metal chains are produced resulting in an amorphorous oxide layer, these are then subjected to heat treatments to produce the required crystalline oxide phase [1].

3.3. Physical Methods

3.3.1. Sputtering

The basic sputtering process consists of a target or cathode which is bombarded by energetic argon ions created in the gas discharge which erodes it [15]. This generates a glow discharge plasma which is situated in front of the cathode. The substrate that is coated is the anode. The bombardment of ions on to the target results in the 'sputtering' of the target atoms, which may then condense as a thin film on a substrate in the presence of chemically reactive gases which mass react with the ejected material and the surface of the target [16]. During ion bombardment, secondary electrons are emitted from the surface of the target, these help maintain the glow discharge plasma [17].

Industrial uses of sputtering range from the microelectronics industry, magnetic recording industry, the solar control industry and the metallurgical coating industry [18].

The basic sputtering process is limited by low deposition rates, low ionisation efficiencies in the plasma and high substrate heating effects. The limitations of sputtering have been overcome by the development of magnetron sputtering and unbalanced magnetron sputtering [17].

3.3.2. Magnetron Sputtering

Magnetron sputtering has been used and improved for many years for the deposition of thin films and is a very successful technique [19]. It has been used to successfully produce NTC NMO thin film thermistors [20-23] and Ni – Co – Mn – O spinel films [24]. Magnetron sputtering can not only be operated at lower pressures with a higher deposition rate in comparison to basic sputter technologies but can also be used to synthesise dense films with fewer 'macro – particles' [25].

The magnetron sputtering configuration consists of both an electric field and a magnetic field which are perpendicular to one another. Magnetrons are used to configure a magnetic field which is parallel to the surface of the target, this constrains secondary electrons to move towards the target. The electrons will spiral around the magnetic field lines at a frequency and radius depending on the strength of the magnetic field. This is achieved by positioning one pole of the magnets at the central axis of the target and a second pole is formed with a ring of magnets around the outer edge of the target. This traps the electrons significantly increasing the probability of the collision of an ionised electron and atom from occurring. An increased ion bombardment is seen, allowing for higher sputtering rates The increase ionisation efficiency allows the discharge to be maintained at lower operating pressures (around 0.75 mTorr) and lower operating voltages (around 500V) [17].

Plasma technologies have been applied to magnetron sputtering such as unbalanced magnetron sputtering, twin magnetron sputtering variable field strength magnetron and ion assisted sputtering [25].

3.3.3. Unbalanced Magnetron Sputtering

Unbalanced magnetron sputtering differs from magnetron sputtering only slightly, however performance is increased significantly. In unbalanced magnetron sputtering the outer ring of magnets are strengthened in comparison to the central pole. Consequently, not all of the magnetic field lines are closed between the central and outer poles of the magnetron. They are instead directed towards the substrate, as a result secondary electrons are able to follow these lines. The plasma is no longer restricted to the target region but flows out towards the substrate. An increase in ion currents can be extracted from the plasma without needing to externally bias the substrate.

Figure 3.1 shows a simple comparison of the plasma densities between a conventional and unbalanced magnetron sputtering.

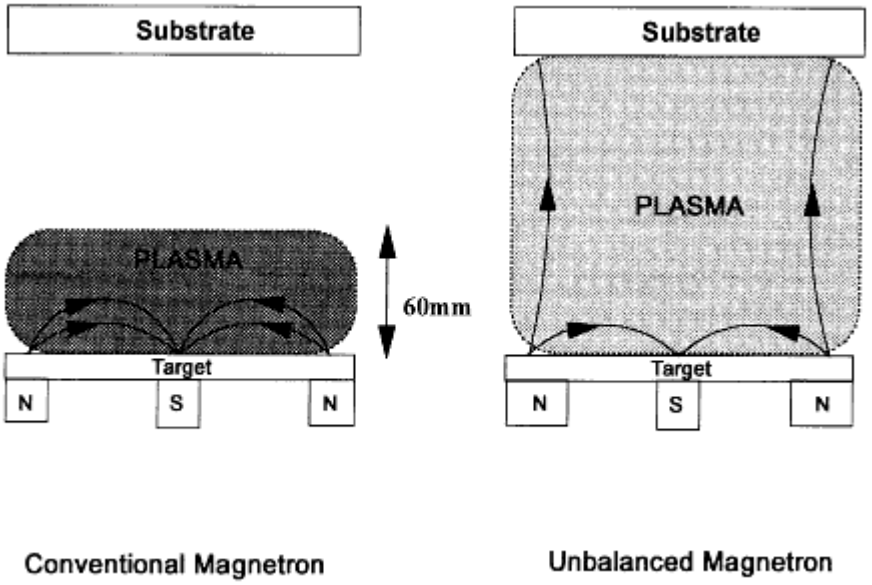

Figure 3.1. A simple comparison of plasma densities between a conventional and unbalanced magnetron (after Arnell [26])

However magnetron sputtering still has a lower deposition rate in comparison to other thin film deposition techniques [25].

3.3.4. Electron Beam Evaporation

Electron Beam Evaporation (EBE) is a PVD technique and belongs to the same class of deposition techniques as cathode arc evaporation or thermal evaporation [27]. EBE is most commonly used for the evaporation of metals such as Au, Ag and Al, transition metals such as Mo and recently ceramic oxides such as the YSZ based system.

In the literature EBE has been used to successfully produce NMO thin films for possible use in thermistors [20, 21, 27-30].

EBE is an extremely straightforward technique which has made it a favourable PVD technique [27]. The source powder that is to be deposited can be of any average grain size and distribution, requiring no additional further development. Deposition generally does not require any specific gas atmosphere and its deposition rate can be easily controlled and adjusted by

changing the intensity of the beam current. However, annealing is usually required after deposition.

The parameters, source to substrate distance, electron – beam focus and the size of the active source area will define the evaporation geometry and the thickness distribution. Its electrons are emitted from a tungsten filament and are accelerated by a high potential drop and is focussed onto a target in a carbon crucible which is water cooled. The size and power of the electron beam is determined by the filament diameter, the filament current and its voltage. Deposition is carried out in a vacuum chamber. A schematic of a EBE system used to deposit NMO [20] is shown if Figure 3.2.

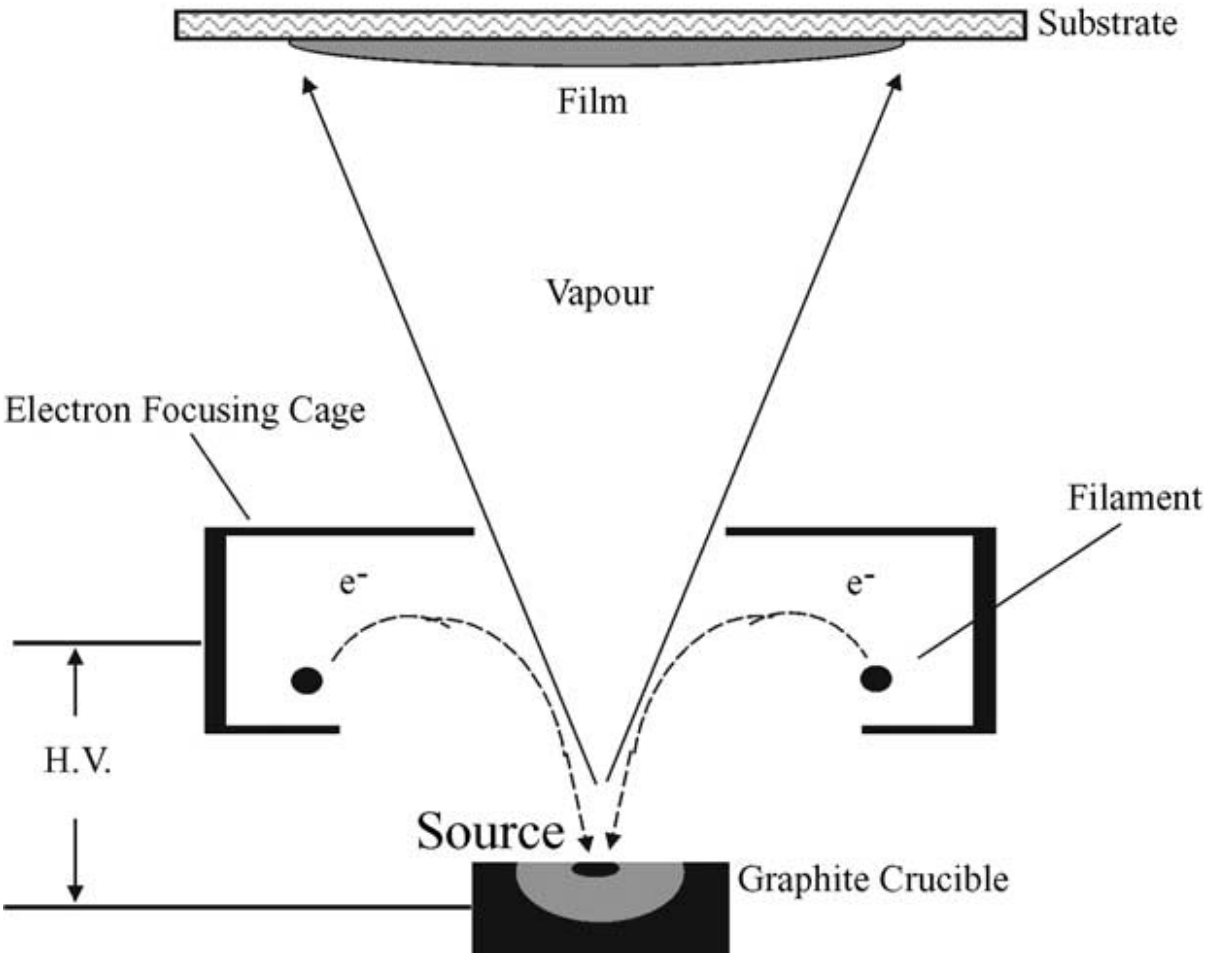

Figure 3.2. A schematic of an EBE system used to deposit NMO [20]

3.3.5. Pulsed Laser Deposition

A relatively new PVD technique, Pulsed Laser Deposition (PLD) was first introduced with the discovery of lasers in the 1960's with interest being lost during the 1970's and 1980's due to the relatively slow development of suitable, dependable and inexpensive pulsed lasers [31]. The first reported case of a pulsed laser to be used for the stoichiometric transfer of a material from a solid source to a substrate is reported in the literature in 1965 [32], where films of semiconducting and dielectric materials were grown using a ruby laser. In the late 1980's PLD was rediscovered with the development of new and more reliable lasers (Excimer lasers) because of its success in growing in – situ epitaxial high – temperature superconducting thin films [33-37].

Excimer laser operate at wavelengths which many materials absorb strongly, they almost always operate in the ultraviolet (UV) region and generate nanosecond pulses. The excimer laser gain medium which is used to amplify the power of light is a gas mixture, usually containing a noble gas such as argon, krypton or xenon and a halogen such as fluorine or chlorine. The excimer gain medium is pumped in short (nanosecond) pulses in a high – voltage electric discharge or with an electron beam, which creates the excimers or excited dimers. Excimers are a dimeric or heterodimeric molecule which is formed from two species that would not bond if they were both in the ground state. The lifetime of excimers are very short generally only nanoseconds. After the excimer has been stimulated, it will rapidly dissociate to prevent the reabsorption of the generated radiation. Different types of excimer lasers emitting wavelengths between 157 to 351 nm are shown in the table below.

Table 3.1. Different types of excimer lasers with their wavelengths

Excimer	**Wavelength**
F_2	157 nm
ArF	193 nm
KrF	248 nm
XeBr	282 nm
XeCl	308 nm
XeF	351 nm

Excimer lasers will typically emit pulses with a repetition rate of up to a few kilohertz with an average output power of between a few watts and hundreds of watts.

PLD has since become one of the most popular and intrinsically simple techniques for depositing a wide range of materials that are to be used in the next generation of smart applications [38]. PLD can be used for the deposition of insulators, semiconductors, metals, polymers and biological materials.

There are several different parameters during the PLD process which can be varied which can have an effect on the thin film produced. The laser fluence is the amount of energy that is fired onto the target divided by the spot size, which is the area of the target that is hit by the laser. The amount of times the laser can fire per second can be manipulated and is known to as the repetition rate, higher repetition rates can lead to thicker films. During deposition the background gas pressure can be changed which in turn can affect the length and shape of the plume produced during deposition.

PLD has several characteristics which make it an extremely competitive technique in the complex oxide thin film research arena in comparison to other thin film techniques [38]. One is its ability of stoichiometric transfer of material from the target of the material of interest or several targets of different elements, its atomic flux is easily regulated through geometric

considerations and control of laser radiation. Other advantages include expensive and time consuming research on precursors are avoided, flexibility and fast response, excited oxidizing species, the simplicity of its set – up, higher deposition rates, and highly preferentially oriented growth of films. Also thin films with a higher bulk density and excellent surface morphology, *in – situ* deposition of multilayers generally does not require an ultra – high vacuum environment, the PLD equipment is relatively simple and inexpensive with the laser being external to the deposition chamber. There is an ease of thickness control and also its ability to be used to investigate the thin film deposition of nearly any oxide compound regardless of its complexity or crystal chemistry [31, 37-39].

Despite these advantages it still suffers from problems such as the deposition of particulates, a small – area of deposition, target degradation and window clogging [31].

Each pulse of the laser vaporises or ablates a small amount of the material which creates a laser plume. The target is usually rotated, or rastered to prevent the repeated ablation on the same spot of the target. Rastering is usually preferred as it allows for the most efficient use of the target [40]. The ablation plume provides the material flux for the thin film growth. The vaporised material then condenses onto a heated substrate, producing the thin film.

To make PLD as efficient as possible it is preferable (i.e. to prevent loss of energy due to carrier or thermal diffusion during absorption) to use short laser pulses with a wavelength that will be strongly absorbed by the target material. When material is ejected during laser ablation it is accompanied by a snapping sound as the velocity of some of the species reach speeds faster than the speed of sound, during which a bright – coloured plasma / plume of emitted particles are formed above the surface of the target [37].

A background gas is introduced into the vacuum system, this is because for the formation of multi-cation thin – film materials a reactive species is required for a component of the flux. For example, oxygen is introduced into the vacuum system for oxides. The interaction between

the background gas and the molecular species in the ablated plume will facilitate multi-cation phase formation. The background gas will also reduce the kinetic energies of the ablated species. The vapour that is formed by the laser ablation compresses the surrounding background gas. This results in the formation of a shock wave which slows down the ablation plume expansion.

Despite the simplicity of the PLD technique the mechanisms involved such as ablation of the target material, plasma formation, plume propagation and nucleation and nucleation growth are on the other hand much more complex. A schematic diagram of a typical PLD system is shown in Figure 3.3.

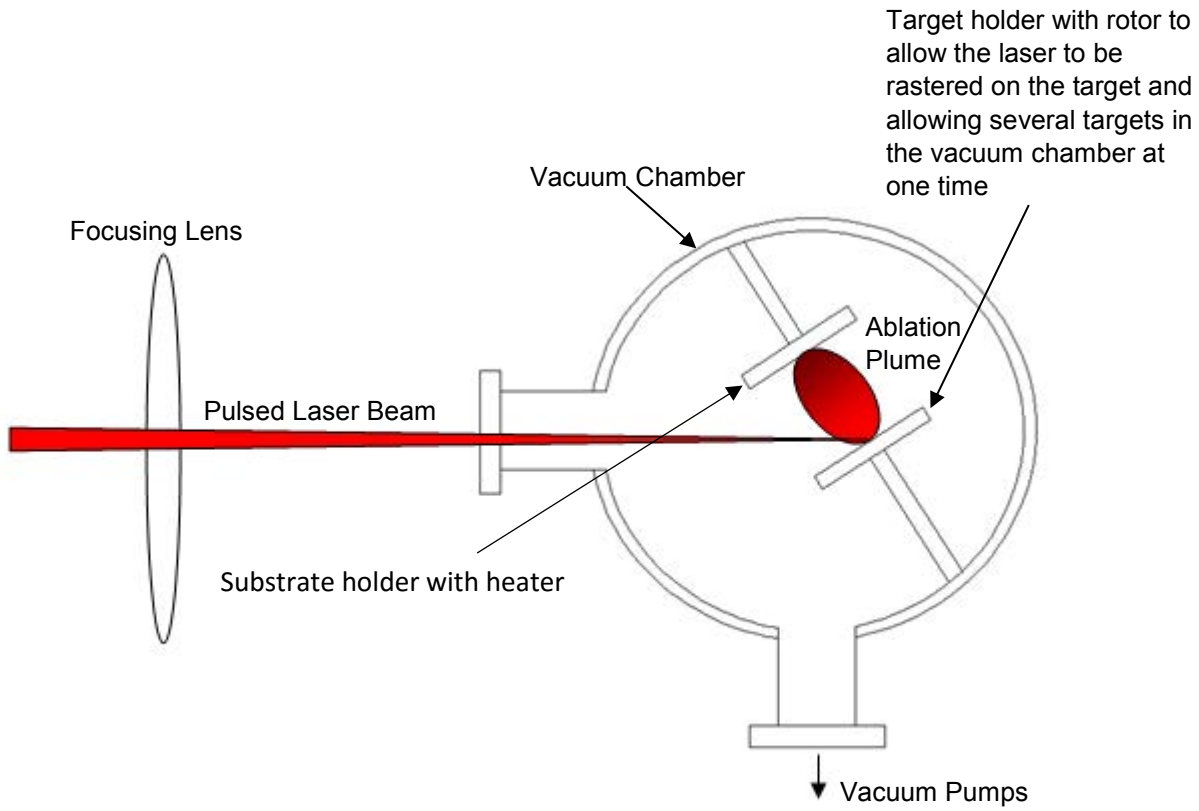

Figure 3.3. Schematic diagram of a typical PLD apparatus.

3.3.5.1. Ablation of the Target Material and Formation of the Plasma

When producing epitaxial films of multi – component inorganics the ablation condition is chosen so that the plasma consists mainly of atomic, diatomic and other low – mass species. This can be achieved using an ultraviolet (UV) laser wavelength and a nano – second pulse width which is strongly absorbed by a small volume of the target material.

During laser ablation, photons are converted to electronic excitations, and then into thermal, chemical and mechanical energy, this causes the rapid removal of material on the surface of the target [41]. Heating rates of 10^{11} Ks^{-1} and instantaneous gas pressures of 10-500 atm on the surface of the target during ablation have been observed [41]. The interaction between solid – laser mechanisms depends on the wavelength of the laser. Significant changes in the energies of species in the laser plume have been observed with the ablation of carbon using a KrF (248 nm) and ArF (193 nm), this in turn affects the growth of the resulting films [41]. Penetration of the laser energy on the surface of the target is extremely important, as the energy absorbed should only be at a very shallow layer in order to prevent unwanted subsurface boiling, which could lead to undesirable large numbers of large particulates on the surface of the film.

Laser fluence also has to exceed a threshold, which in many cases range from 1 to 3 J/cm^{-2} with a 25 ns pulse. These ranges are fairly high and are best achieved with excimer lasers, typically lasers using KrF (248 nm) with a 20 – 35 ns pulse duration are most typically used. Successful films have also been achieved with ArF (193 nm) [42] and XeCl (308 nm).

Surface roughness of the target will affect its interaction with the laser, surface roughness can enhance diffraction of the laser radiation. This consequently causes non – uniform spatial distribution of energy, and non – uniform, non – stoichiometric ablation of the target material.

A problem that arises during the ablation process is the presence of particulates, which can range from 100s of nm to 10s of μm in size, on the surface of the film. These are commonly known as droplets or blobs, they generally travel behind the plume after particles are ejected

from the surface of the target and in general travel at 50 – 200 m/s. More droplets are produced at higher fluences. Target rotation is therefore extremely important and useful in preventing these droplets from forming on the surface of the substrate. Target rotation allows the remnants of previous ablation events to solidify, as they are not re-irradiated by the laser [37, 42].

Figure 3.4. shows a schematic of the thermal cycle which results when a laser pulse strikes a target. Figure 3.4. (a) shows a laser pulse being absorbed by the material, this starts the melting of the target material and the vaporization process. Figure 3.4. (b) shows a melt front diffusing into the target which is then followed by vaporization along with the formation of the laser plume, at (c) it shows that the incident laser radiation is absorbed by the plume along with plasma formation (d) the melt front has receded which results in solidification on the surface.

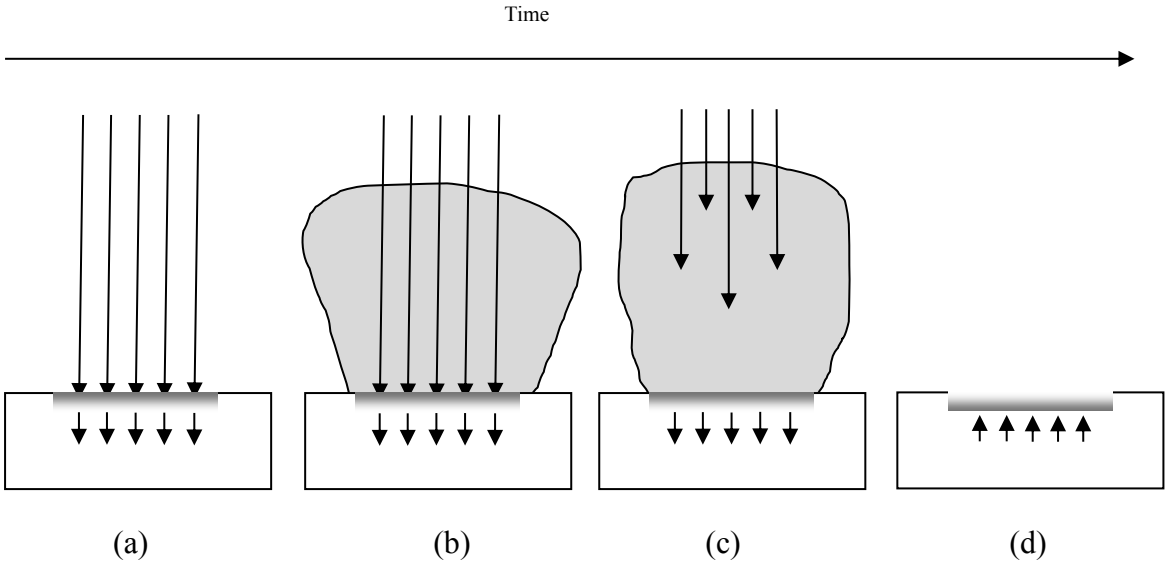

Figure 3.4. Schematic of laser ablation event (a) laser pulse absorbed by the material, (b) vaporization of the target, (c) incident laser radiation absorbed by the plume and (d) solidification of the target

Long pulses that are tens of nanoseconds long, which are typical of excimer lasers, result in a strong interaction between the forming plume and the incident beam leading to further heating of the species [41]. KrF excimer lasers with a longer 25 ns pulse time have been attributed to

the production of superior films in comparison to frequency – quadrupled Nd:YAG (266 nm) with a 5 ns pulse duration [41].

3.3.5.2. Plume Propagation

The size and energy of the plume during deposition is determined by the base pressure inside the vacuum chamber, the laser energy density and the laser spot size. An example of a typical plume is shown in Figure 3.5.

Within the plume neutral atoms, ions, and electrons travel at different velocities. There are also strong interactions between the species of the plasma and the background gas. Thermalisation needs to occur to obtain good film growth and to avoid resputtering of the growing film by the most energetic ions in the plume. Plume expansion is encouraged by plasma pressure gradients and possibly by Coulomb repulsion between the ions [43]. The velocity of the particles in the plume have been measured directly using time – of – flight (TOF) measurements, to be around 2 x 10^6cm/s in 100 mTorr pressures. Particulates that are 7 cm away from the target have been measured using an ion probe to travel at 2 x 10^4cm/s [37].

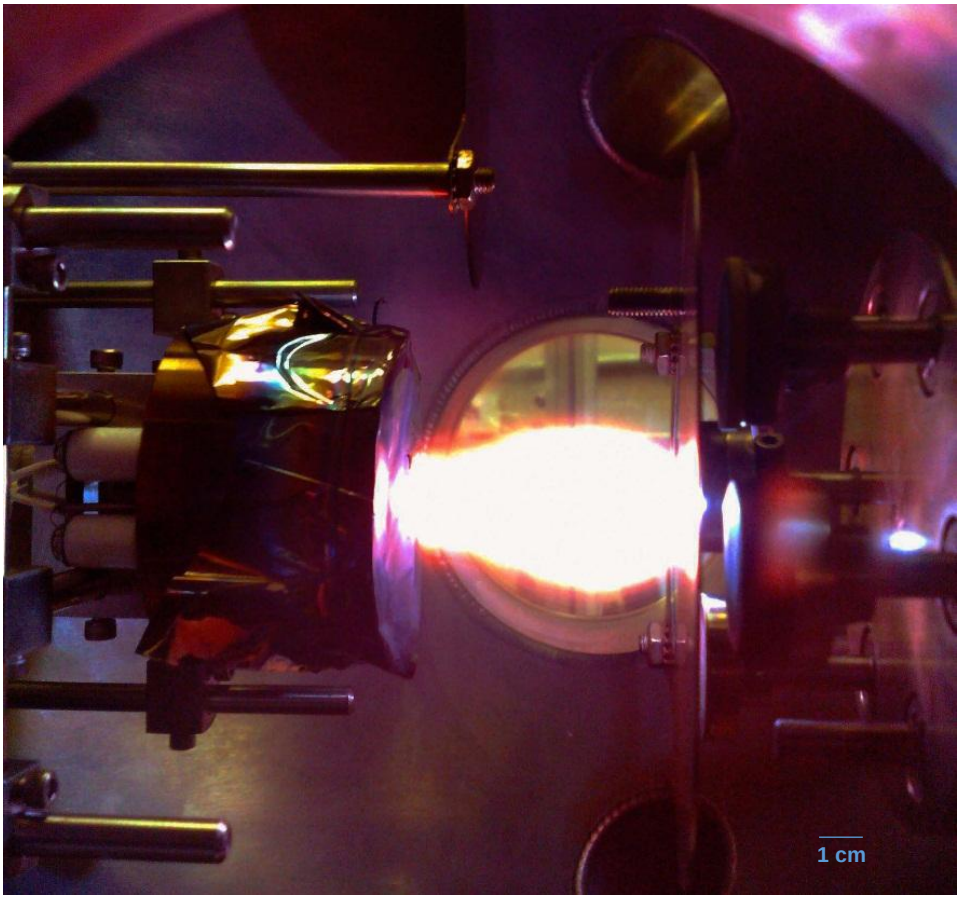

Figure 3.5. Typical laser plume inside the vacuum chamber [44]

3.3.5.3. Nucleation and Growth of Thin Films by PLD

There are three possible modes of crystal growth on surfaces, (a) island or Volmer – Weber, (b) layer plus island or Stranski – Krastanov, or (c) layer or Frank – van der Merwe mode, these have been illustrated in Figure 3.6.

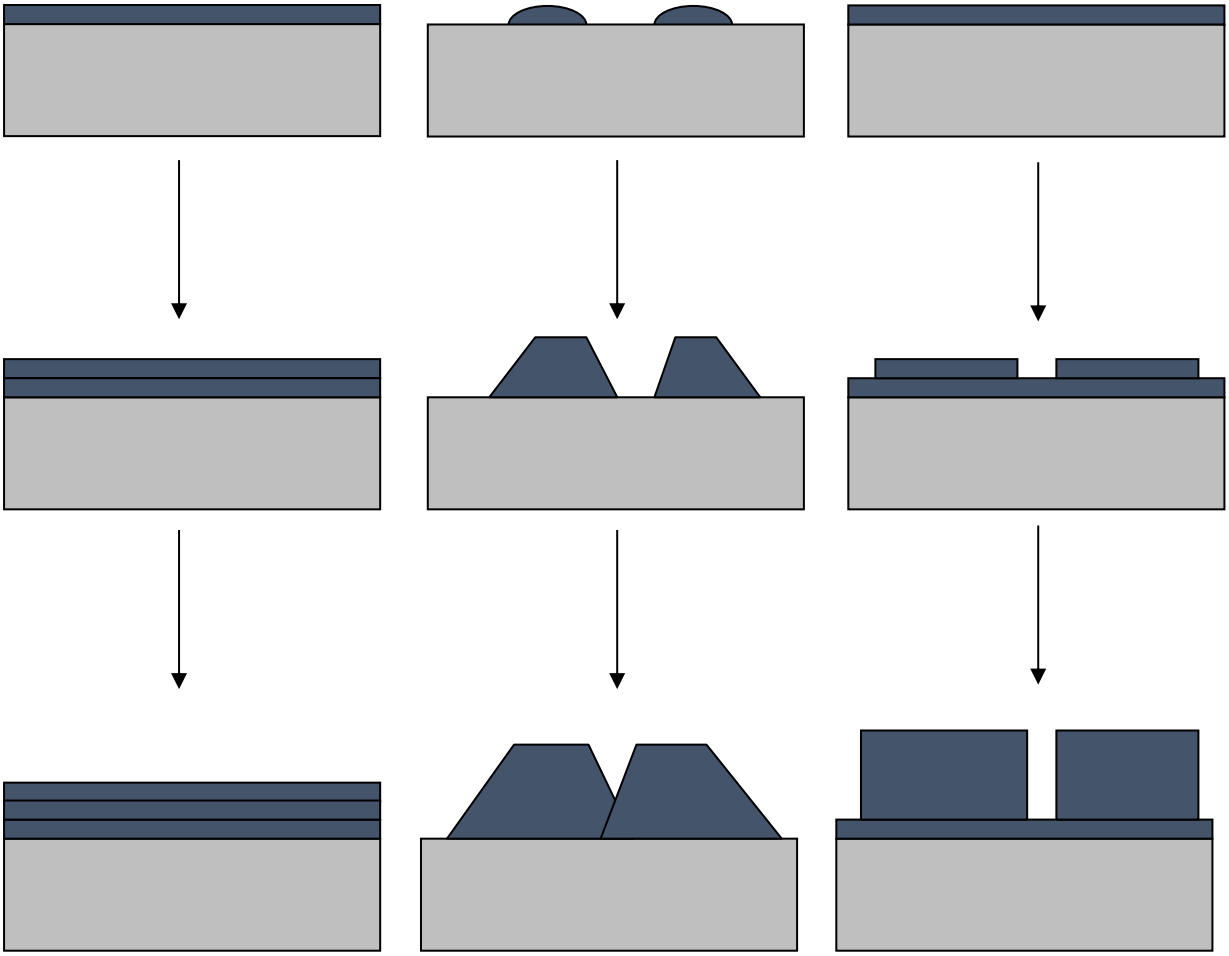

Figure 3.6. Diagram of the three crystal growth modes (a) Frank – Van der Merwe, (b) Volmer – Weber, (c) Stranski – Krastanow.

In the island / Volmer – Weber mode small clusters are nucleated directly on to the surface of the substrate which causes them to grow into islands of the condensed phase [45]. The reason this happens is because the atoms or molecules of the deposit are more strongly bound to each other than to the substrate [45].

The layer, or Frank – van der Merwe mode is a two dimensional monolayer growth mode, and has opposite characteristics to the Volmer – Weber mode. In this mode the atoms or molecules are more strongly bound to the substrate as opposed to each other. The first atoms to condense form a complete monolayer on the surface, this then becomes covered with a second monolayer which is a little less tightly bound. So long as the decrease in the binding is

monotonic towards the value for a bulk crystal of the deposit, the layer growth mode is attained [45].

In the layer plus island, or Stranski – Krastanov growth mode an initial monolayer is grown, a subsequent layer growth then continues. These successive monolayers are unfavourable and lead to the formation of islands on top of this intermediate layer. There have been many possible explanations for this growth, for example any factor which may affect the monotonic decrease in binding energy which is characteristic of layer growth may be the reason. The lattice parameter of, or molecular orientation in, or symmetry of the intermediate layer may not be able to be continued into the crystal of the deposit. The consequence of this is a high free energy of the deposit – intermediate – layer interface which then favours the formation of islands [45].

Kukuruznyak et al [46] has produced complete ternary composition spreads of NiO – Mn_2O_3 – CuO thin films on Nb – doped $SrTiO_3$ substrates using a combinatorial PLD technique. Using a combinatorial method, the authors could propose thin film NTC thermistors with standardised characteristics. It is extremely difficult to obtain standardised thin film thermistor materials because deposited materials have a different crystal structure and transport properties from their bulk targets. The thin film thermistor therefore will have an altered chemical composition. To find a standardised composition is a very time intensive process, therefore the author's use of combinatorial screening allows simultaneous fabrication of large libraries of oxide alloys. The resistivity versus temperature characteristics was determined using a custom – designed scanning graphite probe and it was discovered that at room temperature (25ºC) this characteristic changed with different compositions of the material. However it was stated that the resistivity measurement was limited due to the difficulty of getting meaningful results from the highly insulating films. Therefore, a correct choice of probe is imperative to reduce this effect. The results the resistivity map of this experiment are given in the figure below.

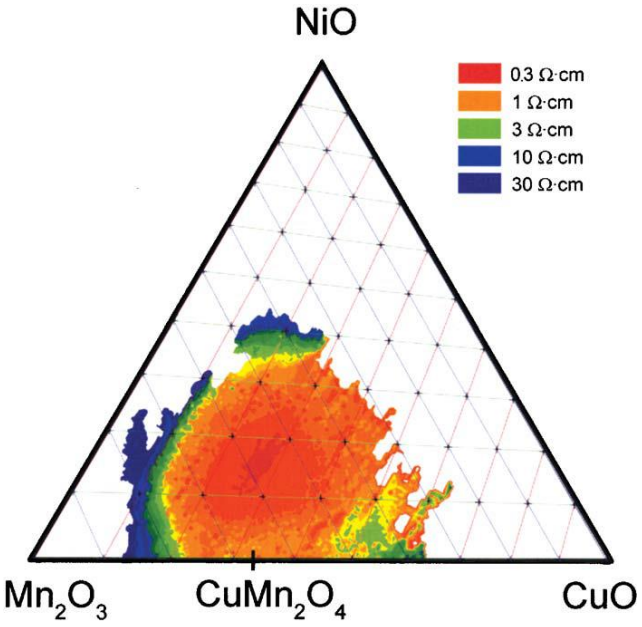

Figure 3.7. The conductivity map of the Mn_2O_3 – CuO – NiO composition spread taken at 25 °C [46]

The transparent parts of the map are the strongly insulating parts of the ternary films, all of the elemental oxides were highly insulating. The standardised NTC thermistor compositions determined from the map by the authors are given in the table below along with their resistivity value.

Table 3.2. Composition and resistivity values of standardised NTC thermistors obtained from a thin film composition spread library at 25°C proposed by Kukuruznyak et al. [46]

Composition	Resistivity (Ω.cm)
$Cu_{1.35}Mn_{1.65}O_4$	1
$Cu_{0.84}Mn_{2.16}O_4$	0.5
$Ni_{0.24}Cu_{0.42}Mn_{2.34}O_4$	3
$Ni_{0.3}Cu_{0.3}Mn_{2.4}O_4$	40

3.4. NMO System Thin Film Literature

NMO thin films have been deposited at substrate temperatures as low as 90°C using spin spray deposition by Ko et al. [47], a reaction solution containing dissolved nickel chloride (2 – 3mM) and an oxidising solution consisting of sodium nitrate or hydrogen peroxide (5 – 10mM) and ammonium acetate or potassium acetate (65mM) as an oxidising agent and pH buffer, respectively. The films after deposition onto crystalline silicon substrates with a 1 μm thick thermally grown SiO_2 buffer layer were post annealed at 400°C in argon for 1 hr. The presence of the spinel phase was confirmed by XRD and TEM with the XRD peaks becoming more prominent after the post deposition annealing. Spectroscopic ellipsometry and SEM was used to measure variations in the surface morphology. The resistivity of the thin films measured are comparable to techniques fabricated by other techniques with resistance measured between 3.5 to 8.0kΩ assumed to be at room temperature. Ko et al [48] also produced thin films of NMO using CSD which were pyrolyzed for 1 – 4 minutes until a desired thickness was achieved. At 100 – 350°C the films were annealed in Ar or air for 1 – 18 hr. The spinel phase was confirmed using XRD and TEM, with a comparison made between the films annealed in Ar and those annealed in air. It was found was that broader and more intense XRD peaks were produced by the films annealed in Ar, in comparison to air, with a shorter annealing time duration required. Different compositions of the films from 0.5 – 0.8 Mn / (Ni + Mn) were made and the resulting TCR, Ea and Resistivity values were measured and shown in the table below.

Table 3.3. Resistivity, Temperature Coefficient of Resistance (TCR) and Activation Energy (Ea) of NMO films by Chemical Solution Deposition (CSD) (Ko et al. [48])

R = Mn / (Ni+Mn)	TCR (%/K)	Ea (eV)	Resistivity (kΩ.cm) at 298 K
0.50	-3.81	0.37	63
0.62	-3.93	0.37	32
0.67	-3.81	0.37	27
0.78	-3.81	0.37	29
0.80	3.90	0.37	12

The measured resistivity of the films annealed in Ar were comparable to the that of the films grown by spin spray deposition [47].

Fau et al. [49] produced thin films of NMO with 0.03 – 2 μm thickness, from a $Ni_{0.75}Mn_{1.25}O_4$ ceramic bulk target using RF reactive sputtering technique and studied the effect of changing the O_2 / Ar gas ratio on the microstructure and electrical properties of the thin films produced. Microscopy slides (76 x 26 mm) were used as a substrate and the following conditions were used for the sputtering of the NMO thin films. A substrate temperature of 13°C, RF input power 200W or 4W/cm^2, a total gas pressure of 15 mTorr, a target to substrate spacing of 5 cm, sputtering gas (O_2 / Ar + O_2) 0 – 0.24% sccm (0, 0.09, 0.17, 0.24) and a growth rate of ~ 6 nm/min. XRD comparison between the thin films and the bulk ceramic target showed that the crystallinity of the thin films was much poorer in contrast to the bulk target. A low percentage of oxygen has little effect on the morphology of the films but has a large influence on the oxygen content of the as deposited films. Reduced oxygen contents in the deposition ambient atmosphere improved the crystallisation of the thin films. The author explains this phenomenon in terms of enhanced adatom mobility on the substrate, because of the high energy oxygen bombardment. It was found that for oxygen ratios > 0.17% the oxygen bombardment becomes too high promoting the disorder of growing films, and films grown at > 0.24% oxygen content were amorphous. Films produced in a pure Argon atmosphere resulted in high resistivity films around 15000Ω.cm and a high activation energy of around 4300K. A reduction

in the resistivity of the thin films was observed with an increase of O_2 into the discharge gas, with the lowest resistivity value measured at 3300Ω.cm and a B value of 4000K using an oxygen percentage of 0.24%. The reasons proposed for the observed drop in the resistivity values were better oxygen stoichiometry in the deposited films and improved crystallisation obtained with an oxygen reactive atmosphere. A. Basu et al [50] concurred with their results by measuring the resistance with an electrometer on two conductive contacts. It was also shown that a further increase of O_2 to 12.5 and 15% lead to similar values of resistance that were produced in annealed films. The authors observed that O_2 pressure of the sputtering environment had a strong influence on the resistivity of the thin films. It was also suggested that a change in the oxygen stoichiometry of the NMO films would lead to an alteration in the ratio of Mn^{3+} to Mn^{4+} ions resulting in increased conductivity in the films [50], and also from better crystallization at lower O_2 pressure [49].

Much work in depositing thin films of NMO has been carried out by Schmidt et al. [51] using different deposition techniques such as EBE, MS, etc. and studying the effect of changing different deposition conditions and annealing. Schmidt et al. has produced many films using magnetron sputtering, in this study [51] a substrate temperature of 35°C was used, in an argon / oxygen (2.5% oxygen) ambient of ~ 37.5 mTorr with a substrate to target distance of 35 mm. The films then had to be annealed at 800°C for 1 hr in air to allow for the spinel phase to form as in the as deposited state the films were found to be amorphous. The resistivity of the films at 50°C dropped from ~ 2900Ω.cm in the as deposited state to ~ 310Ω.cm following annealing. A study of the surface topology [20] showed that the as deposited films generally had a poor crystallinity on the surface, but would adopt a more crystalline character after annealing, which is in agreement with the XRD results given in their previous study [51]. Also the SEM images and EDX data showed that the films produced by RF magnetron sputtering showed higher surface density with little porosity and that the stoichiometry of the films could be controlled.

Another study [50] reported the effect of changing the oxygen pressure during deposition and what effect annealing had on the resistance of the thin films of NMO on silicon substrates. The first set of films were annealed in air at 800°C for 1 hr and then quenched to room temperature. The second set of films was annealed in a similar environment that was used during their deposition (Ar / O_2) at 800°C for 1 h and quenched to room temperature. A comparison of the different resistivity values at 50°C was reported, with the resistivity at lower oxygen content in the as deposited films being much higher than the annealed films. The resistivity in the as deposited films became comparable to that of the annealed films at higher concentrations of oxygen in the argon / air ambient atmosphere at 12 and 15%. There was little variation in the resistivity of the films that were annealed in the same ambient gases that they were deposited in. The resistivity of the films was measured between 100 – 3000Ω.cm, the results showed that the resistivity of the as deposited films were strongly dependent on the oxygen content of the sputtering ambient. Another study involved the characterisation of the effect of different substrate temperatures and annealing on the NMO films using XRD [22]. NMO thin films of around 700nm thickness were deposited on [100] silicon substrates using RF MS in an argon atmosphere of 37.5 mTorr and a target power density of 3W cm^{-2}. Different substrate temperatures were used during deposition 35, 100, 200 and 250°C. The films were then annealed in air at temperatures between 650 and 900 °C in increments of 50°C for 1 hr, followed by quench cooling to room temperature. It was found that an improvement in crystallinity occurred with a preferred orientation along the [100] orientation in the as deposited films at a substrate temperature of 250°C. However after the films were annealed it was discovered that the films grown at 200°C and annealed at 800°C for 1 hr showed a very strong presence of the [100] orientation in comparison to the other films deposited at different substrate temperatures. Further investigation into the effect of changing the annealing temperature in air between 650 to 900°C was explored [22]. An annealing temperature greater than 750°C was needed to

ensure the preferred orientation in the [100] direction. An annealing temperature of 800°C was found to have the developed grain structure with grain sizes in the order of 35 – 40 nm which were approximately two orders of magnitude smaller than the target grains, and the most desirable spinel phase. AFM analysis of the annealed films was conducted [21] studying the effect of changing the substrate temperature during deposition. The as deposited films showed poor crystallinity which is in agreement with their previous study based on XRD data. The best crystallinity was achieved using a substrate temperature of 200°C and with the film being subsequently annealed.

It has also been shown in RF magnetron sputtering by R. Schmidt et al. [21] that an increase in substrate temperature leads to a decrease in the film's thickness, uniform layers of 560 – 830nm thickness were grown with deposition rates of 5 – 10nm min $^{-2}$. This is explained by assuming that there is an increase in the desorption rate of sputtered particles, these are absorbed on the substrate but will gain sufficient thermal energy for desorption, which is provided by the heated substrate. At higher substrate temperatures of over 200°C it is possible for NMO films to experience an equivalent mechanism to that of annealing, regarded as an instant annealing effect. This instant annealing effect improves the crystallinity of the material but has the disadvantage of a reduced deposition rate due to the increased thermal energy. The increase of substrate temperature on the microstructure was also studied by AFM. It was shown that there was no sign of distinct grain formation in the as deposited films with increased temperatures.

Schmidt et al. [20, 21, 27, 30] also used EBE to investigate the characteristics of NMO films using glass microscopy slides and alumina substrates. During the deposition of NMO the substrate was heated to 100°C and the films were subsequently annealed at 800°C in air for 30 mins. It was found that the crystallinity of the surface of the films was poor for those films deposited on alumina substrates in the as deposited state but improved significantly after

annealing, in correlation with the films produced using RF MS on Si [100] substrates. EDX was used to measure the Ni : Mn ratio of the films, and it was found that the films were Ni rich suggesting the stoichiometry of the films was not preserved during deposition. There was also poor control in the crystal orientation of the films, and it was concluded that the electrical properties of the films could not be reliably reproduced. Also the low deposition rate for MS and EBE means to produce thicker films is time consuming, which can be problem because of the high sheet resistance found in the films of up to $10^8\Omega$ at room temperature.

Baliga et al. [23] produced thin films of $Ni_{0.6}Mn_{2.4}O_4$ using RF MS on fused quartz substrates using a gas pressure of 40mTorr with a proportion of oxygen to argon, which was varied between 0 and 100%. An RF input power of 350W was used along with a substrate temperature of 180°C. The films after initial characterisation were annealed for 24 hrs at 250°C in air. Initially the authors determined films produced in 25% oxygen had an extremely flowery morphology as shown in Figure 3.7. They further discovered that this flowery morphology could not eliminated despite varying the oxygen percentage between 5 and 100%, which is in contrast to the films produced by Schmidt [50]. Films were then sputtered in pure argon, this condition produced films which were high in resistance and also unstable around 20mΩ at room temperature. A small amount of oxygen was then introduced (1%) during sputtering producing stable films however the activation energy was still low 3000K. The oxygen was further reduced until a film matching the bulk resistivity and activation energy could be achieved (2500Ω.cm and 3800K). This was achieved was with an oxygen percentage of 0.04% along with a 24 hr anneal in air. The resistivities measured were ~ 7000Ω.cm for the as deposited films which was reduced to 2500Ω.cm after annealing.

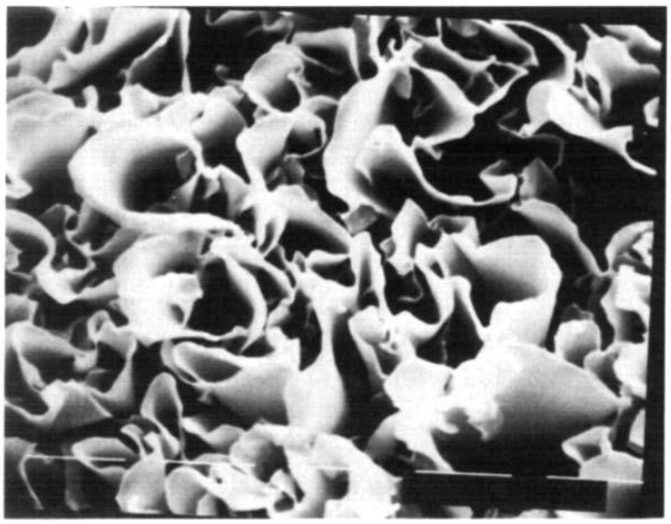

Figure 3.8. SEM image film sputtered at 25% oxygen where 1 bar = 5 μm [23]

NMO films produced by CSD with seven different compositions of NMO were studied by Schulze et al. [5] on thermally grown SiO_2 substrates using spin coating at 3000 rpm for 30 s. Two different precursor solutions were used, an acetate based solution and an acetylacetonate based solution. The 0.3M acetate solution was prepared by dissolving nickel ($(C_2H_3O_2)_2Ni_4 \cdot H_2O$) and manganese ($(C_2H_3O_2)_2Mn_4 \cdot H_2O$) acetates in acetic acid and distilled water at a ratio of 2 :1 at 70°C under an argon blanket. The 0.3M acetylacetonate solution was prepared by dissolving Mn acetylacetonate ($Mn(C_5H_7O_2)_3$) in methanol and ethylene gycol (ratio 6:1) at 60°C for 30 mins. XRD and resistivity data was obtained from the films. It was found that films annealed at 400°C were amorphous by XRD and that the spinel phase was not detected until the films were annealed at 530°C. The resistivity of the spinel films was measured to be between 3500 – 21,000Ω.cm where an increase of Mn in the system resulted in higher resistivity values.

Further reports of the Ni : Mn ratio of thin films of NMO produced by EBE by Parlak et al. [28] being different in comparison to the source material is in agreement with the work carried out by Schmidt et al. Further agreement is noticed in XRD data where fewer peaks are present

in contrast to the source material and increased crystallisation in the annealed films in comparison to the as – deposited. The authors also noted that there is change in the orientation of the films when they are annealed at 600°C in comparison to those films annealed at 500°C. The film resistivity was carried out in air on films deposited at on alumina substrates with a pre – printed platinum comb electrode and using a multimeter at temperatures between room temperature and 600K. A decrease in the film resistivity was noticed with an increase in the annealing temperature. The results obtained from this study are shown in Table 3 at the end of this chapter. Parlek et al. [29] carried out further studies on the effect of annealing on the thin films of NMO of ~ 1μm thickness by comparing the effect of annealing in N_2, O_2 and air on Si substrates. XRD results showed that there were changes in the preferred orientation for those films annealed in different ambient atmospheres. As deposited films displayed only one main peak from the (311) plane of the NMO spinel structure, the XRD patterns for the films annealed in N_2 were similar to the as deposited films although the width of the (311) peak was reduced because of the heat treatment. While those films that were annealed at 600°C in air and O_2 their XRD patterns had up to 5 different peaks present demonstrating that there is a change in the preferred orientation. With the (222) and (220) NMO diffraction peaks being of similar intensity to the (311) peak. The XRD patterns of the films annealed in air and oxygen were very similar as other peaks besides the (311) NMO peak was observed. Changing the annealing temperature from 500 to 600°C led to changes in the preferred orientation. Annealing in N_2 also led to a reduction in resistivity by a factor of ~ 5 when measured from room temperature to 600K while the resistivity of films annealed in an oxygen containing environment decreased by a factor of ~ 3. There was also a bigger decrease in the measured β values of the thermistors for those films grown and annealed in an oxygen containing environment. This study confirmed that it is possible to tune the properties of NMO thermistors by changing their annealing atmosphere. By annealing in N_2 it is possible to increase the loss of oxygen to increase the

films resistivity values or to anneal in air to replenish the oxygen deficiency which results in a decrease in the film resistivity.

NMO films have also been deposited by aerosol – deposition (AD) by Ryu et al. [52] at room temperature on glass substrates with a film thickness of 5μm. Raw materials of Mn_2O_3 (99.9%) and NiO (99.9%) were used for the starting NMO powders or the AD films. The raw powder mixture was then ball milled using high purity 3Y – TZP (tetragonal zirconia polycrystalline) ball media with ethyl alcohol in a polyethylene jar for 24 hr. the mixed slurry was then dried and calcined for 10 hr in an alumina crucible for the NMO spinel phase formation at 850°C. The calcined powder was then crushed by planetary milling for 10 hr to obtain the appropriate particle size distribution for AD of around 1.4μm. Study of the effect of changing the annealing temperature on the characteristics of the thermistor was conducted. The films were analysed by XRD, the as deposited films only showed two strong peaks with the (111) and (220) reflections of the spinel phase, which is in agreement with most as deposited films produced by other methods. After the films were annealed at 700°C for 1 hr in air the peaks became stronger and sharper than the as deposited films indicating an increase in crystallinity. An increase of the annealing temperature caused a decrease in the resistivity value from 20.97kΩ.cm to 4.74kΩ.cm.

Nelson – Cheeseman et al. [53] produced NMO films from a NMO target onto (110) – oriented structure $MgAl_2O_4$ (MAO) and perovskite structure STO and Nb – doped STO (Nb:STO) substrates using PLD. The NMO thin films were produced at 600 °C energy density of 1.2J/cm^2 at 10mTorr of a 99% N_2/1% O_2 gaseous mixture. After deposition the films were annealed at 800°C for 4 hr in air. The resistances were measured for as grown and annealed films at room temperature. The as deposited films proved to be highly insulating at 8.34MΩ.cm while the annealed films were several order of magnitudes lower in resistivity 187kΩ.cm. The authors explain the decrease in resistivity by using the small polaron mechanism, saying with

more octahedral Mn^{4+}, and more electron exchange can occur between the Mn^{3+} and Mn^{4+} cations in the annealed films. With an absence of the octahedral Mn^{4+} there is a decrease in the amount of interactions that can occur with the Mn^{3+} in the as deposited films.

Table 3.4. Summary of Thermistor Characteristics from literature

Reference	Deposition technique	Substrate	Substrate temperature (°C)	Deposition environment	Annealing temperature (°C)	Annealing time	Annealing environment	Resistance (Ω)	Resistivity (Ω.cm) at 298 K	Thermistor Constant – B (K)
Ko et al. [47]	Spin spray	Single crystal Si with SiO_2 layer	90	N/A	400	1 hr	Ar	-	3.5 – 8.0 k	-
Ko et al. [48]	CSD	Single crystal Si with SiO_2 layer	100 – 350	Air	400	1 hr	Ar	-	~ 10 k	-
Basu et al. [51]	RF MS	Single crystal Si [100]	35	Ar / O_2	800	1 hr	Air	-	~ 2900 – AD ~ 310 – A	-
Basu et al. [50]	RF MS	Single crystal Si [100]	35	Ar / O_2	800	1 hr	Air Ar / O_2	-	~ 400 – 3,000 – AD ~ 100 – 600 – A	-
Schmidt et al. [20-22]	RF MS	Single crystal Si [100]	200	Ar	650 – 900	1 hr	Air	-	-	-
Schmidt et al. [20, 21, 30]	EBE	Soda lime glass, Polycrystalline Al_2O_3	100	Vacuum	800	30 mins	Air	10^8	-	-

Baliga et al. [23]	RF MS	Fused quartz	180	O_2 / Ar	250	24 hr	Air	-	~ 7000 – AD ~ 2500 – A	-
Schulze et al. [5]	CSD	Single crystal Si with SiO_2 layer	100 – 500	Air	630 – 930	1 min	Air		3500 – 21,000	-
Fau et al. [49]	RF MS	Microscopy glass slides	13	O_2 / Ar	-	-	-		3,300 – 15,000	4,000 – 4,300
Parlak et al. [28]	EBE	Glass, Polycrystalline Al_2O_3, Single crystal Si [100]	~ 80 °C	Vacuum	500 + 600	30 mins	Air	2.2×10^{7} – AD 1.7×10^{5} - 500°C A 5.1×10^{4} - 600°C A (300K)	4.6×10^{3} AD 3.6×10^{1} - 500°C A 1.2×10^{1} - 600°C A (300 K)	5790 AD 3980 - 500°C A 3940 - 600°C A
Parlak et al. [29]	EBE	Glass, Al_2O_3, Single crystal Si [100]	~ 80 °C	Vacuum	500 + 600	30 mins	N_2	3.9×10^{7} - AD 2.9×10^{7} - 500°C A 1.2×10^{8} - 600°C A (300K)	8.4×10^{3} - AD 6.2×10^{3} - 500°C A 2.5×10^{4} - 600°C A (300K)	6460 AD 6040 - 500°C A 6110 - 600°C A
Ryu et al. [52]	AD	Glass	RT	Vacuum	400, 500, 600, 700	1 hr	-	41 M - AD 18 M - 400°C A	20.978 k AD 9.425 k 400°C	3906 - AD 3689 - 400°C A

								14 M - 500°C A 10 M - 600°C A 9 M - 700°C A	7.406 k 500°C 5.203 k 600°C 4.741 k 700°C	3601 - 500°C A 3559 - 600°C A 3528 - 700°C A
B. B. Nelson – Cheeseman et al. [53]	PLD	Single crystal $MgAl_2O_4$ [110], Single crystal STO, Single crystal Nb:STO	600 °C	99 % N_2 / 1 % O_2 gaseous mixture at 10 mTorr	800	4 hr	Air	-	9.43 MΩ.cm - AD 187k - Ω.cm A	-

Key:

AD = As deposited films
A = Annealed films

3.5. Summary

In this chapter the general properties of NMO were presented with detailed descriptions of the thermal and electrical properties. The importance of cationic distribution in the system was stressed and its effects on the conductivity and resistivity on NMO.

Details of the phase stability of the NMO system was also given, which is essential in explaining the required composition and temperature required in producing the desired spinel structure.

The undesirable effects of aging were discussed along with the effect dopants can have on improving aging along with the conductivity and resistivity of NMO.

Different thin film growth techniques were also analysed, with their advantages and disadvantages described, with particular emphasis on the PLD technique which is used in this project along with its growth technique. A review of literature of the deposition of thin films of NMO was conducted.

3.6 Aims and Objectives of the Project

The aim of the project was to investigate depositing thin films of NMO using PLD to see if it could possibly be used as an NTC thermistor material. The project is to focus on using cheap unpolished polycrystalline alumina substrates to give the project a more commercial aspect as opposed to using single crystal polished substrates. An investigation is to be conducted to see if the performance of bulk NMO material can be replicated in thin film form using by PLD. Further aims of the project are listed below:

- Investigate the use of different substrates and their suitability for deposition of NMO was studied.
- Investigation into determining a suitable measurement technique for characterisation of the electrical properties of the films produced

- Comparison of electrical properties measurements techniques carried out at Birmingham and at Amphenol
- Examine the effect of changing the substrate temperature from 400°C to 550°C during deposition on the NTC characteristics of the thin films.
- Characterise the different films structure in terms of the structure and microstructure.
- Inspect the effect of changing the oxygen pressure during deposition from 50mTorr to 250mTorr on the NTC properties of the thin films.
- Duplicate the as deposited films and investigate the effect of ex situ annealing at 800°C for 1 hr in O_2 environment.
- Study the repeatability of the deposited and annealed films in terms of their electrical and structural properties

References

1. Sakka, S., *Handbook of Sol-Gel Science and Technology: Processing, Characterization and Applications, V. I - Sol-Gel Processing/Hiromitsu Kozuka, Editor, V. II - Characterization of Sol-Gel Materials and Products/Rui M. Almeida, Editor, V. III - Applications of Sol-Gel Technology/Sumio Sakka, Editor*2004: Springer.
2. He, L., et al., *Effects of annealing temperature on microstructure and electrical properties of Mn-Co-Ni-O thin films.* Materials Letters, 2011. **65**(11): p. 1632-1635.
3. Schulze, H.M., *Synthesis and characterization of nickel manganite thin films for application in uncooled microbolometers*, in *Materials Science and Engineering,* 2008, The Pennsylvania State University. p. 184.
4. Kukuruznyak, D.A., J.G. Moyer, and F.S. Ohuchi, *Improved aging characteristics of NTC thermistor thin films fabricated by a hybrid sol-gel-MOD process.* Journal of the American Ceramic Society, 2006. **89**(1): p. 189-192.
5. Schulze, H., et al., *Synthesis, Phase Characterization, and Properties of Chemical Solution-Deposited Nickel Manganite Thermistor Thin Films.* Journal of the American Ceramic Society, 2009. **92**(3): p. 738-744.
6. Hou, Y., et al., *Characterization of $Mn_{(1.56)}Co_{(0.96)}Ni_{(0.48)}O_{(4)}$ films for infrared detection.* Applied Physics Letters, 2008. **92**(20).
7. Kim, B.J., et al., *New MOD solution for the preparation of high J(c) REBCO superconducting films.* Physica C-Superconductivity and Its Applications, 2006. **445**: p. 582-586.
8. Kukuruznyak, D.A., et al., *Preparation and properties of thermistor thin-films by metal organic decomposition.* Thin Solid Films, 2001. **385**(1-2): p. 89-95.
9. Kukuruznyak, D.A., et al., *Relationship between electronic and crystal structure in Cu-Ni-Co-Mn-O spinels - Part A: Temperature-induced structural transformation.* Journal of Electron Spectroscopy and Related Phenomena, 2006. **150**(2-3): p. 275-281.
10. Moyer, J.G., et al., *Thermopower and electrical conductivity of $Mn_{1.68-x}Cu_{0.6+XplusY+Z}Co_{0.24-Y}Ni_{0.48-Z}$ thin film oxides obtained through metal organic decomposition processing.* Journal of Applied Physics, 2006. **100**(8).
11. Benzi, P., et al., *Metal-organic deposition of $YBa_2Cu_3O_x$ and $Bi_2Sr_2Ca_1Cu_2O_x$ films on various substrates starting from different fluorine-free metallorganic compounds.* Journal of Chemical Sciences, 2007. **119**(6): p. 631-635.
12. Zhang, W., et al., *$NiMn_2O_4$ spinel as an alternative coating material for metallic interconnects of intermediate temperature solid oxide fuel cells.* Journal of Power Sources, 2011. **196**(13): p. 5591-5594.
13. Ponce, J., et al., *Electrochemical study of nickel-aluminium-manganese spinel $NixAl_{1-x}Mn_2O_4$. Electrocatalytical properties for the oxygen evolution reaction and oxygen reduction reaction in alkaline media.* Electrochimica Acta, 2001. **46**(22): p. 3373-3380.
14. Wang, J. and J. Zhang, *Structural and electrical properties of $NiMg_xMn_{2-x}O_4$ NTC thermistors prepared by using sol-gel derived powders.* Materials Science and Engineering B-Advanced Functional Solid-State Materials, 2011. **176**(7): p. 616-619.
15. Brauer, G., et al., *Magnetron sputtering - Milestones of 30 years.* Vacuum, 2010. **84**(12): p. 1354-1359.
16. Safi, I., *Recent aspects concerning DC reactive magnetron sputtering of thin films: A review.* Surface & Coatings Technology, 2000. **127**(2-3): p. 203-219.
17. Kelly, P.J. and R.D. Arnell, *Magnetron sputtering: a review of recent developments and applications.* Vacuum, 2000. **56**(3): p. 159-172.

18. Window, B., *Recent advances in sputter-deposition.* Surface & Coatings Technology, 1995. **71**(2): p. 93-97.
19. Kelly, P.J. and J.W. Bradley, *Pulsed magnetron sputtering - process overview and applications.* Journal of Optoelectronics and Advanced Materials, 2009. **11**(9): p. 1101-1107.
20. Schmidt, R., A. Basu, and A.W. Brinkman, *Production of NTCR thermistor devices based on $NiMn_2O_{4+delta}$.* Journal of the European Ceramic Society, 2004. **24**(6): p. 1233-1236.
21. Schmidt, R., et al., *An investigation into the surface topology and thickness profile of functional ceramic spinel manganate sputtered, evaporated and screen-printed layers.* Applied Surface Science, 2006. **252**(24): p. 8760-8767.
22. Schmidt, R., et al., *Structural properties of rf magnetron sputter deposited nickel manganate thin films.* Surface Science, 2005. **595**(1-3): p. 239-248.
23. Baliga, S. and A.L. Jain, *Deposition and properties of rf magnetron sputtered $Ni_{0.6}Mn_{2.4}O_4$.* Materials Letters, 1989. **8**(5): p. 175-178.
24. Baliga, S. and A.L. Jain, *Hopping conduction in sputtered Ni-Co-Mn-O spinel films.* Materials Letters, 1991. **11**(5-7): p. 226-228.
25. Yu, X., et al., *Recent developments in magnetron sputtering.* Plasma Science & Technology, 2006. **8**(3): p. 337-343.
26. Arnell, R.D. and P.J. Kelly, *Recent advances in magnetron sputtering.* Surface & Coatings Technology, 1999. **112**(1-3): p. 170-176.
27. Schmidt, R., M. Parlak, and A. Brinkman, *Control of the thickness distribution of evaporated functional electroceramic NTC thermistor thin films.* Journal of Materials Processing Technology, 2008. **199**(1-3): p. 412-416.
28. Parlak, M., et al., *Electron beam evaporation of nickel manganite thin-film negative temperature coefficient thermistors.* Journal of Materials Science Letters, 1998. **17**(23): p. 1995-1997.
29. Parlak, M., et al., *Effect of heat treatment on nickel manganite thin film thermistors deposited by electron beam evaporation.* Thin Solid Films, 1999. **345**(2): p. 307-311.
30. Schmidt, R. and A.W. Brinkman, *Preparation and characterisation of $NiMn_2O_4$ films.* International Journal of Inorganic Materials, 2001. **3**(8): p. 1215-1217.
31. Dieleman, J., E. Vanderiet, and J.C.S. Kools, *Laser ablation deposition - mechanism and application.* Japanese Journal of Applied Physics Part 1-Regular Papers Short Notes & Review Papers, 1992. **31**(6B): p. 1964-1971.
32. Smith, H.M. and A.F. Turner, *Vacuum deposited thin films using a ruby laser.* Applied Optics, 1965. **4**(1): p. 147-&.
33. Venkatesan, T., et al., *Advances in processing high-temperature superconducting thin-films with lasers.* Acs Symposium Series, 1988. **377**: p. 234-264.
34. Singh, R.K., O.W. Holland, and J. Narayan, *Theoretical-model for deposition of superconducting thin-films using pulsed laser evaporation technique.* Journal of Applied Physics, 1990. **68**(1): p. 233-247.
35. Singh, R.K., *Target ablation characteristics during pulsed-laser deposition of thin-films.* Journal of Non-Crystalline Solids, 1994. **178**: p. 199-209.
36. Singh, R.K., D. Bhattacharya, and J. Narayan, *Subsurface heating effects during pulsed laser evaporation of materials.* Applied Physics Letters, 1990. **57**(19): p. 2022-2024.
37. Boyd, I.W., *Thin film growth by pulsed laser deposition.* Ceramics International, 1996. **22**(5): p. 429-434.
38. Eason, R., *Pulsed Laser Deposition of Thin Films: Applications-Led Growth of Functional Materials*2007: Wiley.

39. Zhao, Y.F., et al., *Development of preparation of the functional thin films by pulsed laser deposition.* Surface Review and Letters, 2005. **12**(4): p. 597-604.
40. Ashfold, M.N.R., et al., *Pulsed laser ablation and deposition of thin films.* Chemical Society Reviews, 2004. **33**(1): p. 23-31.
41. Christen, H.M. and G. Eres, *Recent advances in pulsed-laser deposition of complex oxides.* Journal of Physics-Condensed Matter, 2008. **20**(26).
42. Afonso, C.N. and J. Gonzalo, *Pulsed laser deposition of thin films for optical applications.* Nuclear Instruments & Methods in Physics Research Section B-Beam Interactions with Materials and Atoms, 1996. **116**(1-4): p. 404-409.
43. Schmidt, R., *Production and performance of thin and thick film NTCR thermistors based on $NiMn_{(2)}O_{(4)+}$*, 2003, University of Durham: Durham.
44. Dang, V.-S., *Nanotechnology of pinning centres in high temperature superconducting $YBa_2Cu_3O_7$ films*, in *Metallurgy and Materials*2011, University of Birmingham. p. 329.
45. Venables, J.A., G.D.T. Spiller, and M. Hanbucken, *Nucleation and growth of thin-films.* Reports on Progress in Physics, 1984. **47**(4): p. 399-459.
46. Kukuruznyak, D.A., et al., *Combinatorial screening of ternary NiO-Mn_2O_3-CuO composition spreads.* Journal of Applied Physics, 2005. **98** (4).
47. Ko, S.W., et al., *Spin Spray-Deposited Nickel Manganite Thermistor Films For Microbolometer Applications.* Journal of the American Ceramic Society, 2011. **94**(2): p. 516-523.
48. Ko, S.W., et al., *Low Temperature Crystallization of Metastable Nickel Manganite Spinel Thin Films.* Journal of the American Ceramic Society, 2012. **95**(8): p. 2562-2567.
49. Fau, P., et al., *Thin-films of nickel manganese oxide for ntc thermistor applications.* Applied Surface Science, 1993. **65-6**: p. 319-324.
50. Basu, A., A.W. Brinkman, and R. Schmidt, *Effect of oxygen partial pressure on the NTCR characteristics of sputtered $Ni_xMn_{3-x}O_4$+delta thin films.* Journal of the European Ceramic Society, 2004. **24**(6): p. 1247-1250.
51. Basu, A., et al., *A study of the electronic states of $Ni_xMn_{3-x}O_{4+delta}$ thin films using scanning tunneling microscopy and current imaging tunneling spectroscopy.* Journal of the European Ceramic Society, 2004. **24**(6): p. 1149-1152.
52. Ryu, J., et al., *Highly Dense and Nanograined $NiMn_2O_4$ Negative Temperature coefficient Thermistor Thick Films Fabricated by Aerosol-Deposition.* Journal of the American Ceramic Society, 2009. **92**(12): p. 3084-3087.
53. Nelson-Cheeseman, B.B., et al., *Modified magnetic ground state in $NiMn_2O_4$ thin films.* Physical Review B, 2010. **82**(14): p. 7.

Chapter 4

Experimental Methods

4.1. Introduction

The experimental procedures used to fabricate and characterise the NMO films are described in this chapter. The substrate and target preparation is discussed prior to the deposition of the films, followed by a discussion of the pulsed laser deposition technique. The characterisation techniques used are then discussed.

4.2. Pulsed Laser Deposition

PLD has become an extremely popular thin film deposition technique for the deposition of complex oxides such as NMO, mainly due to its extreme simplicity and it's relatively low cost.

A Neocera PLD system was used in this project which consisted of both a target holder and a substrate holder which is housed inside a vacuum chamber with a high vacuum pumping system. A turbo molecular pump was used to evacuate the chamber which allowed for a base

pressure of around 10^{-7} to 10^{-9} Torr to be achieved. The substrate holder in the system has a heater which can be controlled digitally by software on an external computer, allowing for temperatures of up to 900 °C to be achieved, the temperature of the heater is measured by a thermocouple. The target holder has a target rotation system which allows for several targets to be present inside the vacuum chamber at any one time. Several different layers of different compositions or elements can therefore be deposited onto one substrate without the need to bring the chamber back up to atmospheric pressure in order to allow a user to change the target. A Penning gauge is also present in the chamber allowing the user to measure the pressure inside the chamber. The pressure can be manipulated by feeding either oxygen or nitrogen into the chamber. Oxygen and nitrogen flow is controlled by valves that are present on the PLD system.

A Lambda Physik LPX300 excimer KrF laser from Germany, with a wavelength of 248 nm was used as an external laser energy source for the material vaporisation of the NMO target. Optical components between the laser and the chamber allow the laser beam to be focused onto the surface of the target at an angle of 45°, the set-up is shown in Figure. 3.1. This method makes it a potentially suitable technique for the large scale production of NMO thin film thermistors. The laser system used was located in the PLD Laboratory at the School of Metallurgy and Materials at the University of Birmingham. A schematic representation of the PLD system used is shown in Figure 4.2.

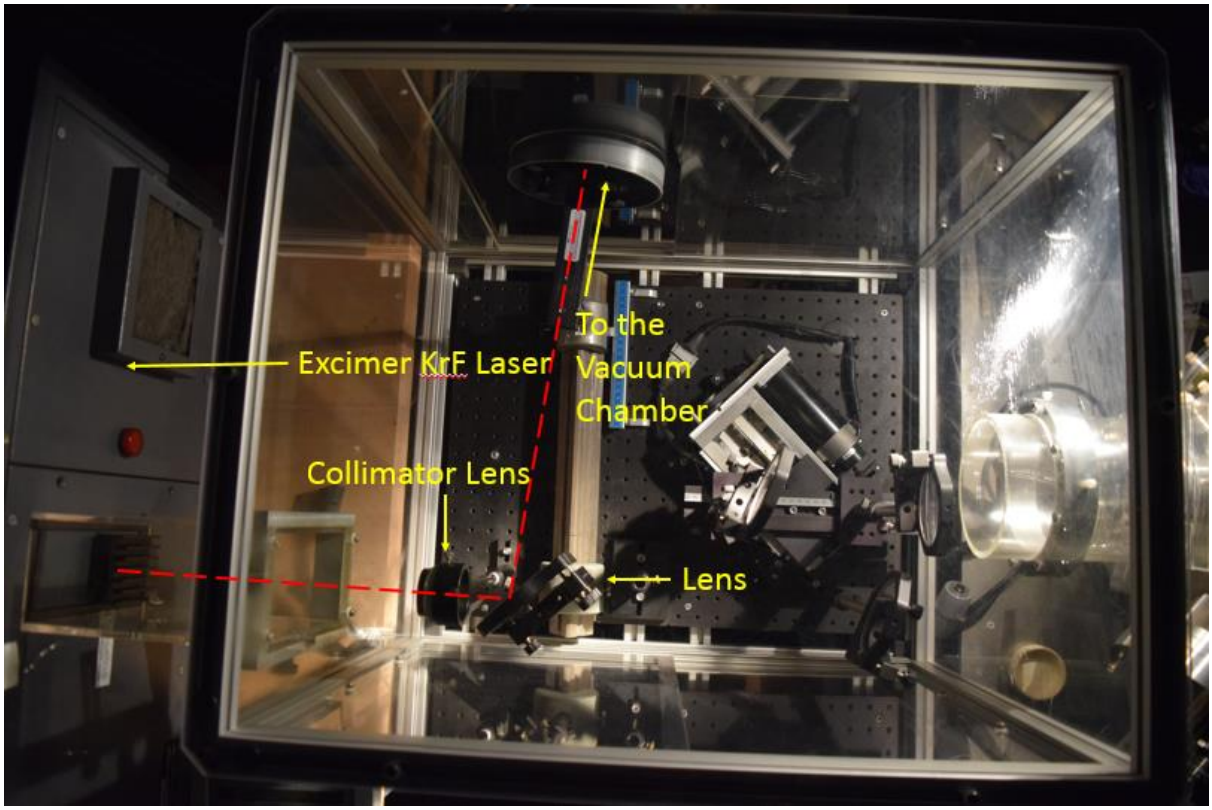

Figure 4.1. Optics chamber of the PLD system used in this project

4.2.1. Deposition Parameters

Initial work was carried out to determine the influence of some of the deposition parameters on the NMO films that were produced. The variable parameters changed were the laser repetition rate, substrate temperature and the oxygen pressure inside the vacuum chamber. Laser repetition rate was varied from 1 to 10 Hz, and the oxygen pressure was 50 to 250 mTorr. The substrate was heated to temperatures between 400°C to 550°C at a rate of 20°C / min, and held constant during the deposition period.

The invariable parameters were the laser fluence which was set at 1 J/cm^2, a substrate to target distance of 50 mm, a deposition time of 40 minutes and a laser pulse duration of 30 ns. After each deposition, the substrates were cooled down at a cooling down rate of 6°C / min under an oxygen background pressure of 350 mTorr which was introduced into the chamber

over a period of 5 minutes while the substrate temperature was maintained. These values were based on past conditions used in reference [1].

During deposition a pulsed laser beam is focussed onto the NMO target, with a high energy density and a high repetition rate. During each pulse a small amount of the target material is ablated from the target in a forward – directed plume towards the substrate. The production of the thin film process can be put into three different stages, 1) the production of an appropriate atomic, molecular or ionic species, 2) the transport of these species from the target to the substrate through a medium, 3) the condensation of the ablated material onto a substrate either directly or via a chemical / electrochemical reaction.

Films deposited using the above conditions resulted in very thin films necessitating the deposition conditions to be changed. Subsequent depositions were carried out using the following conditions: the substrate to target distance was decreased to 40 mm, deposition time was increased to 60 mins and the laser fluence was increased to 2 J/cm^2.

4.3. Powder Characterisation

NiO, Mn_2O_3 and calcined NMO powders were supplied by Amphenol, these powders were characterised in terms of their particle morphology. Their grain size was measured using the average grain intercept method.

4.4. Target Production / Preparation

Two types of targets have been used in this project. The first target was supplied by Amphenol so was therefore pre – prepared, this target was solely used for PLD throughout the project.

Sintered NMO pellets were also produced with a 5.5 mm radius. 1 g of calcined NMO powder (supplied by Amphenol) was placed in a 13 mm diameter Specac die press and using an Instron 5507 the powder was pressed at 10 kN for 2 minutes into 2 – 3 mm thick pellets.

The resultant pellets were then placed on Al_2O_3 plates and then sintered in a tube furnace at 1260°C in air for 9 hours.

The sintered NMO targets were mounted onto the target carousel with silver paste. Before being used for deposition the target surface was conditioned with 1000 pulses at 10 Hz in order to remove any contamination. After five depositions the target was abraded with wet and dry disks with a grit designation P400, P800 and P1200, in order to prevent particulate formation during the deposition process. Particles of nano or micron sizes which are ablated from the edges of craters that are left on the target after laser ablation will have an influence on thin film growth [2, 3].

4.5. Substrate Preparation

The NMO thin films were deposited on three different substrates so that its interaction with different substrates could be investigated. The three substrates used were polycrystalline alumina (Al_2O_3), (100) strontium titanate ($SrTiO_3$) (supplied by PI-KEM) single crystalline and silicon (Si) substrates (PI-KEM). These substrates were chosen due to their relative low cost, good expansion matching to NMO and their lack of reactivity in the oxygen rich conditions used in this project. The sizes of the substrates are presented in the Table 4.1.

Table 4.1. Substrate sizes

Substrate	**Size (w x l x h) mm**
Alumina (Al_2O_3)	10 x 10 x 0.5
Strontium Titanate ($SrTiO_3$)	5 x 5 x 0.5
Silicon (Si)	~ 10 x 10 x 0.5

All of the substrates required cleaning before the deposition of the NMO thin film to remove grease and dirt particles on their surface which can be detrimental to the growth of thin films. The substrates were all cleaned ultrasonically sequentially in baths of acetone, ethanol, propanol and distilled water for about five minutes each, drying by compressed air after each solvent. Laboratory gloves were worn throughout the sample preparation to prevent any further surface contamination. The substrates were mounted onto the substrate stage holder using silver DAG paste (AGG302 Agar Scientific).

4.6. Characterisation of Samples

4.6.1. Scanning Electron Microscopy (SEM)

SEM is often a favoured tool for measuring the surface morphology and microstructure of a material. An electron microscope uses an electron beam to produce a magnified image of a sample. There are three different types of electron microscopy: *scanning, transmission* and *emission*. Scanning and transmission electron microscopes use an electron beam focused on the sample which is used to produce the image while in field emission microscopy the sample itself is the source of the electrons [4]. An SEM consists of an electron gun, a lens system, scanning coils, an electron collector, and a cathode ray display tube (CRT) [4]. A schematic diagram of a typical SEM system is shown in Figure 4.3. Using an electron microscope enables the user to achieve much higher magnifications in comparison to optical microscopes as electron wavelengths are much smaller than photon wavelengths and their depth of field is much higher.

The surface morphology of the thin films was characterised using SEM. Initially using a Jeol 6060 SEM equipped with an Oxford Inca Energy Dispersive X – ray Spectrometer (EDS) based in the Centre of Electron Microscopy at The University of Birmingham. A Jeol JSM – 7000F SEM equipped with X – ray, energy dispersive spectroscopy (EDS) and electron

backscattered diffraction (EBSD) detectors was also used. The EBSD within the 7000F was used to determine a change in the orientation of the material following deposition to thin film.

The particle size, the particle morphology and microstructure of NiO, Mn_2O_3 powder and calcined NMO powder was also measured. The measurements were taken under the accelerating voltage of 20 kV. Sintered NMO material produced by Amphenol and produced at the University of Birmingham were also investigated and compared.

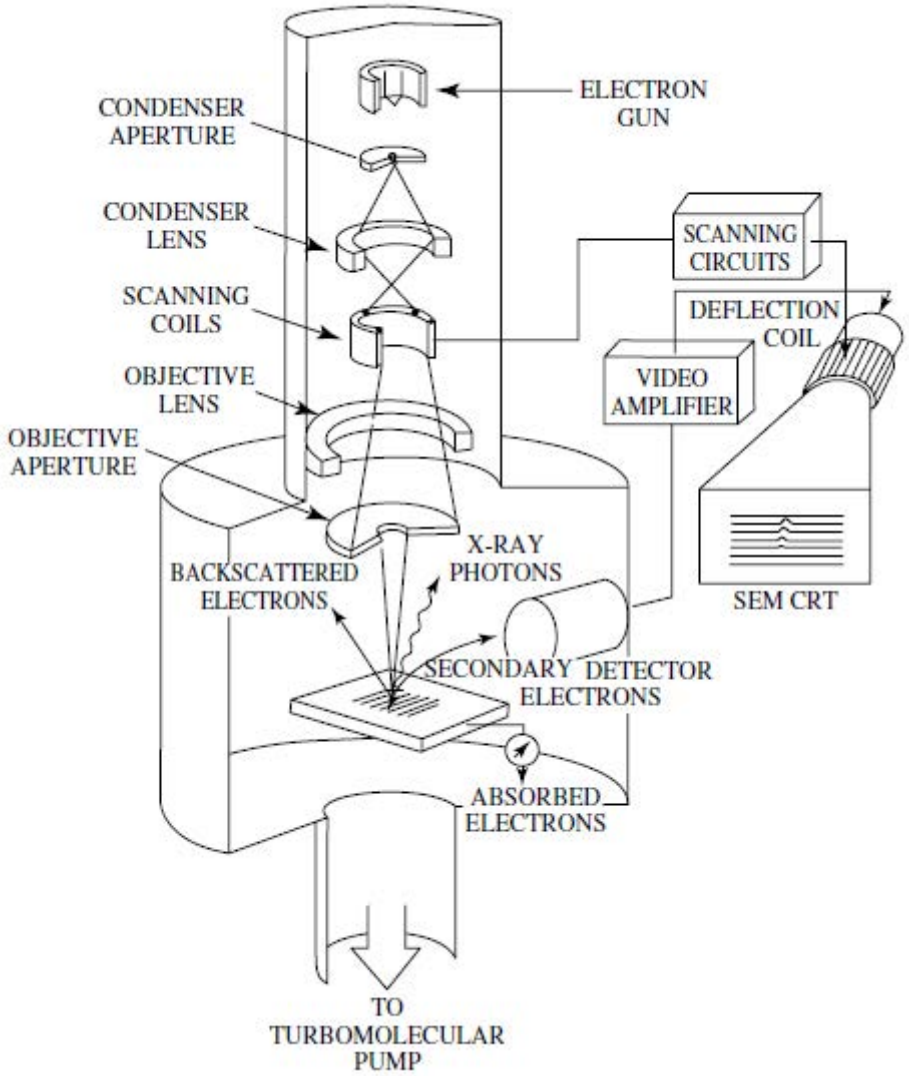

Figure 4.2. Schematic of a typical SEM (Schroder [4])

4.6.2. X – Ray Diffraction (XRD)

XRD is a non – destructive analytical method that is used to determine the crystallinity and phase of a sample. It can also be used to determine the grain size, phase composition and crystal orientation. Initially a Philips X'pert X – ray diffractometer with a Cu K_α source was used to detect diffraction peaks in a $\theta - 2\theta$ scan, with an X – ray wavelength of 0.154 nm and a beam size of 3 mm. A Bruker D2 Phaser benchtop powder diffractometer with a Co source was used for later characterisation.

When the X – rays are diffracted many waves cancel each other out destructively however a few are constructive in specific directions. These few constructive waves can be determined using Bragg's law.

$$2d\sin\theta = n\lambda \tag{3-1}$$

where d is the interplanar spacing, θ is the diffraction angle, n is the integer called the order of diffraction and λ is the wavelength of an incident monochromatic X – ray beam. The pattern that is ultimately produced is identified by comparing with an internationally recognized data base powder diffraction file (PDF) reference patterns.

All films, powders and sintered target materials were analysed using XRD.

4.6.3. Thickness Measurement

A profilometer Dectak 3 operated in a clean room was used to produce step profiles of the thin films. A PLD clamp was used to produce the step which was required for the profile measurement from the substrate to the films surface, where part of the alumina substrate surface was covered prior to deposition with the clamp. The Dectak is then used to produce a step

profile by dragging a diamond tipped stylus along this profile. The results are then converted to graph form, an example of the graph produced is given in Figure 4.3

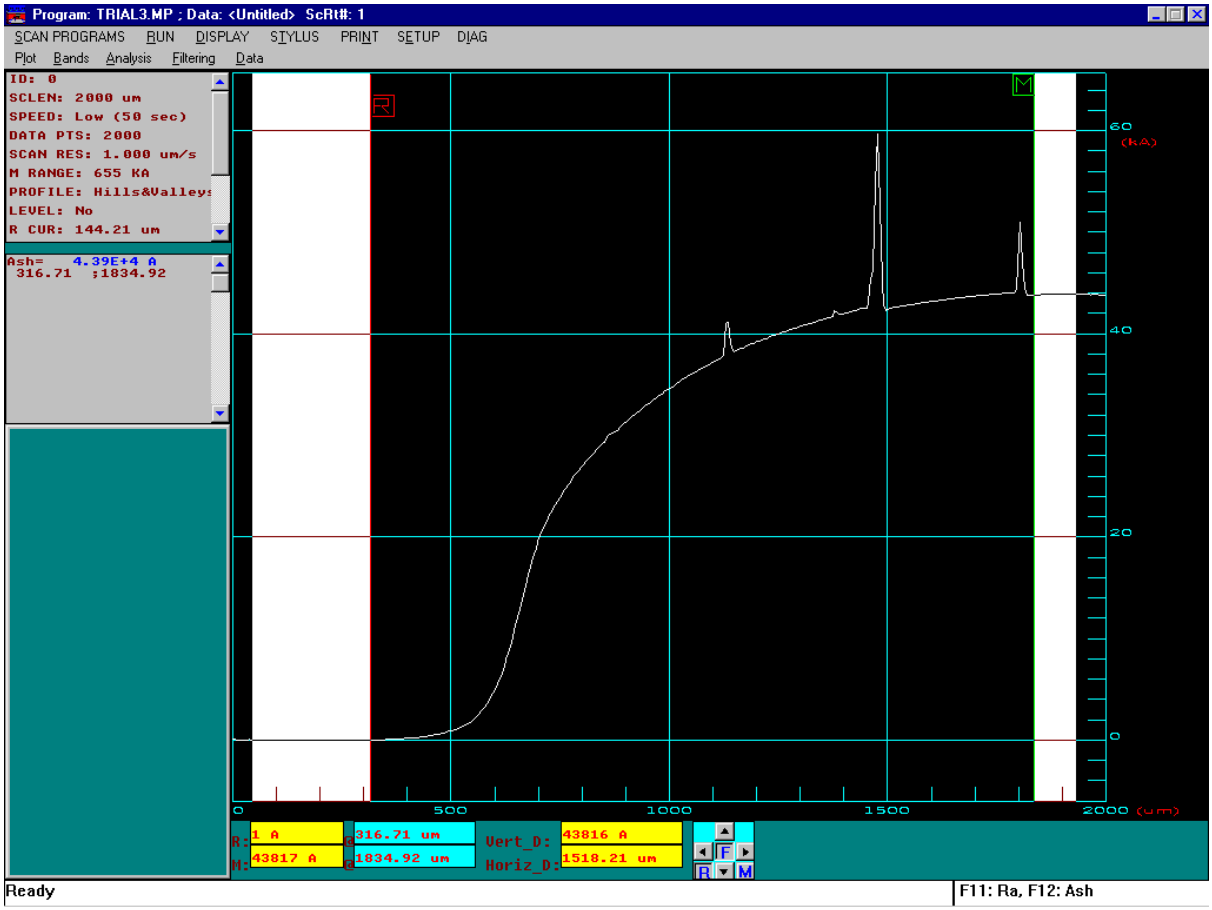

Figure 4.3. Dectak surface profile graph

Cross sections of some samples were also produced to confirm the Dectak's results. The films and substrates were broken into a cross section by a diamond cutter. The broken side of the film was then encased in Epo fix epoxy resin and polished. The thickness of the film was measured using a Jeol 7000F SEM. The thickness was best obtained by making several measurements along the sample from the edges to the centre. The results were then averaged. An example of a cross section is given below in Figure 4.4.

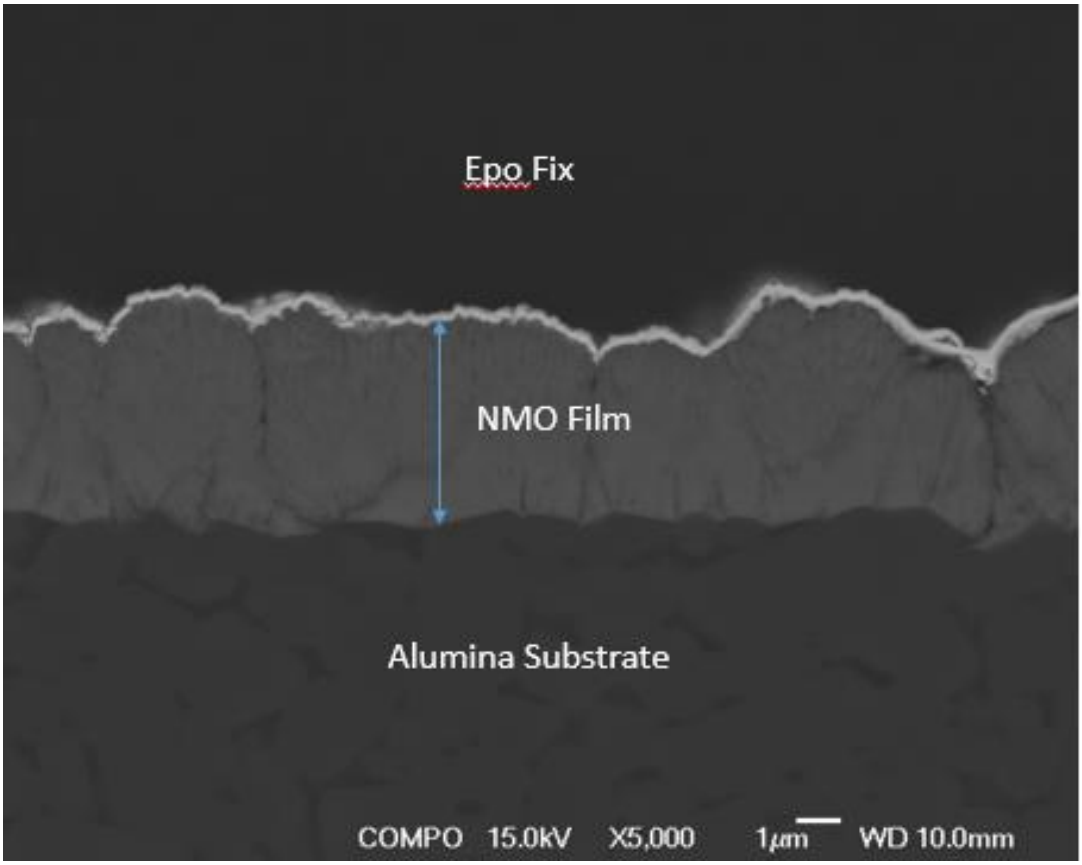

Figure 4.4. Example cross section of an NMO thin film on polycrystalline alumina substrate

4.7. Resistivity Measurements

4.7.1. Through – Thickness Resistance Measurements

Resistivity measurements of the sintered material (supplied by Amphenol) and the sintered pellets produced at Birmingham using calcined powder from Amphenol were carried out using a four point probe technique at room temperature. The sintered materials had silver paste doctor bladed onto their faces which was then sintered at 700°C for 10 minutes in air. Four silver wires were then soldered onto the faces of the sintered material. A Hewlett Packard 6625A system DC power supply and a Keithley 181 nanovoltmeter were then attached to the wires, this same technique was then used to measure the resistivity of the sintered pellets. Figure 4.8. shows a schematic diagram of the experimental set up used.

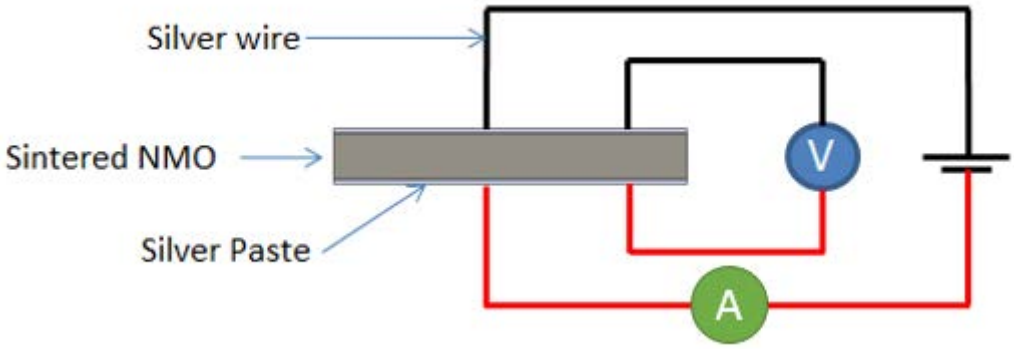

Figure 4.5. Schematic of 4 point probe technique used for measuring resistivity in the sintered materials.

This was also repeated without sintering silver paste onto the faces but instead using a conductive silver epoxy as a solder replacement. These measurements have been compared, on the same samples, to those made using a commercial four – point jig which is intended to be used for the characterisation of the thin films. Figure 4.6. shows the jig used for the resistivity measurement.

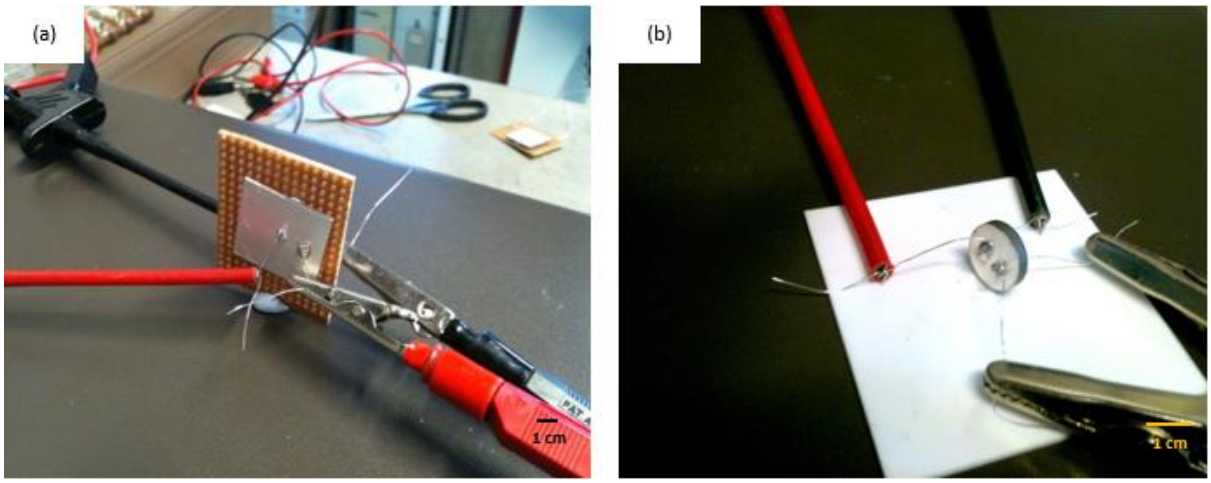

Figure 4.6. (a) Sintered target used for resistivity measurement, (b) sintered pellet used for resistivity measurement.

The resistance was determined by ohm's law as represented below:

$$R = \frac{V}{I} \tag{4-2}$$

where R is the resistance measured in Ω, V is voltage is measured in V, and I is current which is measured in A. Using this equation, the measured voltage on the voltmeter is divided by the current on the power supply to determine the resistance.

The resistivity was then determined using the following equation.

$$\rho = R \times \frac{A}{\ell} \tag{4-3}$$

where ρ is the resistivity in Ω.m, R is the resistance in Ω, A is the cross sectional area of the specimen in m^2, and l is the thickness of the piece of material in m measured using calipers.

4.7.2. Four Point Probe

A Jandel multi height four point probe with a RM3000 test unit is a simple apparatus which is used to measure the resistivity of semiconductors, it was used to measure the bulk resistivity of the thin films and bulk samples produced in this project. The configuration of the probes is shown in the diagram below.

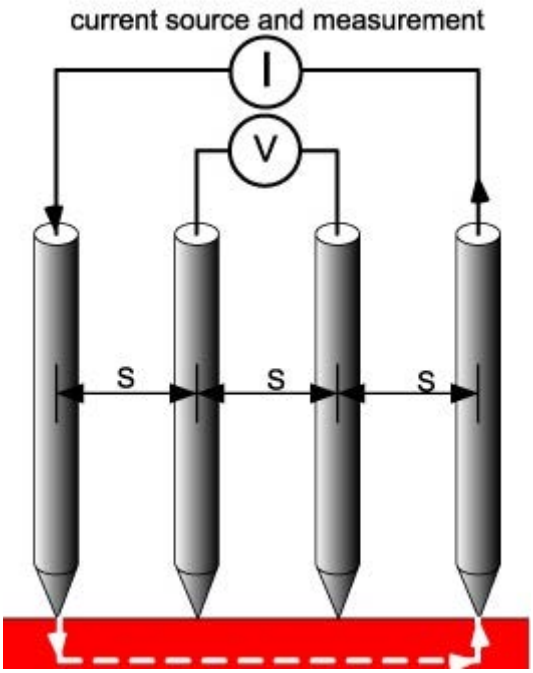

Figure 4.7. Four point probe configuration [6]

A current is passed through the two outer probes the voltage is measured through the inner two probes which allows for a measurement of the sample's resistivity. The bulk resistivity is measured in Ω.cm by the use of the following equation in samples where the wafer thickness is less than half of the probe spacing (s) so was used for the measurement of the thin films bulk resistivity.

$$\rho = \frac{\pi}{\ln(2)} t \left(\frac{V}{I}\right) = 4.523t \left(\frac{V}{I}\right) \quad (4\text{-}4)$$

where t is the layer/wafer thickness in cm.

In thicker samples another equation is used:

$$\rho = \frac{V}{I}\frac{\pi t}{ln\left(\frac{sinh\left(\frac{t}{s}\right)}{sinh\left(\frac{t}{2s}\right)}\right)}$$

where s is the probe spacing.

4.7.3. Van der Pauw (VDP) Technique

Electronic transport properties measurements (the Hall coefficient and resistivity vs. temperature) are extremely useful and straightforward methods for characterizing conducting materials such as metals, semiconductors and superconductors. Temperature dependent transport coefficients are particularly important in the study of thermodynamic properties and transport mechanisms in understanding the physics of charge carriers. Common resistivity and Hall measurements are generally carried out with a test bar as shown in Figure 4.11.

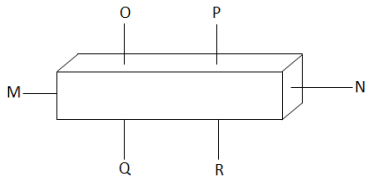

Figure 4.8. Test bar used for measurement of resistivity and Hall measurements

With traditional bar shaped samples, six contacts are needed for simultaneous measurement of the resistivity and Hall coefficient. Also all dimensions of the sample and the distance between the contacts for resistance measurement need to be known. The resistivity is determined from the potential difference and the distance between the contacts O and P, the current (I) and the dimensions of the bar. When measuring resistances at low temperatures (e.g in liquid nitrogen) the point contacts possess resistances of the order of mega ohms. Therefore

voltages cannot be determined accurately. A “bridge shaped” geometry can be used to overcome this:

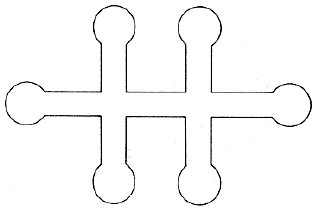

Figure 4.9. “Bridge shaped” sample with large contact faces to reduce contact resistances

The voltage and current contacts have a relatively large surface area, therefore the contact resistances are low. These methods are based on the fact that the geometry of the sample maintains a simple pattern of parallel current stream – lines. However, despite this, formulae has been devised which can correct from the deviation of parallelism.

Van der Pauw (VDP) [7] gives us a mathematical method which allows the user to measure the resistivity and Hall coefficient in semiconducting samples of an arbitrary shape.

The VDP technique is useful when determining the resistivity and Hall coefficient of a sample as it does not require any modification of the sample shape or making any pattern on the surface. This therefore eliminates the risk of any chemical attack to the sample during chemical etching or exposing it to heat treatment during photolithography. When using the VDP technique to measure the resistivity of a lamella, four small contacts are placed at arbitrary positions around the edge of the sample M, N, O and P, like in Figure 4.10. To use the VDP technique certain criteria have to be met:

1. The sample must have a flat shape of uniform thickness.
2. The sample must not have any isolated holes.
3. The sample must be homogeneous and isotropic.
4. All four contacts must be located at the edges of the sample.

5. The area of the contact must be much smaller than the area of the entire sample.

Specific probe location is not vital for reliable measurements, however the sample thickness still remains important. Instead of measuring the distance between the contacts, the in – plane geometric factor is determined by switching the probes used for current and voltage.

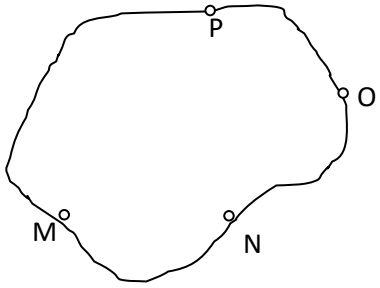

Figure 4.10. Arbitrarily shaped sample, with four contacts M, N, O and P on the periphery. The Hall coefficient can also be measured on a sample on this kind [7].

A current is applied between contact points M and N (I_{MN}). Then the potential difference in measured between points P and O (V_P-V_O):

$$R_{MN,OP} = \frac{V_P - V_O}{I_{MN}} \tag{4-5}$$

Analogously

$$R_{No,MP} = \frac{V_M - V_p}{I_{NO}} \tag{4-6}$$

This method of measurement is based on the theorem that between $R_{MN,OP}$ and $R_{NO,PM}$, a simple relation exists:

$$\exp\left(-\frac{\pi t}{\rho} R_{MN,OP}\right) + \exp\left(-\frac{\pi t}{\rho} R_{NO,PM}\right) = 1 \tag{4-7}$$

where t is the thickness of the lamella and ρ is the resistivity of the material.

Therefore if t and the "resistances" $R_{MN,OP}$ and $R_{NO,PM}$ are known, then using the previous equation ρ is the only unknown quantity.

When the sample has a line of symmetry, M and O are placed on the line of symmetry while N and P are disposed symmetrically with respect to this line.

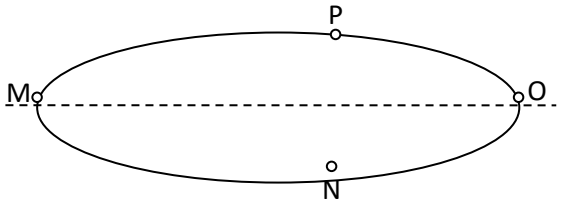

Figure 4.11. Symmetrical sample, if two of the contacts are situated on the line of symmetry and the other two are symmetrically located with respect of this line, then only one measurement is necessary to determine the resistivity.

Then $R_{NO,PM} = R_{MN,OP}$, ρ can then be found from:

$$\rho = \frac{\pi t}{ln2} R_{MN,OP} \dots\dots \quad (4\text{-}8)$$

In this project the following set up was initially used to determine the bulk resistivity of a sample. All samples were square in shape so configuration of the current source and voltmeter are as outlined in Figure 4.12.

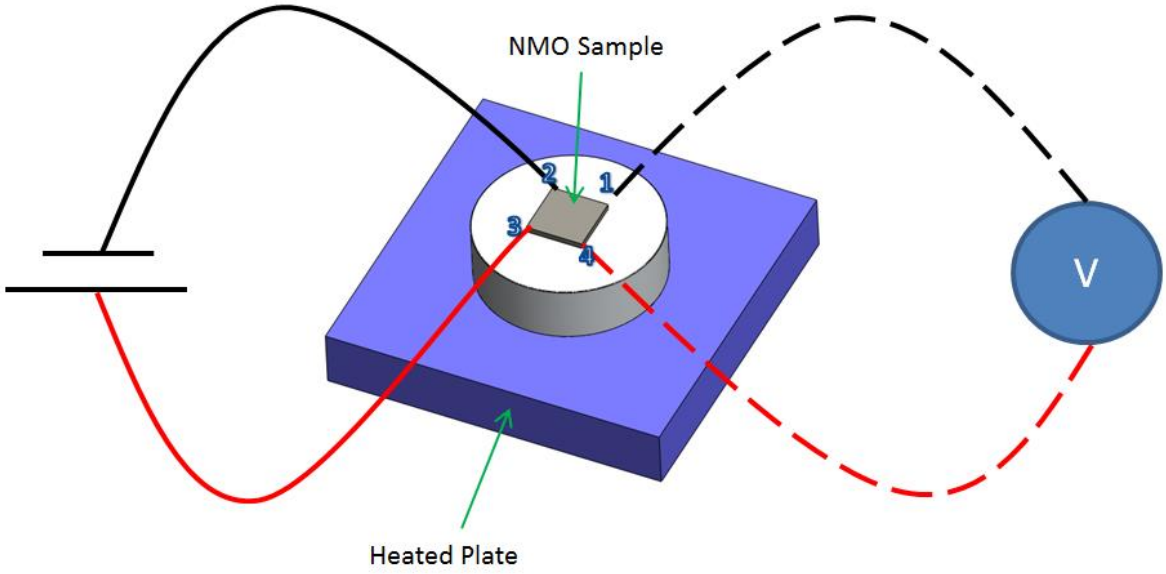

Figure 4.12. Van der Pauw configuration used to determine bulk resistivity

A heated plate was used to allow for resistance measurements to be made at different temperatures. Good ohmic contacts were made by the use of silver epoxy which was also used to attach copper wires onto the surface. A current was then supplied using the Hewlett Packard 6625A system DC power supply and the voltage was measured using the Keithley 181 nanovoltmeter.

The resistivity can be worked out by:

$$R_{12,34} = \frac{V_{34}}{I_{12}} \tag{4-9}$$

where 1, 2, 3 and 4 are the ohmic contact locations for the voltage and current. The bulk ohmic resistivity of the sample can be determined by inverting the VDP equation:

$$exp\left(-\frac{\pi d R_A}{\rho}\right) + \exp\left(-\frac{\pi d R_B}{\rho}\right) = 1 \tag{4-10}$$

where R_A and R_B are the two side resistances.

$$R_A \equiv (R_{43,12} + R_{34,21} + R_{12,43} + R_{21,34})/4 \quad (4\text{-}11)$$

$$R_B \equiv (R_{32,41} + R_{23,14} + R_{41,32} + R_{14,23})/4 \quad (4\text{-}12)$$

4.7.4. Four Wire Resistance Measurement Technique

A four wire resistance measurement technique was designed to determine accurately the electrical properties of the thin films. The films were firstly masked with Kapton tape, and Cr and Au electrodes were sputtered onto the edges of the films as shown in Figure 4.13. The samples were attached to an SEM stub with double sided sellotape and copper wires attached to the electrodes using silver epoxy. A thermocouple was placed on the surface of the thin film to determine the temperature of the films during measurement. The copper wires were then connected to a Keithley 181 nanovoltmeter and a HP 6625A system DC power supply, a multimeter was attached between the sample and power supply in order to determine the current. During measurement 20 V was applied across the sample. A schematic of the setup is shown in Figure 4.14 below.

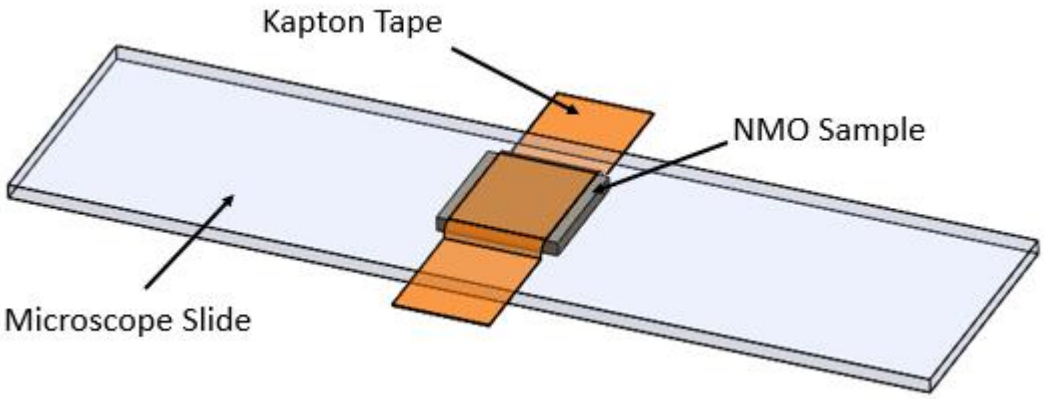

Figure 4.13. Masked NMO sample on microscope slide

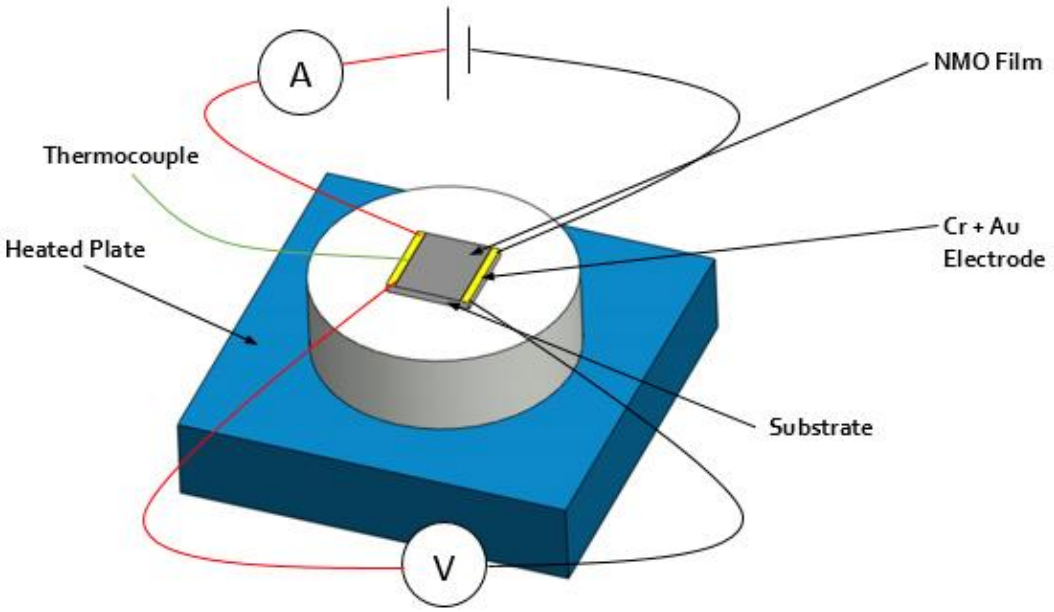

Figure 4.14. Schematic of four wire resistance measurement technique

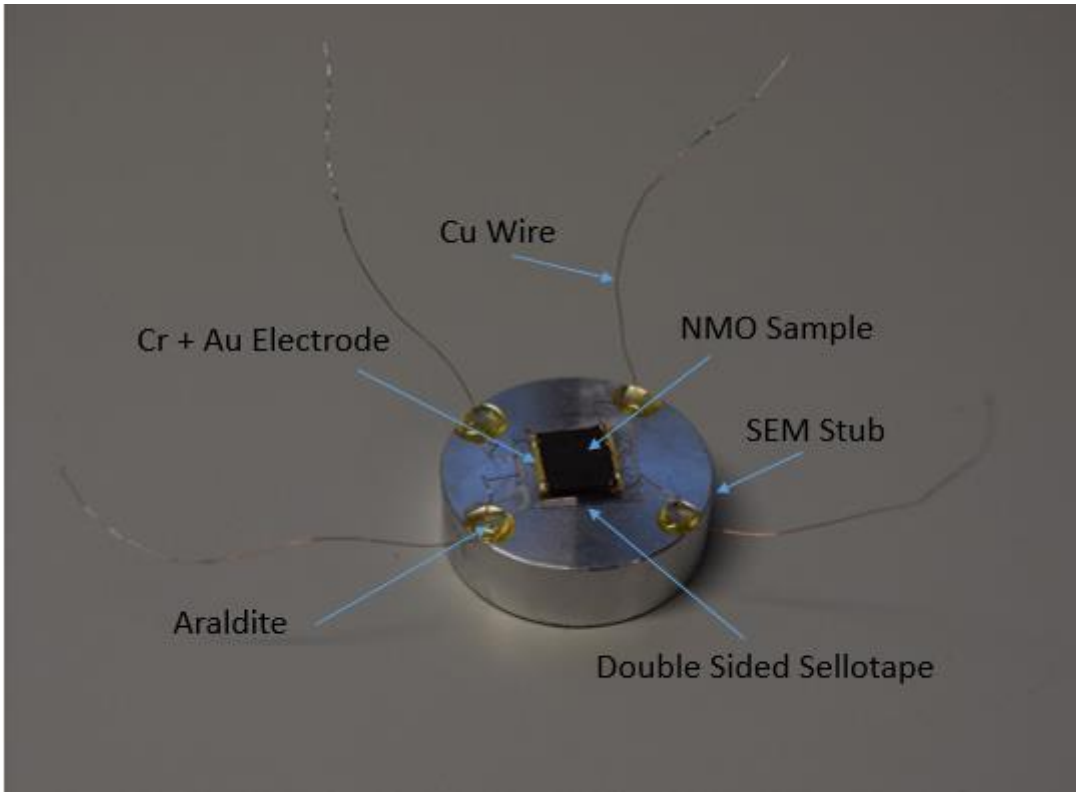

Figure 4.15. Photograph of sample set up

The β value of the films was determined using the following equation

$$\beta = \frac{\ln(R_1) - \ln(R_2)}{[1/T_1 - 1/T_2]} \quad (4\text{-}13)$$

where R_1 and R_2 is the resistance in ohms (Ω) at 25 and 85°C respectively and T_1 and T_2 are the two temperatures in Kelvin (K).

4.7.5. Further Improvement to the Four Wire Resistance Measurement

The method of heating the sample was changed to help improve the accuracy and homogeneity of the sample temperature. This was achieved by using a Lunair Ltd. environmental chamber TJR as opposed to the heating plate to change the temperature of the samples environment. The exact same layout of the resistance measurement technique as used previously was employed.

4.7.6. LabVIEW use in Resistance Measurements

To allow for automatic measurements of the temperature, voltage and current of the thin films a LabVIEW program was produced. The program was designed so that every minute different measurements would be taken to allow for the determination of the resistance, these included the temperature of the film from a thermocouple, the current and the voltage. The program also included a graph to allow for a real time measurement of the resistance versus temperature to be viewed. The user interface for the LabVIEW is shown below in Figure 4.16.

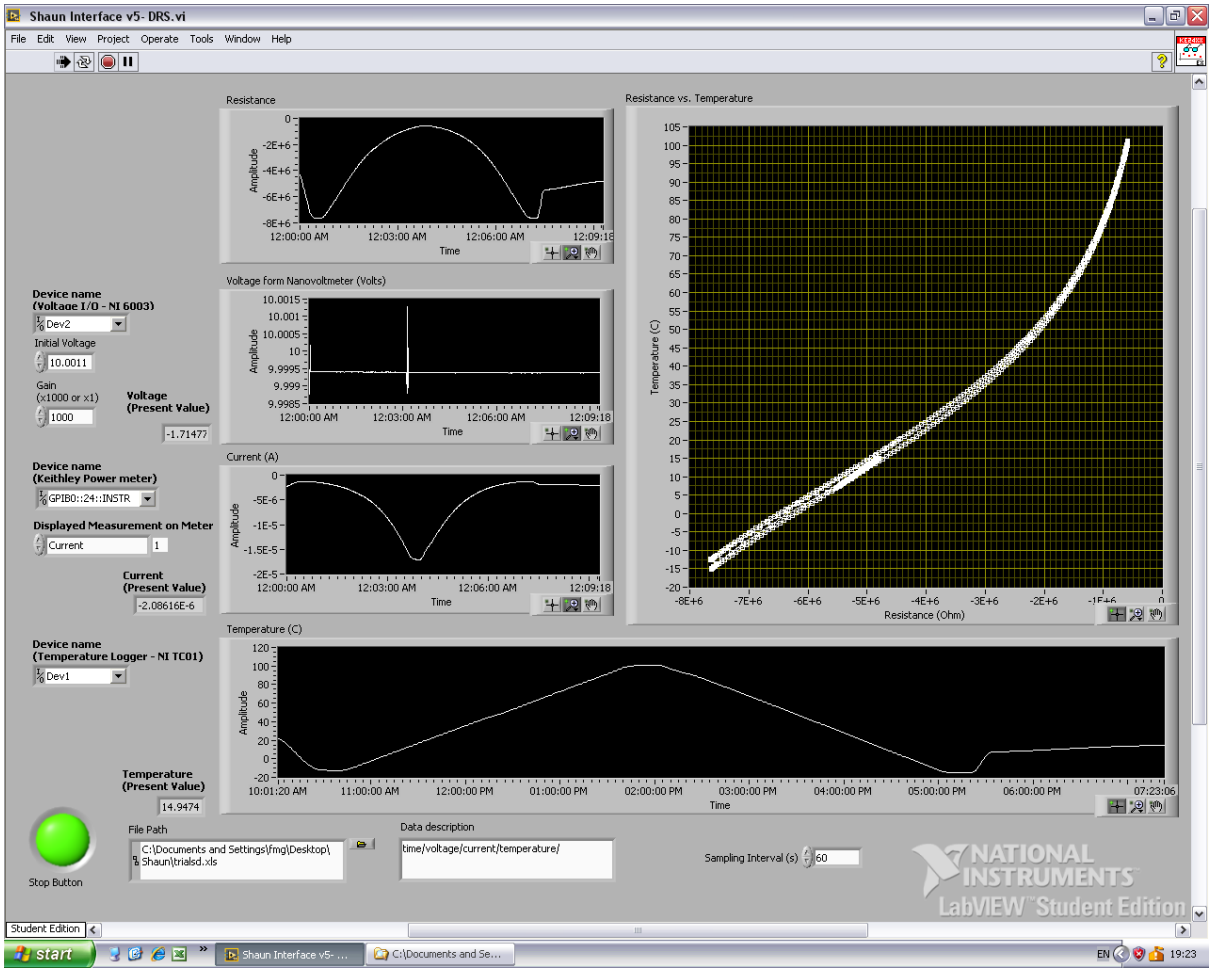

Figure 4.16. Screenshot of LabVIEW program used for the resistance measurement

4.7.7. Resistance Measurements on a Commercial Resistor

A resistor of a known value (Ohmite SM102031007FE resistor, 1 GΩ) which is consistent over a wide temperature range was measured using the four wire resistance measurement technique used in this investigation to determine if any errors could be attributed to the experimental equipment, which could explain any differences in repeats. The results showed that the resistance was consistent throughout measurements over the temperature range used in this investigation, therefore any changes in resistance could only be attributed to the films themselves.

The four wire technique used in this investigation was used to measure a commercial resistor whose resistance is known and unchanging over a wide temperature range. This was to ensure that there were no changes in the resistance measured during the experimental procedure. If any changes in resistance was measured these would therefore be attributed to experimental layout.

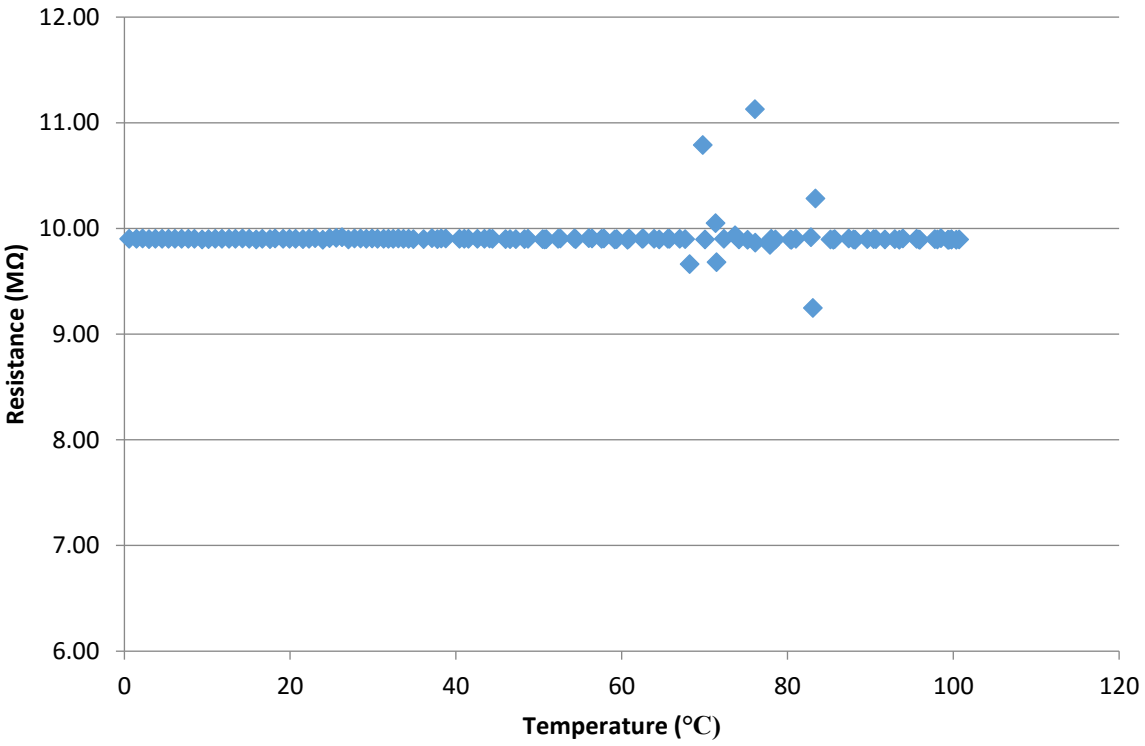

Figure 4.17. Resistance vs. Temperature graph of an Ohmite resistor, 1 GΩ

The graph above shows that the resistance is consistent throughout the experiments whole temperature range. Therefore, changes in resistance measured using this technique are due to the sample and the experimental equipment.

4.7.8. Amphenol Test System

Repeat measurements of some of the films were undertaken using some of the sponsoring company's equipment. A Keithley 2700 multimeter was used to determine the film's resistance and an environmental chamber was used to control the film's temperature. The temperature of the film was recorded by the use of a thermistor inside the chamber.

References

1. Kukuruznyak, D.A., et al., *Combinatorial screening of ternary NiO-Mn_2O_3-CuO composition spreads.* Journal of Applied Physics, 2005. **98**(4).
2. Kukuruznyak, D.A., et al., *Preparation and properties of thermistor thin-films by metal organic decomposition.* Thin Solid Films, 2001. **385**(1-2): p. 89-95.
3. Zheng, J.P. and H.S. Kwok, *Preparation of indium tin oxide-films at room-temperature by pulsed-laser deposition.* Thin Solid Films, 1993. **232**(1): p. 99-104.
4. Schroder, D.K., *Semiconductor Material and Device Characterization*. 2006: Wiley.
5. University, R.A.; Available from: http://abinitio.iehk.rwth-aachen.de/glossar/?text_id=159&division=Array&scale=Array.
6. Education, P.; Available from: http://www.pveducation.org/pvcdrom/characterisation/four-point-probe-resistivity-measurements.
7. Pauw, V.D., *A Method of Measuring the Resistivity and Hall Coefficient on Lamellae of Arbitrary Shape.* Phillips Technical Review, 1958. **20**: p. 220 - 224.

Chapter 5

Initial Results and Establishment of Processing and Characterisation Techniques

5.1 Introduction

The initial experiments involved characterising the target material and the powders used for the fabrication of the targets and substrates that were subsequently used for the PLD experimentations. In this chapter the characterisation of the metal oxide powders used to fabricate the targets are reported. These powders were supplied by the sponsoring company of this project, Amphenol Thermometrics. The powders were characterised by SEM and also underwent XRD. Resistivity measurements were also carried out on the sintered target to allow for a comparison between the bulk material and the resulting thin films. An analysis of the use of different substrates was also carried out to allow for an evaluation of the suitability of the different substrates to determine their advantages or disadvantages. Initial deposition of thin

films were carried out using conditions determined from literature [1] and then their structure and microstructure were characterised by XRD and SEM. The Van der Pauw technique was used to measure the electrical properties of the films and also to ascertain the suitability of the technique.

5.2 Characterisation of Starting Powders

5.2.1 SEM Results

NiO and Mn_2O_3 powders and calcined NMO powder (prepared and provided by Amphenol) were investigated by SEM to determine the particle size of the powders and their particle morphology, the results are shown in Figure 5.1, Figure 5.2. and Figure 5.3. respectively. The NiO and Mn_2O_3 powders were calcined at 850°C for 4 hr.

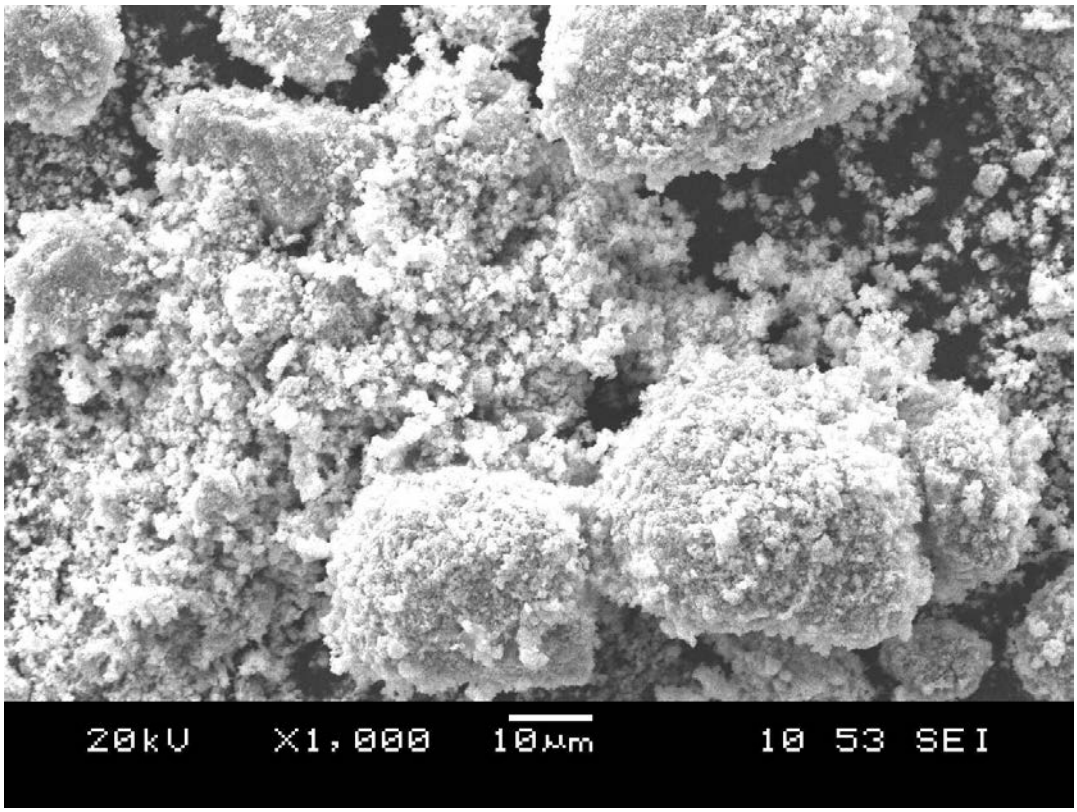

Figure 5.1. SEM micrograph of NiO powder (Jeol 6060)

In the micrograph, the NiO powder shows a regular morphology with a particle size of around 2 µm. The NiO particles have agglomerated into larger clumps of around 30 – 40 µm which would need to be broken down if a calcined NMO powder is to be made.

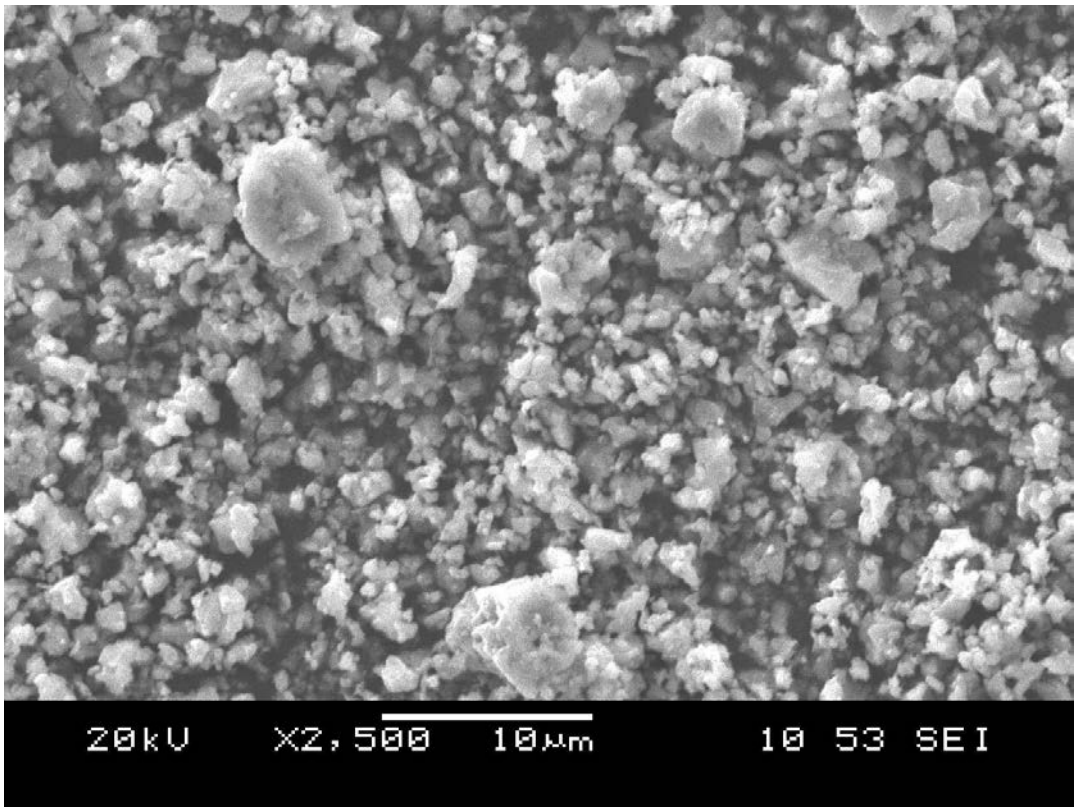

Figure 5.2. SEM micrograph of Mn_2O_3 powder (Jeol 6060)

The Mn_2O_3 powder is not uniform in size however the particles do have similar shapes, it has a particle size range of 0.6 to 1.87 µm. There is not much sign of agglomeration in comparison to the NiO powder.

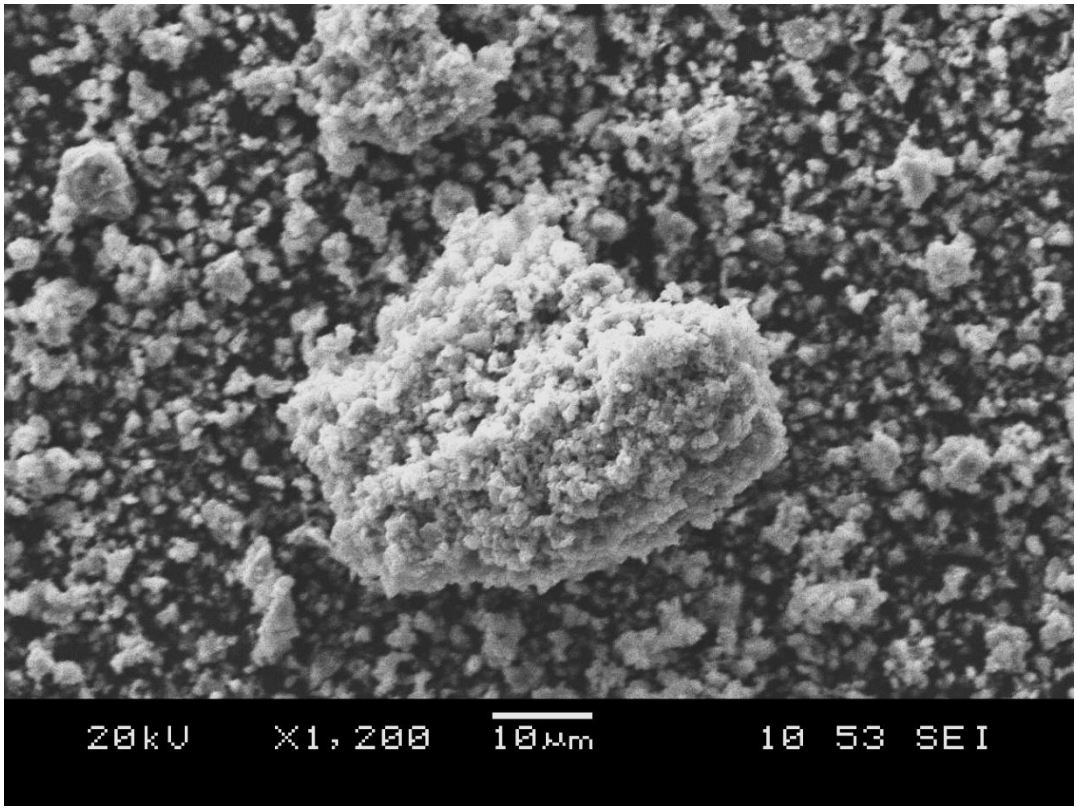

Figure 5.3. SEM micrograph of calcined NMO powder (Jeol 6060)

From the calcined NMO micrograph it can be seen that the particle morphology is not uniform in size and it is irregular in shape. An average particle size is difficult to determine as the sizes observed are too different.

5.2.2 XRD of Starting Powders

XRD patterns of the starting powders NiO and Mn_2O_3 were measured to determine the phase and crystallinity of the materials and to enable comparison with XRD patterns of the sintered material or the thin films. Figure 5.4. and Figure 5.5. show the XRD diffraction patterns of NiO and Mn_2O_3, respectively.

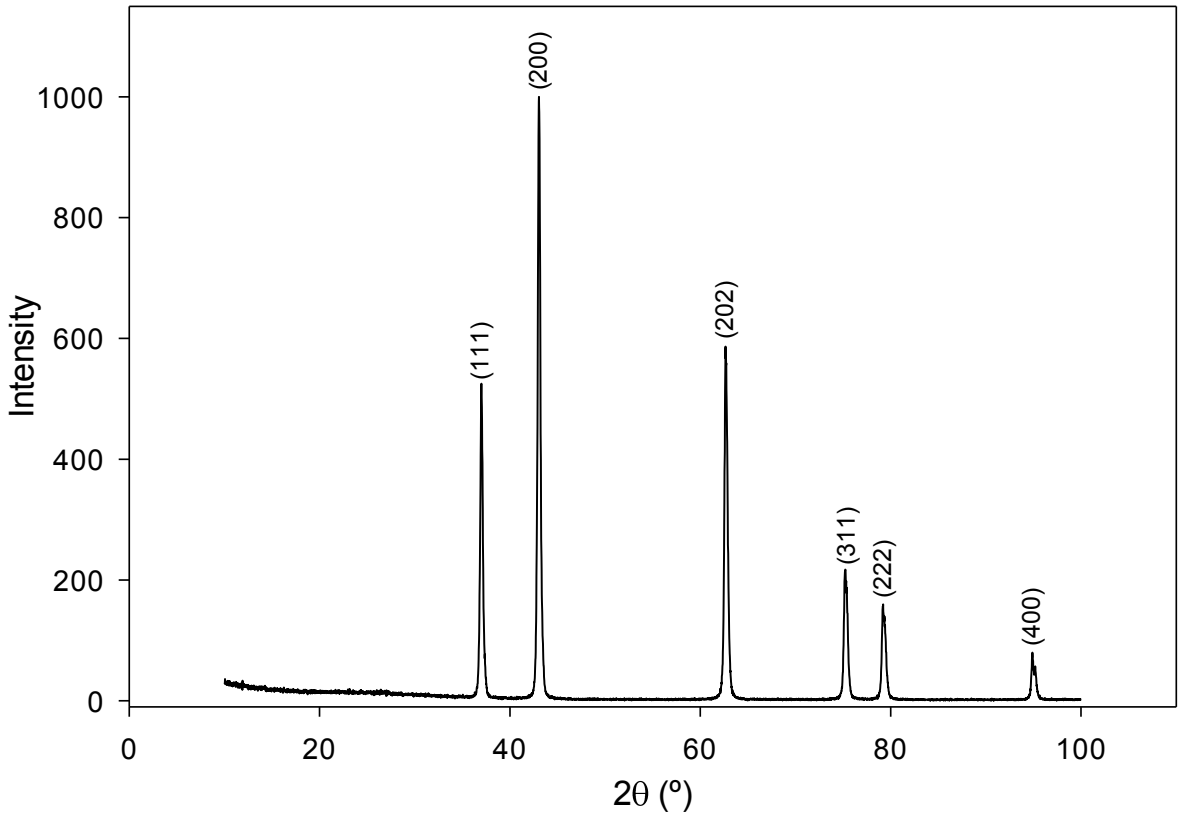

Figure 5.4. XRD pattern of NiO (Cu radiation)

All peaks observed in the XRD diffraction pattern shown in Fig 5.4 could be attributed to NiO. The diffraction pattern of NiO shows peaks at 2θ values of 37.29º (111), 43.33º (200), 62.94º (202), 75.50º (311), 79.48º (222) and 95.20º (400). Index data was obtained from reference [2] (*JCPDS* card 47-1049).

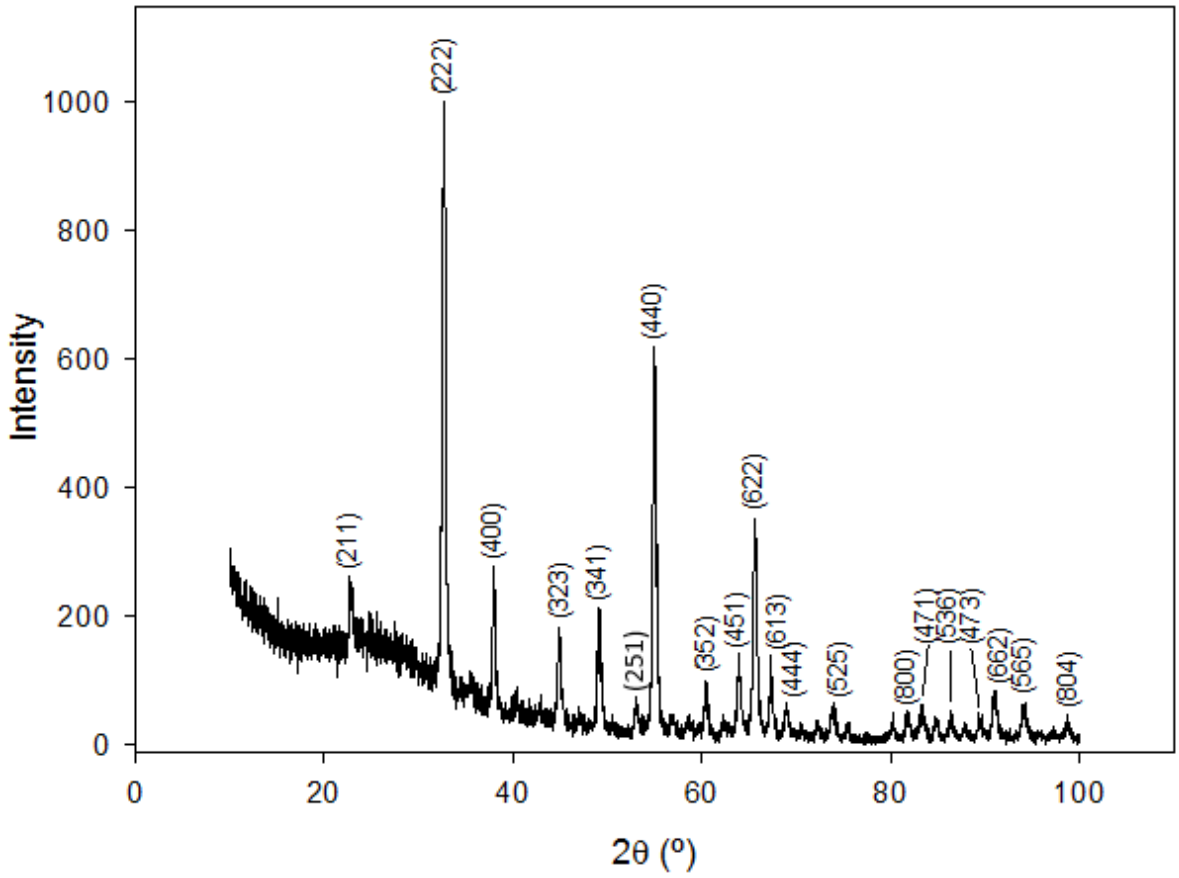

Figure 5.5. XRD pattern of Mn_2O_3 (Cu radiation)

All peaks observed in the XRD diffraction pattern shown in Figure 5.5 could be attributed to Mn_2O_3. The diffraction pattern of Mn_2O_3 shows peaks at 2θ values of 23.10º (211), 32.98º (222), 38.28º (400), 45.26º (323), 49.39º (341), 53.34º (251), 55.22º (440), 60.70º (352), 64.13º (451), 65.86º (622), 67.58º (613), 69.00° (444), 73.93° (525) 81.64° (800) 83.37° (471) 86.24° (536) 89.46° (473) 91.08° (662) 94.06° (565) 98.79° (804). Index hkl data was obtained from reference [3] *JCPDS* 01-089-2809

The calcined NMO powder, the sintered NMO and the thin films were characterised by XRD analysis to determine if they displayed the expected structure and if any unreacted or secondary phases were present.

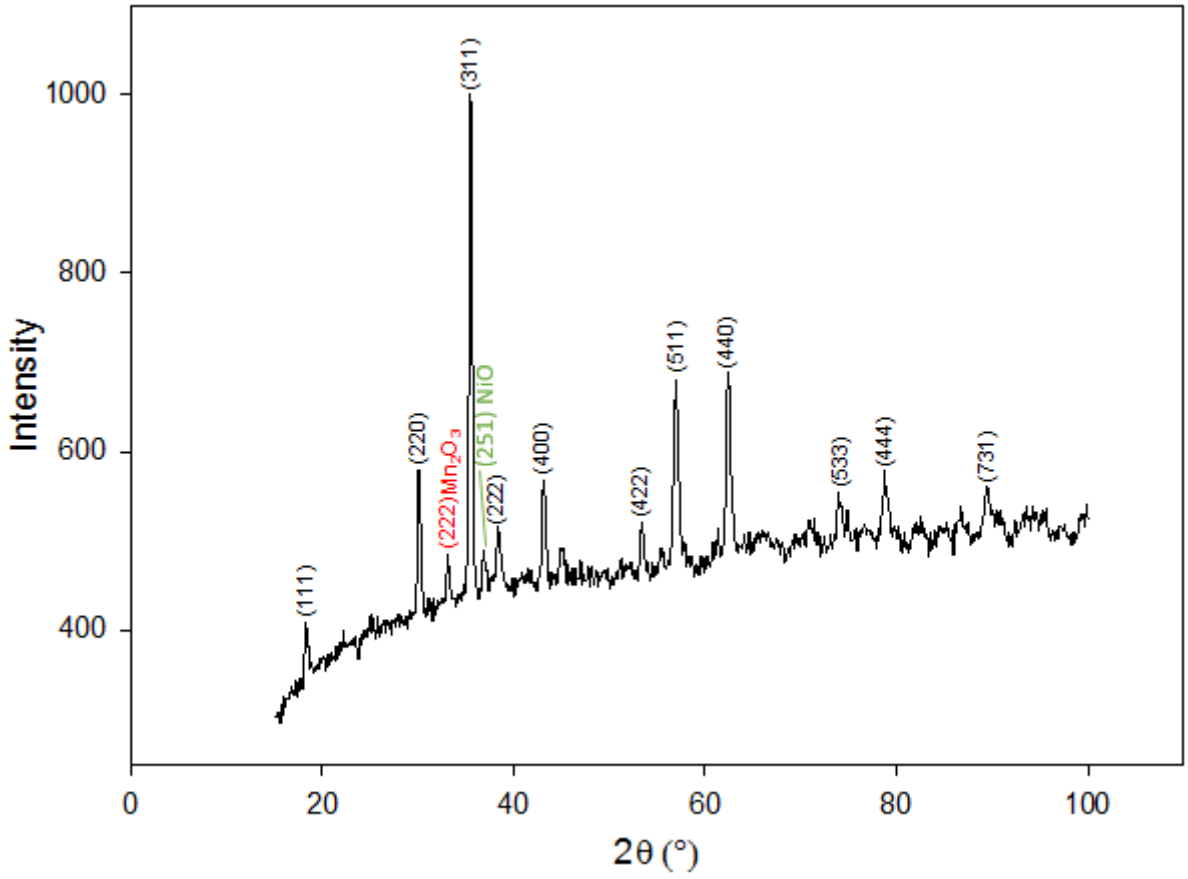

Figure 5.6. XRD pattern of calcined NMO powder (Cu radiation)

The diffraction pattern of the NMO powder calcined at 850 °C for four hours is shown in Figure 5.6 shows peaks at 18.305º (111), 30.08º (220), 35.48º (311), 38.32º (222), 43.25° (400) 53.34º (422), 56.90º (511), 62.31º (440), 73.85º (533), 78.70º (444) and 89.45° (731). This diffraction pattern matches the literature pattern except at 33.12º which may indicate the presence of Mn_2O_3 (the 222 reflection from the Mn_2O_3 structure) and at 36.89° which may indicate the presence of NiO 251 reflection.

5.3 Characterisation of Sintered NMO Target Material

5.3.1 SEM Results

The microstructure of the sintered NMO material supplied by Amphenol was investigated along with the sintered NMO pellets (1260°C for 9 hr in air) produced at Birmingham from the calcined powder. Representative micrographs from these samples are shown in Figures 5.7. and 5.8. respectively. These act as a baseline to enable a comparison to be made with the microstructure of the thin films.

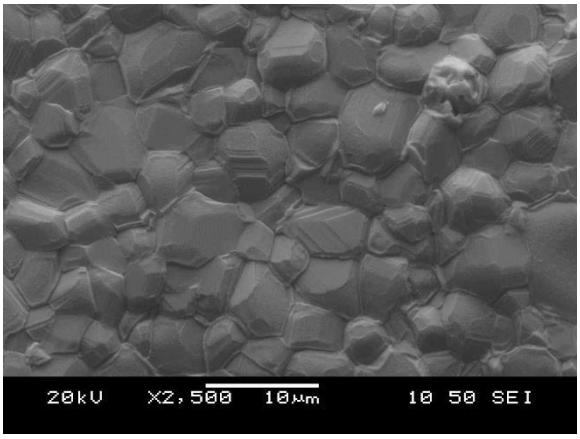

Amphenol sintered NMO,

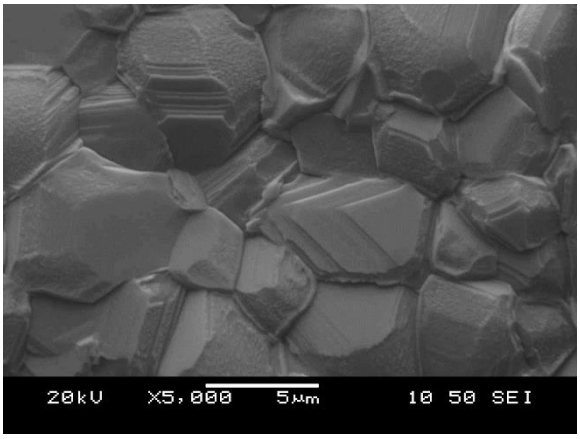

Amphenol sintered NMO

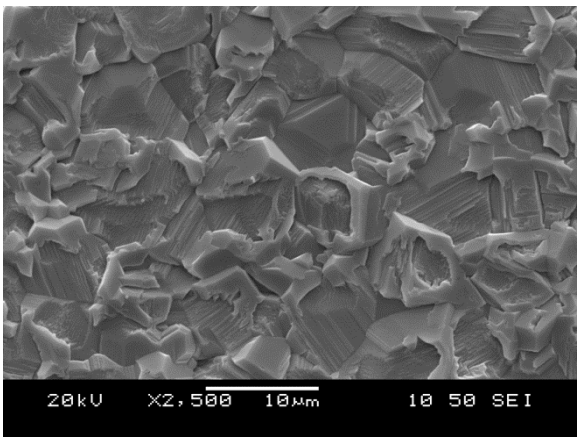

UoB sintered NMO

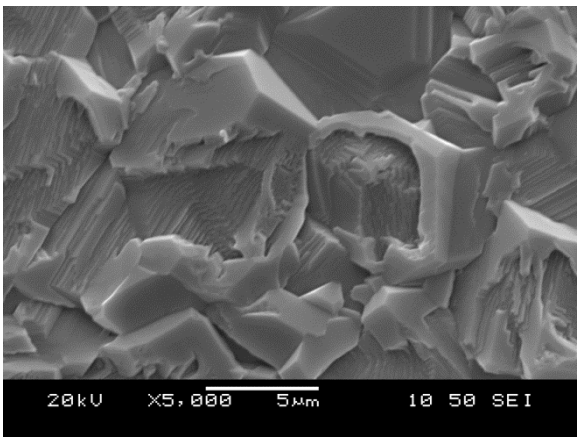

UoB sintered NMO

Figure 5.7. SEM micrographs of fracture surfaces of the NMO material sintered by Amphenol and at UoB (Jeol 6060)

Figure 5.7 shows the grain size of the Amphenol sintered NMO is estimated to be approximately 6 µm and shows low porosity indicating that it has a dense structure, and its grains can be seen to be equiaxed. The grain size of the UoB sintered NMO pellets is also approximately 6 µm as shown in Figure 5.8. There is low porosity indicating that it has a dense structure, however the grains have a much more irregular structure compared to those of the Amphenol materials. This irregular structure may affect the electrical conductivity of the pellets in comparison to the equiaxed grains found in the NMO material sintered by Amphenol [5, 6].

5.3.2 Energy Dispersive X – Ray Spectroscopy (EDX) Results

The NMO material sintered by Amphenol, whilst in the SEM, was put through EDX analysis to determine atomic ratios. Figure 5.8. shows the EDX spectrum of the material sintered by Amphenol.

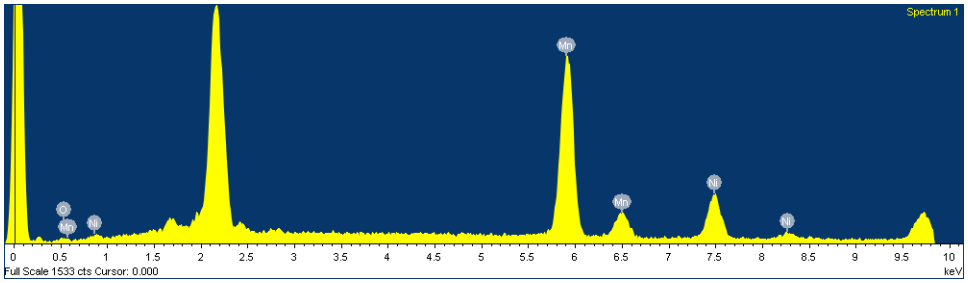

Figure 5.8. EDX Spectrum of sintered NMO by Amphenol.

The atomic ratios are as shown in Table 5.1.

Table 5.1. Atomic ratio of sintered NMO material.

Element	Weight %	Atomic %
O K	9.50	26.77
Mn K	71.12	58.35
Ni K	19.38	14.88

Only peaks attributed to Ni, Mn, and O could be found during EDX analysis so no unexpected elements were discovered suggesting that they are suitable for the fabrication of thin films. Several calculations of the Ni to Mn atomic ratio were made ranging from 1:4 – 1:1.27 which suggests that the EDX data is unreliable when determining the amount of Ni, Mn and O present in the material. Also other possible reasons such as non-homogeneity of the

sample structure, make it hard to get reproducible results. Therefore, EDX analysis was not to be used as a characterisation technique for the measurement of this material and the thin films produced from it.

5.3.3 XRD Results

A literature NMO XRD pattern was obtained [7] as seen in Figure 5.9. so comparisons could be made against the calcined NMO powder, the sintered NMO material and the thin films produced.

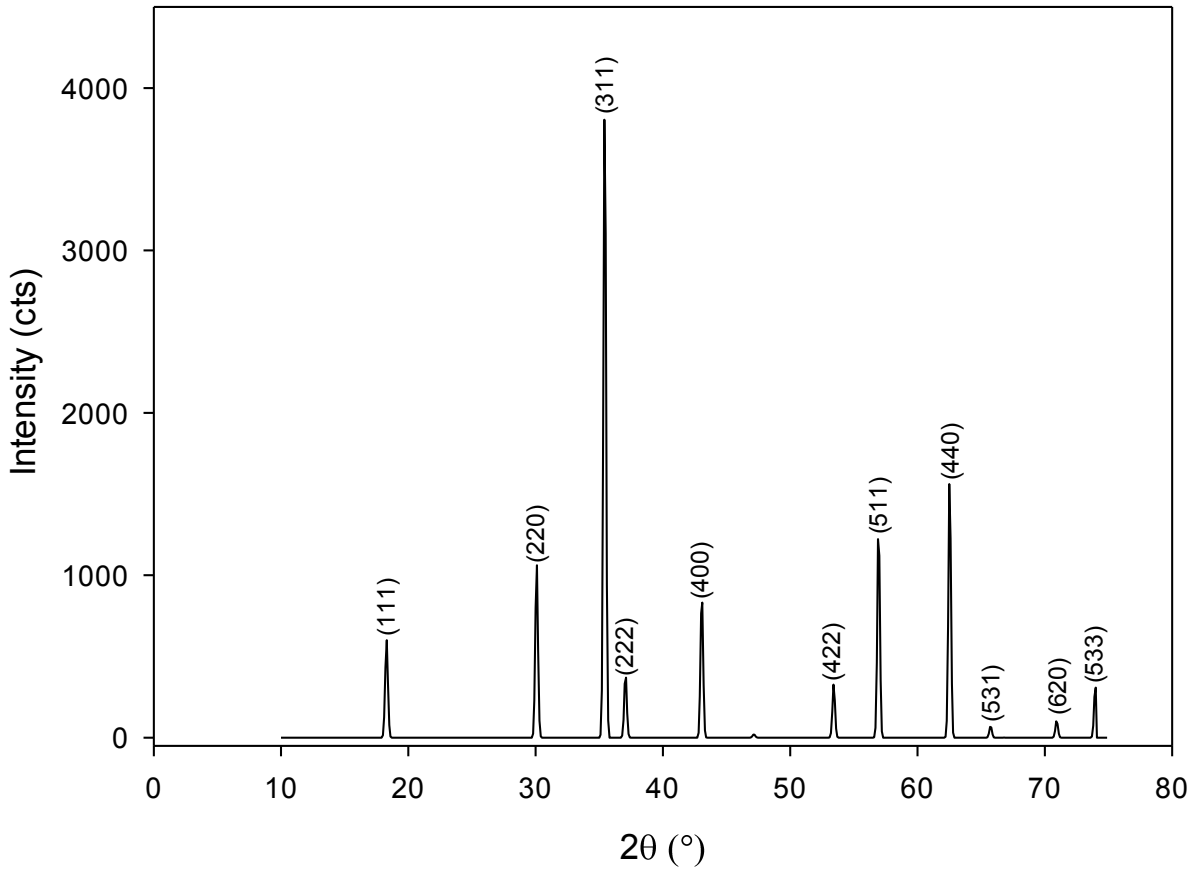

Figure 5.9. Literature $NiMn_2O_4$ XRD pattern [7]. (Cu radiation)

The diffraction pattern of the literature NMO shows 2θ peaks at 18.27º (111), 30.05º (220), 35.40º (311), 37.03º (222), 43.02º (400), 53.37º (422), 56.89º (511), 62.47º (440), 65.75° (531) 71.10° (620) and 73.90º (533) consistent with the partially inverse spinel structure.

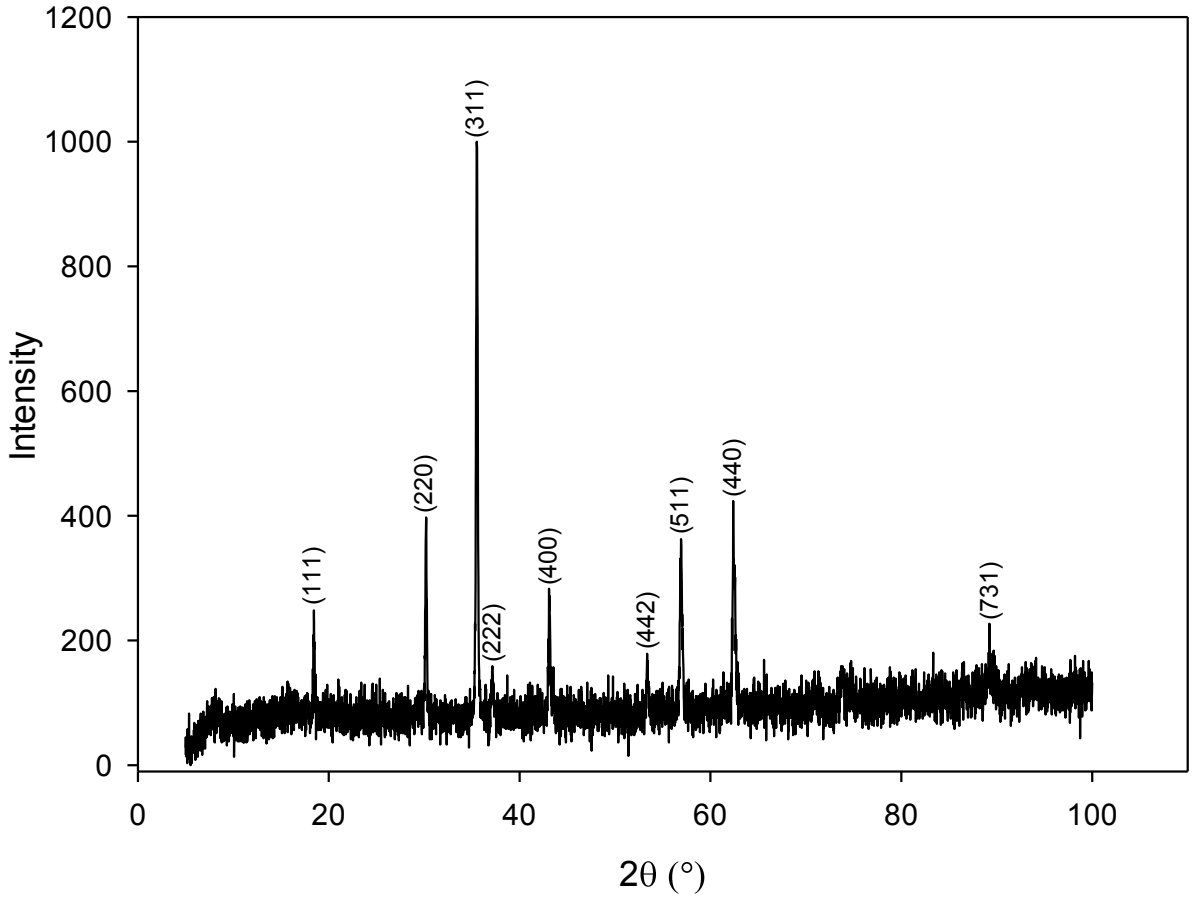

Figure 5.10. XRD pattern of Amphenol sintered NMO material (Cu radiation)

The XRD pattern of a sintered NMO sample produced by Amphenol is shown in Figure 5.11. All peaks observed could be attributed to the NMO structure. The processing conditions for the Amphenol sintered target involve the calcined powders (NMO) to be sintered at 1260°C for 9 hr in air. The sintering of the calcined powders is likely to have an effect on the material in respect to its phase diagram. The high temperature of 1260°C will cause a change in in its phase from cubic spinel to cubic spinel and a rock salt phase as according to the phase diagram proposed by Tang et al [4]. Which is likely to result in the final phase of sintered target material to not be purely cubic spinel. Peaks are present in the diffraction pattern of the Amphenol sintered NMO material at 18.25º (111), 29.98º (220), 35.30º (311), 36.93º (222), 42.89º (400), 53.20º (422), 56.70º (511), 62.25º (440) and 89.13º (731) indicating it has the correct partially

inverse spinel structure. All of the peaks observed in the Amphenol sintered structure were present in the literature sample, however there were more peaks detected in the literature sample which are missing in the Amphenol sintered sample. The peaks at 65.75° (531) 71.10 (620) and 73.90º (533) were not detected in the Amphenol sintered sample suggesting that there is a slight difference in the crystal structure in the two samples.

5.3.4 Resistivity Results

The resistivity of the sintered NMO material was measured to determine a standard value of the resistivity to allow for a comparison to be made between the thin films produced using this material. A literature value of $3.7 \times 10^3\ \Omega cm$ at room temperature (20°C) [8] is also known to allow for a determination for which resistivity technique will be suitable for the measurement of the NMO material. The through thickness method was used to determine the resistance and resistivity results and is explained in further detail in section 4.7.1

The average resistance of the Amphenol sintered NMO material was established by measuring the current and the voltage data as shown in Figure 5.12 using the method as described in section 4.7.1. The slope of the graph was then calculated.

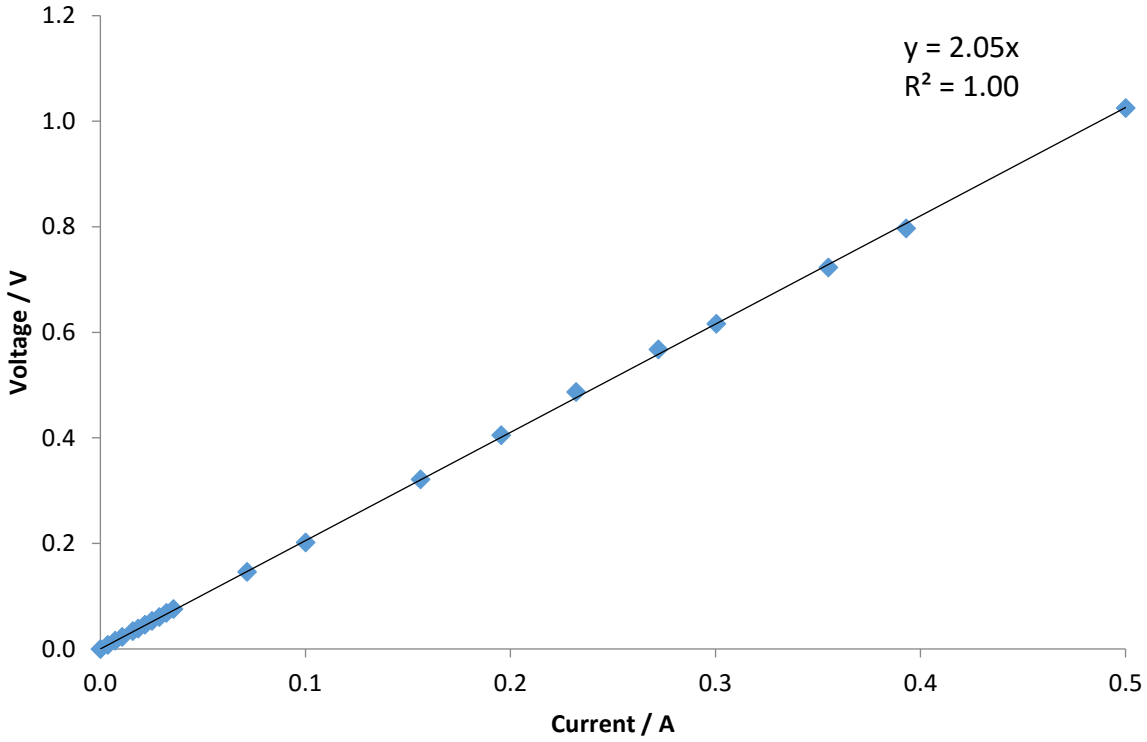

Figure 5.11. Voltage vs Current of Amphenol sintered NMO material with silver paste electrodes.

The resistance value was 2.0453 Ω as seen from the graph. Therefore, the resistivity of the sintered material was calculated as $1.22 \times 10^2\ \Omega.\mathrm{cm}$ determined using equation (4-3).

The measurements were then repeated on a separate piece of the Amphenol sintered NMO material and the average resistance was determined as 1.9691 Ω. The resistivity was then worked out to be $1.17 \times 10^2\ \Omega.\mathrm{cm}$.

The experiment was then repeated without sintering silver paste onto the faces of the Amphenol sintered NMO material, and the results are shown in Figure 5.12.

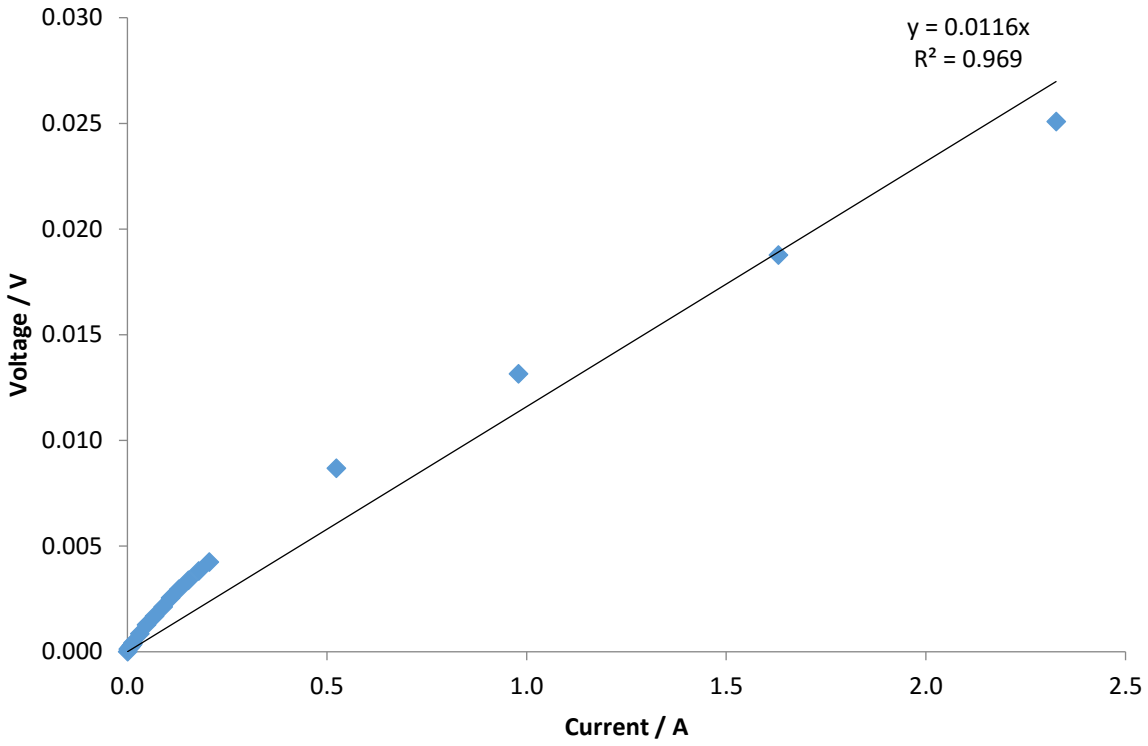

Figure 5.12. Voltage vs Current of repeat sintered NMO material without silver paste.

The resistance was determined to be 0.011 Ω and the resistivity was calculated to be 0.625 Ω.cm. The measurements were then repeated on a separate piece of the Amphenol sintered NMO material. The average resistance was found to be 0.0173 Ω and the resistivity was found to be 1.03 Ω.cm. The graphs of the non – silvered NMO material were not as linear as those from samples with silvered electrodes and the resistance measurements are also much lower in comparison to the samples with silver electrodes and the literature value. During the calculation of the resistivity the cross sectional area of the samples was assumed to be 625 mm^2 (i.e the full area of the sample), however the silver epoxy used to attach the silver wires onto the material in reality was much smaller than this. This may therefore account for some errors in the calculation of the resistivity. The measurements without the silver paste have therefore been disregarded as unreliable.

The average resistance of a UoB sintered pellet made from calcined powder was determined as 1.9691 Ω and its resistivity as 8.03 Ω.cm. The measurements were then repeated on a separate sintered NMO pellet also made at UoB with an average resistance of 2.0453 Ω and the resistivity measuring 8.20 Ω.cm. The resistivity measurements of the NMO material sintered by Amphenol and at the University of Birmingham (UoB) differed by a factor of fifty with the Amphenol sintered material having an increased resistivity. This may be due to differences in processing and the different microstructure observed in the two types of samples. A further difference is noticed in comparison to the literature value [8] which may be due to the different sintering time of fifty hours having an effect on NMO inversion parameter and changing its oxygen stoichiometry [8, 9].

A Jandel multi height four point probe with RM3000 test unit was also used to confirm the bulk resistivity of the sintered material prepared by Amphenol, as shown in Table 5.2 and described in section 4.7.2.

Table 5.2. Four point probe bulk resistivity measurements of Amphenol sintered NMO material

Entry	Current Range (μA)	Reading (mV)	Bulk Resistivity For Wafers (Ω.cm)
1	10	92	439
2	10	107	512
3	10	117	561
4	10	80	384
5	10	91	435
6	10	94	451
7	10	93	444
8	10	87	417
9	10	97	464
10	10	88	419
			Average: 453

A repeat value was determined as 378 Ω.cm.

The four point probe resistivity measurements varied substantially. After testing and discussion with Jandel, a conclusion was made that contact resistance was an issue, despite the fact that the four point probe method is intended to remove these effects. However with the NMO semiconductors these issues are still present due to their highly insulating nature as discussed by Kukuruznyak et al. [1]. This therefore may explain why such variable results were obtained.

5.3.4.1 Measurement of NMO Target Using Four Wire Resistance Technique

The resistivity of the NMO Amphenol sintered bulk target material was measured using the four wire resistance technique described in section 4.7.4 to determine a reference measurement for comparison with the thin films produced using this material. The NMO material's resistance was measured at temperatures between – 10 and 100°C and the results are shown in Figure 5.13, and the calculated resistivity is shown in Figure 5.14.

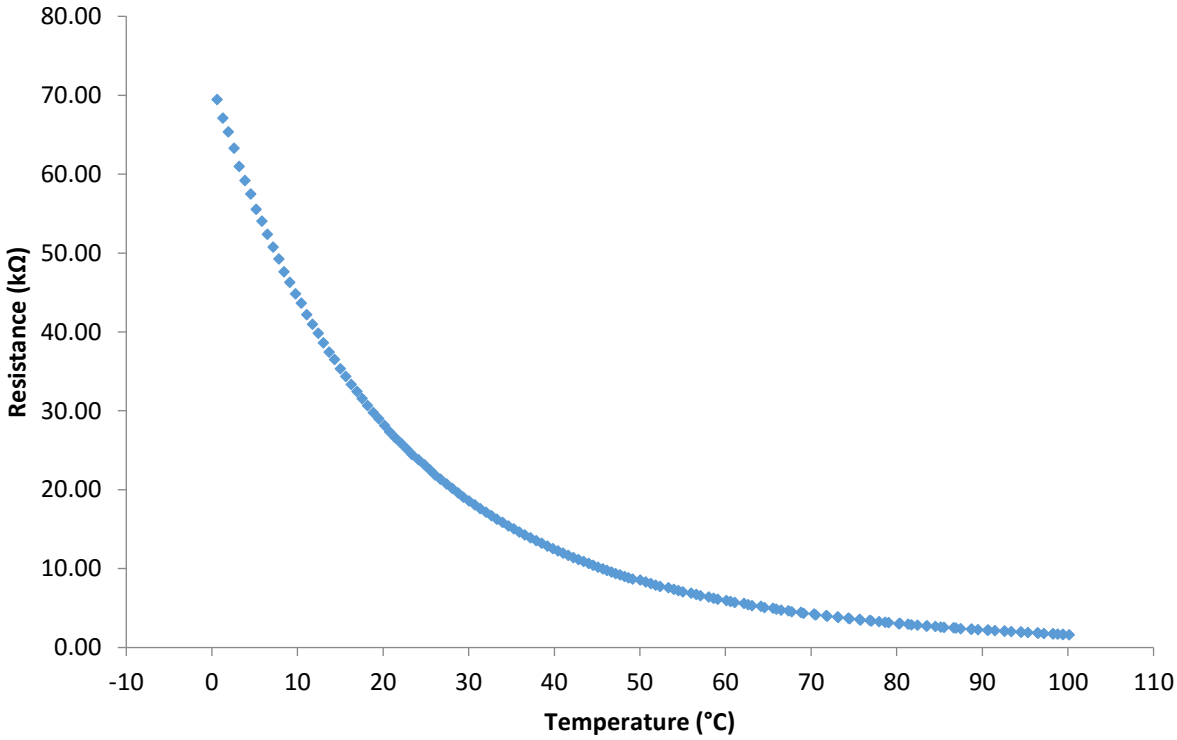

Figure 5.13. Resistance vs. temperature graph for the NMO Amphenol sintered target material

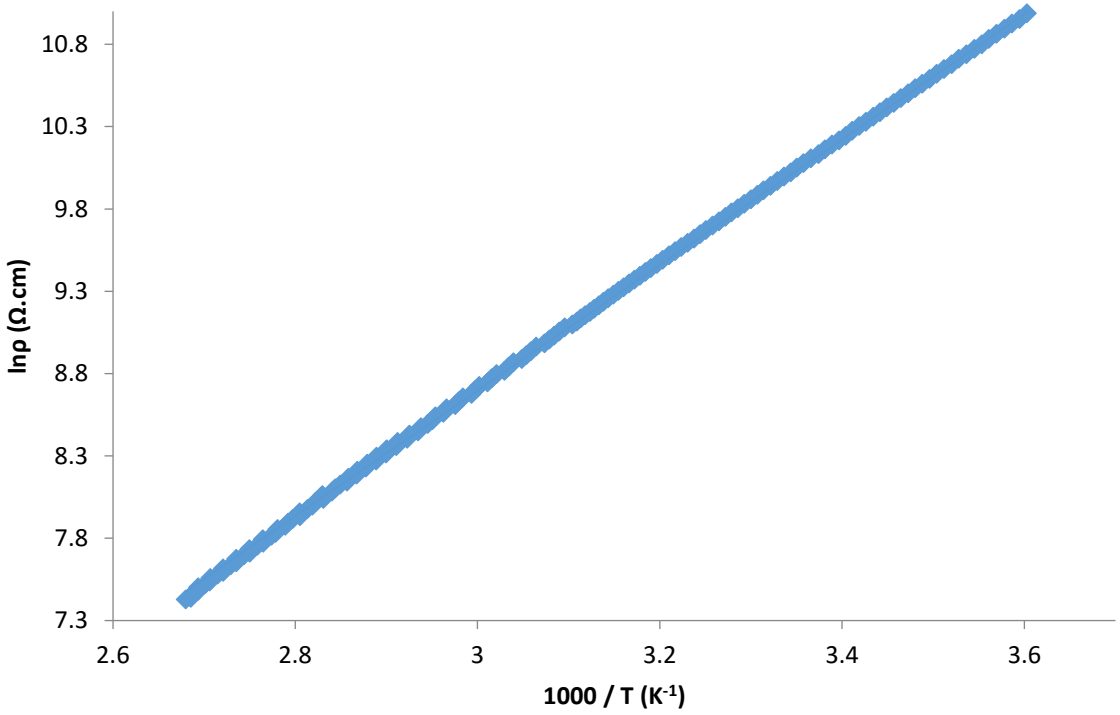

Figure 5.14. Lnρ vs 1000/T graph for the NMO Amphenol sintered target material

From the graphs in Figures 5.13 and 5.14 it can be seen that both the resistance and resistivity decrease with an increase of temperature meaning the material has an NTC characteristic. For comparison the bulk material was also measured using the equipment available at Amphenol. The results are shown in the graph below.

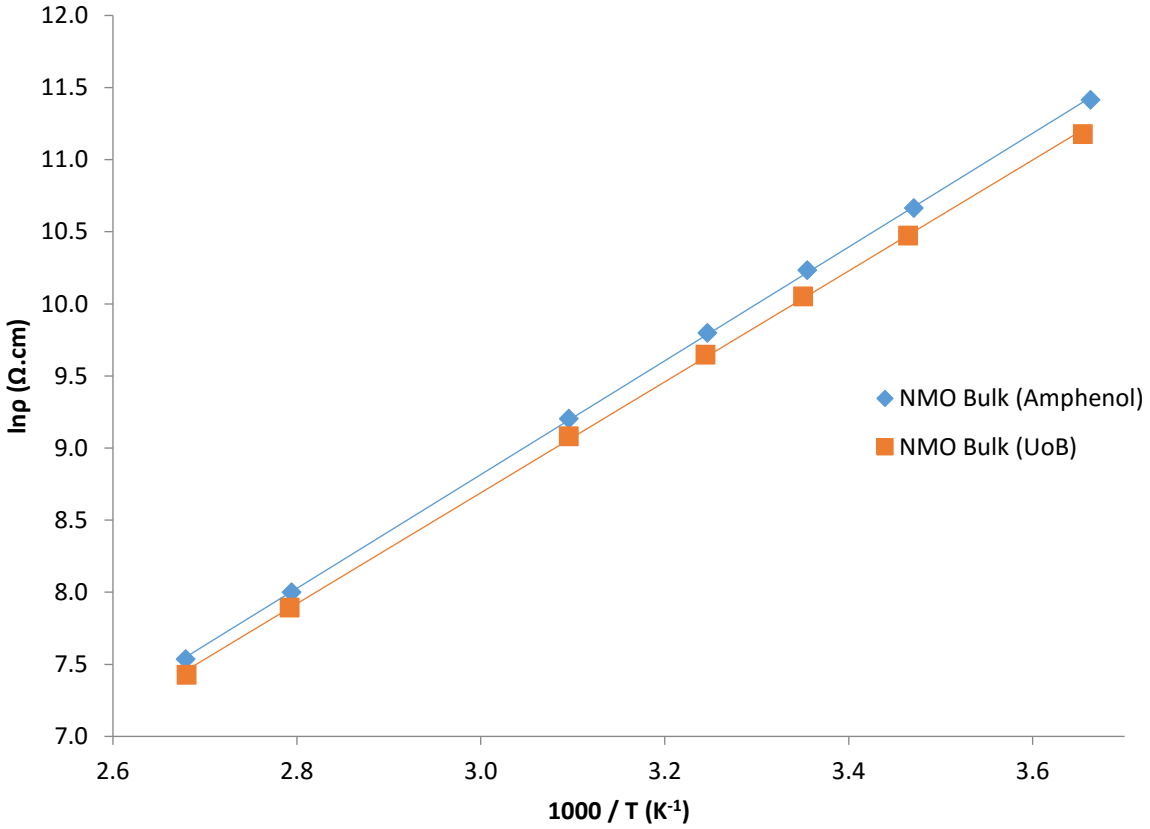

Figure 5.15. Resistivity comparison of bulk material measured at UoB and Amphenol

The thermistor characteristics were determined from this data and are shown in Table 5.3 to allow for a comparison of the measurement techniques.

Table 5.3. Thermistor characteristics measured and calculated electrical properties for sintered NMO target material.

Measurement Technique	25°C Resistivity (Ω.cm)	85°C Resistivity (Ω.cm)	Thermistor constant B Value (K)
UoB	2.32E+04	2.68E+03	3838
Amphenol	2.70E+04	2.90E+03	3972

Table 5.3 shows how the same bulk material measured using both the system at UoB and at Amphenol. The similarity in the results achieved by both systems shows that the system used at UoB is reliable and the results that are obtained from this technique is trustworthy. Therefore this resistance measurement technique was used for the measurements of all future films.

5.4 Initial Thin Film and Substrate Characterisation

5.4.1 X – Ray Diffraction Results

An XRD pattern of one of the polycrystalline Al_2O_3 substrates used in this work is shown in Figure 5.16. Index data was obtained from reference [10]. The XRD peaks of the polycrystalline Al_2O_3 2θ locations were found to be similar to those present in the NMO crystal. For example, the main NMO (311) peak at 35.40° may overlap with the Al_2O_3 (104) peak at 34.98°.

Some preliminary thin films depositions have been carried out. Figure 5.17 shows the diffraction pattern of a NMO thin film produced using the following conditions: 100 mJ laser energy, 1 Hz repetition rate, 2400 laser pulses, 400ºC substrate temperature and 50 mTorr oxygen pressure. Strong peaks are present at 2θ values of 35.15º, 43.35º and 57.49º indicating that the NMO structure has been formed, however a peak is not found at around 18º as would be expected. A possible reason for peak absences compared to the sintered material (Figure 5.10) might be that the films possess some texture as a result of the deposition process. Other

peaks are also present which indicate that the Al_2O_3 substrate has been detected and this is also to be expected, no peaks were detected which could not be indexed, indicating that there is no impurity's present in the film. The change in relative intensity of the peaks found at 35.15° and 57.49° compared to the polycrystalline ceramic pattern (Figure 5.17) again could suggest some texture is present, indicating that the NMO material deposited by PLD on alumina prefers the (111) orientation.

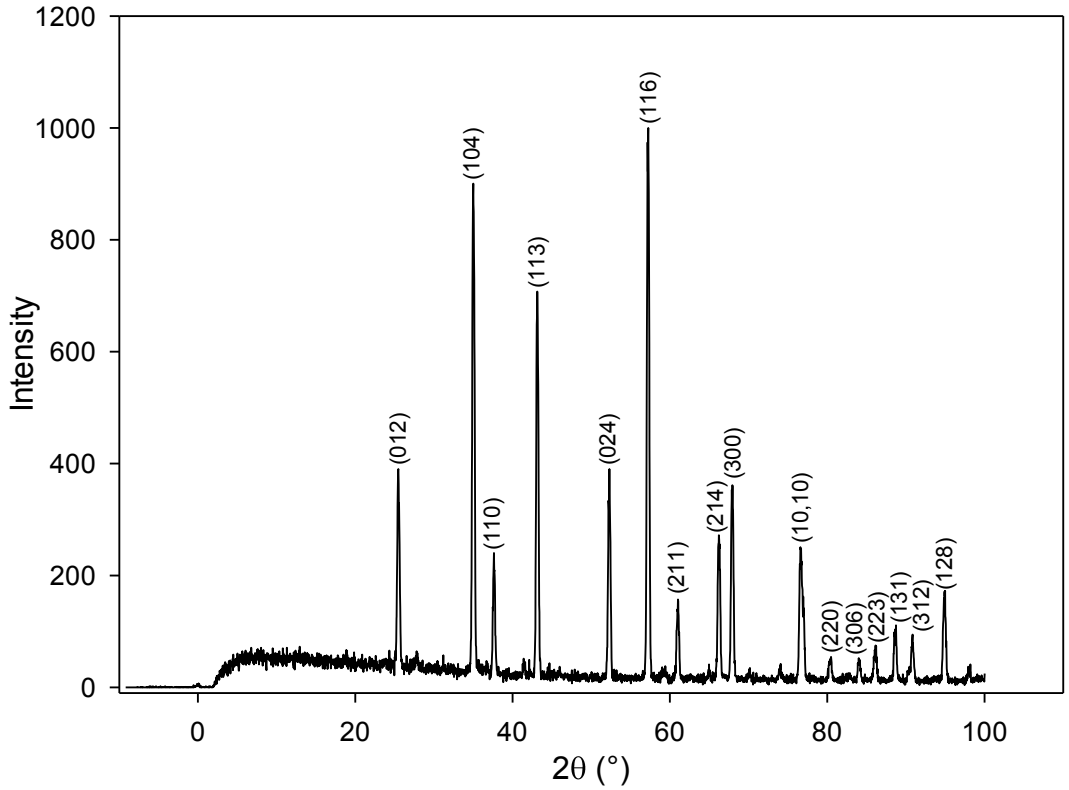

Figure 5.16. XRD pattern of Al_2O_3 substrate (Cu radiation)

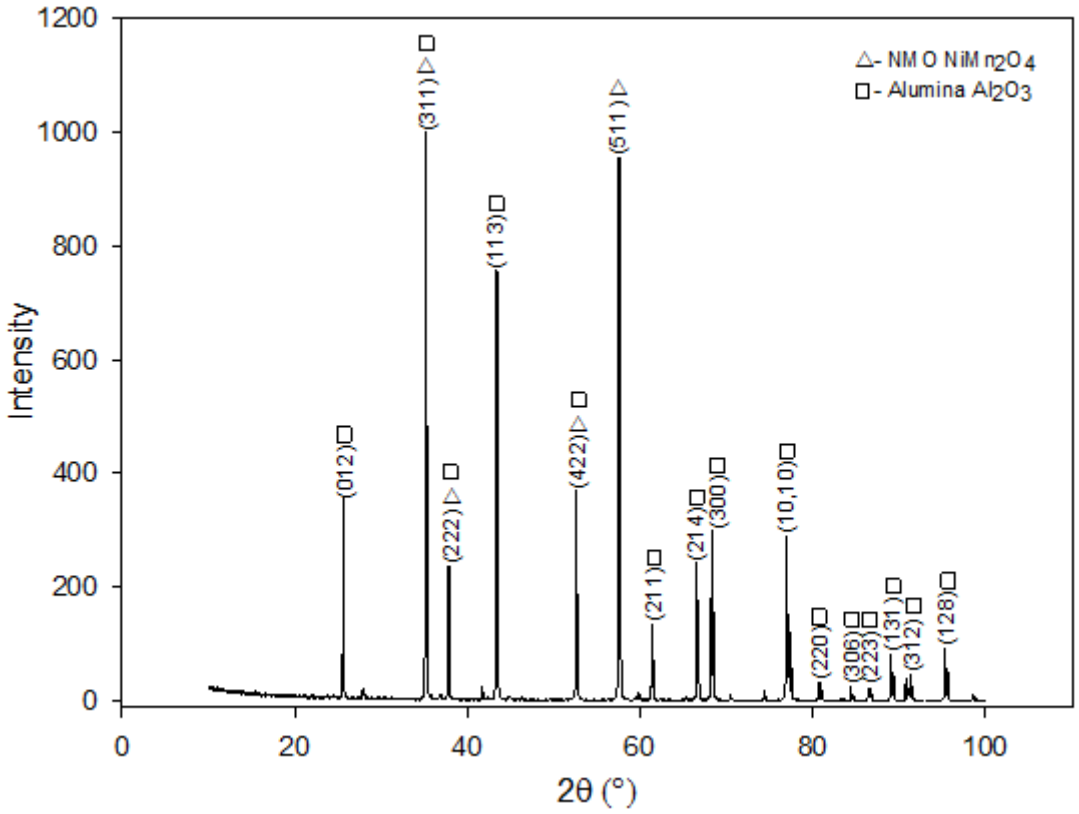

Figure 5.17. XRD diffraction pattern of NMO thin film (Cu radiation)

Figure 5.17 shows the XRD pattern of the NMO thin film on the alumina substrate, it is possible that at three of the measurements of the NMO peaks are not NMO but possibly the alumina substrate. These are indicated in the figure at 35.44° as a possible (104) reflection, 37.07° as a possible (110) reflection and 53.44 as a possible (024) reflection.

5.4.2 SEM Results

Figure 5.18 shows the SEM micrographs of the same thin film at different magnifications.

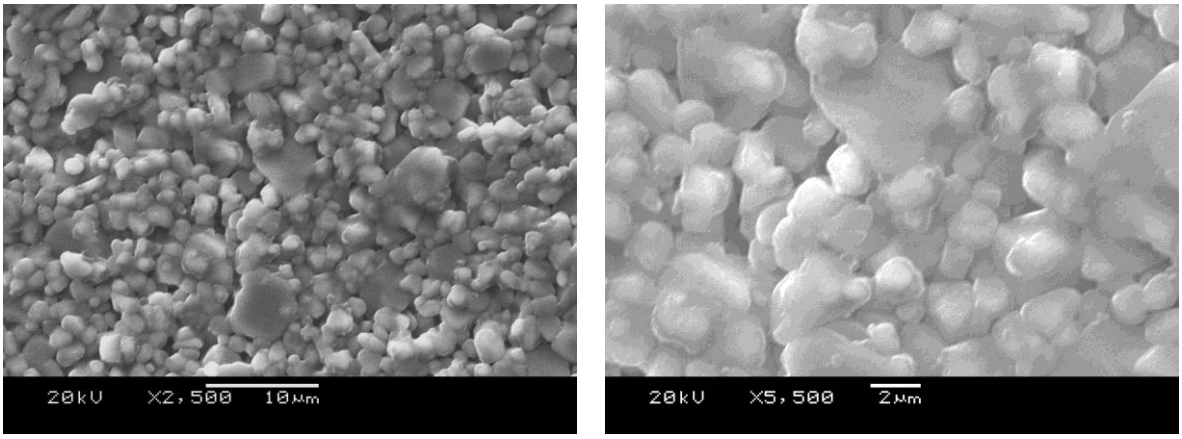

Figure 5.18. SEM micrograph of surface of initial thin film deposited by PLD (Jeol 6060)

It can be seen from the SEM micrographs that the thin film produced has some porosity and therefore the grains may not be fully interconnected and therefore consequently may not be a dense film. Therefore, this may have a damaging effect on the resistivity and conductivity of the thin film. The grains can be seen to have a regular structure with sizes ranging from 2 – 5 µm.

Through thickness resistance measurements were attempted by depositing a thin layer of gold (Au) by sputtering on the alumina substrate before deposition of the NMO film by PLD. However, no measurements were able to be taken as the films appeared to be too insulating. Therefore, further investigation was taken into the thin films by first attempting to measure the film thickness.

5.4.3 Thin Film Thickness

A cross section of the NMO thin film was prepared and measured as shown in Figure 5.19. Looking at the micrograph it is hard to identify exactly where the film is located and therefore a reliable thickness measurement could not be taken. Therefore, it was decided to try using a Dectak profilometer to see if this method would enable a thickness measurement to be made.

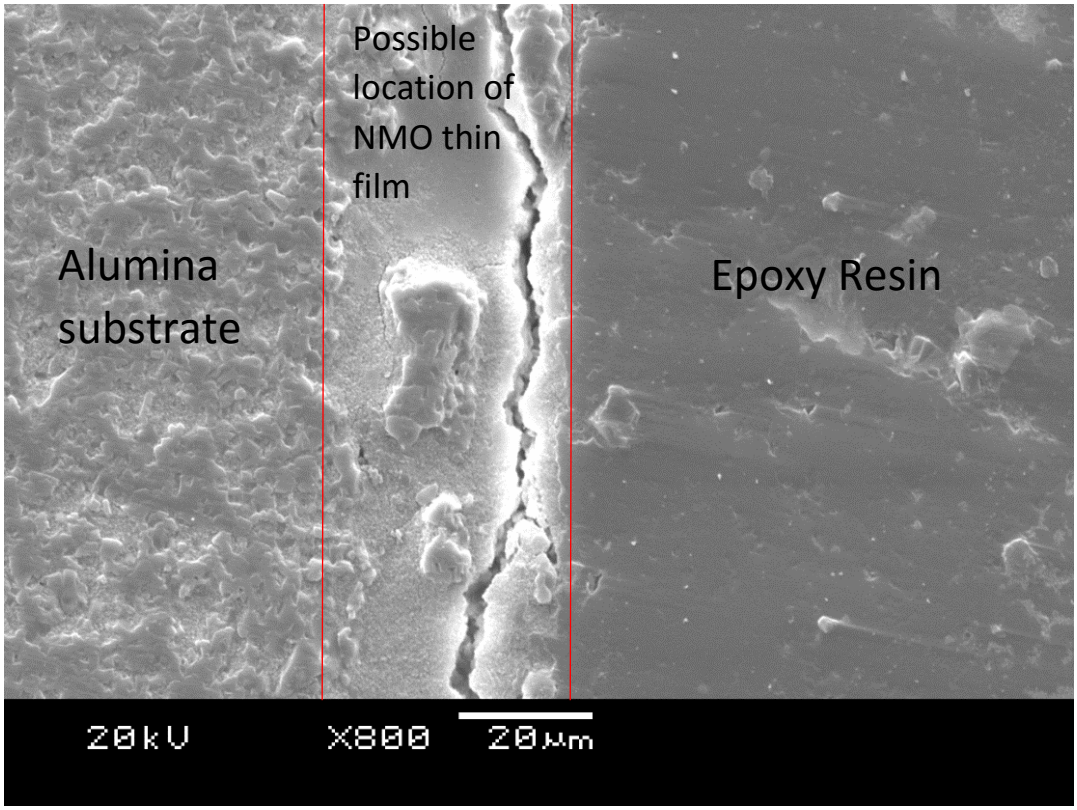

Figure 5.19. Cross section of NMO film on alumina substrate (Jeol 6060)

A step profile of the thin film was taken with the Dectak and this is shown in Figure 5.20. It was immediately noticed that the surface of the alumina and consequently the surface of NMO thin film was extremely rough. This meant that measurement of the thickness was going to be next to impossible as there is no way to determine where on the surface profile graph the NMO thin film is present on the substrate.

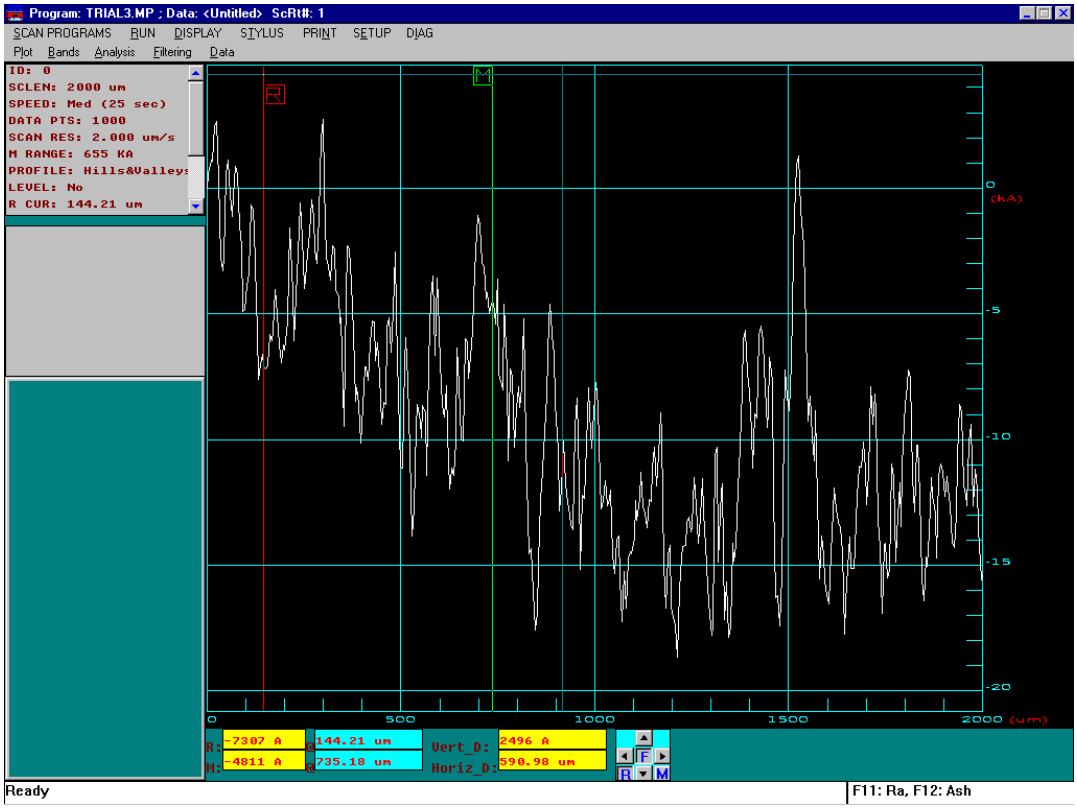

Figure 5.20. Surface profile of NMO film on Alumina substrate

This discovery led to an investigation into the surface profile of the polycrystalline alumina substrates that were being used as substrates for this project. The Dectak was used for a surface profile measurement again and it was also used to measure the Ra value of the alumina substrates. The Ra value is the arithmetic average of the absolute values measured by the dektak while the Rz is the average distance between the highest peak and lowest valley in each sampling length. A Tallysurf was also used to measure Ra for a comparison with the Dectak values, however results appeared to be too varied so were discarded due to unreliability. The surface profile graph of the alumina is shown in Figure 5.21, an Ra value at 0.2103 µm and an Rz value of 0.9425 µm.

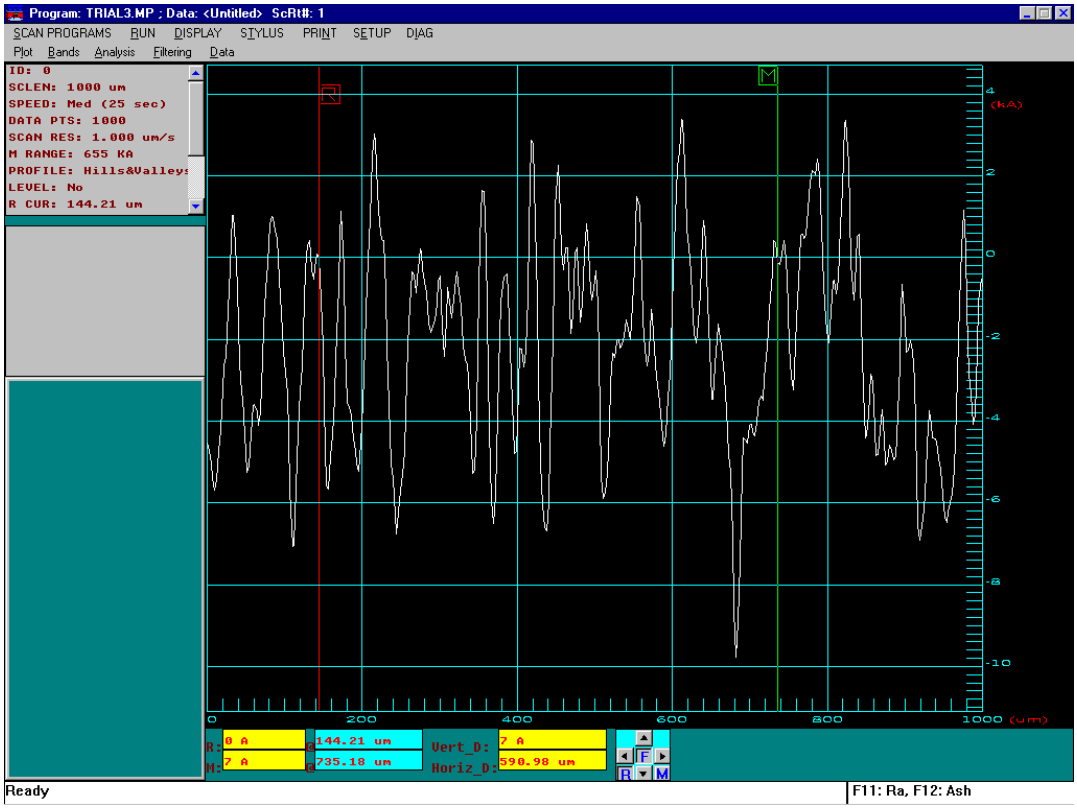

Figure 5.21. Surface profile of alumina substrate

It was therefore deduced that the thin films were much too thin to be detected using this substrate, as a thickness of around 500 nm was to be expected. However, a peak to valley measurement of the substrate showed sizes of around 700 nm. In order to investigate the film thickness in more detail films were also deposited on polished substrates of single crystal STO and Si, where a more accurate measurement of film thickness should be possible. Both STO and Si were analysed by the Dectak and their graphs are given in Figure 5.23. The roughness of the polycrystalline Al_2O_3 substrate has been a problem in past literature and methods such as adding a glass phase have been used to improve the surface topography [11]. However, the films produced by Schmidt el al. were much thicker than the films produced in this project allowing for a much easier measurement.

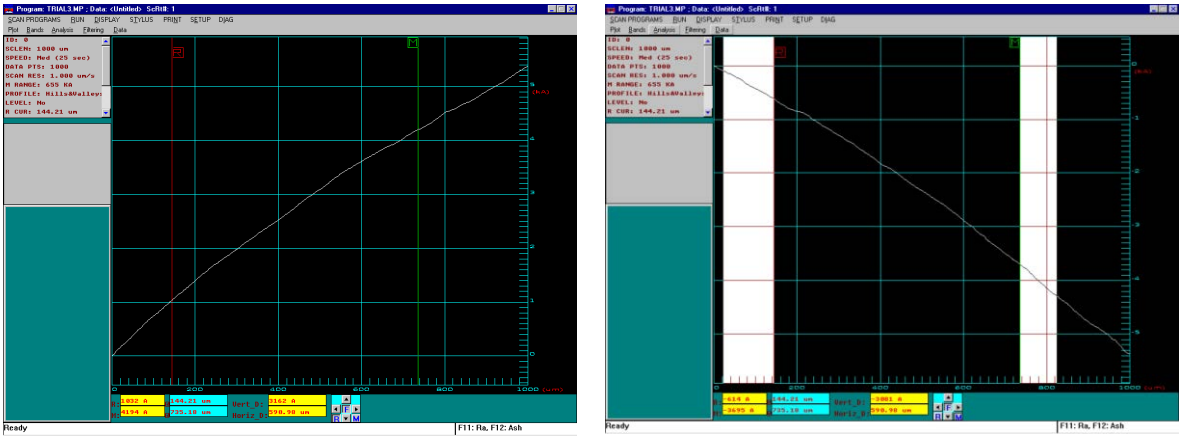

STO substrate Si substrate

Figure 5.22. Surface profile of STO substrate and Si substrate

On the STO and Si substrates a dramatic improvement was seen immediately on the surface profiles as they are much smoother in comparison to the alumina substrates measured previously. SEM was then used to confirm the results from the Dectak. The microstructure of the alumina, polished STO and polished Si are shown in Figure 5.23.

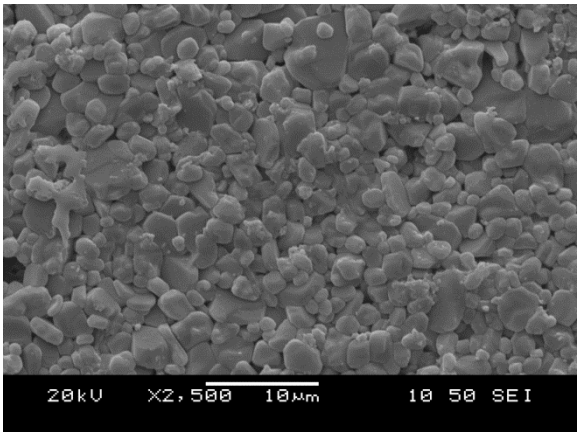

Alumina substrate x 2,500

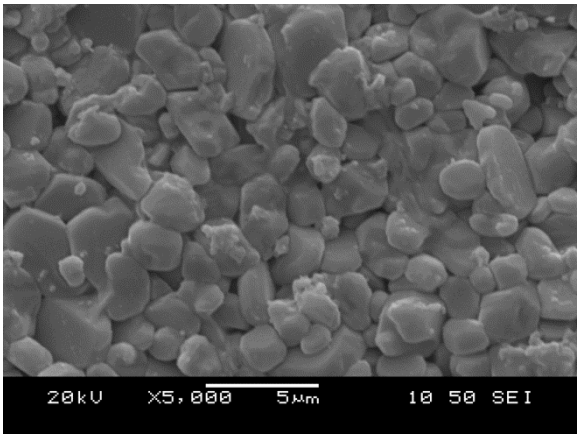

Alumina substrate x 5,000

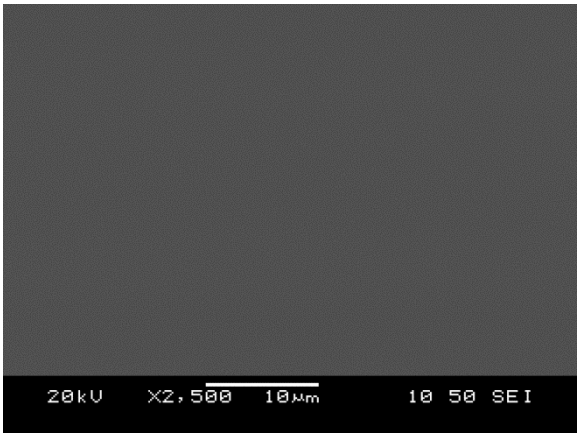

STO substrate x 2,500

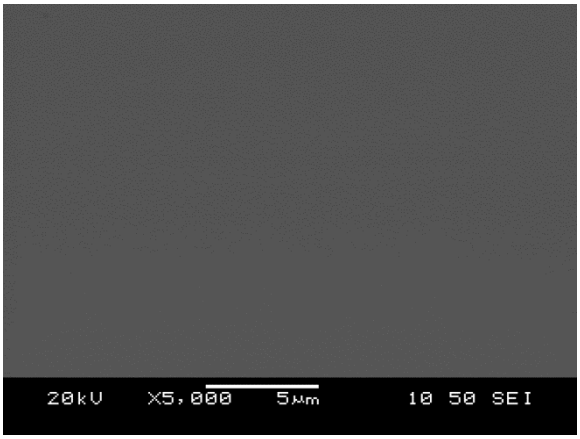

STO substrate x 5,000

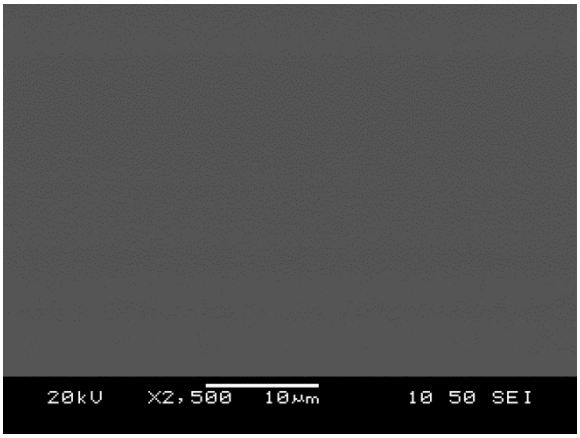

Si substrate x 2,500

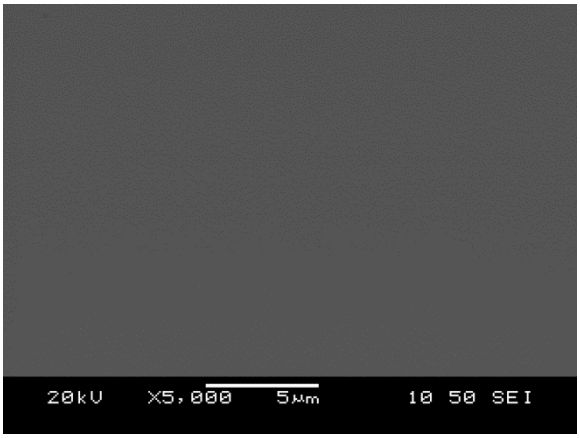

Si substrate x 5,000

Figure 5.23 SEM Micrographs of surface microstructure of the different substrates (Jeol 6060)

The microstructure of STO and Si substrates show that their surface is very smooth in a huge contrast to the alumina substrates, and supports the surface profile data. In the alumina micrographs grains approximately 2 μm in diameter can be seen, thus producing a very uneven surface, which explains the noisy graph produced by the profilometer. Further reflection on the

initial SEM micrographs in Figure 5.18, after the profilometer measurements. The NMO films measured were so thin that what is actually seen in the figure is not the NMO grains at all but in fact the grains of the alumina substrate. The 2 – 5 μm grain size initially measured is not consistent with the measurements made by the profilometer. Therefore, what is more likely is that what is actually seen is a very thin layer of the NMO over the alumina grain structure.

It was therefore decided to produce some thin films of NMO using the same PLD conditions but using the different substrates of STO and Si and to measure a step profile.

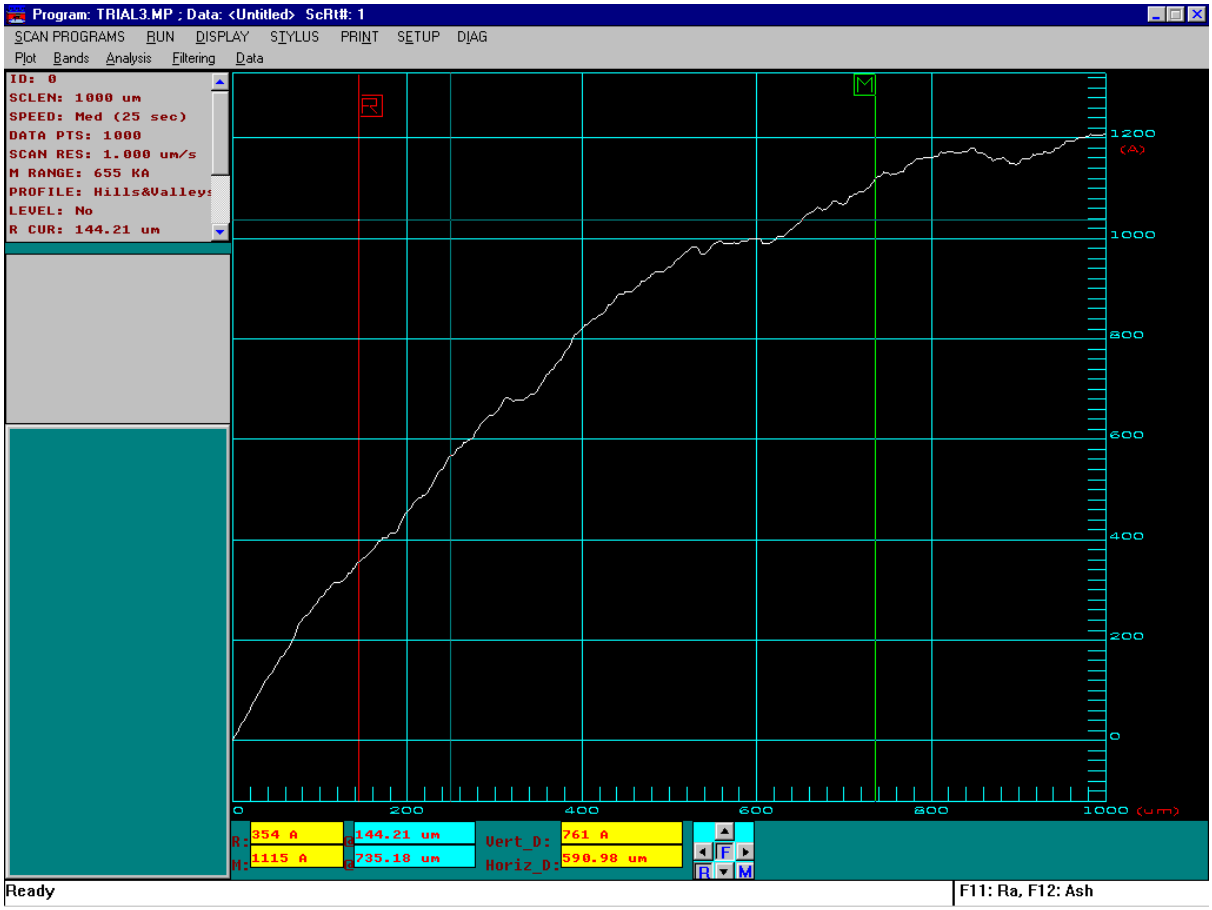

Figure 5.24. NMO thin film step profile produced on STO substrates

A typical profilometer result is shown in Figure 5.24 for a film on an STO substrate and shows an average film thickness value of less than 130 nm. This proved to be not adequately

thick enough for analytical measurements such as resistance measurement, as ideally a much thicker film is required to be produced to allow for easier measurement. Therefore, a change in PLD conditions was required to increase the films thickness. This led to the following changes listed below:

- Decrease in the target to substrate distance from 50mm to 40mm
- Increase in the Laser fluence from 1 J / cm² to 2 J / cm²
- Increase in deposition time from 40 mins to 60 mins

These new conditions were based on literature for the growth of $LiMn_2O_4$ thin films produced using PLD. These new conditions were then used to produce NMO films on the different substrates, alumina, STO and Si. The microstructure of the films produced using the new conditions were determined by SEM to allow for a comparison with the films produced using the initial conditions, and are shown in Figure 5.25.

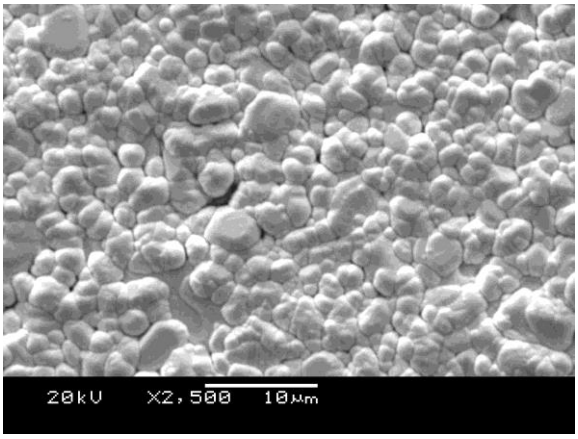

NMO film on alumina substrate x2,500

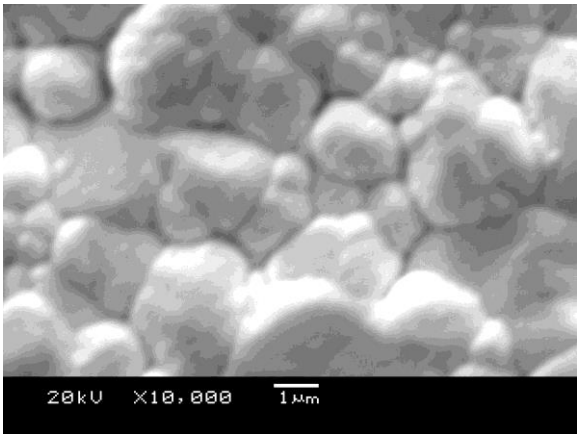

NMO film on alumina substrate x2,500

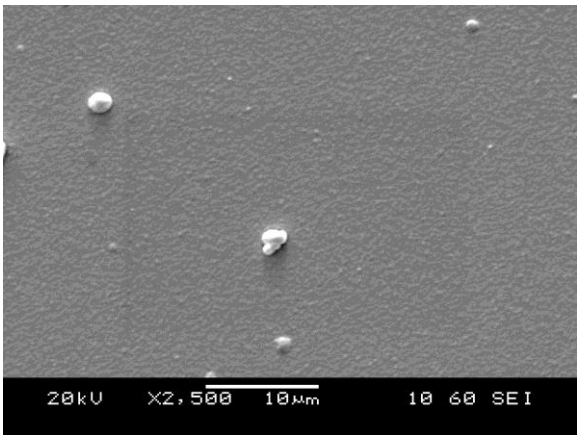

NMO film on STO substrate x2,500

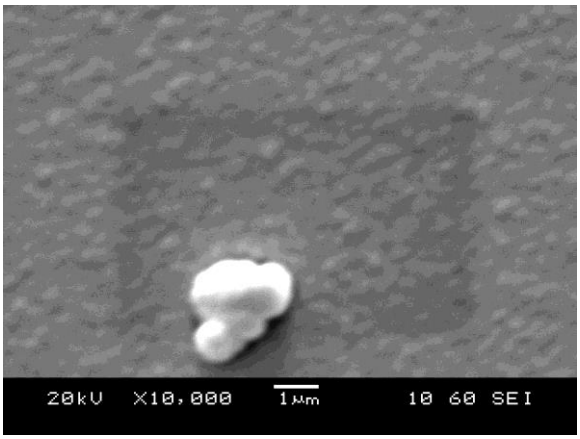

NMO film on STO substrate x10,000

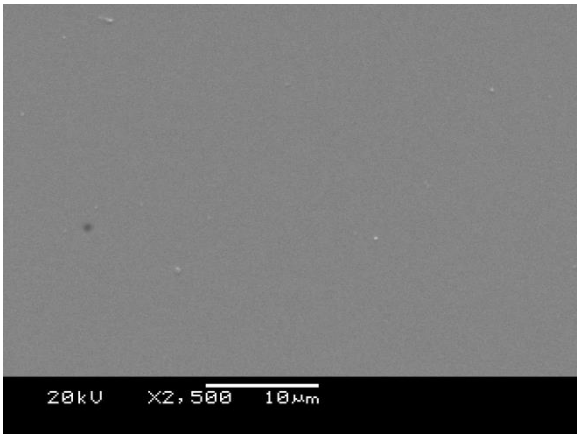

NMO film on Si substrate x2,500

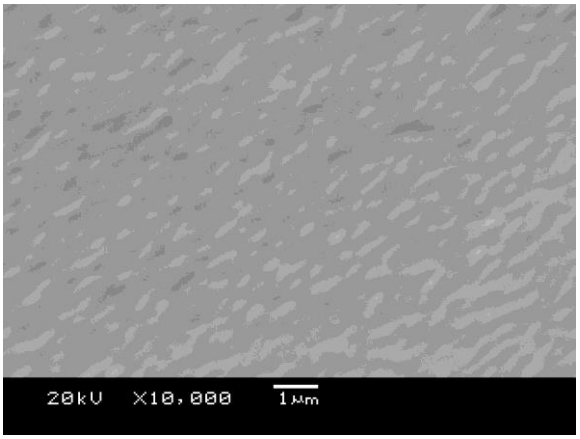

NMO film on Si substrate x10,000

Figure 5.25. Micrographs of surface microstructure of NMO deposited on Al_2O_3 STO and Si substrates using the new PLD conditions 400°C, 50 mTorr, 2 J/cm², 60 min, (Jeol 6060)

The SEM micrographs show that the deposition of NMO on Al_2O_3 substrates follows the alumina substrate's characteristic uneven polycrystalline grain structure. This is somewhat surprising as a thicker film may be expected to produce some planarization of the surface. The

deposition of NMO on STO substrates produced dense films with a smooth surface which is highly desirable. However, particulates were present on the surface which is undesirable as they may have an effect on the resistivity and overall reliability. On Si substrates the deposition of NMO produced smooth, dense films with no evidence of particulates being formed, this is highly desirable and as a substrate a much better alternative to STO due to its relatively low price.

XRD was then used to analyse the structure of the films deposited using the new PLD conditions and different substrates, and the diffraction patterns are shown in Figure 5.26.

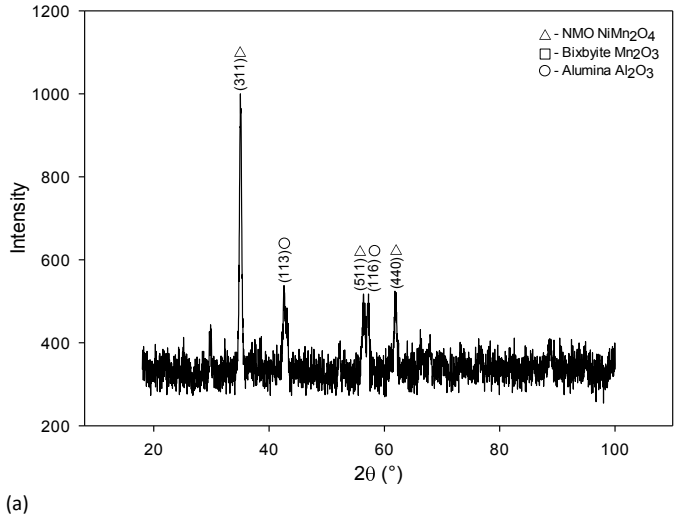

(a)

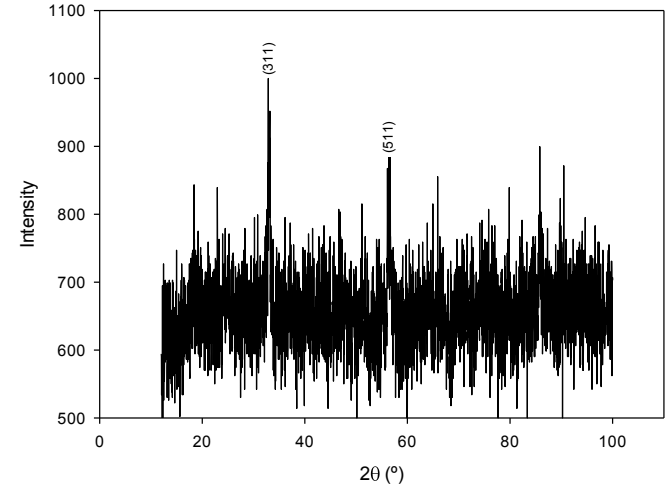

(b)

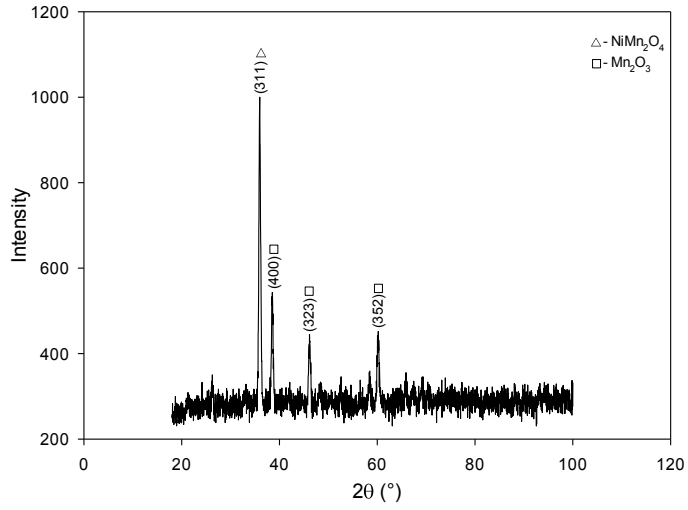

(c)

Figure 5.26. XRD patterns of NMO thin film deposited on Al_2O_3 (a), STO (b) and Si (c) substrates.

The XRD patterns show that the films produced using the new conditions have an increase in absence of NMO peaks, suggesting that its preferred orientation has changed in comparison to the previous films. However, there is a substantial increase in background noise in comparison to the results produced using the initial conditions, so some peaks may be hidden behind this noise. The films thickness was measured using both the Dectak profilometer and SEM cross section as shown in Figure 5.27.

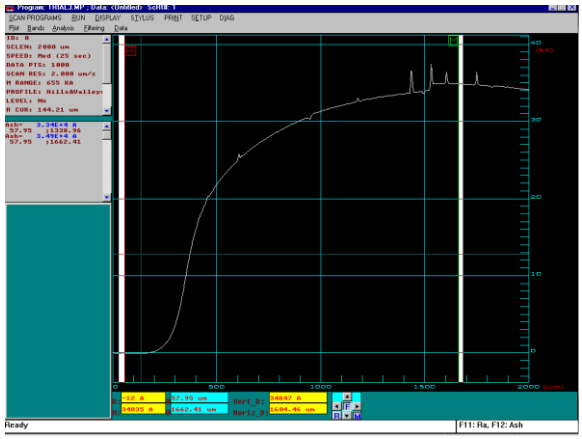

Step profile of NMO film

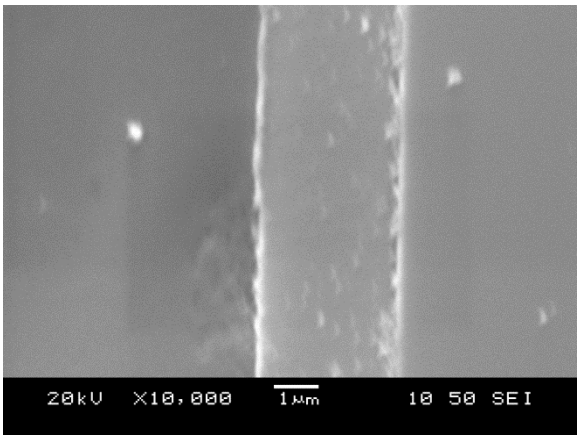

Cross section of NMO x10,000

Figure 5.27. Step profile using profilometer and SEM micrograph (Jeol 6060) of NMO films thickness using new PLD conditions (400°C substrate temperature, 50 mTorr of O_2, Laser Energy of 2 J, repetition rate of 10 Hz, deposition tie of 60 mins) using a Si substrate

The film thickness was measured at different positions and the results were then averaged to give an average film thickness of 1.95 μm with a standard deviation of 1.65 μm. Due to increase of the film's thickness it was considered that it would be possible to now measure a film on the commercial alumina substrates. After discussion with the sponsoring company Amphenol it was decided that the films would continue to be deposited on only the commercial polycrystalline alumina substrates due to the commercial viability of the substrate in comparison to the STO and Si substrates.

5.5. Annealing Results

Annealing was performed on the films that were prepared using the new standard conditions where a thicker film was produced, annealing was not performed on the initial films. Annealing was conducted to see if any improvement in crystallinity in the XRD patterns could be achieved. This was done by annealing at 800°C for 60 minutes in 150 cm^3 / min of flowing O_2. The XRD pattern for an annealed film on an alumina substrate is shown in Figure 5.28.

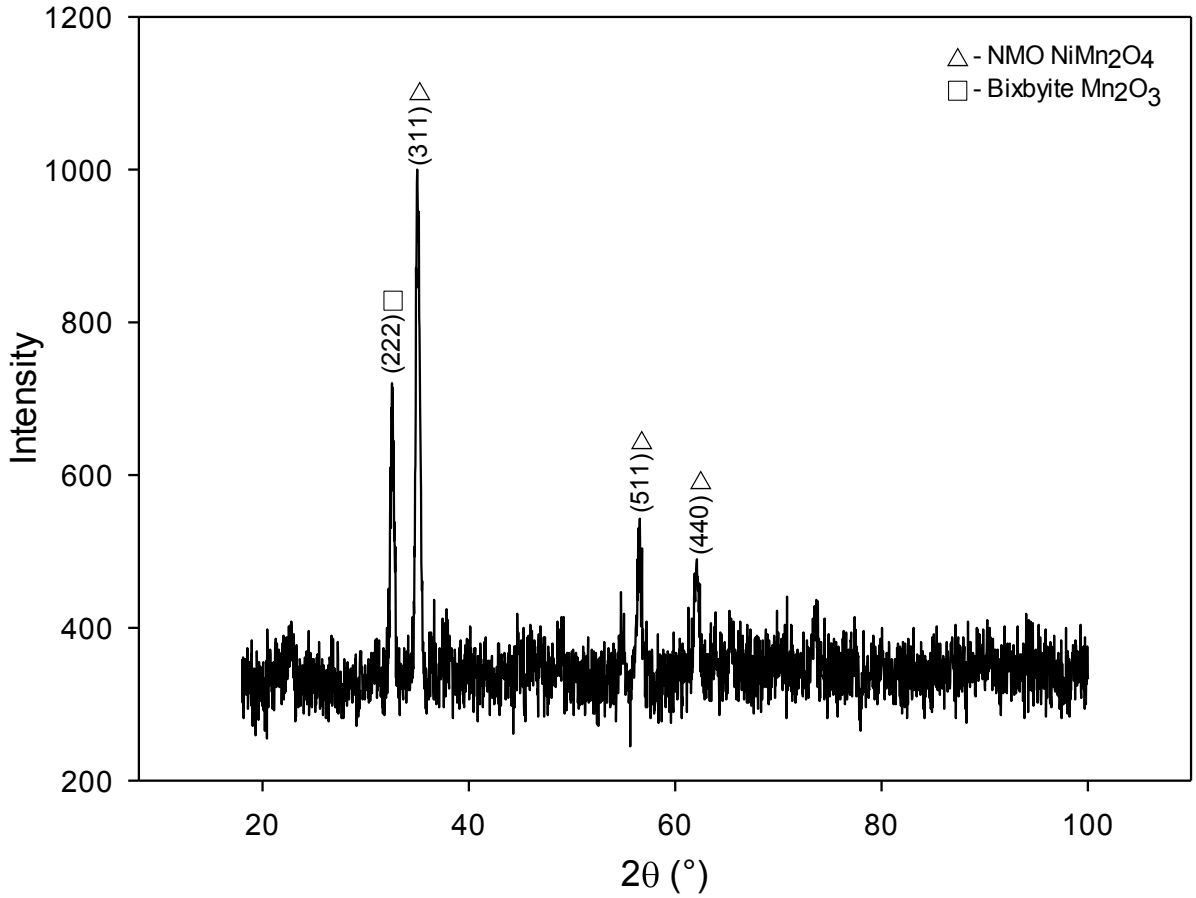

Figure 5.28. XRD pattern of annealed NMO films on Al_2O_3 substrates

XRD of the annealed film shows that there is a decrease in background noise in comparison to the as deposited films. The XRD patterns of the annealed films show there is an increase in

the amount of NMO peaks available suggesting a change in the samples preferred orientation and texture.

5.6. Van der Pauw Resistivity Measurements

Resistivity measurements were taken using the Van der Pauw method on as deposited films on alumina substrates at temperatures of 25°C and 85°C. Results of the bulk resistivity of NMO films deposited in a range of pressures of O_2 at a substrate temperature of 400°C are shown in Table 5.4 where it can be seen that there was a decrease in the resistivity of the films with an increase in their body temperature, therefore the films exhibited NTC properties.

Table 5.4. Van der Pauw resistivity measurements on as-deposited NMO films fabricated in a range of pressure of O_2 (50, 150, 250 mTorr) and a substrate temperature of 400°C on alumina substrates.

	Resistivity at specific temperature (Ω.cm)	
Films deposited at 400 °C and at specific O_2 pressure (mTorr)	25°C	85°C
50	1.56×10^{-4}	1.65×10^{-5}
150	7.64×10^{-4}	1.70×10^{-5}
250	2.46×10^{-5}	4.37×10^{-6}

Films were also produced using the same conditions but with an increased substrate temperature of 550°C, and their resistivity was measured using the same Van der Pauw technique. However, these films appeared to be insulating and resulted in nothing useful being measured.

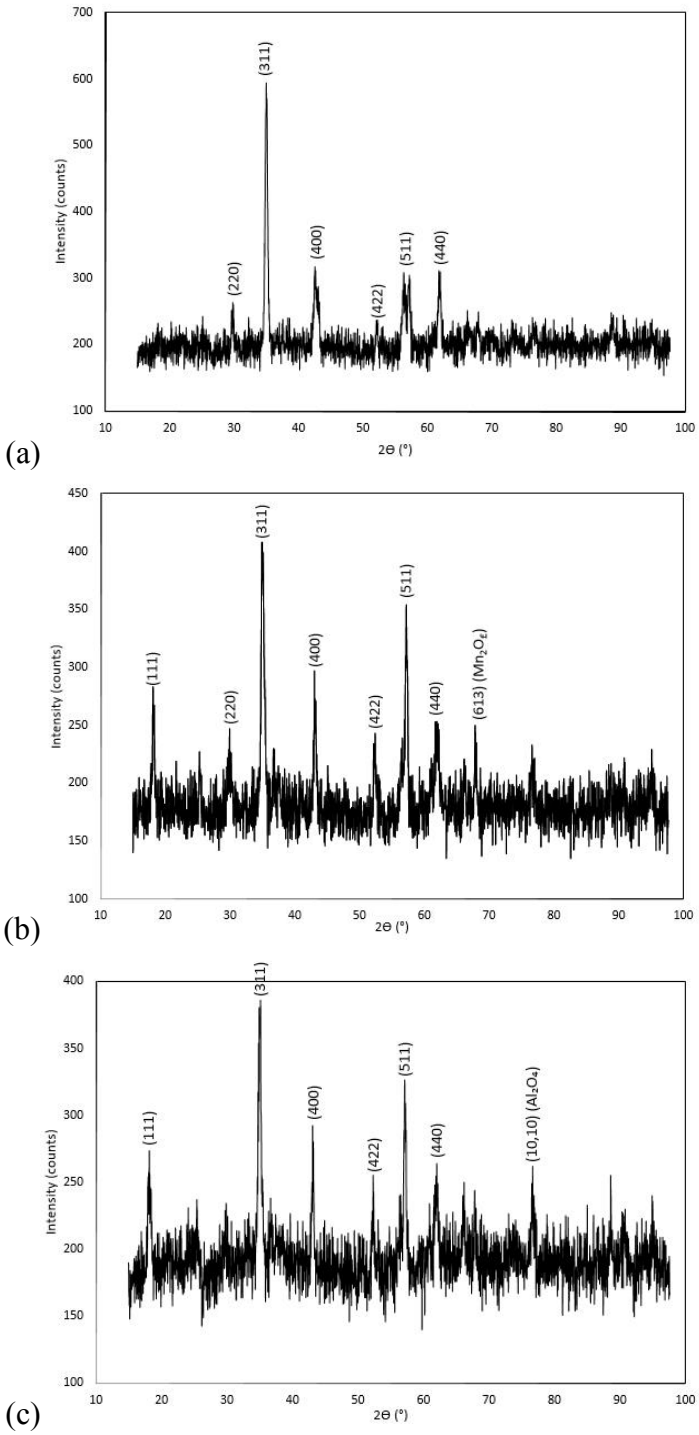

Figure 5.29. XRD patterns of NMO spinel films produced at 550°C substrate temperature and different oxygen pressure (a) 50 mTorr, (b) 150 mTorr and (c) 250 mTorr

NMO spinel crystallinity is identified in the films produced at 550°C substrate temperature. This suggests that you should be able to measure an NTC resistivity in these films, therefore it is possible that the VDP technique may not be suitable for the measurement of these films.

The films produced at 400°C however were annealed and measurements are shown in Table 5.5.

Table 5.5. Van der Pauw resistivity measurements on annealed NMO films (800 °C for 1hr in an O_2 environment) fabricated in a range of pressure of O_2 (50, 150, 250 mTorr) and a substrate temperature of 400 °C on alumina substrates

	Resistivity at specific temperature (Ω.cm)	
Annealed films deposited at 400 °C and at specific O_2 pressure (mTorr)	25°C	85°C
50	1.31×10^{-4}	1.27×10^{-5}
150	1.77×10^{-4}	5.15×10^{-5}
250	1.14×10^{-4}	2.61×10^{-5}

The films NTC characteristics were maintained after annealing, however there was a decrease in the films room temperature of resistivity in comparison to the as deposited films. It is possible that because the films have been annealed in O_2 this has replaced the oxygen deficit in the NMO films which has increased the amount of Mn^{3+} available on the octahedral sites increasing the films conductivity and decreasing the films resistivity.

The value of resistivity measured using the VDP method was extremely low compared to the bulk NMO material, around $10^{-4} – 10^{-5}$ Ω.cm. This reason, and because films produced at a 550°C substrate temperature could not be measured, it was decided that an alternative method for the measurement of resistivity should be investigated. This led to the use of the four wire resistance measurement technique as described in the next section.

5.7. Problems Encountered When Depositing at 2 J / cm^2 Laser Energy

The four wire technique was used to measure the resistance of the thin films and to allow for measurements of the resistance at different temperatures between 25°C and 85°C as described in Chapter 4.

During the fabrication of thin film samples for these measurements it was found that when using a laser fluence of 2 J/cm2 the laser energy during the long deposition times proved to be too high for the excimer laser itself, resulting in runs being cut short and the abandonment of experiments. It was therefore decided that the laser fluence should be decreased to prevent cut off and to allow for continuous depositions. Therefore, the laser fluence was reduced to 1.5 J /cm^2, resulting in better laser maintenance and continuous depositions.

A resistance technique for measuring the thin films was established and will be used for the resistance measurements of the future thin films using the new PLD conditions.

5.8. Films Produced Using the New Conditions

Films were produced using the revised conditions of a lower laser energy of 1.5 J, a decrease in target to substrate distance of 40 mm and an increased deposition time of 60 mins. energy and then measured using the four wire resistance measurement technique. The resistivity measurements for the films produced at 400 and 550°C as deposited and annealed are shown in Figure 5.30.

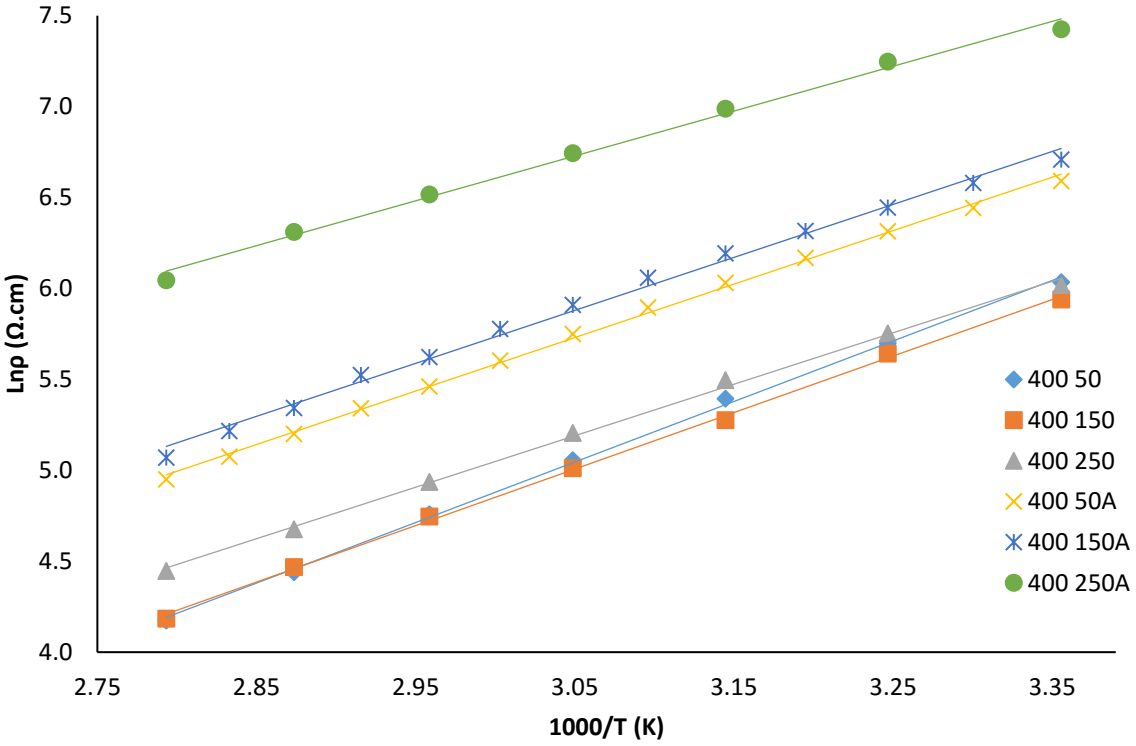

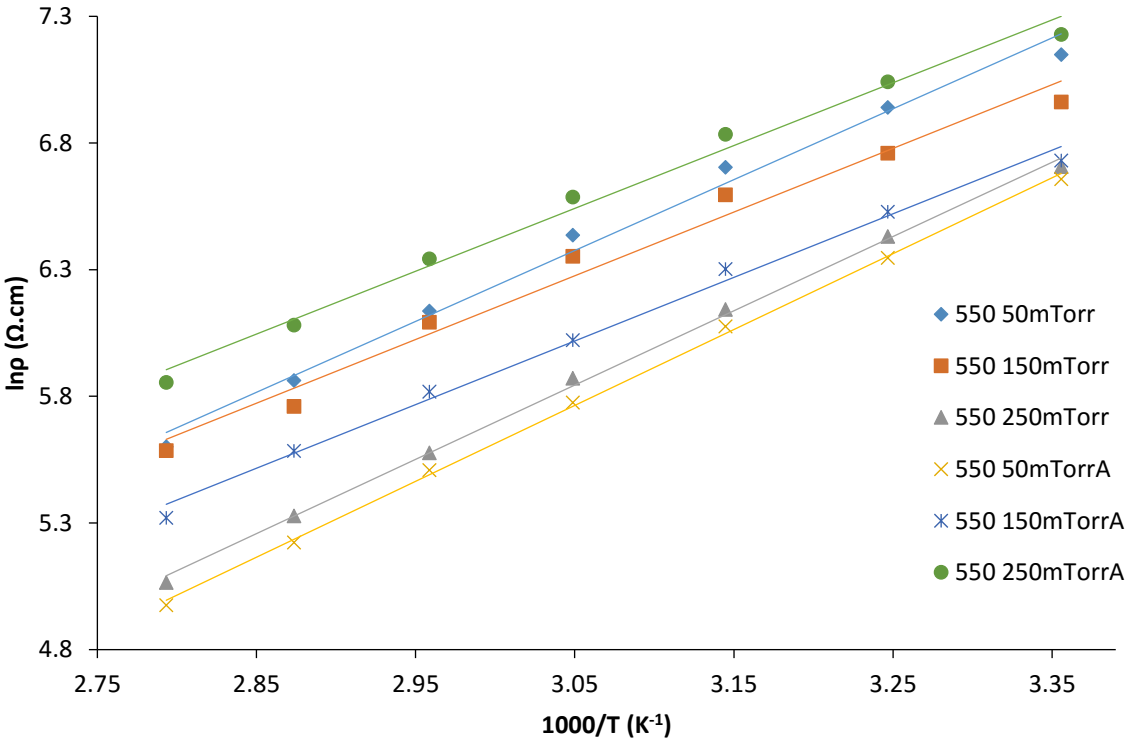

Figure 5.30. Resistivity graphs of NMO thin films on alumina substrates using the new conditions produced at 400°C and 550°C and different oxygen pressures and annealed

The graphs show that the films produced using these conditions exhibited an NTC effect as their resistivity decreased with an increase of the films body temperature. It was shown that with an increase of pressure in the as deposited films at a substrate temperature of 400°C there was an increase in the resistivity in contrast with the films deposited with a substrate temperature of 550°C there was a decrease in resistivity with an increase of pressure. When the films were annealed the films followed the same resistivity pattern regardless of annealing.

It was discovered during the deposition of these films that there was a decrease in laser energy after several depositions and that consequently the laser energy was not constant for all the depositions. As a result, there were problems with reproducibility and, when compared with films where the laser energy was consistently measured before each deposition, there were differences noticed in the resistivity measurements and a lack of consistency.

5.9. Summary and Conclusions

This chapter has been concerned with the characterisation of the NMO starting materials and substrates, the establishment of PLD parameters for the deposition of reproducible thin films, and the development of a reliable measurement of resistivity.

The resistivity of the sintered NMO material provided by Amphenol was determined by a through thickness measurement and compared with a sintered sample produced at the University of Birmingham. The resistivity of the Amphenol material at room temperature was calculated to be between 1.17×10^2 - 1.22×10^2 Ω.cm which when compared with the literature value of 3.7×10^3 Ω.cm is quite low. A corresponding measurement on a sintered pellet produced at the University of Birmingham showed a resistivity 8.03 – 8.20 Ω.cm which was also extremely low, therefore suggesting there may be something wrong with either the experimental procedure or the samples.

The use of a commercial four point probe technique resulted in the measurement of higher resistivity values. However, these results varied considerably and it was considered that contact resistance was a significant issue in using this technique on the NMO materials.

Initial thin films of NMO were deposited by PLD and the presence of the spinel phase confirmed by XRD. Fewer XRD peaks were present in comparison to the bulk NMO target suggesting a change in the crystallinity and some preferred orientation.

The film thickness was measured by profilometry and cross section measurements. It was found that the surface roughness of the polycrystalline alumina substrates prevented an accurate thickness determination. The NMO films were therefore deposited on polished single crystal STO and Si substrates resulting in a dramatic improvement in the ability to measure the film thickness. The film's thickness was determined to be less than 100 nm which proved to be too thin for analytical measurements when the NMO was deposited on alumina. A change in the PLD conditions was therefore deemed necessary to allow for adequate analytical measurement of the NMO thin films.

A huge change was noticed when the films deposited using the new PLD parameters were analysed by XRD, with a large increase in the background noise, fewer NMO peaks being present and a presence of Mn_2O_3 peaks in some conditions. The film thickness was measured to be at an average of 1.95 μm. The effect of annealing the thin films in O_2 was also investigated and it was shown that there was decrease in the background noise, an increase in the peak intensity's and an increase in the amount of NMO peaks available in the XRD patterns.

The resistivity of the thin films produced using the new deposition conditions at different temperatures were measured using the Van der Pauw technique. NTC properties were measured but the calculated resistivity was very low between 10^{-4} to 10^{-5} Ω.cm and deemed to be unreliable.

Accurate and reproducible measurements of the NMO target were finally achieved using a four wire technique, and this was also adopted for the measurement of films.

References

1. Kukuruznyak, D.A., et al., *Combinatorial screening of ternary NiO-Mn_2O_3-CuO composition spreads.* Journal of Applied Physics, 2005. **98**(4).
2. Smith, N., *The structure of thin films of metallic oxides and hydrates.* Journal of the American Chemical Society, 1936. **58**: p. 173-179.
3. Geller, S., *Structures of alpha-Mn_2O_3,$(Mn_{0.983}Fe_{0.017})_2O_3$ and $(Mn_{0.37}Fe_{0.63})_2O_3$ and relation to magnetic ordering.* Acta Crystallographica Section B-Structural Crystallography and Crystal Chemistry, 1971. **B 27**(APR15): p. 821-&.
4. Tang, X.X., A. Manthiram, and J.B. Goodenough, *$NiMn_2O_4$ revisited.* Journal of the Less-Common Metals, 1989. **156**: p. 357-368.
5. Schmidt, R. and A.W. Brinkman, *Preparation and characterisation of $NiMn_2O_4$ films.* International Journal of Inorganic Materials, 2001. **3**(8): p. 1215-1217.
6. Schmidt, R., M. Parlak, and A. Brinkman, *Control of the thickness distribution of evaporated functional electroceramic NTC thermistor thin films.* Journal of Materials Processing Technology, 2008. **199**(1-3): p. 412-416.
7. Boucher, B., *Structure magnetique du manganite de nickel.* Comptes Rendus Hebdomadaires Des Seances De L Academie Des Sciences, 1959. **249**(4): p. 514-516.
8. Schmidt, R., et al., *Electron-hopping modes in $NiMn_2O_{4+delta}$ materials.* Applied Physics Letters, 2005. **86**(7).
9. Gillot, B., et al., *Electrical-conductivity of copper and nickel manganites in relation with the simultaneous presence of Mn_{3+}-ions and Mn_{4+}-ions on octahedral sites of the spinel structure.* Solid State Ionics, 1992. **51**(1-2): p. 7-9.
10. Saalfeld, H., *Strukturuntersuchungen im system Ai_20_3-Cr_20_3.* Zeitschrift Fur Kristallographie, 1964. **120**(4-5): p. 342-&.
11. Schmidt, R., et al., *Screen printing of co-precipitated $NiMn_2O_{4+delta}$ for production of NTCR thermistors.* Journal of the European Ceramic Society, 2003. **23**(10): p. 1549-1558.

Chapter 6

Analysis of Thin Films Produced at Different Substrate Temperatures and Oxygen Pressures

6.1 Introduction

This chapter is concerned with NMO thin films produced by PLD on polycrystalline alumina substrates using the following conditions, 150 mJ laser energy, 1.5 J/cm^2 laser fluence, a target to substrate distance of 40 mm and a deposition time of 60 minutes. A range of substrate temperatures and oxygen pressures inside the vacuum chamber were used, and their effect on the films phase, microstructure, thickness and electrical properties of the resulting films were investigated. The substrate temperature was manipulated between 400 – 550°C and the oxygen pressure was altered between 50 and 250 mTorr. The effects of annealing the films in O_2 was also studied.

To the author's knowledge the effect of changing the substrate temperature and O_2 pressure on the growth of NMO thin films using PLD has not been reported previously. Based on other

methods used in the literature and similar spinel NTC materials studied using PLD, it is possible to predict what effects these variables may have on the thin films properties.

6.2 Characterisation of As – Deposited NMO Films Produced at 400°C

6.2.1 Optical Microscopy

Optical microscopy was used to see if there were any defects or scratches on the surface of the films, which may cause reproducibility problems or resistivity measurement problems.

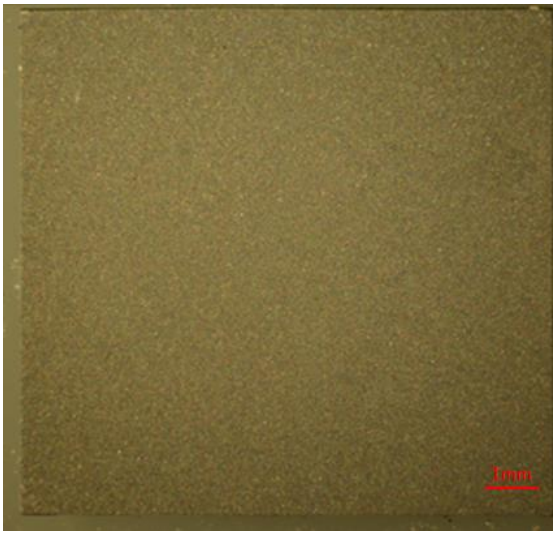

400°C 50mTorr

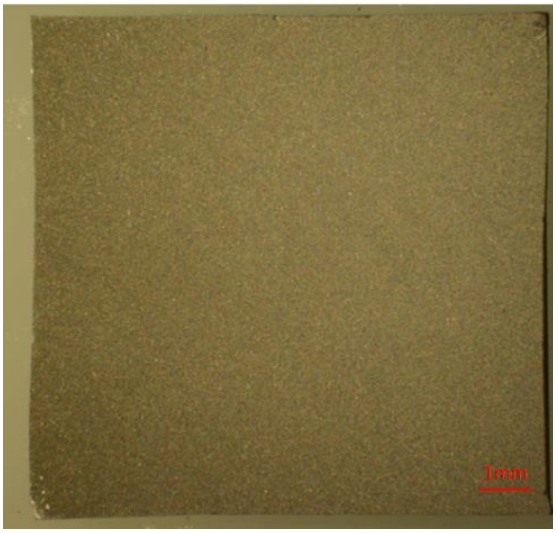

400°C 150mTorr

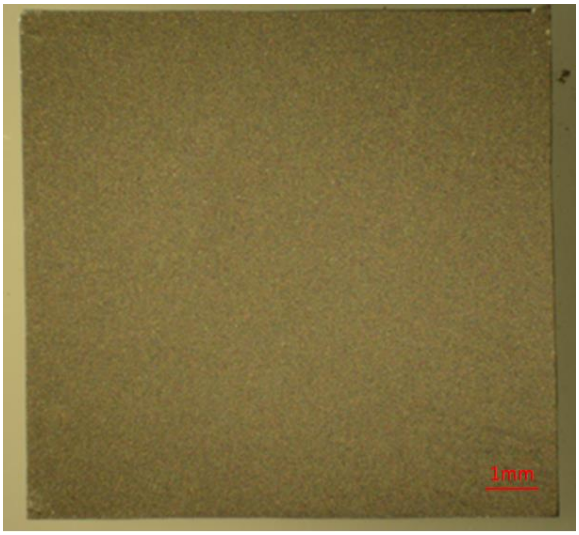

400°C 250mTorr

Figure 6.1. Optical microscopy images of films produced on alumina substrates at 400°C substrate temperature and O_2 pressures of 50 mTorr, 150 mTorr and 250 mTorr

The optical microscopy images in Figure 6.1 show that the films deposited on the commercial alumina substrates are quite dull suggesting that the films are quite rough. Despite their roughness there doesn't appear to be any scratches or defects so changes in the analysis of the films are not due to the films getting damaged. With comparison to the roughness measurements made in Chapter 5, the films rough appearance is due to alumina substrates. Changes are therefore due to a change in the substrate temperature and oxygen pressure during deposition.

6.2.2 XRD Results

The XRD patterns of NMO thin films produced using a growth temperature of 400°C in a range of oxygen pressures are shown in Fig 6.2. The XRD pattern from the NMO target supplied by Amphenol has also been included for reference. Most of the observed peaks can be attributed to either NMO or the alumina substrate which were in agreement with the reference spectra obtained from the JCPDS database, which allowed for unequivocal identification (Al_2O_3 PDF no. 01-073-1512 and NMO PDF no. 01-071-0852). A few peaks were also attributed to a secondary phase identified as Mn_2O_3 (indicated by a '□' in the XRD traces) (Mn_2O_4 PDF no. 01-089-2809). The XRD data for the thin films and target material was analysed using Eva software, which also enables subtraction of the background.

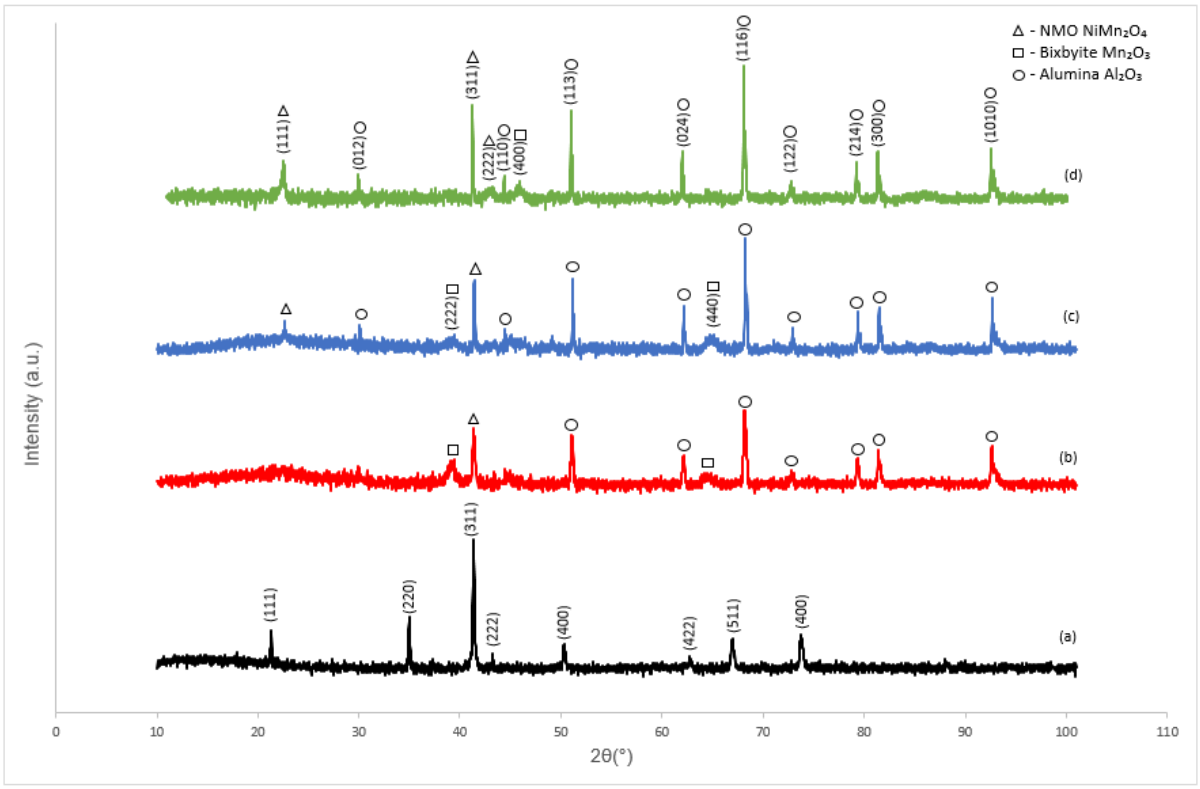

Figure 6.2. XRD patterns with a Co source of NMO as – deposited films grown at 400°C (a) NMO target, (b) 50 mTorr O_2, (c) 150 mTorr O_2 and (d) 250 mTorr O_2

From the XRD patterns it is clear that the patterns of the films have changed significantly in comparison to the target material, as less NMO peaks are evident in the films. However, the XRD patterns show that with an increase of O_2 pressure there is an increase in the number of NMO peaks present. There is also an increase in the NMO peak intensity with an increase of O_2 pressure suggesting that there is improvement in the crystallinity of the films and perhaps also an increase in grain growth [1]. Only the 250 mTorr film shows one clear NMO broad peak at a 2θ value of around 21° corresponding with the (111) reflection. The main NMO peak line at a 2θ value of 41° could be overlapped by an Al_2O_3 peak which is also around observed around 2θ = 41°. There is broadening of the NMO (111) peak with increasing O_2 pressure which indicates that may be a decrease in the grain size [2]. Peak broadening at the spinel (311) reflections indicate an onset of tetragonal distortion, which is typical of more manganese rich spinels [3]. There is a decrease in the intensity of peaks attributed to the Mn_2O_3 secondary

phase with an increase of O_2 pressure, and there appears to not be any Mn_2O_3 peaks evident in films produced at a pressure of 250 mTorr.

6.2.3 Surface Microstructure by SEM

The SEM micrographs in Figure 6.3 – 6.5 show the microstructure of the NMO films grown at 400°C and at pressures between 50 – 250 mTorr. Dense films have been produced as there is low porosity. The films exhibit a granular structure with grain sizes estimated to be between 3 and 5 μm, the grain sizes are not uniform and there doesn't appear to be any difference in size between the different O_2 pressure conditions.

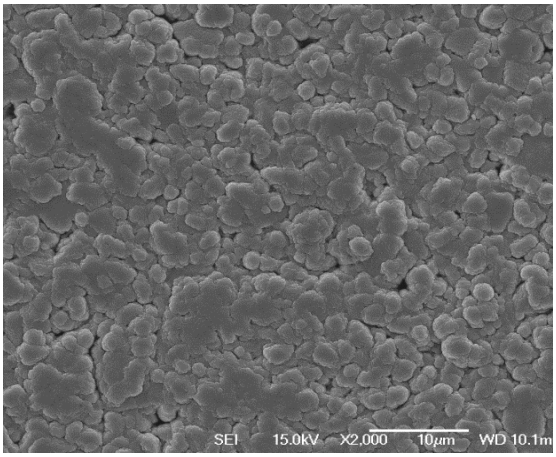

400°C 50 mTorr

400°C 50 mTorr

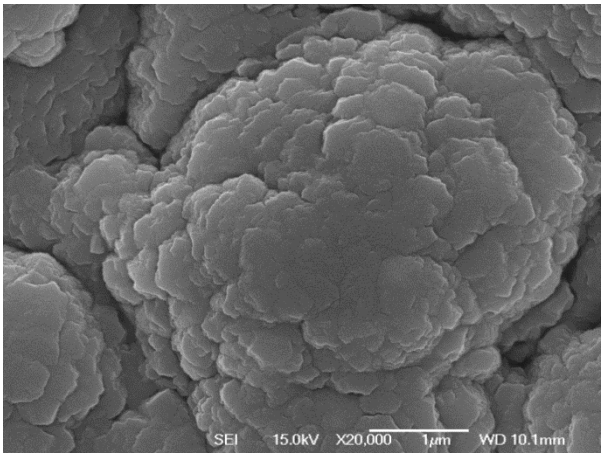

400°C 50 mTorr

Figure 6.3. SEM surface microstructure images of NMO film produced at 400°C and 50 mTorr (Jeol 7000F)

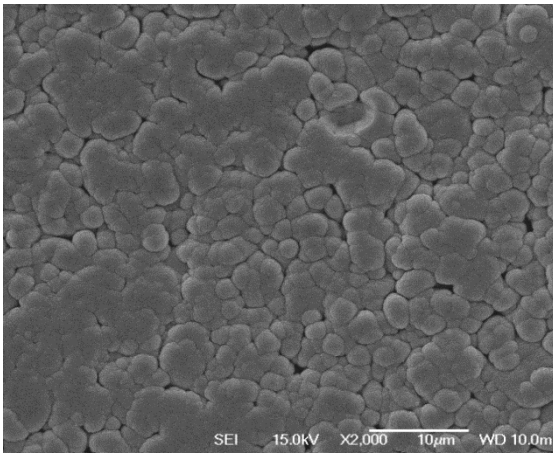

400°C 150 mTorr

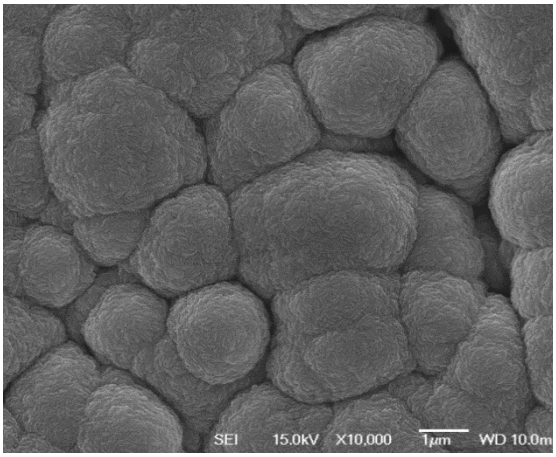

400°C 150 mTorr

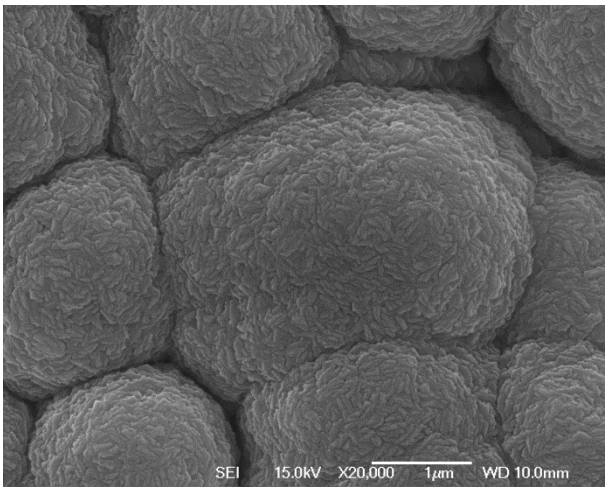

400°C 150 mTorr

Figure 6.4. SEM surface microstructure images of NMO film produced at 400°C and 150 mTorr (Jeol 7000F)

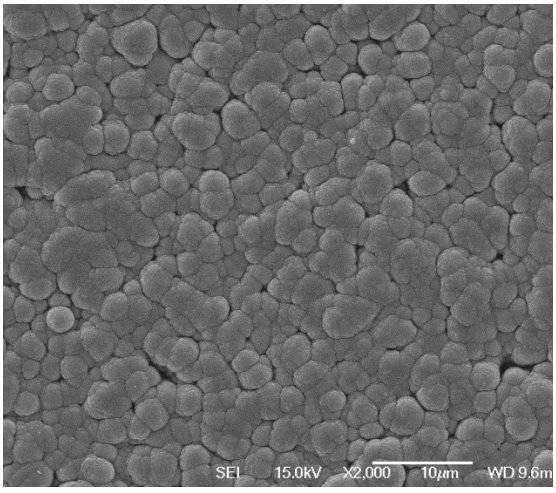

400°C 250 mTorr

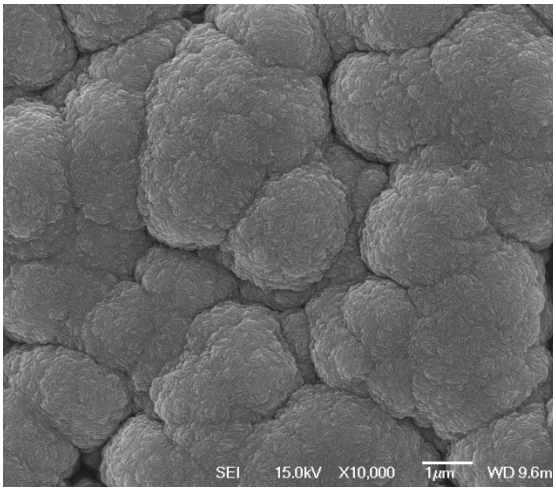

400°C 250 mTorr

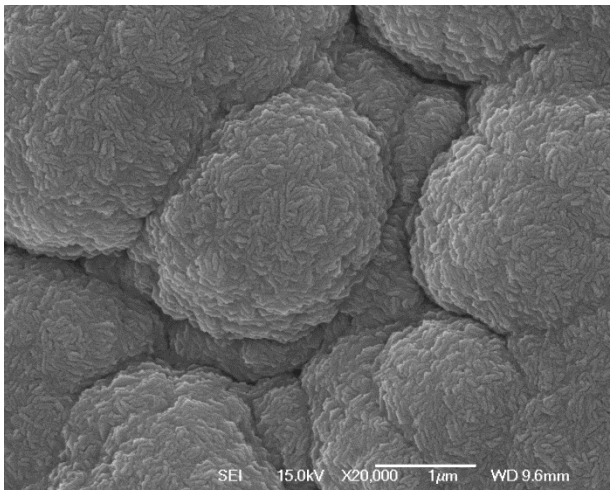

400°C 250 mTorr

Figure 6.5. SEM surface microstructure images of NMO film produced at 400°C and 250 mTorr (Jeol 7000F)

There is similarity in the films grain sizes in comparison to the substrates grains as observed in Chapter 5 (Figure 5.18) suggesting that these films have followed the pattern of the surface substrate. It is known that what is observed are the films and not a coating of the alumina grains, as the new deposition conditions will produce a much thicker film, this is proved in the cross sections reported later in this chapter. With an increase of pressure there does appear to be a change in the appearance of the grains in comparison to the films produced at 50 mTorr, with the presence of smaller grains on the larger grains. The smaller grains on the films produced at 50 mTorr are much larger in comparison to the smaller grains on the films produced at 150 and

250 mTorr. This suggests that deposition in higher O_2 pressures (150 mTorr and higher) that there is a change in the growth mechanism of the grains.

6.2.4 Resistance Measurements

The resistance vs. temperature measurements were carried out using the four wire measurement which is described in detail in Chapter 3. The resistance vs temperature graph for the as deposited samples grown at 400°C is shown in Figure 6.6 and shows that the resistance of the films decreased with an increase of their body temperature, thus indicating that all the films have NTC characteristics.

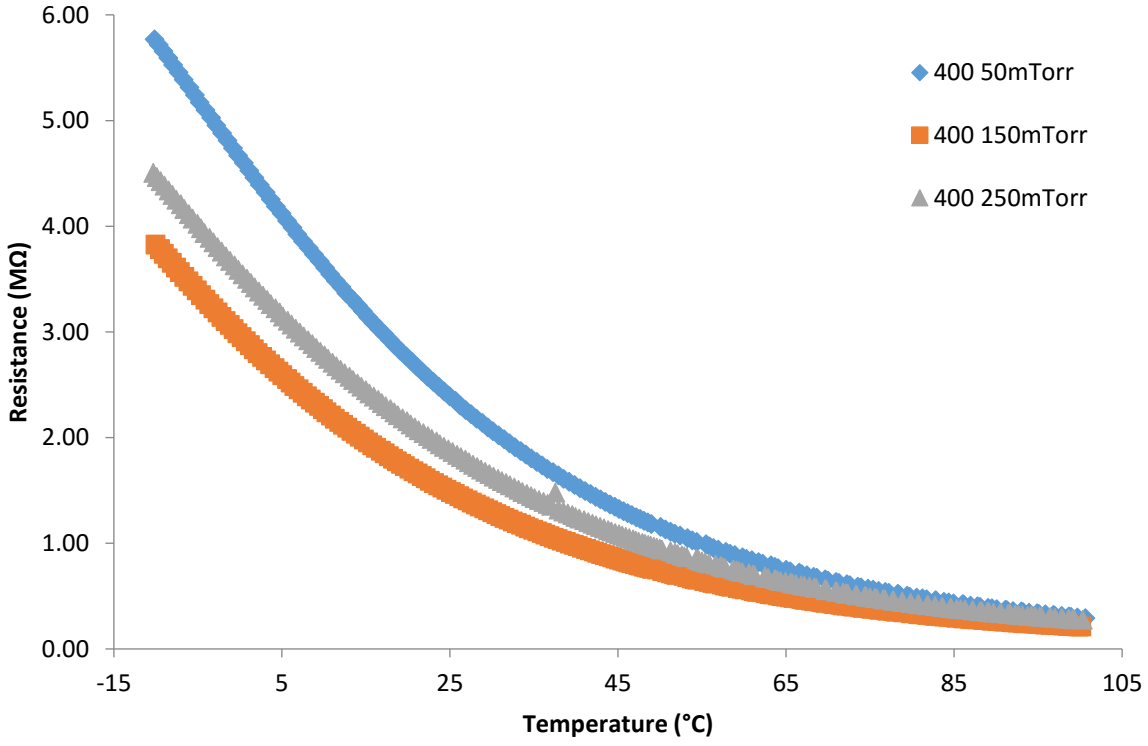

Figure 6.6. Resistance vs. Temperature graph of films grown at 400°C with O_2 pressure of 50, 150 and 250mTorr.

It appears that an increase of O_2 pressure from 50 to 150 mTorr during deposition leads to a decrease in the film resistance. A slight increase in resistance was observed for a further increase of O_2 pressure from 150 to 250 mTorr, although this may be within the experimental variation of the measurement. This is in agreement with literature [4] which saw a similar pattern in the change in resistivity with an increase in oxygen content during deposition in films produced using RF magnetron sputtering. The table below shows the resistance measurements of the films at 25°C and 85°C.

Table 6.1. Resistance measurements of as deposited films at 400°C substrate temperature and different O_2 pressure.

	Resistance measurement temperature	
O_2 pressure (mTorr)	**25°C**	**85°C**
50	2.35×10^6 Ω	4.32×10^5 Ω
150	1.49×10^6 Ω	2.99×10^5 Ω
250	1.86×10^6 Ω	3.81×10^5 Ω

The resistance measurement of the target bulk material at 25°C was 2.25×10^4 Ω and at 85°C it was measured at 2.61×10^3 Ω. There is an increase in resistance measured in the films in comparison to the bulk material, which was to be expected.

6.2.5 Film Cross Sections by SEM

Figures 6.7 – 6.9 shows the SEM micrographs of the as deposited films grown at 400°C and at different oxygen pressures. What can instantly be seen is that the films have been deposited on unpolished commercial alumina substrates. The defects that can be seen through the thickness of the film in all the micrographs appear to be grain boundaries, but it is not clear if

these ‘boundaries’ are coincident with the grain boundaries in the substrate. However, the defects are not visible on all films and may just be due to the preparation technique.

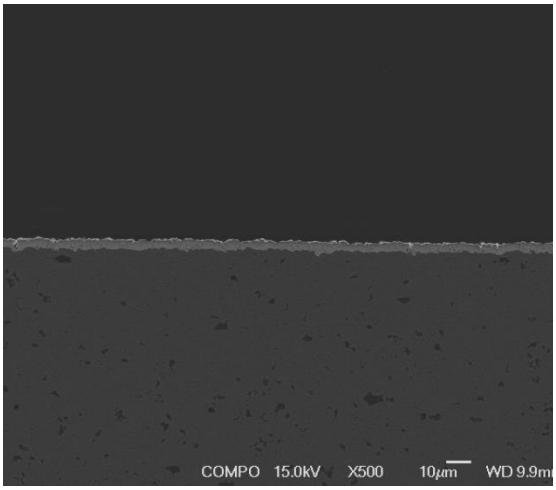

400°C 50 mTorr

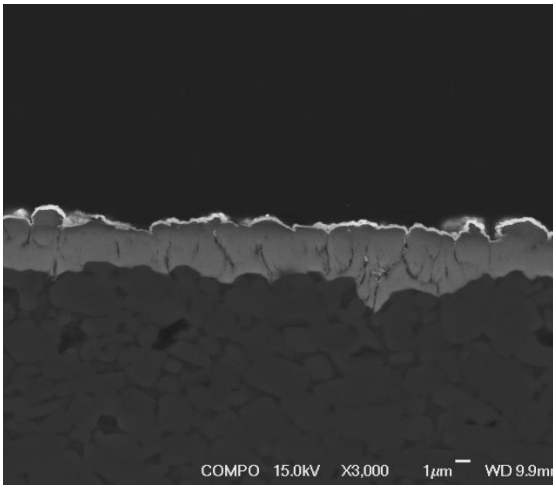

400°C 50 mTorr

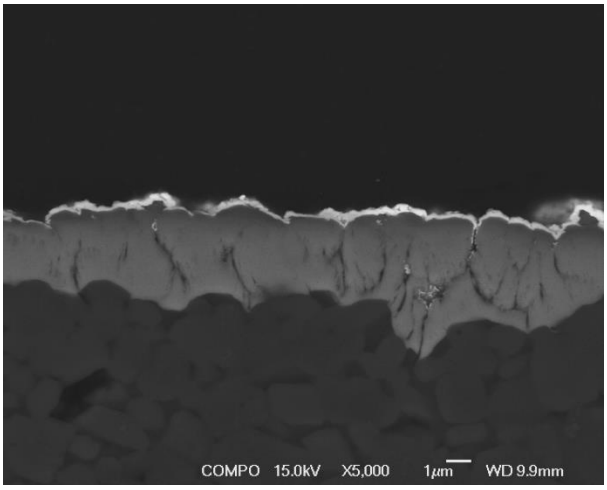

400°C 50 mTorr

Figure 6.7. SEM Micrograph of a cross-section of a NMO film grown at 400°C and 50 mTorr O_2 (Jeol 7000F)

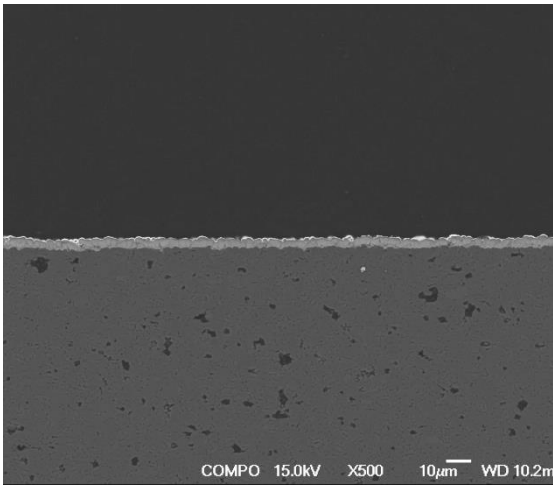

400°C 150 mTorr

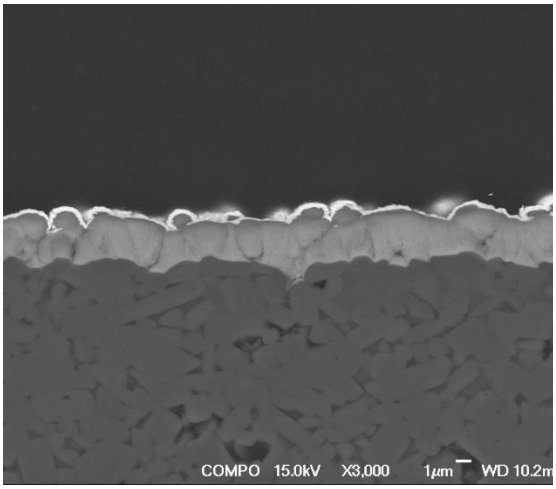

400°C 150 mTorr

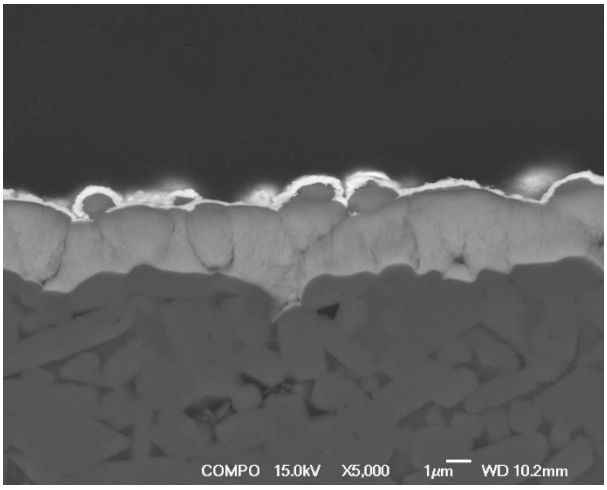

400°C 150 mTorr

Figure 6.8. SEM Micrograph of a cross-section of a NMO film grown at 400°C and 150 mTorr O_2 (Jeol 7000F)

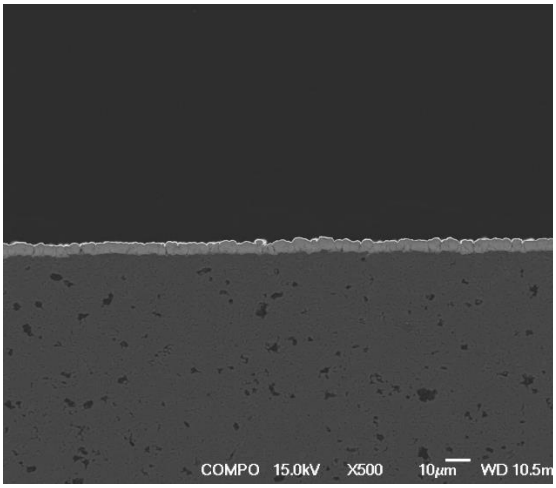

400°C 250 mTorr

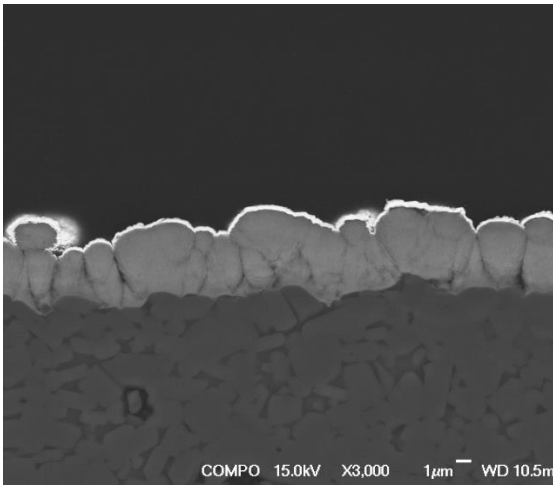

400°C 250 mTorr

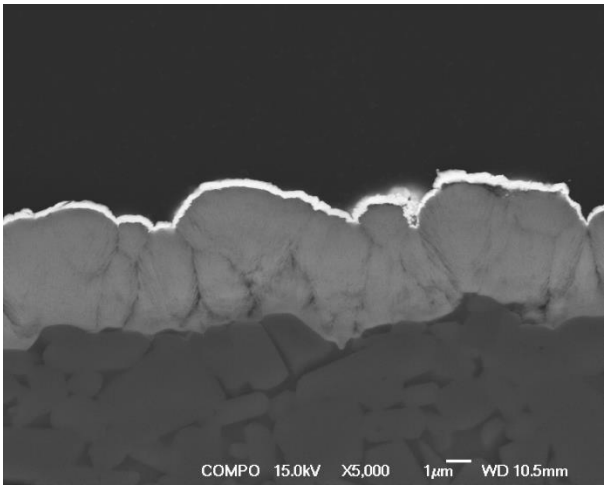

400°C 250 mTorr

Figure 6.9. SEM Micrograph of a cross – section of a NMO film grown at 400°C and 250 mTorr O_2 (Jeol 7000F)

Due to the commercial focus of the project the roughness of the substrate has led to the thickness of the films to be uneven. Therefore, only an average thickness of around 2 – 3 μm can be determined which will inevitably lead to errors and problems with reproducibility of resistivity measurements

6.2.6 Film Thickness Measurements

Using the cross sectional micrographs technique reported in section 4.6.3, the thickness of each films was measured at five different locations along the whole 10mm cross section as

indicated schematically in Figure 6.10. The mean values have been used in the subsequent resistivity calculations.

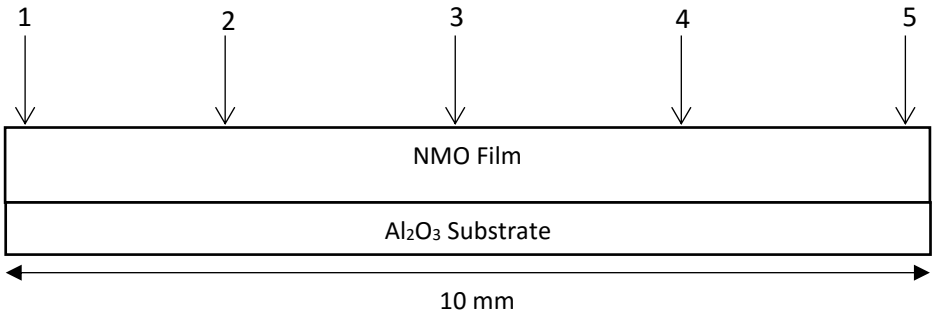

Figure 6.10. Approximate locations of thickness measurements on the cross section of the film.

Table 6.2. Average film thickness determination for films produced at 400°C and different O_2 pressures

400°C 50mTorr As Deposited					
Measurement Position	1	2	3	4	5
Thickness (μm)	2.40	2.26	3.60	3.00	3.30
Mean (μm)	2.91 ± 0.51				

400°C 150mTorr As Deposited					
Measurement Position	1	2	3	4	5
Thickness (μm)	2.07	2.67	4.00	3.67	2.13
Mean (μm)	2.91 ± 0.79				

400°C 250mTorr As Deposited					
Measurement Position	1	2	3	4	5
Thickness (μm)	2.47	2.80	2.40	2.33	2.47
Mean (μm)	2.49 ± 0.16				

The film thickness measurements show that the films produced at 50 and 150 mTorr are of similar size and are also thicker than the film produced at 250 mTorr. In general, it is seen that the films are thicker in the centre and reduce in thickness towards the outer edges. This suggests

that the films do not grow with a uniform thickness but instead have varying thickness along the substrate. Therefore, there is a difference in the rate of the growth of thin films in relation to the plasma plume produced during their deposition i.e. higher rate of growth will be evident towards the centre of the plume. The errors of the thickness of the films indicate that the mean thickness is not entirely accurate. This will have an effect on the film's resistivity as these mean thicknesses are used in the equation to determine the films resistivity.

6.2.7. Calculation of Resistivity and Thermistor Characteristics of the As – Deposited Films Produced at 400°C Substrate Temperature

The β value or thermistor constant of the films was determined from the slope of the resistance vs temperature graph (Figure 6.11).

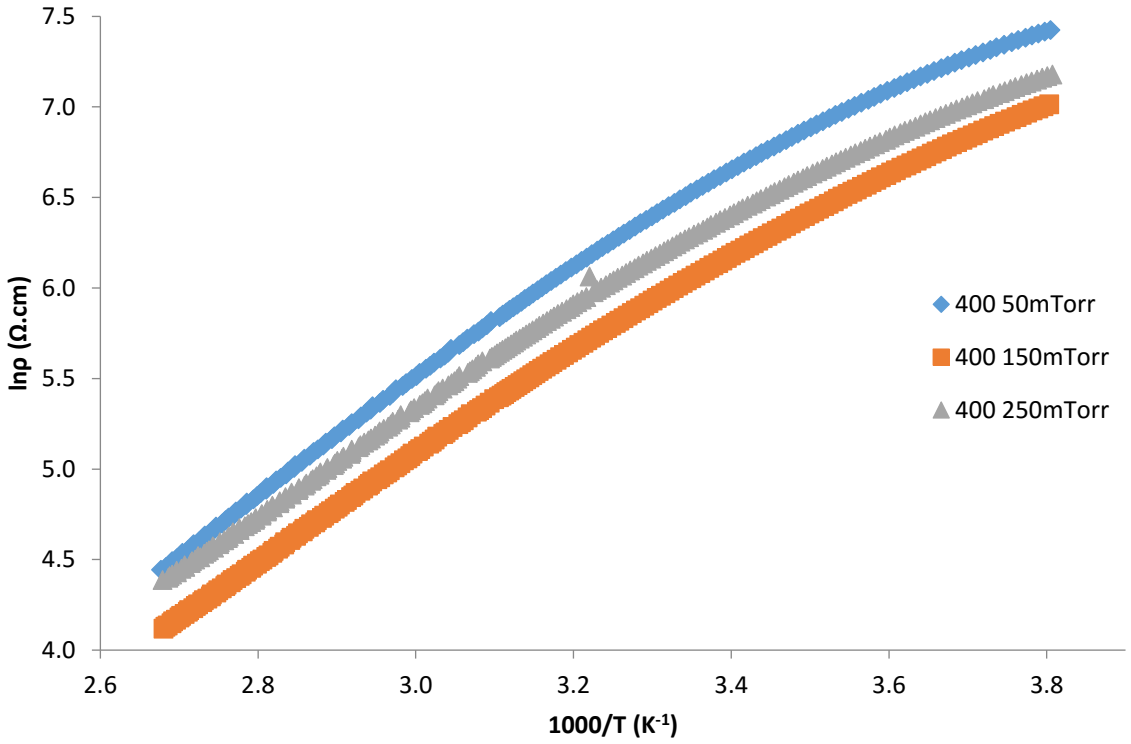

Figure 6.11. Lnρ vs 1000/T graph of NMO films grown at 400°C at different O_2 pressures

In Figure 6.11 it can be seen that the log resistivity of all the films decreased approximately linearly with increasing temperature, confirming that the films have NTC characteristics. With

an increase of O_2 pressure for deposition from 50 to 150 mTorr there is a decrease in resistivity, with a further increase of O_2 pressure to 250 mTorr there is a small increase in resistivity. This is suggesting that there may be a change in the Mn valence states and / or the available oxygen vacancies. It may also be due to a change in the inversion parameter.

We are able to calculate the films activation energy, temperature coefficient and stability factor.

Table 6.3. Thermistor characteristics measured and calculated electrical parameters

Substrate Temperature (°C)	O_2 Pressure (mTorr)	25°C Resistivity (Ω.cm)	85°C Resistivity (Ω.cm)	Thermistor constant β Value (K)	Activation Energy (eV)
400	50	7.45E+02	1.34E+02	3053	0.2631
400	150	4.29E+02	9.55E+01	2671	0.2302
400	250	4.70E+02	1.10E+02	2583	0.2226

The thermistor constant or the β value is the sensitivity of the thermistor to changes in temperature and is an important parameter that is taken into consideration when selecting a thermistor for a specific application. With an increase of oxygen pressure a decrease in the β value is noticed suggesting that the sensitivity decreases. The activation energy is an indication of the energy required for the hopping process from a cation M^{n+} to $M^{(n+1)}$ on the tetrahedral to the octahedral sites. Conduction in the material at low temperature is due to the hopping of electrons between the Mn^{3+} and Mn^{4+} ions while at higher temperatures it is due to polaron hopping [5]. The activation energies decrease with an increase of oxygen pressure and resistivity.

6.3. Characterisation of NMO Films Produced at 400°C and Annealed

6.3.1 Optical Microscopy

Duplicate films were grown using the same conditions for the as – deposited films at a growth temperature of 400°C and with varied oxygen pressures. These films were then annealed for an hour at 800°C and slow cooled to room temperature in 1 atm of O_2.

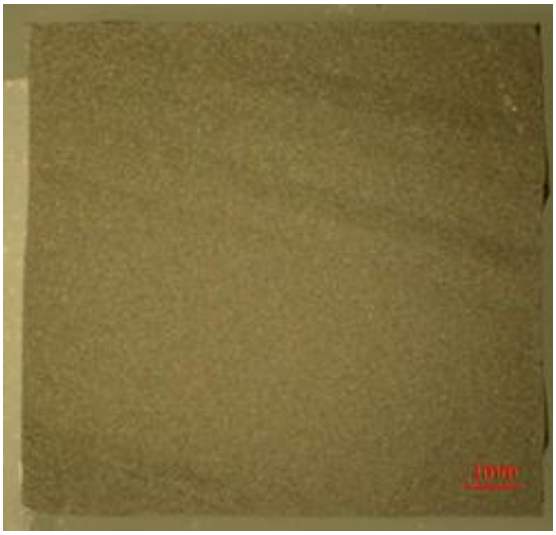

400°C 50 mTorr Annealed

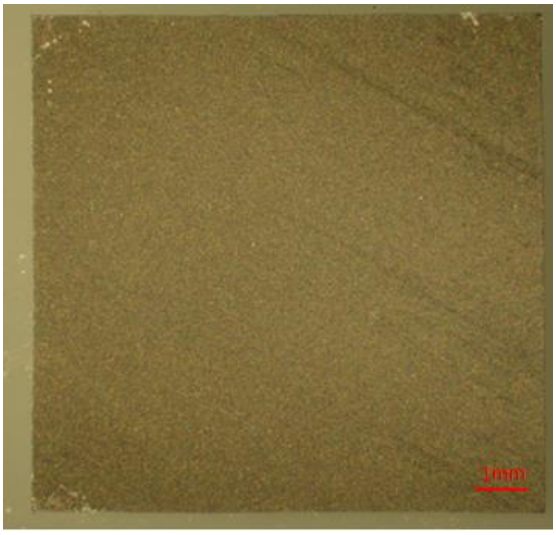

400°C 150 mTorr Annealed

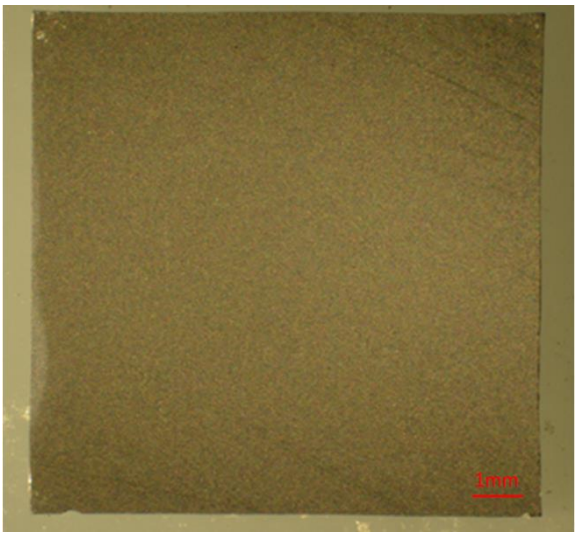

400°C 250 mTorr Annealed

Figure 6.12. Optical microscopy images of films produced on alumina substrates at 400°C substrate temperature and O_2 pressures of 50 mTorr, 150 mTorr and 250 mTorr and annealed

The optical microscopy images of the surfaces of the annealed films deposited on the commercial alumina substrates are shown in Figure 6.12. These images look identical to those of the as-deposited films (Figure 6.1), being quite dull suggesting that the films are quite rough. Despite their roughness there doesn't appear to be any scratches or defects so changes which might be observed in the analysis of the films are not due to the films getting damaged. Changes are therefore due to a change in the substrate temperature, oxygen pressure during deposition and the effect of annealing.

6.3.2 XRD Results

The annealed films were then analysed using XRD, and their resulting patterns are shown in Figure 6.13 - 6.18 along with their as – deposited film counterpart patterns for reference. With the annealed films having the 2θ position between 35 and 50° magnified for better comparison.

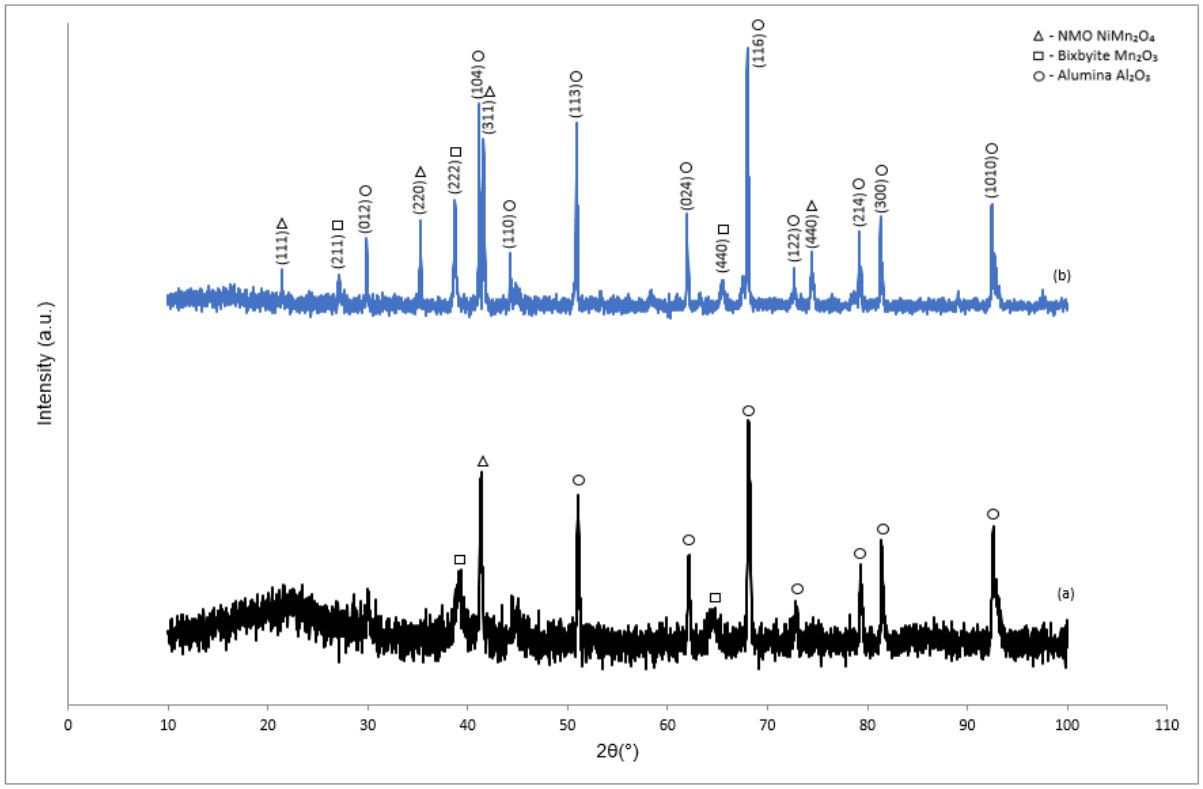

Figure 6.13. XRD patterns with a Co source of NMO films grown at 400°C (a) 50 mTorr as deposited, (b) 50 mTorr annealed

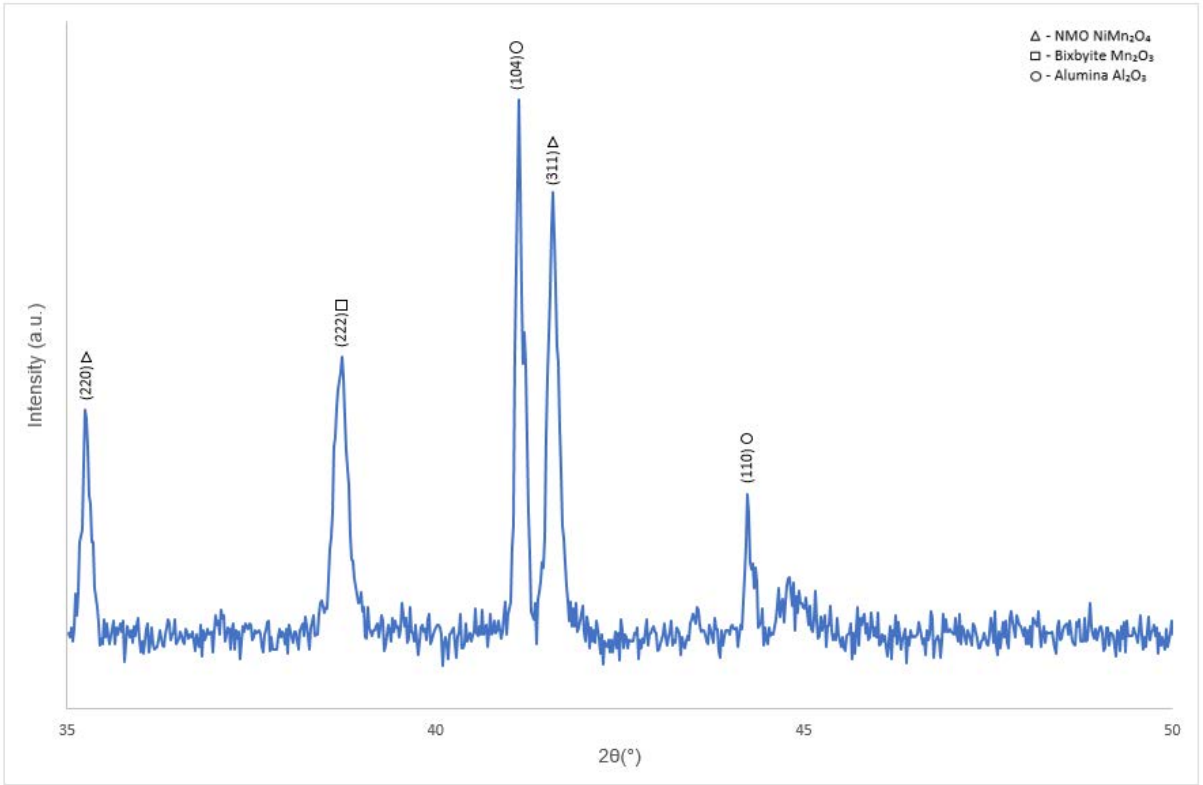

Figure 6.14. XRD patterns with a Co source of NMO films grown at 400°C 50 mTorr as annealed at 35 - 50°

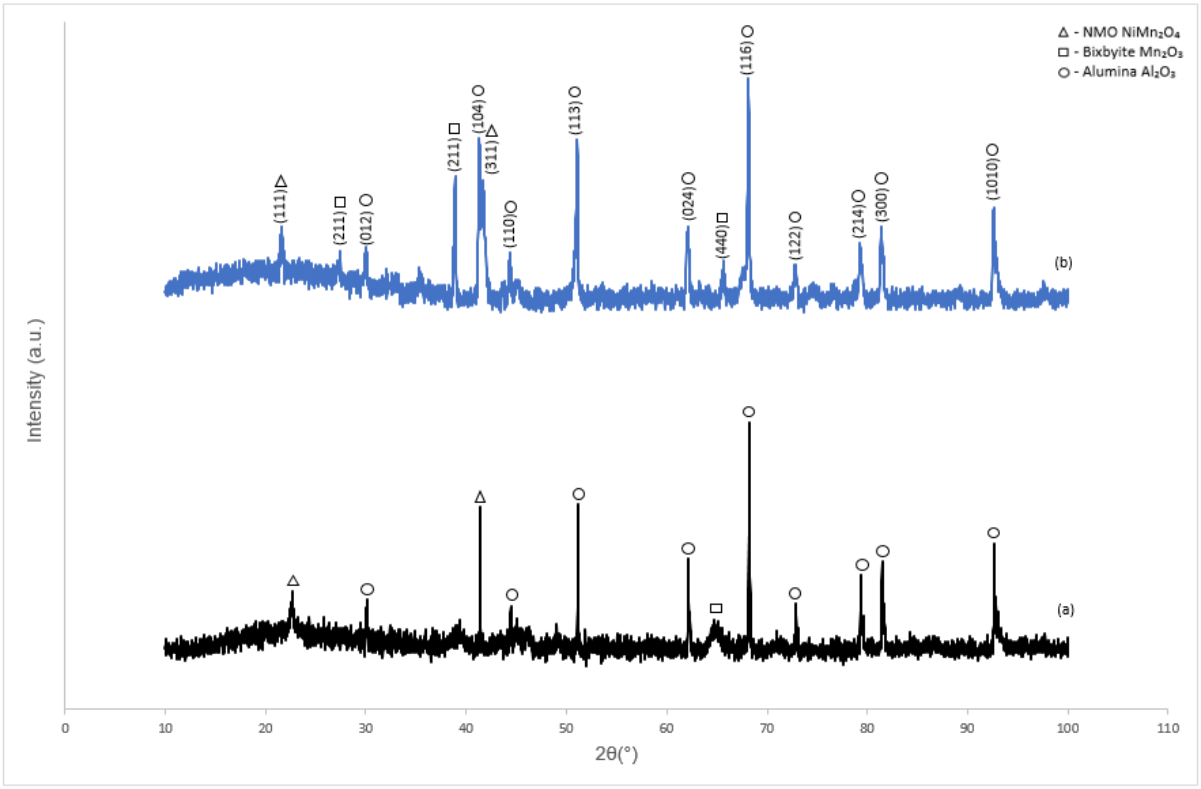

Figure 6.15. XRD patterns with a Co source of NMO films grown at 400°C (a) 150 mTorr as – deposited, (b) 150 mTorr annealed

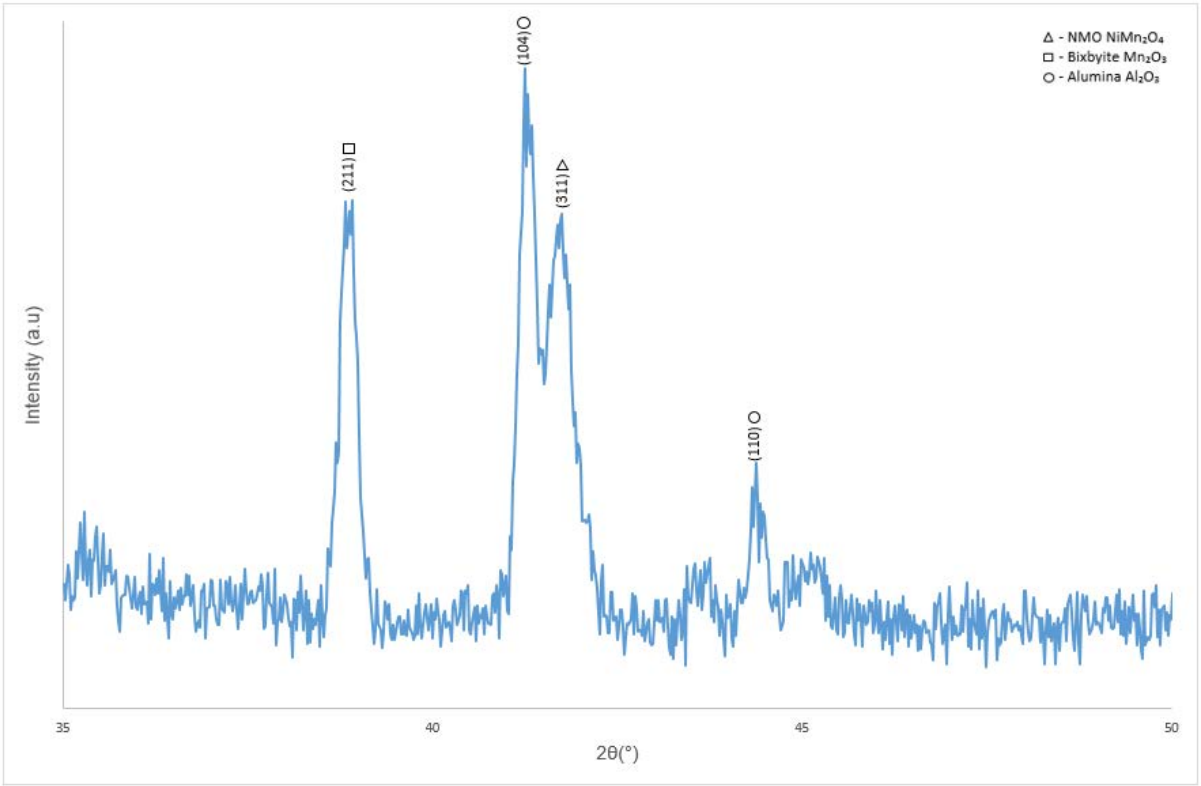

Figure 6.16. XRD patterns with a Co source of NMO films grown at 400°C 150 mTorr as annealed at 35 - 50°

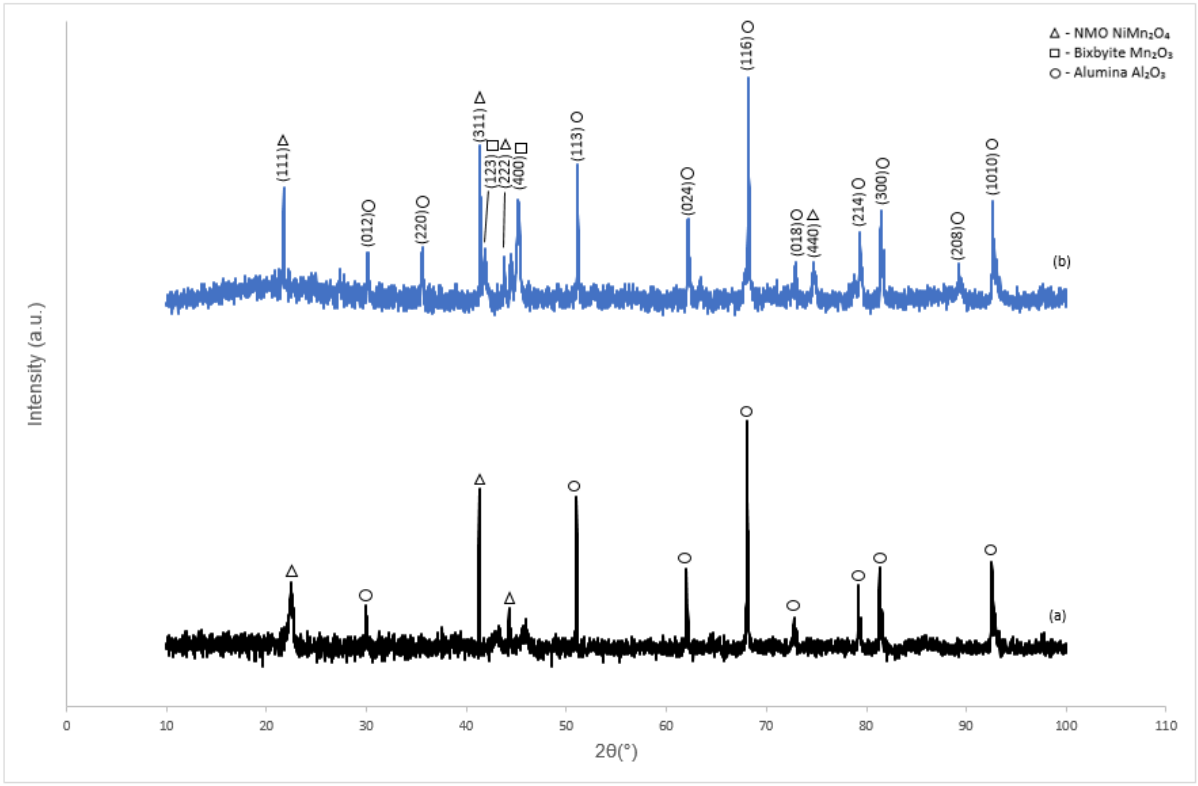

Figure 6.17. XRD patterns with a Co source of NMO films grown at 400°C (a) 250 mTorr as – deposited, (b) 250 mTorr annealed

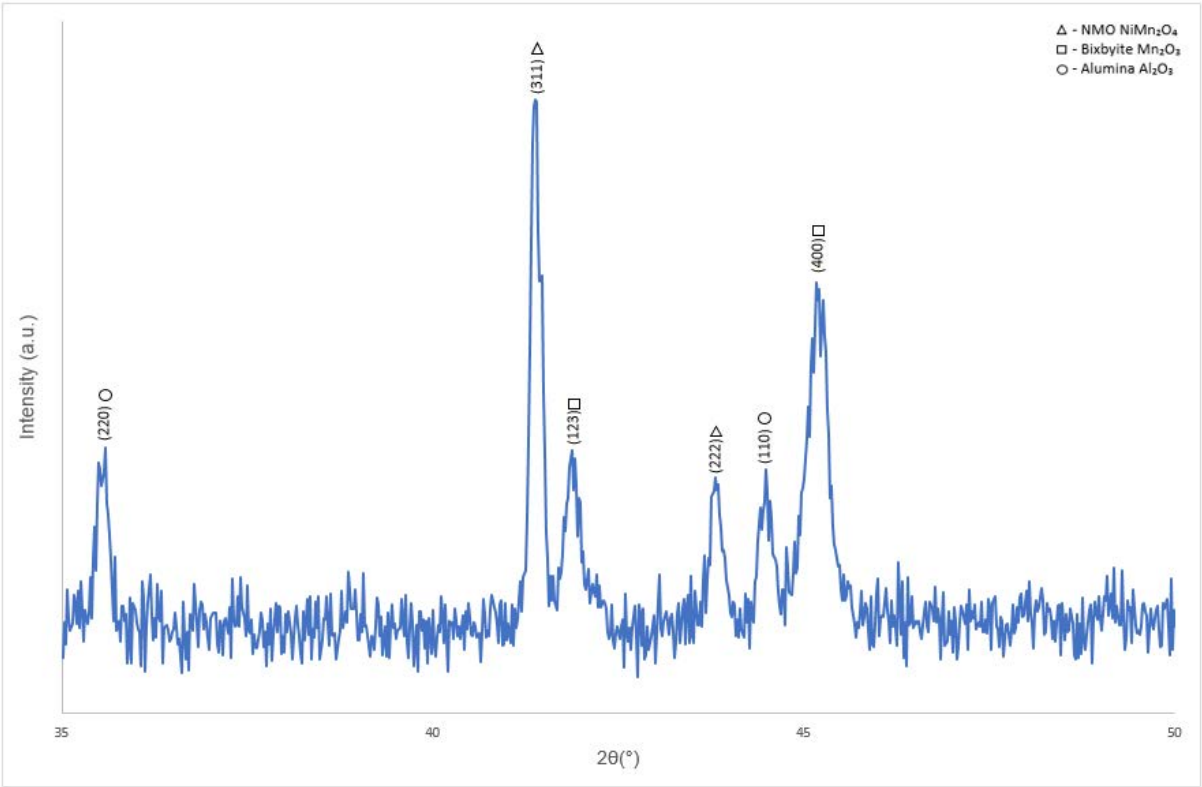

Figure 6.18. XRD patterns with a Co source of NMO films grown at 400°C 250 mTorr as annealed at 35 - 50°

The majority of the observed peaks could be attributed to either NMO or the alumina substrate which were in agreement with the reference spectra obtained from the JCPDS database, which allowed for unequivocal identification (Al_2O_3 PDF no. 01-073-1512 and NMO PDF no. 04-008-6982). A few peaks were also attributed to a secondary phase identified as Mn_2O_3 (indicated by a '□' in the XRD traces) (Mn_2O_4 PDF no. 01-089-2809). The XRD data for the thin films was analysed using Eva software [6] with the background subtracted using this software.

The XRD patterns show that following annealing the same peak intensity ratio is maintained as the as – deposited films. Consequences of annealing the as – deposited films however include an increase in the number of NMO peaks observed along with an increased intensity from these NMO peaks. This is suggesting there is an improvement in their crystallinity following annealing. The (111) NMO spinel peak 2θ position in the 150 and 250 mTorr samples decreases following annealing which is a possible indication of strain relief. It also may indicate that the lattice constant has increased during annealing [2]. This can be caused by oxidation – reduction reactions and cation migrations between or within the sublattices of the spinel structure which can be expressed as [7, 8]:

$$Mn_A^{2+} + Mn_B^{4+} + Ni_B^{2+} \rightarrow 2Mn_B^{3+} + Ni_A^{2+}$$

There is also a large increase in the intensity of the peaks from the secondary phase Mn_2O_3 following annealing. This secondary phase is likely to have an effect on the Mn^{3+} and Mn^{4+} ratio in the octahedral sites of the spinel, which may result in changes to the electrical properties of the films.

6.3.3 Surface Microstructure by SEM

SEM images of the surfaces of the annealed films are shown in Figures 6.19 - 6.21. Annealing of the NMO films has had very little effect on the appearance of the grains microstructure of the thin films. Films appear to be dense but with an uneven surface, giving the appearance of cracks or pores as the growth of the film follows the pattern of the alumina substrate. Compared to the as – deposited films (Figures 6.3 – 6.5), the fine surface features on the grains appear to be slightly more prominent, and the intergranular cracks appear slightly larger, particularly for the film deposited in 250 mTorr O_2 (Figure 6.21).

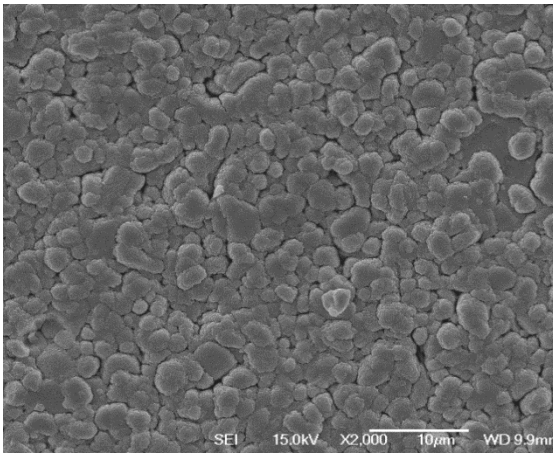

400°C 50 mTorr Annealed

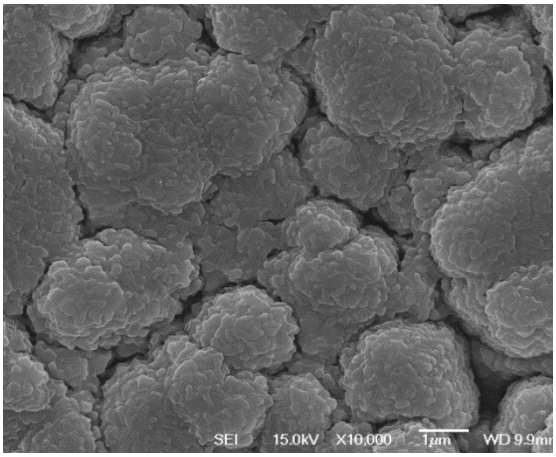

400°C 50 mTorr Annealed

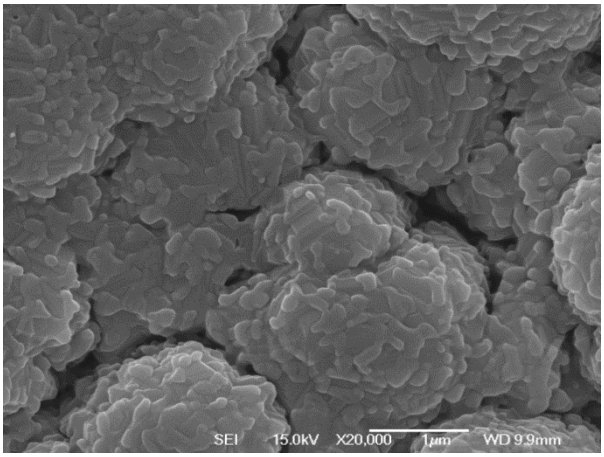

400°C 50 mTorr Annealed

Figure 6.19. SEM surface microstructure of annealed NMO film produced at 400°C and 50 mTorr (Jeol 7000F)

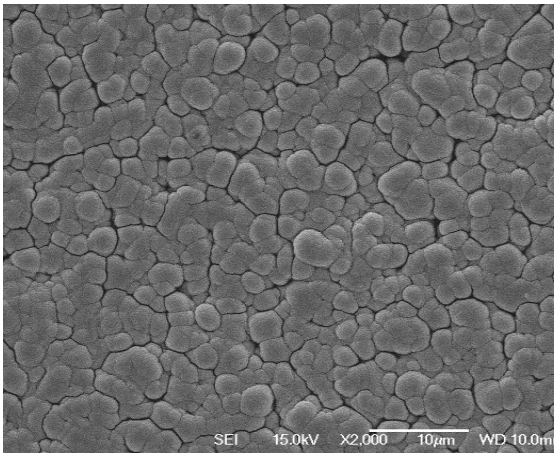

400°C 150 mTorr Annealed

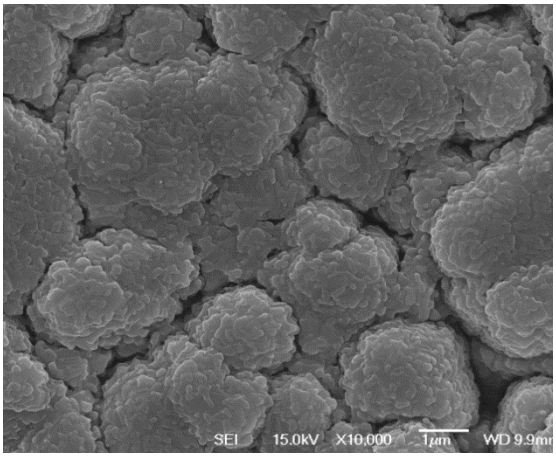

400°C 150 mTorr Annealed

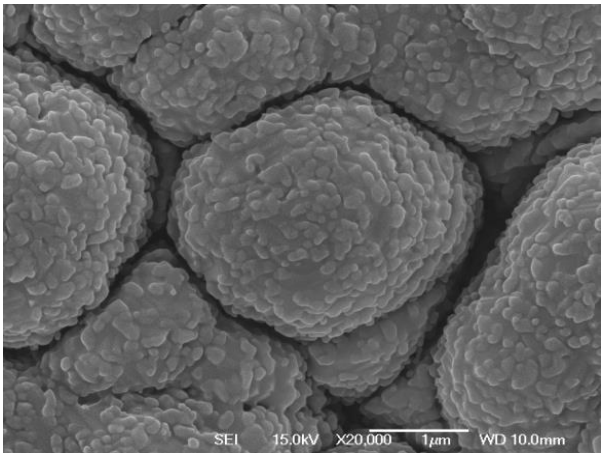

400°C 150 mTorr Annealed

Figure 6.20. SEM surface microstructure of annealed NMO film produced at 400°C and 150 mTorr (Jeol 7000F)

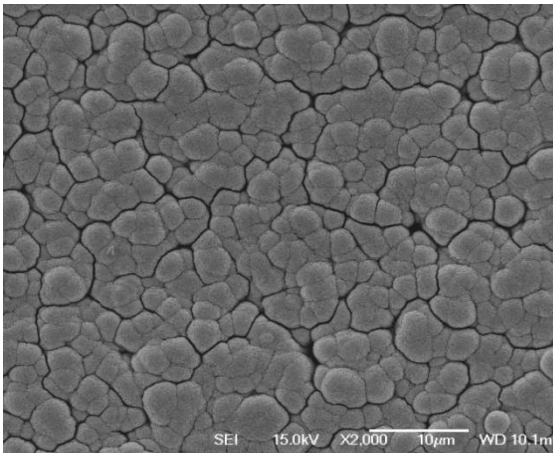

400°C 250 mTorr Annealed

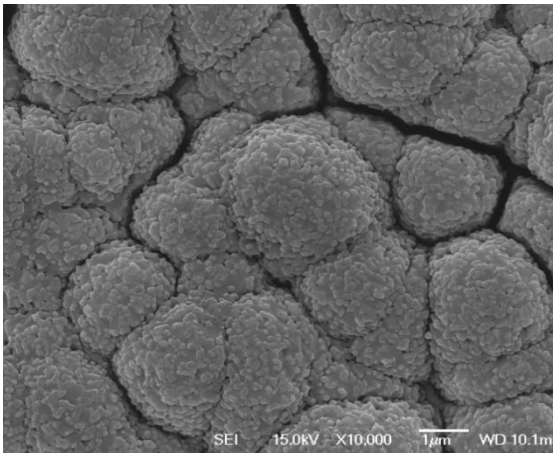

400°C 250 mTorr Annealed

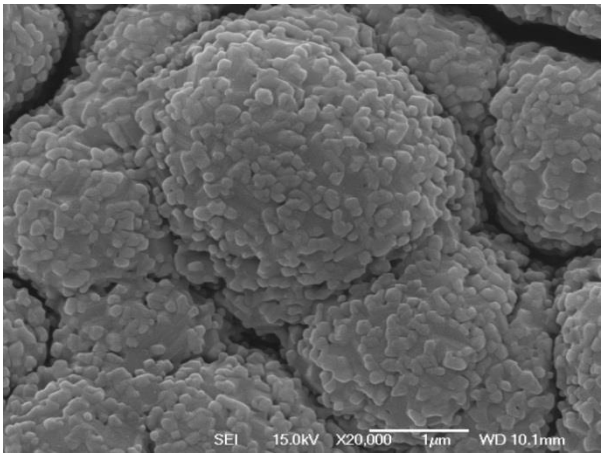

400°C 250 mTorr Annealed

Figure 6.21. SEM surface microstructure of annealed NMO film produced at 400°C and 250 mTorr (Jeol 7000F)

6.3.4 Resistance Measurements

The resistance vs. temperature graph for the annealed films deposited at 400°C is shown in Figure 6.22, all the films have retained their NTC behaviour after the annealing process. Annealing of the films has led to a clear distinction between the three different films in terms of their resistance. With an increase of oxygen pressure followed by annealing there is an increase in the film's resistance.

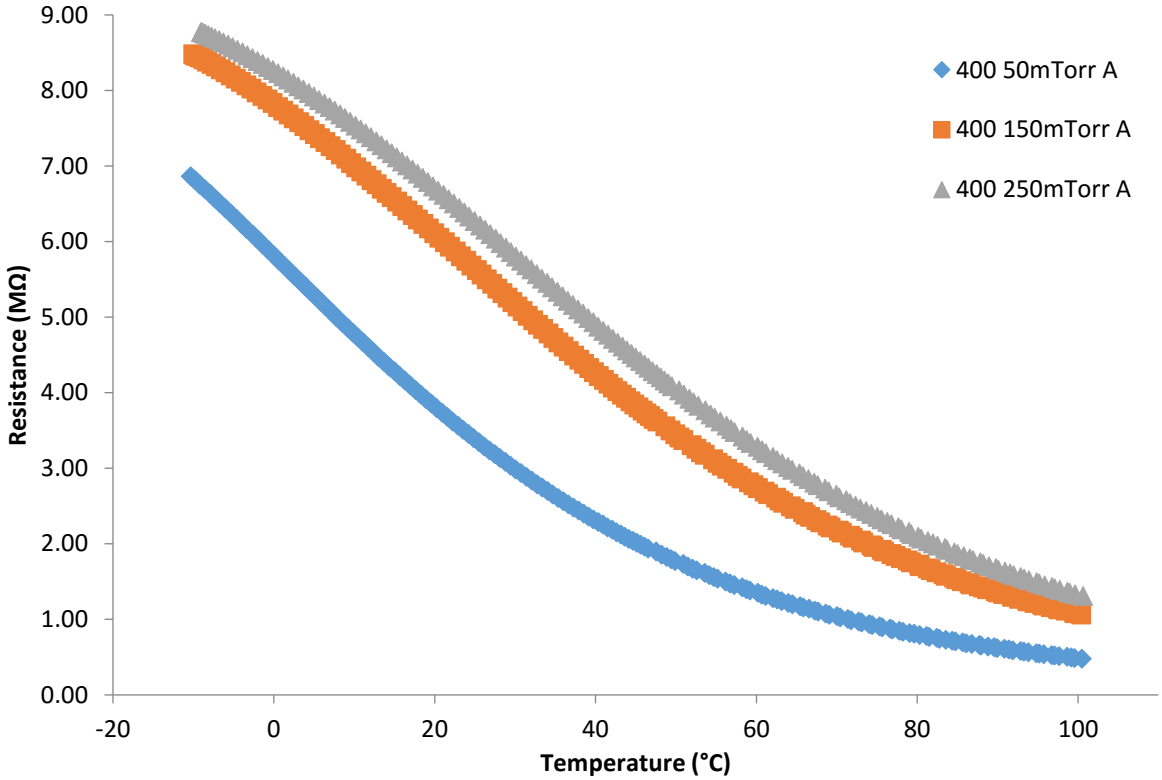

Figure 6.22. Resistance vs. Temperature graph of annealed films grown at 400°C in a range of O_2 pressures

A comparison of the resistance between the as deposited and annealed films, show that in general the films resistance increases following annealing as shown in the table below. The change in the resistance suggests the oxygen deficiency in the as deposited films is having an effect on their resistivity.

Table 6.4. Resistance measurements of as deposited films and annealed films at 400°C substrate temperature and different O_2 pressure deposition conditions

	As deposited		**Annealed**	
	Resistance measurement temperature		**Resistance measurement temperature**	
O_2 pressure (mTorr)	**25°C**	**85°C**	**25°C**	**85°C**
50	2.35×10^6 Ω	4.32×10^5 Ω	3.34×10^6 Ω	7.08× 105 Ω
150	1.49×10^6 Ω	2.99×10^5 Ω	5.62×10^6 Ω	1.51×10^6 Ω
250	1.86×10^6 Ω	3.81×10^5 Ω	6.27×10^6 Ω	1.86×10^6 Ω

It should be noted that the annealed films are different films from the as deposited i.e. the as deposited films have not been annealed, rather a separate set of films were produced.

6.3.5 Film Cross Sections by SEM

Figures 6.23 – 6.25 show the SEM cross sections of the films grown at 400°C and at different pressures and annealed in oxygen. Films appear less dense than the as-deposited films with an increase in the number of cracks especially in the film produced with a 250 mTorr O_2 pressure. This is consistent with the cracks observed in the surface microstructure (Figure 6.21).

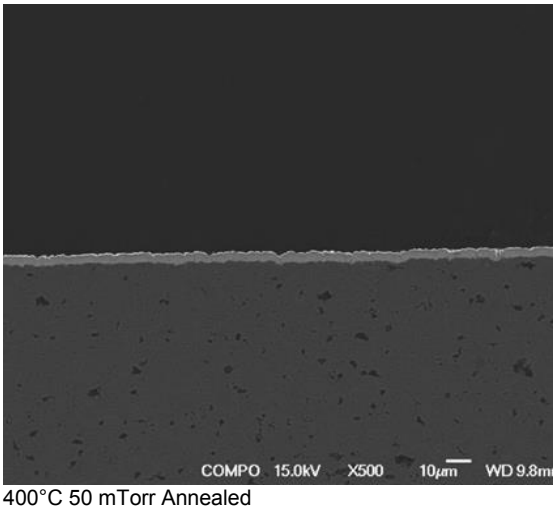

400°C 50 mTorr Annealed

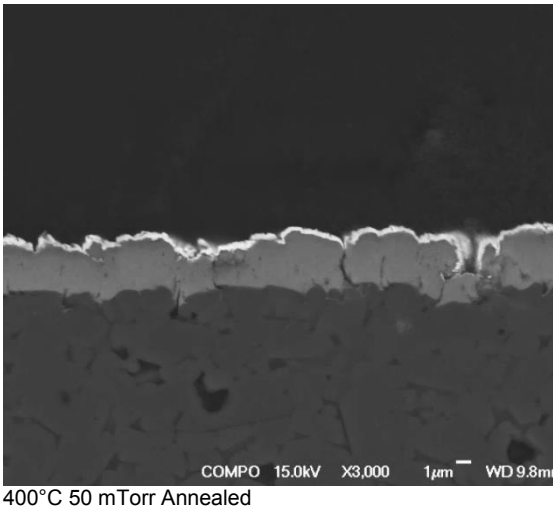

400°C 50 mTorr Annealed

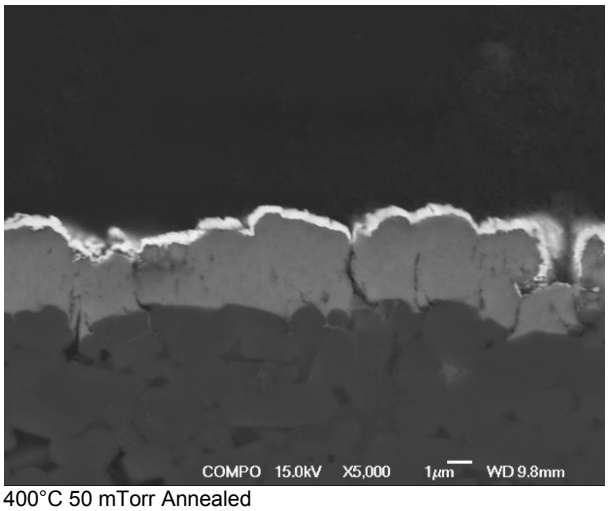

400°C 50 mTorr Annealed

Figure 6.23. SEM micrograph of a cross section of a NMO film grown at 400°C and 50 mTorr O_2 and annealed (Jeol 7000F)

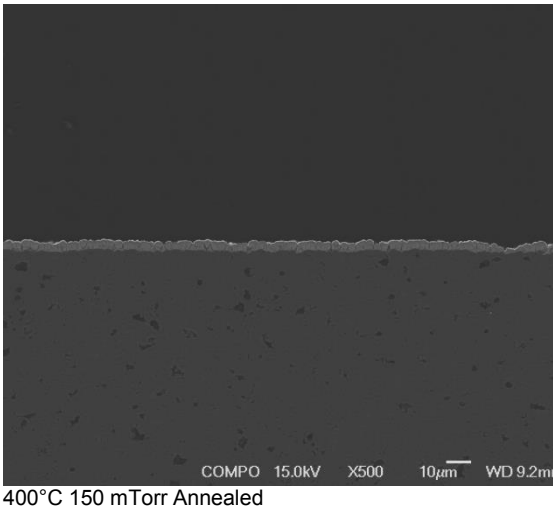

400°C 150 mTorr Annealed

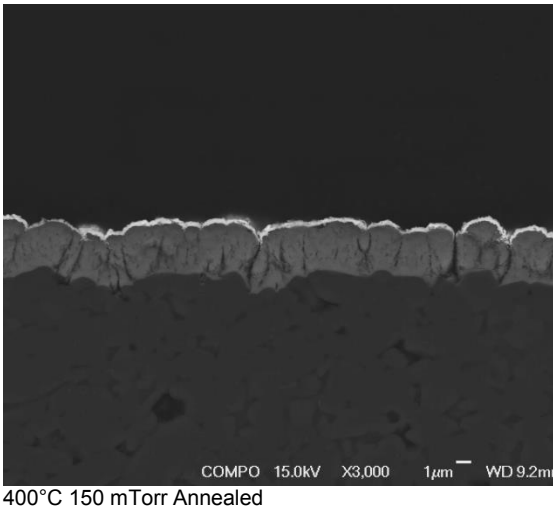

400°C 150 mTorr Annealed

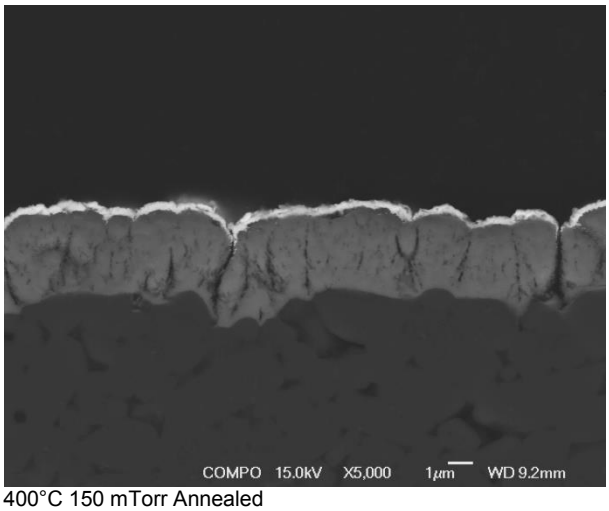

400°C 150 mTorr Annealed

Figure 6.24. SEM micrograph of a cross section of a NMO film grown at 400°C and 150 mTorr O_2 and annealed (Jeol 7000F)

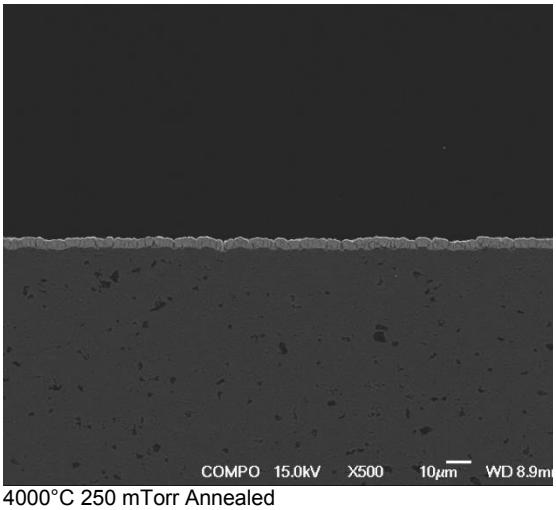

4000°C 250 mTorr Annealed

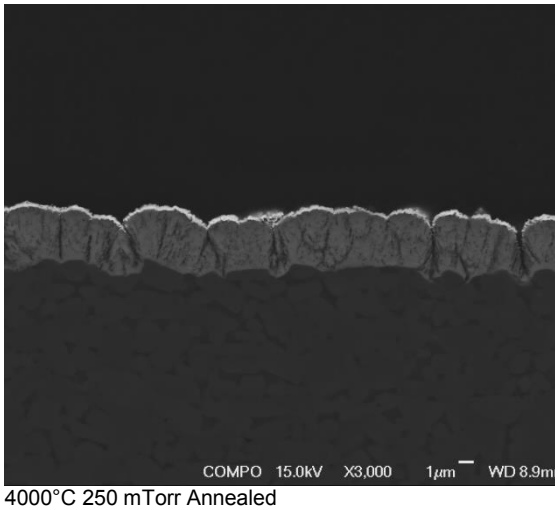

4000°C 250 mTorr Annealed

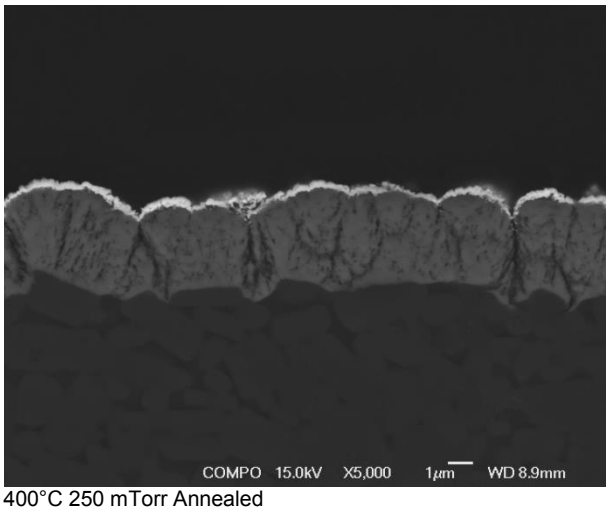

400°C 250 mTorr Annealed

Figure 6.25. SEM micrograph of a cross section of a NMO film grown at 400°C and 250 mTorr O_2 and annealed (Jeol 7000F)

Table 6.5. Average film thickness determination for films produced at 400°C and increasing O_2 pressure and annealed in oxygen

400°C 50mTorr Annealed					
Measurement Position	1	2	3	4	5
Thickness (μm)	2.13	2.13	2.00	2.00	2.00
Mean (μm)	2.05 ± 0.06				

400°C 150mTorr Annealed					
Measurement Position	1	2	3	4	5
Thickness (μm)	2.13	1.46	2.00	2.00	1.80
Mean (μm)	1.88 ± 0.23				

400°C 250mTorr Annealed					
Measurement Position	1	2	3	4	5
Thickness (μm)	2.87	3.00	3.00	3.00	2.60
Mean (μm)	2.89 ± 0.16				

Table 6.5 shows the average thickness measurements of the annealed films. From the values measured it appears that the films produced at 50 and 150 mTorr have a thinner thickness in comparison to the film produced at 250 mTorr. This is the same pattern when compared with the as deposited films, however there are big differences when the thickness of the annealed films is compared with their as deposited counterparts. With differences of sometimes more than 1 μm it is likely that there is a lot of variation in the films deposition process, this as well as being deposited on unpolished alumina substrates has made it very difficult to gain accurate measurements. This inevitably will lead to problems with the reproducibility of these film's resistivity if their thickness measurements cannot be accurately obtained.

6.3.6 Calculation of Resistivity and Thermistor Characteristics of the Annealed Films Produced at 400°C Substrate Temperature

A linear graph has been produced proving that the film exhibits NTC properties. Following annealing there is an increase in the films resistivity in comparison to the as deposited films.

This change in resistivity is a suggestion of a deficiency in oxygen in the as deposited films, in comparison to the annealed films, therefore an increase in oxygen leads to higher values of resistivity.

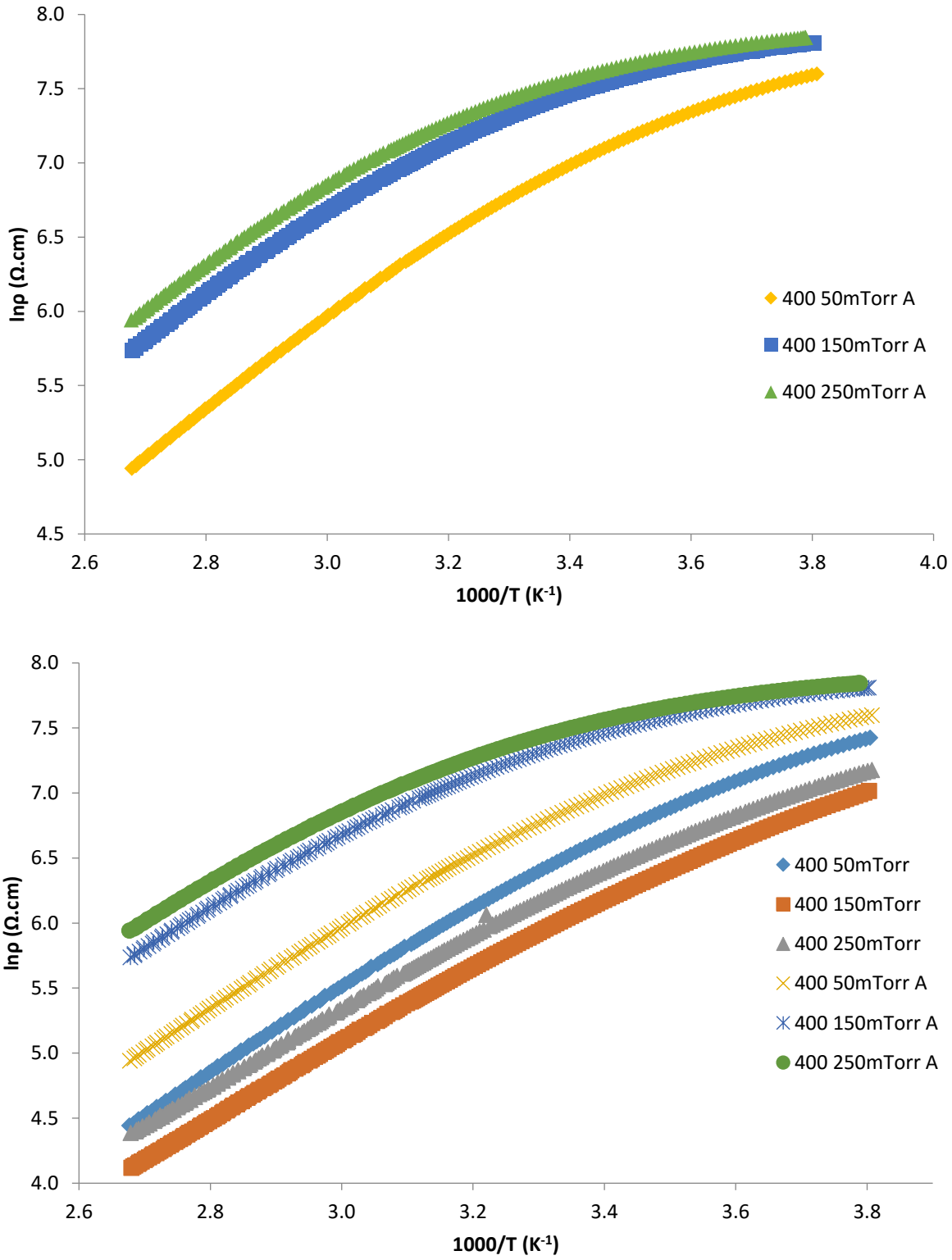

Figure 6.26. lnρ vs. reciprocal temperature of as deposited and annealed films produced at 400°C substrate temperature and varying oxygen pressures

Table 6.6. Thermistor characteristics measured and calculated electrical parameters of the annealed films

Substrate Temperature (°C)	O_2 Pressure (mTorr)	25°C Resistivity (Ω.cm)	85°C Resistivity (Ω.cm)	Thermistor constant β Value (K)	Activation Energy (eV)
400	50	1.14E+03	2.36E+02	2796.84	0.2410
400	150	1.74E+03	4.67E+02	2343.97	0.2020
400	250	1.81E+03	5.42E+02	2142.62	0.1846

As already discussed on page 170, there is a decrease in the β value which suggests that there is a decrease in the thermistors sensitivity. Also the activation energies decrease with an increase of oxygen pressure. These values appear to be similar to their as deposited counterparts with bigger changes being made to the films actual resistivity.

6.3.7 Discussion and Comparison of the Annealed Films with As – Deposited Films Produced at 400°C

What must be noted before this comparison is that the annealed films were not the as deposited films that are discussed in this chapter and then under gone ex situ annealing. Rather they are duplicate films that have been produced using the same conditions as the as deposited films and then undergone annealing.

Annealing has led to an increase in all the film's resistivity produced at the different O_2 pressures, with a big difference being observed in the films produced at 150 and 250 mTorr. This film's resistivity increased so much that it became more resistive than the 50 mTorr film which in the as deposited comparison had the highest resistivity. These big changes in resistivity are suggesting that there are changes in the films crystallinity and oxygen content following annealing which are having an effect on the films resistivity.

There is the continued trend of with an increase of O_2 pressure there is a decrease in the β value and activation energy, regardless of annealing.

This is confirmed when comparing the XRD patterns with each other, annealing led to an increase in the number of NMO peaks that were observed along with an increase in their intensity. The spinel crystallinity therefore has increased following annealing, however what was also noticed was an increase in the Mn_2O_3 secondary phase which was not as prominent in the 250 mTorr annealed film. The film produced at 250 mTorr had the highest resistivity following annealing which suggest that the influence of the Mn_2O_3 secondary phase observed in the other films may cause their resistivity to be not as great as this film.

The microstructure of the films shows that following annealing the intergranular grain cracks are larger in comparison to the as deposited films. However, it should be noted as these are replica films, it is not known whether these cracks were there before annealing. This is likely to decrease the conductivity of the films in comparison to a film with a denser structure as electron hopping will be easier achieved.

6.4 Characterisation of As – Deposited NMO Films Produced at 550°C

6.4.1 Optical Microscopy

The optical microscopy images show the films deposited on the commercial alumina substrates are shown in Figure. 6.27 and it can be seen that the surfaces are quite dull suggesting that the films are quite rough. Despite their roughness there doesn't appear to be any scratches or defects so changes in the analysis of the films are not due to the films getting damaged. Changes are therefore due to a change in the substrate temperature and oxygen pressure during deposition.

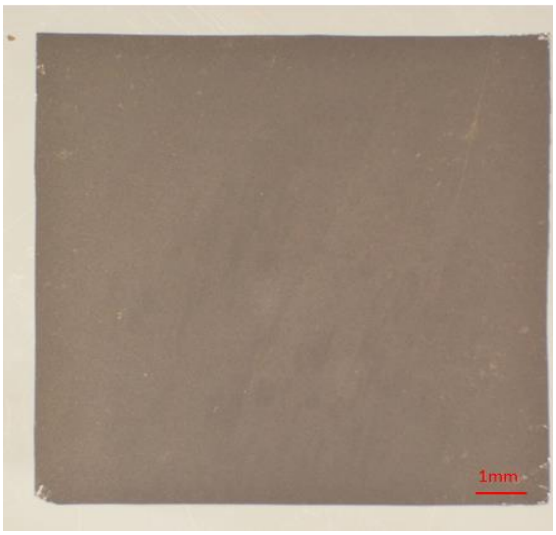

550°C 50 mTorr

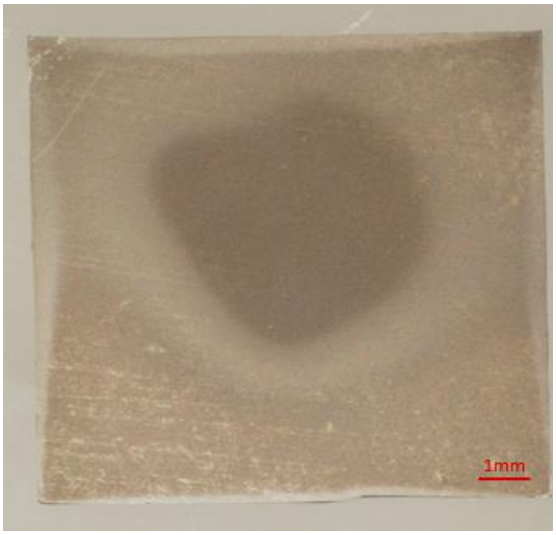

550°C 150 mTorr

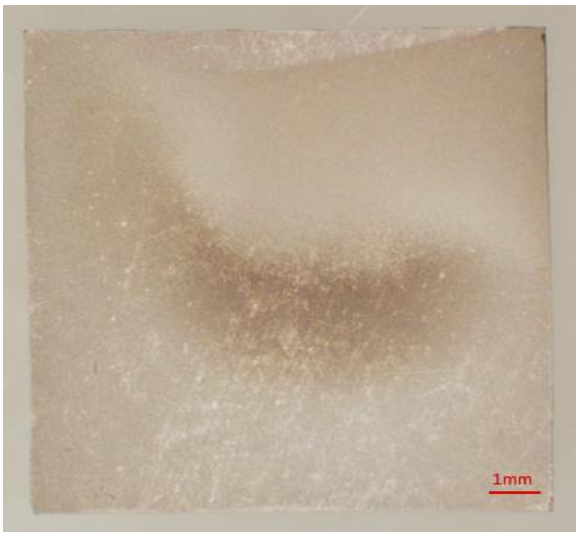

550°C 250 mTorr

Figure 6.27. Optical microscopy images of films produced on alumina substrates at 550°C substrate temperature and O_2 pressures of 50 mTorr, 150 mTorr and 250 mTorr

On the films produced at 150 and 250 mTorr there appears to be darker areas in the centre of the films. This was due to the position of the plasma plume, where the film appears darker it's thickness will be greater. The darker area indicates that this is where the centre of the plume was located during deposition. This is not seen in the films produced at 50 mTorr and is not seen as predominately in the films produced at 250 mTorr, suggesting that the shape of the plume changes with a change of the oxygen pressure in the chamber.

6.4.2 XRD Results

Figure 6.28 illustrates the XRD patterns of the NMO thin films produced at a growth temperature of 550°C and with increasing oxygen pressure. The XRD pattern from the NMO target has also been included for reference. All of the observed peaks could be attributed to either NMO or the alumina substrate which were in agreement with the reference spectra obtained from the JCPDS database, which allowed for unequivocal identification (Al_2O_3 PDF no. 01-073-1512 and NMO PDF no. 01-071-0852). A few peaks were also attributed to a secondary phase identified as Mn_2O_3 (indicated by a '□' in the XRD traces) (Mn_2O_4 PDF no. 01-089-2809). The XRD data for the thin films and target material was analysed using Eva software with the background subtracted using this software.

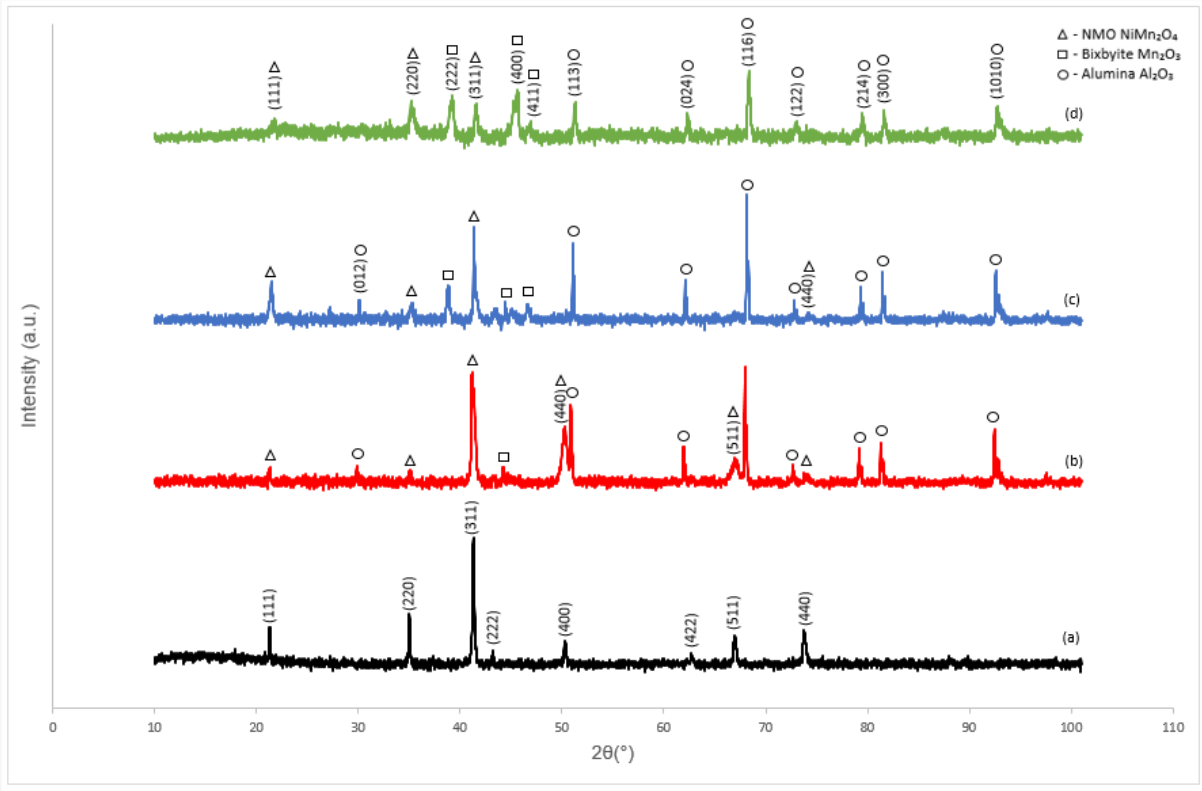

Figure 6.28. XRD patterns with a Co source of NMO films grown at 550°C (a) NMO target, (b) 50 mTorr, (c) 150 mTorr and (d) 250 mTorr

An indication of texture is also observed in the films grown at 550°C as there is a significant change in the XRD patterns of the film in comparison to the target material. With the films grown at 550°C their crystallinity followed a different pattern to the films grown at 400°C. With an increase of oxygen pressure there is a decrease in the number of NMO peaks observed, along with a decrease in their intensity. Crystallinity of these films has therefore decreased with an increase of oxygen pressure. Further evidence of a decrease in their crystallinity are the broadening of the NMO peaks with an increase of oxygen pressure which also means grain size is likely to be smaller and an indication of an onset of tetragonal distortion, which is typical of more manganese rich spinels [3]. Similar to the films grown at 400°C only one clear NMO peak at around 21° is observed, which has been indexed as the (111) reflection. The main NMO peak at 41° could be overlaid by the Al_2O_3 peak which is also around 41°. An increase in the number of the secondary phase Mn_2O_3 peaks is observed along with an increase in their intensities with an increase of O_2 pressure. This secondary phase is likely to have an effect on the Mn^{3+} and Mn^{4+} ratio in the octahedral sites of the spinel.

6.4.3 Surface Microstructure

The SEM micrographs in Figure 6.29 – 6.31 show the microstructure of the NMO films grown at 550°C and at pressures between 50 – 250 mTorr. An obvious difference seen in the 550°C films in comparison to the 400°C films (Figure.6.3 – 6.5) is their adoption of a more crystalline appearance. Further increase of oxygen pressure to 250 mTorr shows a possible decrease in the number of pores and a much smoother, denser surface structure compared to the films deposited at 400°C.

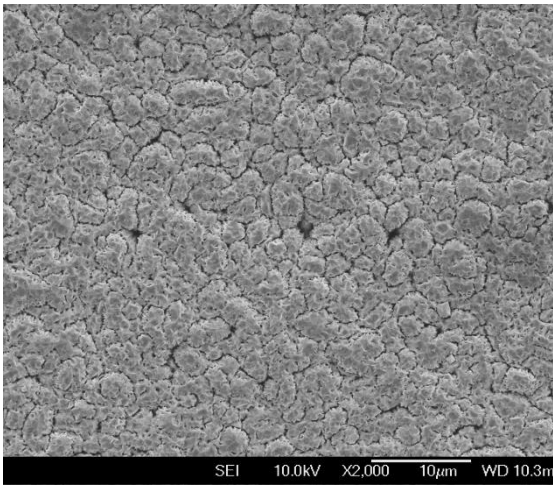

550°C 50 mTorr

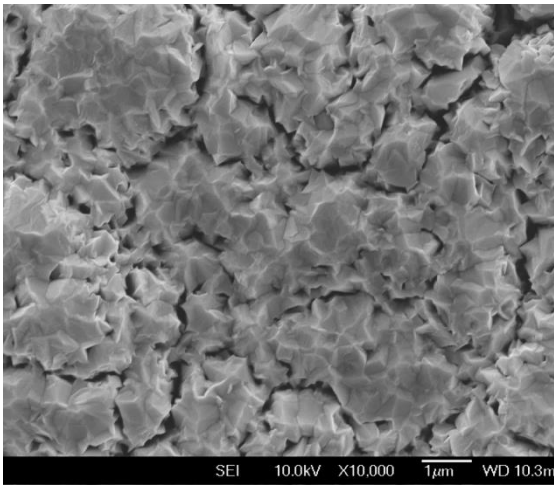

550°C 50 mTorr

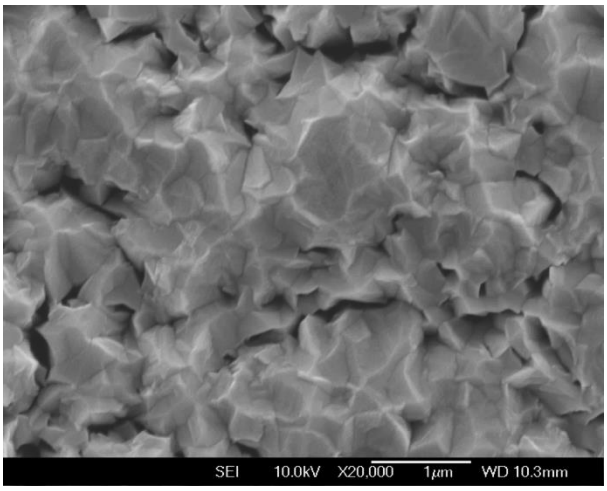

550°C 50 mTorr

Figure 6.29. SEM surface microstructure of NMO film produced at 550°C and 50 mTorr (Jeol 7000F)

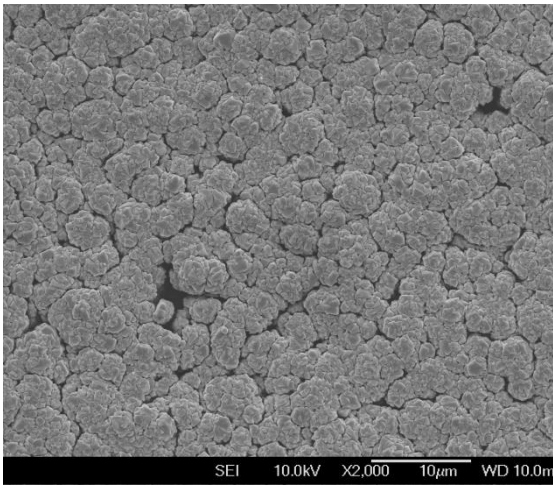

550°C 150 mTorr

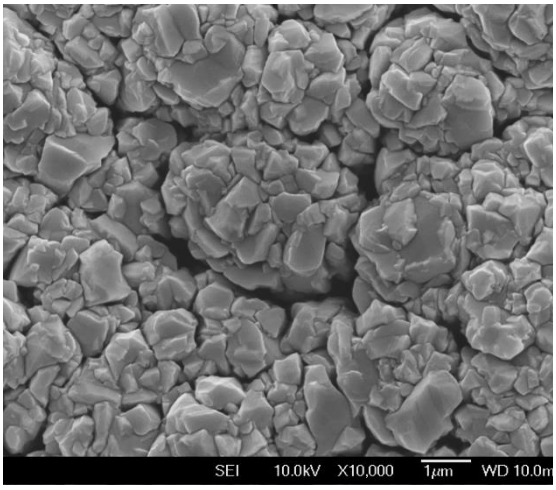

550°C 150 mTorr

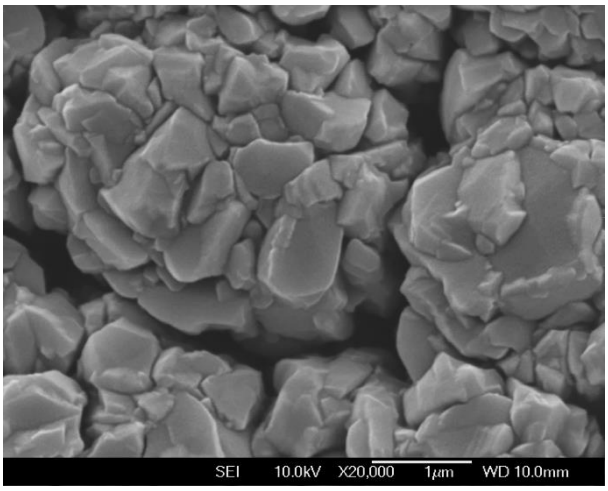

550°C 150 mTorr

Figure 6.30. SEM surface microstructure of NMO film produced at 550°C and 150 mTorr (Jeol 7000F)

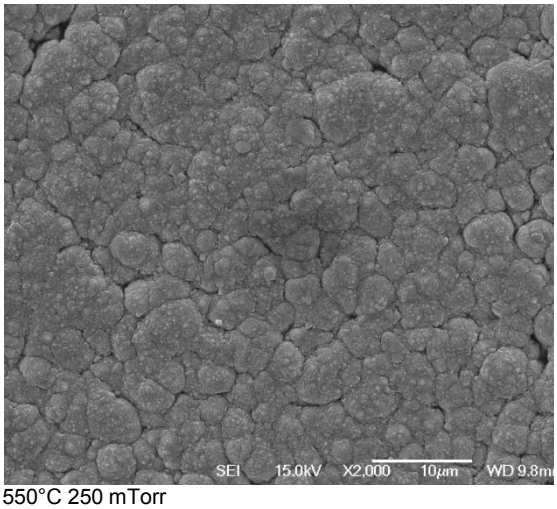

550°C 250 mTorr

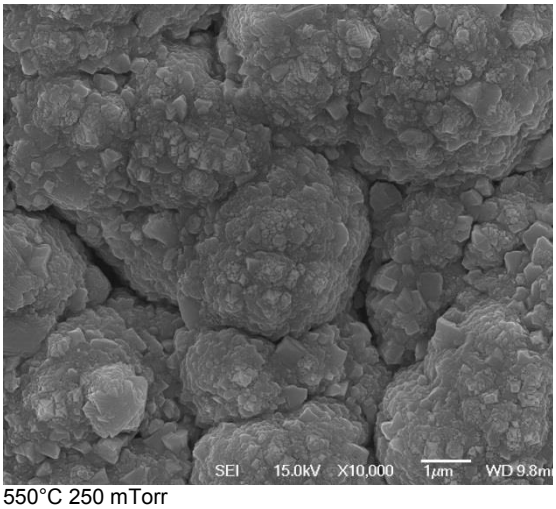

550°C 250 mTorr

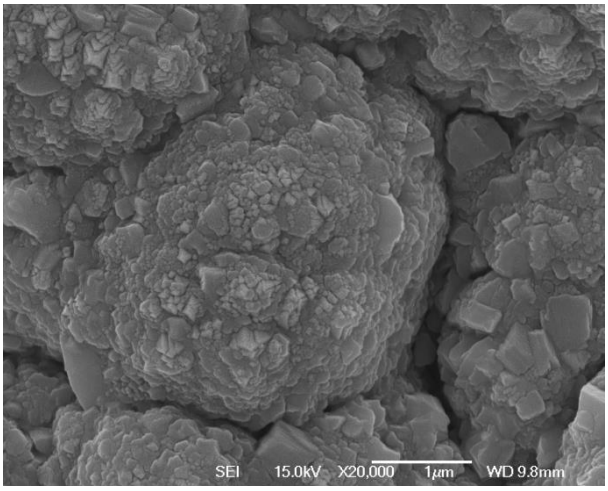

550°C 250 mTorr x 20,000

Figure 6.31. SEM surface microstructure of NMO film produced at 550°C and 250 mTorr (Jeol 7000F)

The surface morphology is different for each of the films as the O_2 pressure is increased. The films produced at 50 mTorr appear to have much larger grain sizes in comparison to the films produced at higher pressures. Films appear to be most crystalline at 150 mTorr, less at 50 mTorr and this appearance seems to diminish with a further increase to 250 mTorr. In comparison to the films produced at a deposition temperature of 400°C where their morphology's appear to be similar despite increase in O_2 pressure, big changes are observed in the 550°C deposited films. The increase of O_2 pressure has more of an effect on the appearance of the films at a deposition temperature of 550°C.

6.4.4 Resistance Measurements

Figure 6.32 shows the resistance versus temperature characteristics of the NMO films, a marked decrease in resistance is observed with an increase in temperature confirming the films have NTC characteristics. The resistance in the films produced at 550°C seem to be quite similar in comparison to each other therefore a better comparison may be made with the calculation of their resistivity with the film's thickness determined.

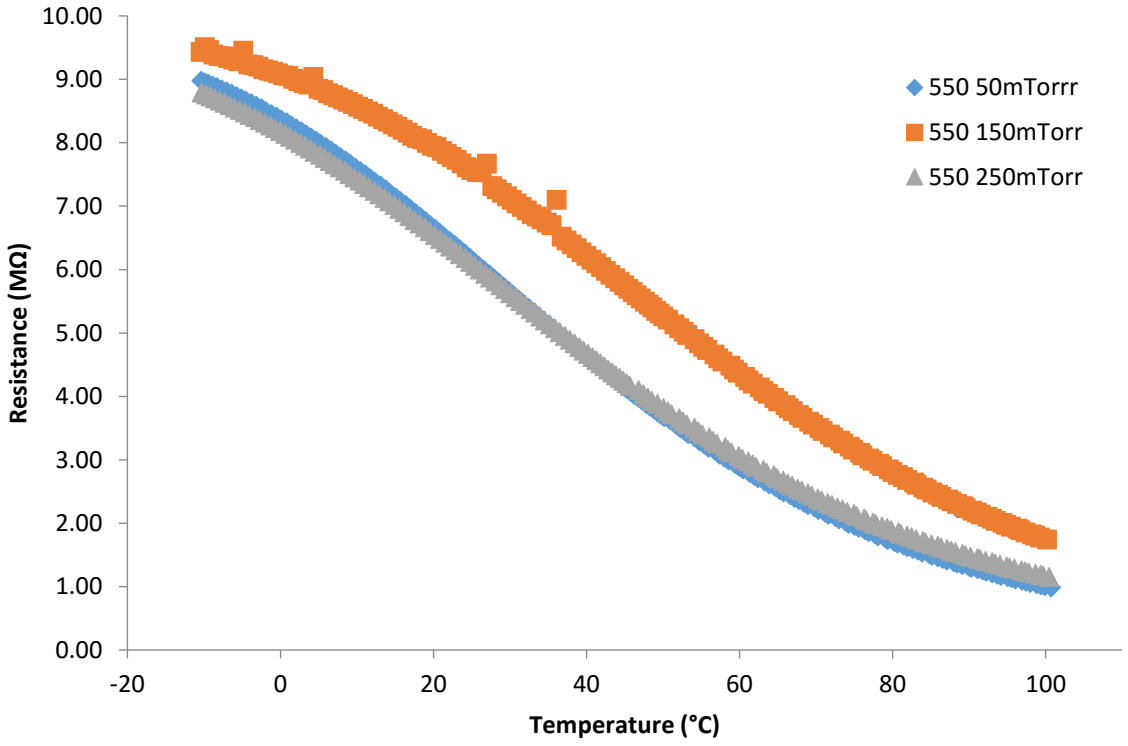

Figure 6.32. Resistance vs. Temperature graph of films grown at 550°C with O_2 pressures of 50, 150 and 250mTorr.

Table 6.7. Resistance measurements of as deposited films at 550°C substrate temperature and different O_2 pressure deposition conditions

	Resistance measurement temperature	
O_2 pressure (mTorr)	**25°C**	**85°C**
50	6.12×10^6 Ω	1.49×10^5 Ω
150	7.57×10^6 Ω	2.49×10^5 Ω
250	6.06×10^6 Ω	1.67×10^5 Ω

When compared to the films at 400°C the resistance appears to be greater for the films deposited at 550°C when measured at higher and lower temperatures.

6.4.5 Film Cross Sections by SEM

In these films grown at 550°C substrate temperature, there is an increase in the amount of cracking suggesting that these films are less dense in comparison to the films deposited at 400°C. The NMO films however still follow the substrate pattern well.

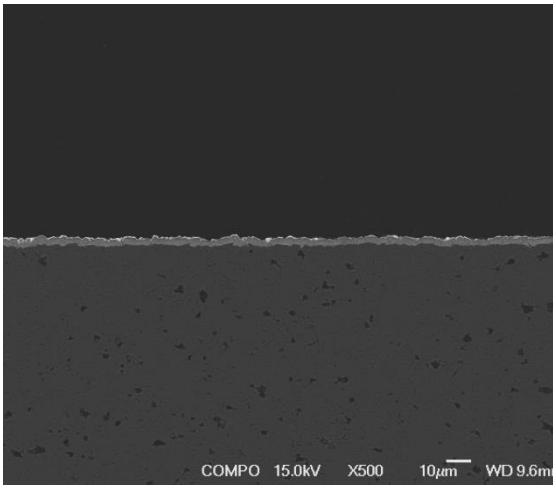

550°C 50 mTorr

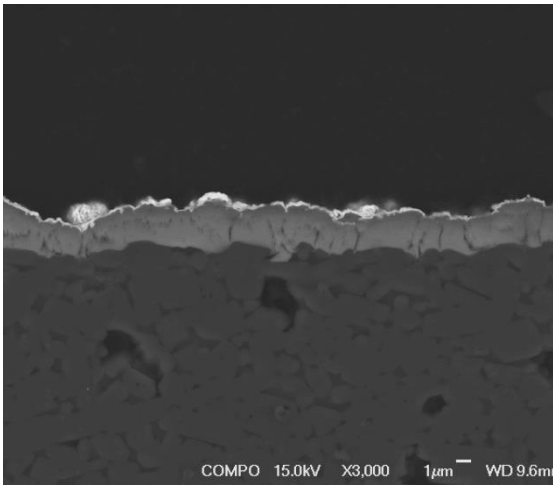

550°C 50 mTorr

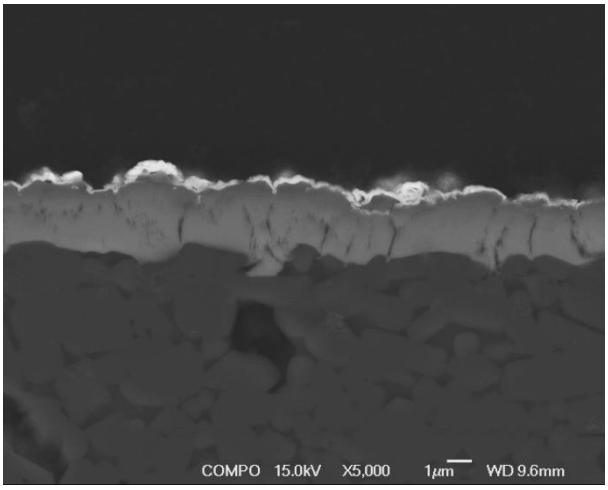

550°C 50 mTorr

Figure 6.33. SEM Micrograph cross section of NMO films grown at 550°C and 50 mTorr O_2 (Jeol 7000F)

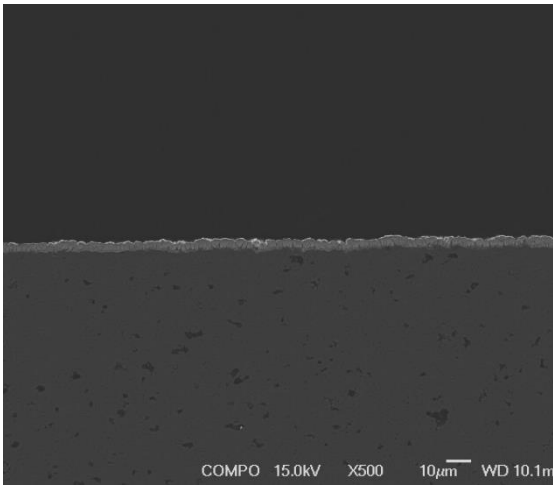

550°C 150 mTorr

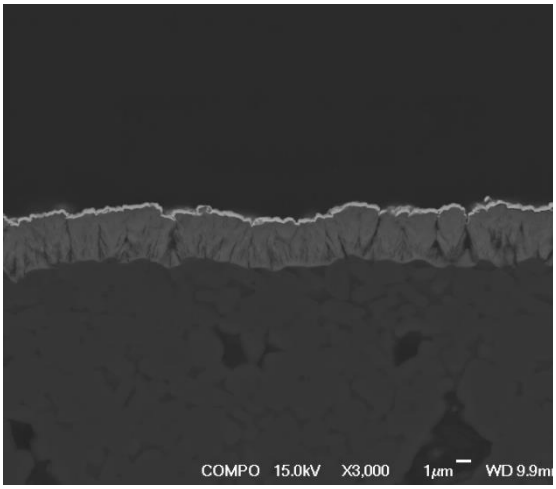

550°C 150 mTorr

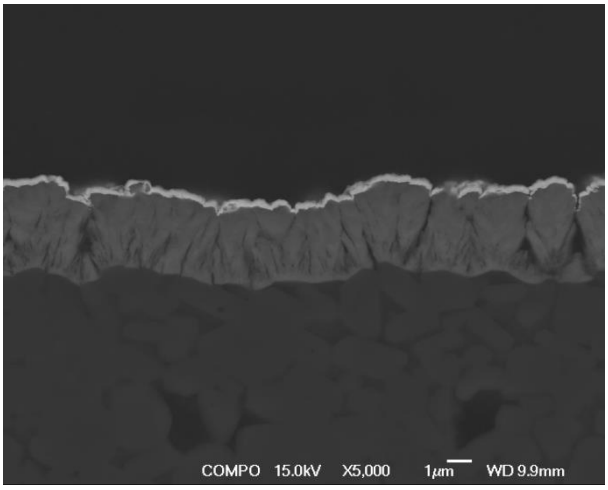

550°C 150 mTorr

Figure 6.34. SEM Micrograph cross section of NMO films grown at 550°C and 150 mTorr O_2 (Jeol 7000F)

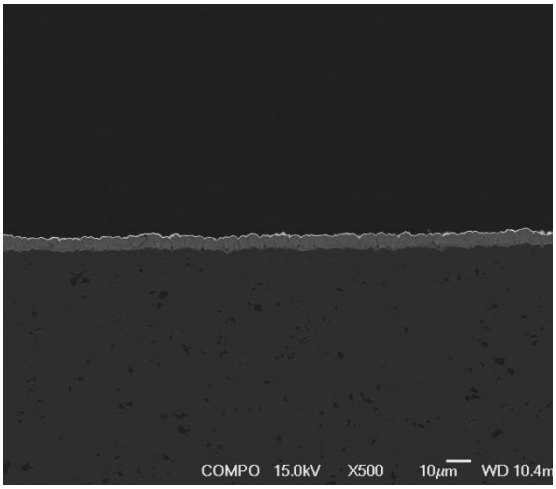

550°C 250 mTorr

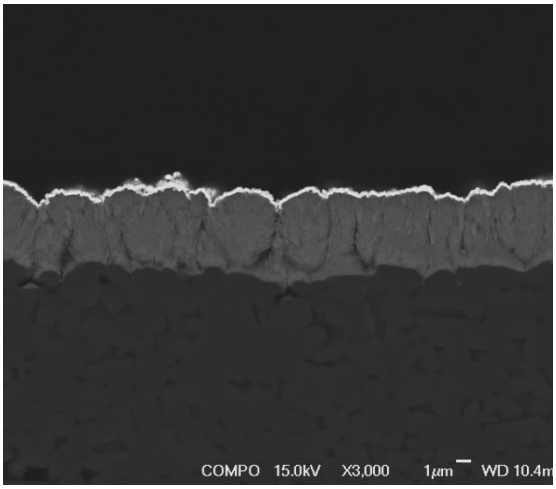

550°C 250 mTorr

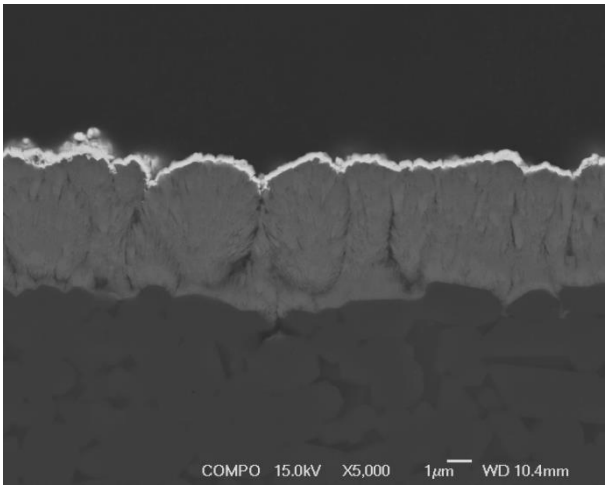

550°C 250 mTorr

Figure 6.35. SEM Micrograph cross section of NMO films grown at 550°C and 250 mTorr O_2 (Jeol 7000F)

6.4.6 Film Thickness Measurements

An increase of O_2 pressure during deposition at 250 mTorr led to an increase in the films thickness in comparison to the films produced at a lower pressure.

Table 6.8. Average film thickness determination for films produced at 550°C and increasing O_2 pressure

550°C 50mTorr As – Deposited					
Measurement Position	1	2	3	4	5
Thickness	2.33	2.13	2.00	2.07	1.93
Mean (μm)	2.09 ± 0.14				

550°C 150mTorr As – Deposited					
Measurement Position	1	2	3	4	5
Thickness	2.00	1.53	1.53	1.33	1.87
Mean (μm)	1.65 ± 0.33				

550°C 250mTorr As – Deposited					
Measurement Position	1	2	3	4	5
Thickness	3.07	3.00	3.00	3.00	2.87
Mean (μm)	2.98 ± 0.07				

6.4.7 Resistivity

The ln resistivity of all the films decreased linearly with increasing temperature, confirming that the films have NTC characteristics. The resistivity increases with an increase of O_2 pressure which may be due to a change in the Mn valence states and / or the available oxygen vacancies. A change in the inversion parameter may also be a reason.

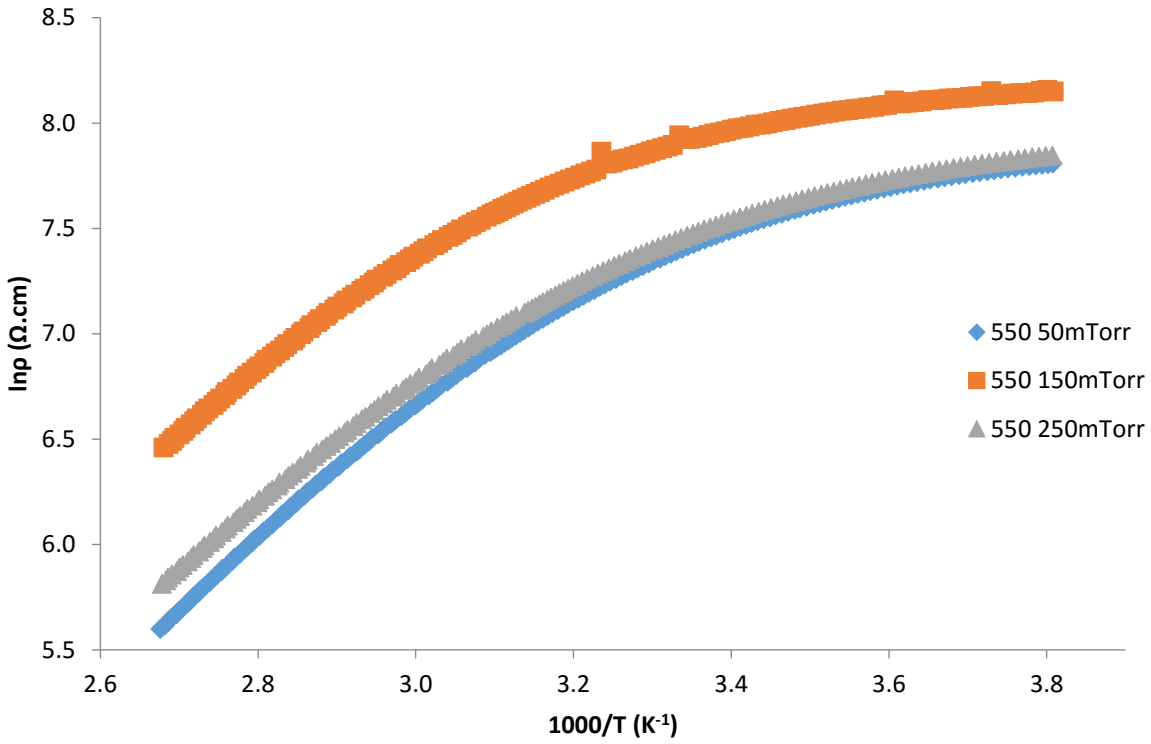

Figure 6.36. lnρ vs. reciprocal temperature of as deposited films produced at 550 °C substrate temperature and varying oxygen pressures

With an increase of oxygen pressure an increase in the β value is noticed suggesting the thermistor's sensitivity decreases as seen in Table 6.9. The activation energy is the energy required for the hopping process from a cation M^{n+} to $M^{(n+1)}$ on the octahedral sites. Conduction in the material at low temperature is due to the hopping of electrons between the Mn^{3+} and Mn^{4+} ions while at higher temperatures it is due to polaron hopping [5]. The activation energies increase with an increase of oxygen pressure and resistivity.

Table 6.9. Thermistor measured and calculated electrical parameters

Substrate Temperature (°C)	O_2 Pressure (mTorr)	25°C Resistivity (Ω.cm)	85°C Resistivity (Ω.cm)	Thermistor constant β Value (K)	Activation Energy (eV)
550	50	1.60E+03	3.39E+02	2761.59	0.2380
550	150	2.50E+03	8.25E+02	1910.38	0.1646
550	250	1.10E+03	1.58E+02	2653.31	0.2286

The resistivity of the 550°C as deposited films are higher than the films produced at 400°C, the β values and activation energies of all the as deposited films are however similar in value.

6.4.8 Discussion and Comparison of the As – Deposited Films Produced at 400°C with the As – Deposited Films Produced at 550°C

The higher deposition temperature of 550°C has resulted in a higher resistivity value in comparison to the films grown at 400°C. The β values and activation energies in the films produced at 550°C and 150 mTorr are lower than those produced at 50 and 250 mTorr which is contrast to those produced at 400°C, where there is a decrease in these values with an increase of O_2 pressure. Therefore, no trend is noticed in these parameters in contrast to the 400°C films The order of the most resistive is different for the films produced at 550°C with the film produced at 150 mTorr O_2 being the most resistive and 50 mTorr being the least while the opposite is seen in the films produced at 400°C.

Optical microscopy shows instantly that there is difference in the films in how they have been produced as a dark spot can be seen in the 550°C films at 150 and 250 mTorr. These dark spots suggest there has been a change in the shape of the plume during deposition which has caused these areas to be thicker in comparison to the rest of the film.

There is also a difference in the XRD patterns where the NMO spinel intensity increases with an increase of O_2 pressure in the 400°C and decreases in the 550°C films. There is also a decrease of the Mn_2O_3 secondary phase with an increase of O_2 pressure while the opposite is seen in the 550°C films. There appears to be no link with crystallinity and the amount of Mn_2O_3 secondary phase when compared with the 550°C films produced at 50 and 250 mTorr being similar in resistivity and their difference in XRD patterns.

When compared under SEM however there does appear to be big differences in the films appearance, as the films produced at 550°C appear to have more predominate cracks. This may

explain why the films are more resistive in comparison to their 400°C counterparts, as a denser film will be more conductive. The increase in cracking in observed in the cross sections.

6.5 Characterisation of NMO Films Produced at 550°C and Annealed

The as deposited films grown at 550°C substrate temperature were reproduced and then annealed at 800°C in an O_2 (1 atm) environment for 60 mins. These films were characterised and compared with their as deposited equivalents to determine what effect annealing had on them.

6.5.1 Optical Microscopy

The films appear to have the same appearance to the as deposited films without the darker spots where the films are thicker. It is therefore possible that the position of the substrate during deposition was not in the exact location as for the previous film deposited in the same conditions.

550°C 50 mTorr Annealed

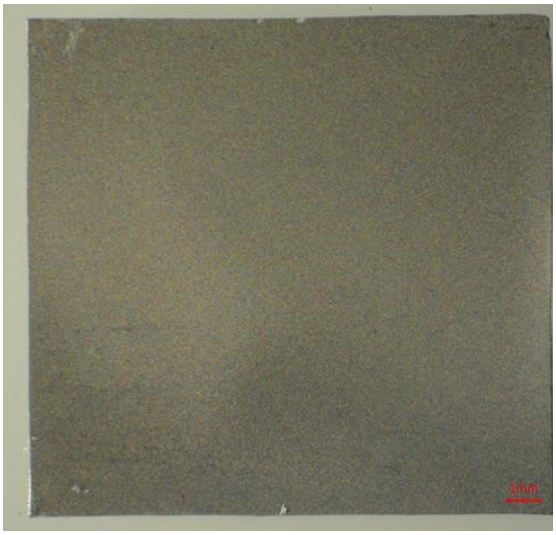

550°C 150 mTorr Annealed

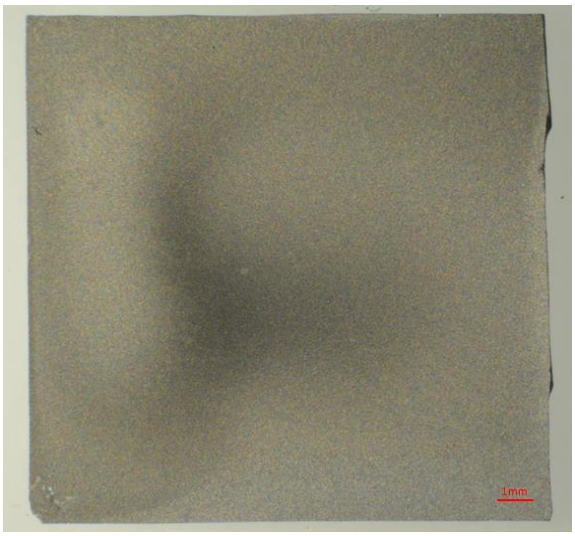

550°C 250 mTorr Annealed

Figure 6.37. Optical microscopy images of films produced on alumina substrates at 550°C substrate temperature and O_2 pressures of 50 mTorr, 150 mTorr and 250 mTorr and annealed in oxygen at 800°C for 1 hour

6.5.2 XRD Results

The annealed films were analysed using XRD and their resulting patterns are shown below along with those of the as deposited films patterns for reference. The annealed films have had the 2θ 35 - 50° magnified to allow for better comparison.

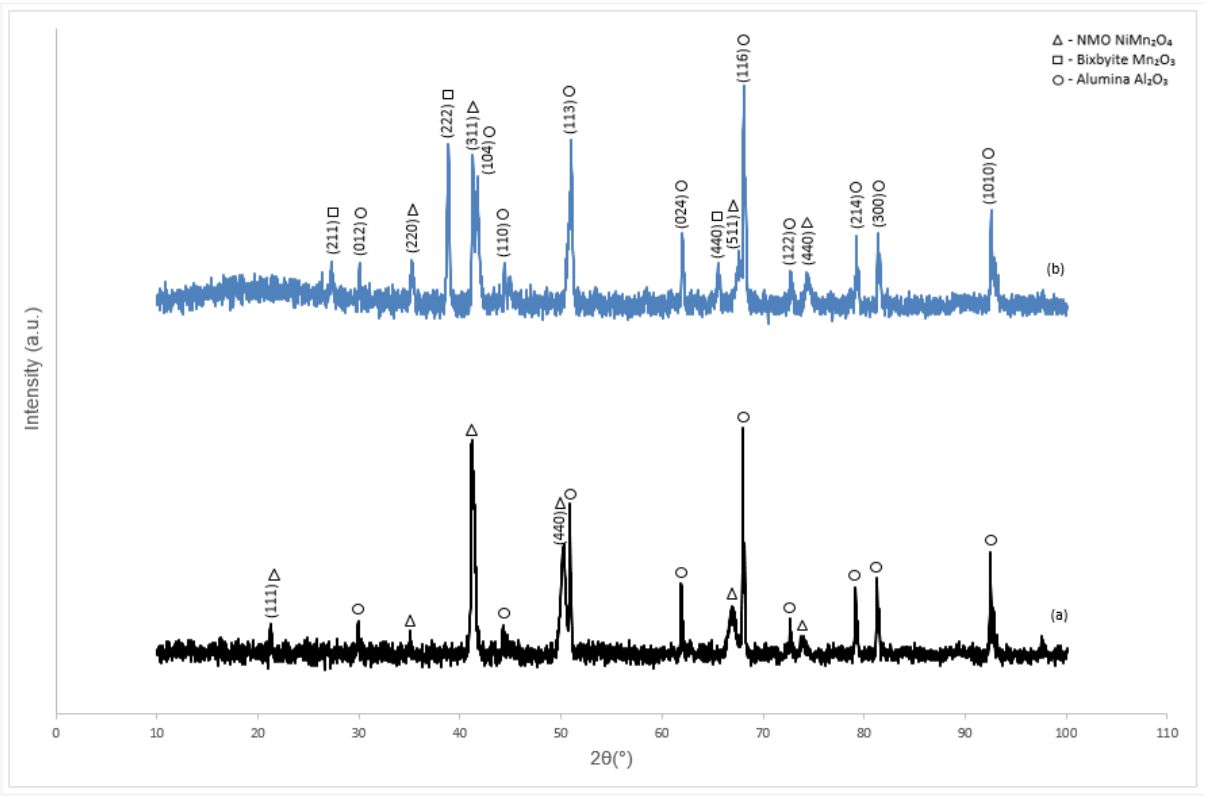

Figure 6.38. XRD patterns with a Co source of NMO films grown at 550°C (a) 50 mTorr as – deposited, (b), 50 mTorr annealed

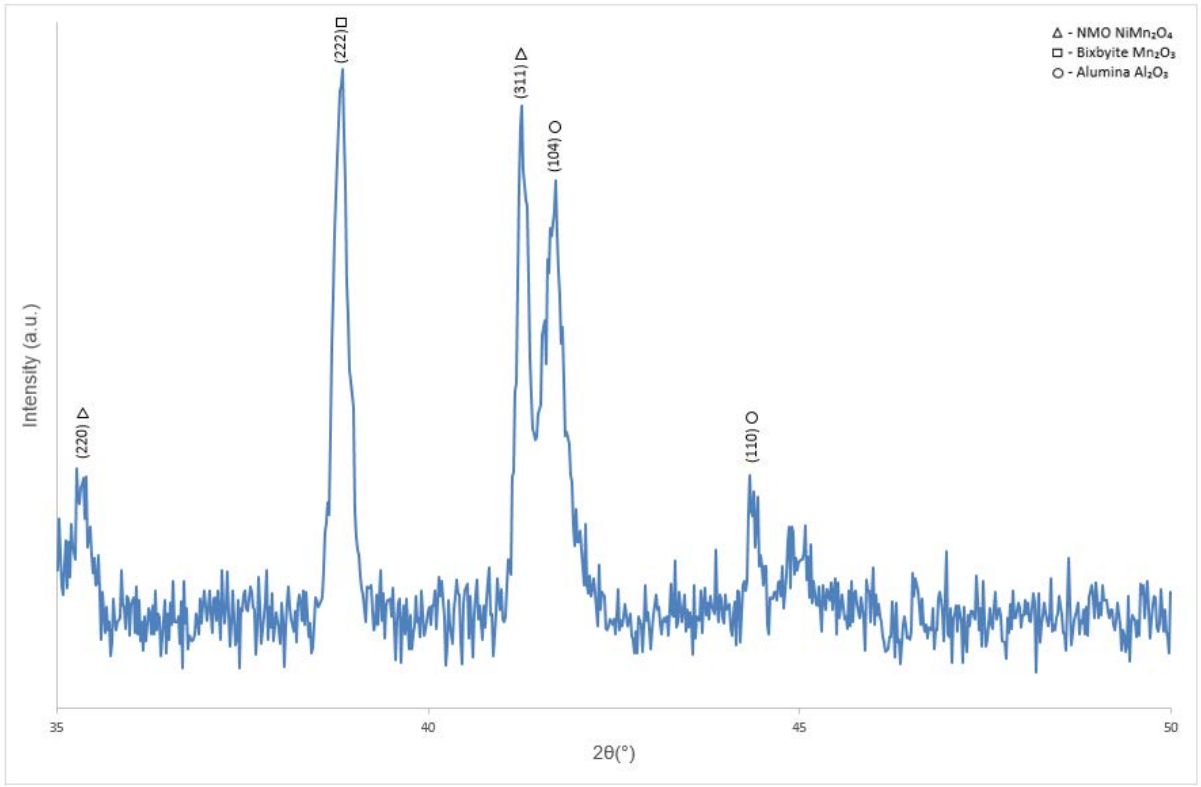

Figure 6.39. XRD patterns with a Co source of NMO films grown at 550°C 50 mTorr as annealed at 35 - 50°

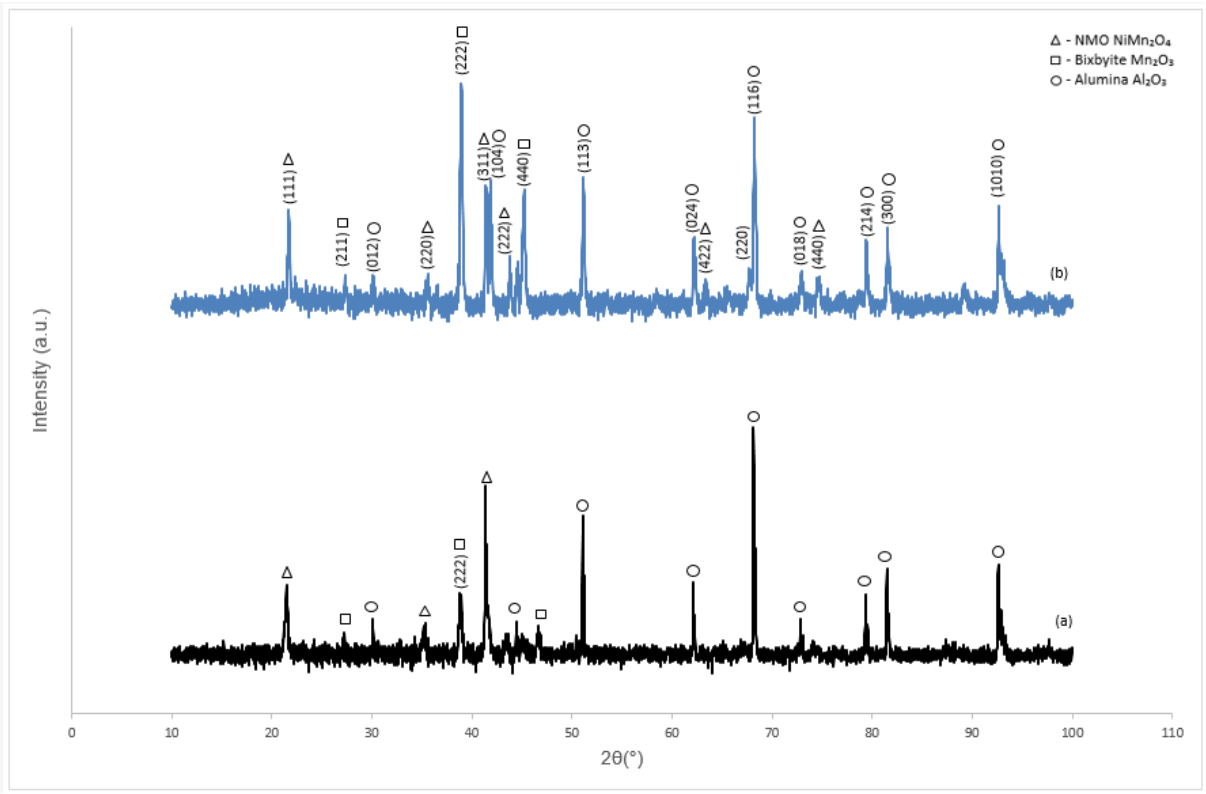

Figure 6.40. XRD patterns with a Co source of NMO films grown at 550°C (a) 150 mTorr as – deposited, (b), 150 mTorr annealed

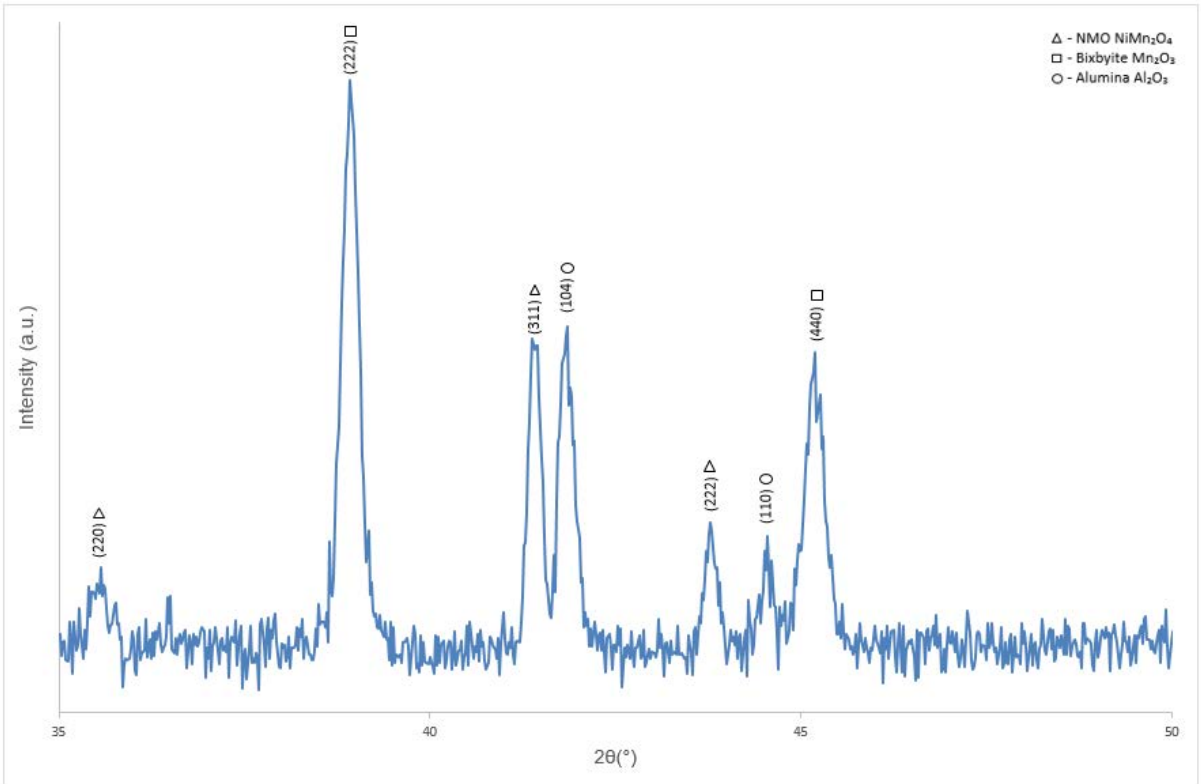

Figure 6.41. XRD patterns with a Co source of NMO films grown at 550°C 150 mTorr as annealed at 35 - 50°

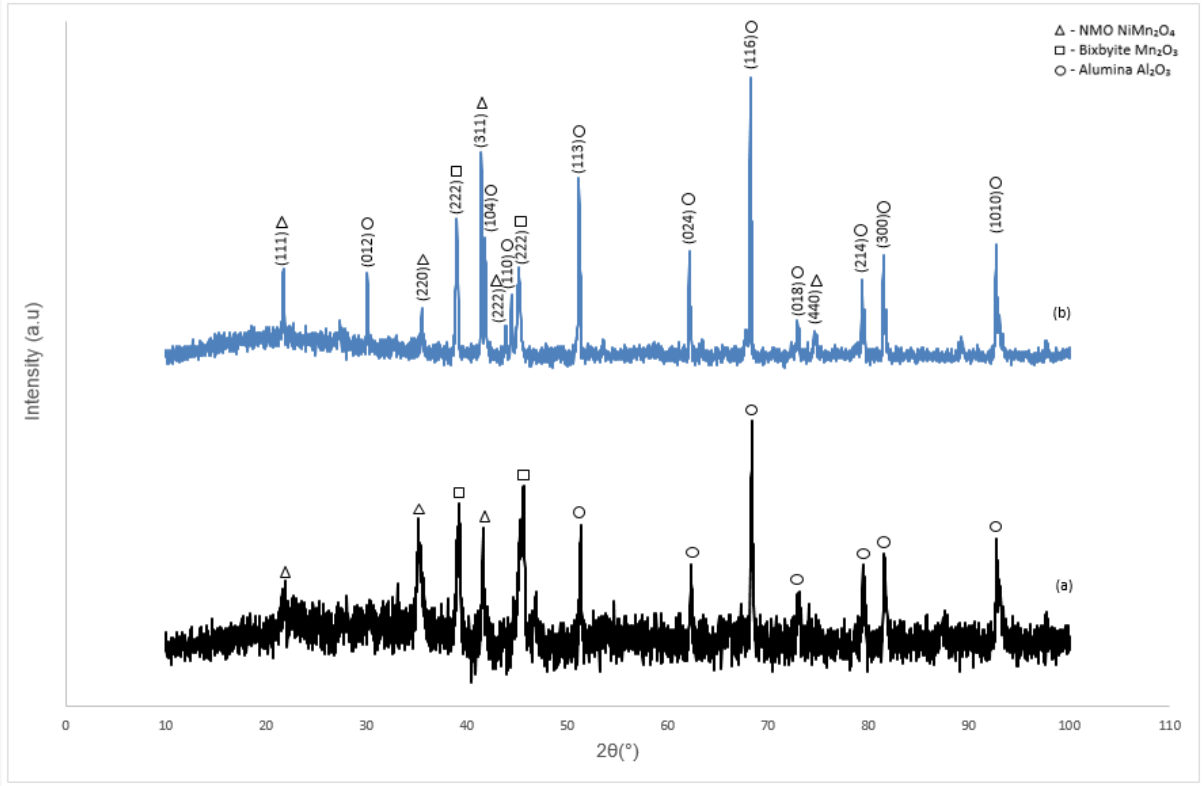

Figure 6.42. XRD patterns with a Co source of NMO films grown at 550°C (a) 250 mTorr as – deposited, (b), 250 mTorr annealed

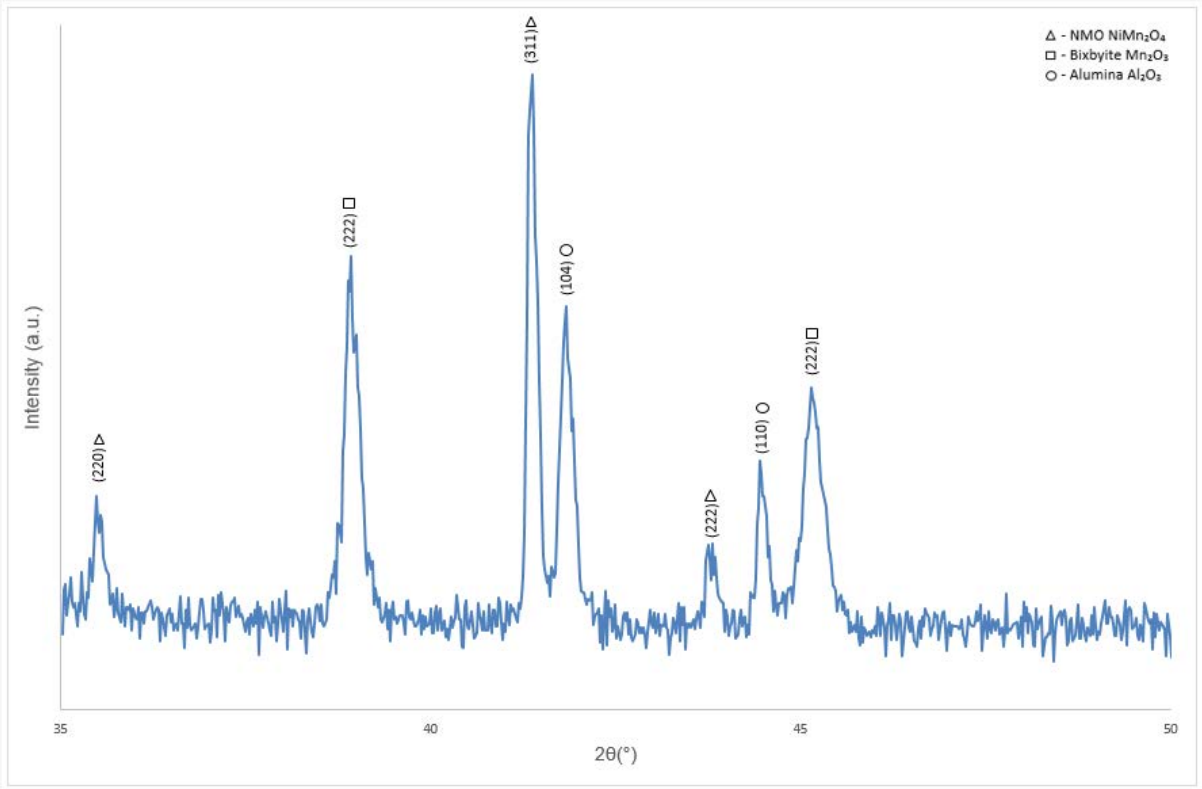

Figure 6.43. XRD patterns with a Co source of NMO films grown at 550°C 250 mTorr as annealed at 35 - 50°

The majority of the observed peaks could be attributed to either NMO or the alumina substrate which were in agreement with the reference spectra obtained from the JCPDS database, which allowed for unequivocal identification (Al_2O_3 PDF no. 01-073-1512 and NMO PDF no. 01-071-0852). A few peaks were also attributed to a secondary phase identified as Mn_2O_3 (indicated by a '□' in the XRD traces) (Mn_2O_3 PDF no. 01-089-2809). The XRD data for the thin films and target material were analysed using Eva software with the background subtracted using this software.

Annealing has had a marked effect on the patterns of the as – deposited films. Intensity of the NMO has increased, along with a change in crystallinity with an increase in the number of peaks observed. These changes in crystallinity are likely to have an effect on the electrical properties of the films. An increase in the number of peaks from the secondary phase Mn_2O_3 is also noticed along with an increase in their intensity. The increase in the secondary phase is likely to increase the films resistivity in comparison to their as – deposited counterparts as less Mn^{3+} and Mn^{4+} cation pairs will be available for conduction.

6.5.3 Surface Microstructure by SEM

Figure 6.44 – 6.46 shows the SEM micrographs of the annealed films grown at 550°C in various oxygen pressures. The effect of annealing on the films is quite obvious on the 250 mTorr film. After annealing the grains are more strongly differentiated, with many smaller grains with a cubic morphology observed, effectively causing the appearance of surface to be more rough. This may be due to increased phase separation which occurs at intermediate temperatures of ≥ 400°C according to the phase diagram described in Chapter 2 [9]. Development of surface topography after annealing is evident and the grains appear to have adopted a more crystalline, well defined appearance.

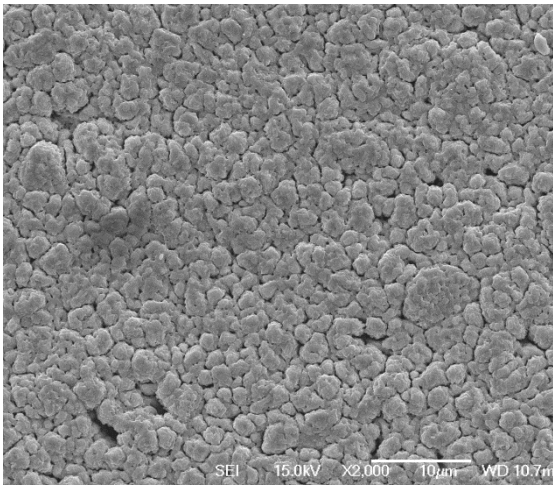

550°C 50 mTorr Annealed

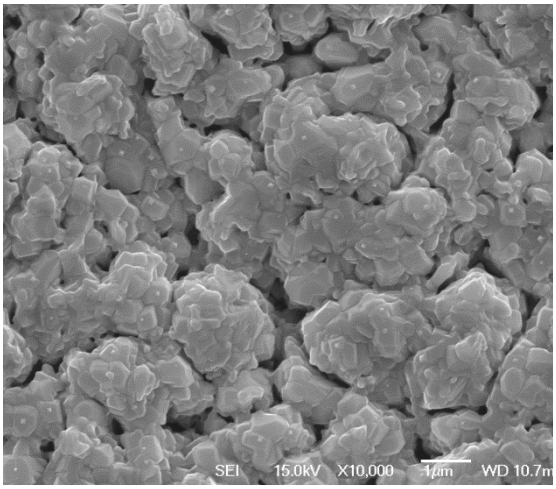

550°C 50 mTorr Annealed

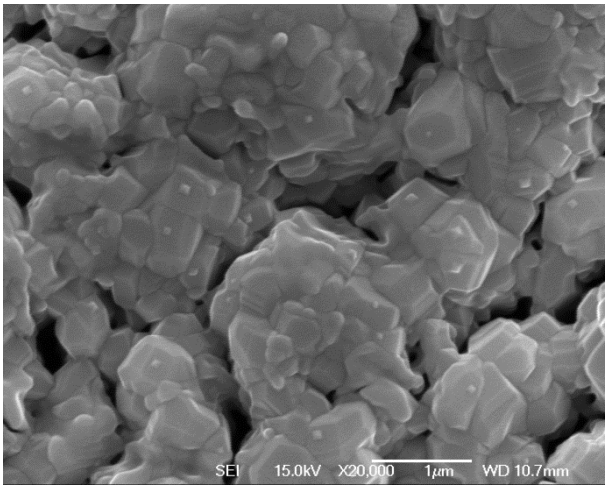

550°C 50 mTorr Annealed

Figure 6.44. SEM surface profile of annealed NMO film produced at 550°C and 50 mTorr (Jeol 7000F)

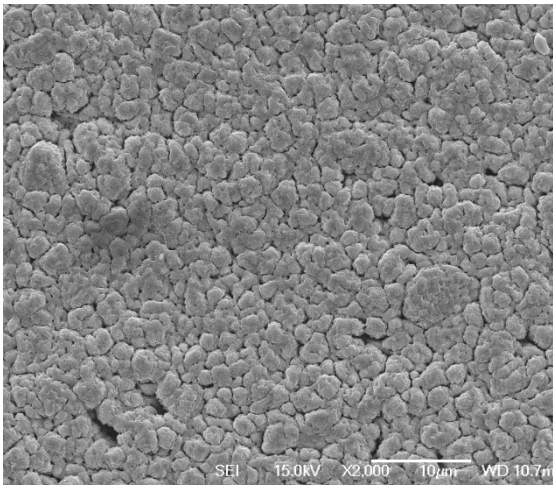

550°C 150 mTorr Annealed

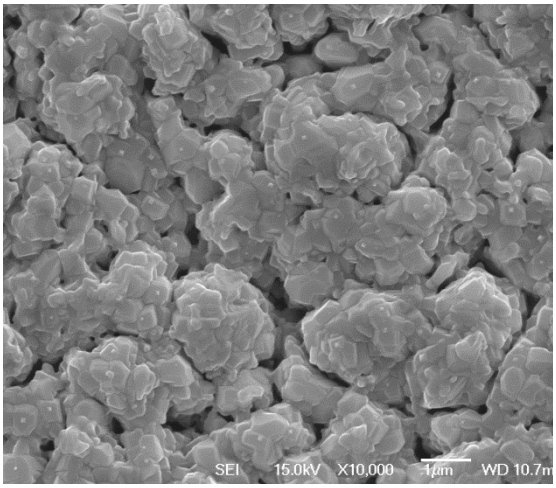

550°C 150 mTorr Annealed

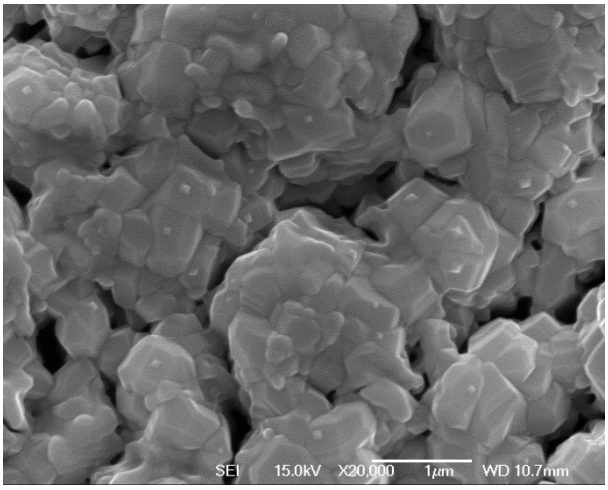

550°C 150 mTorr Annealed

Figure 6.45. SEM surface profile of annealed NMO film produced at 550°C and 150 mTorr (Jeol 7000F)

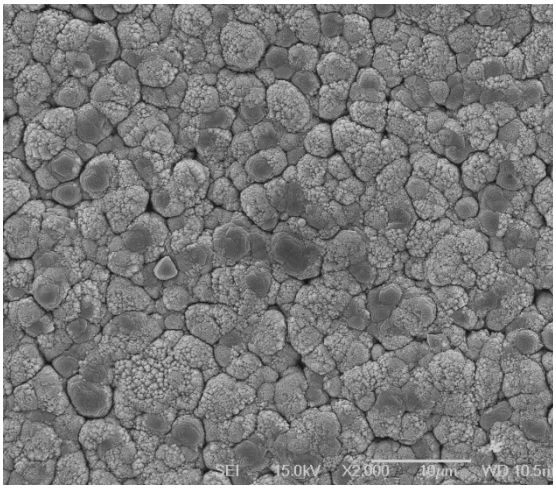

550°C 250 mTorr Annealed

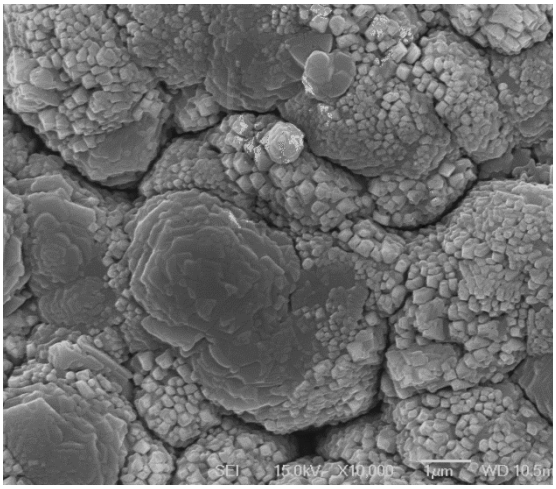

550°C 250 mTorr Annealed

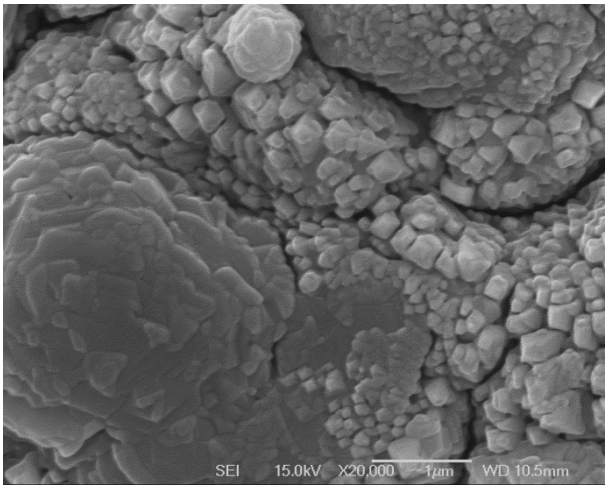

550°C 250 mTorr Annealed

Figure 6.46. SEM surface profile of annealed NMO film produced at 550°C and 250 mTorr (Jeol 7000F)

6.5.4 Resistance Measurement of Films Deposited at 550°C and Undergone Annealing

Figure 6.47 shows the resistance of the films grown at 550°C and annealed in O_2. Annealing of the films leads to similar behaviour that is observed in the as deposited film with a decrease of resistance observed for the 50 and 250 mTorr films.

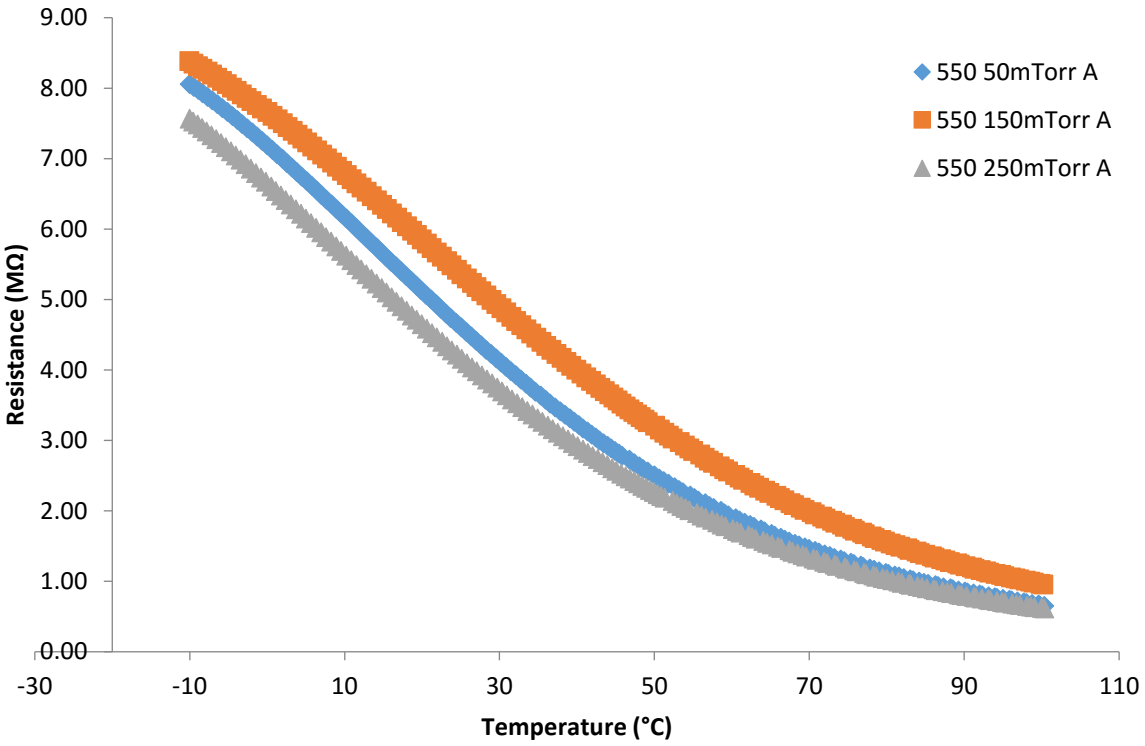

Figure 6.47. Resistance vs. Temperature graph of films grown at 550°C in oxygen pressures of 50, 150 and 250mTorr, and annealed at 800ºC for 1 hour in O_2

Table 6.10. Resistance measurements of as deposited films and annealed films at 550°C substrate temperature and different O_2 pressure deposition conditions

	As deposited		**Annealed**	
	Resistance measurement temperature		**Resistance measurement temperature**	
O_2 pressure (mTorr)	**25°C**	**85°C**	**25°C**	**85°C**
50	6.12×10^6 Ω	1.49×10^6 Ω	4.60×10^6 Ω	9.64×10^5 Ω
150	7.57×10^6 Ω	2.49×10^6 Ω	5.36×10^6 Ω	1.38×10^6 Ω
250	6.06×10^6 Ω	1.67×10^6 Ω	4.16×10^6 Ω	9.02×10^5 Ω

Following annealing the films have a lower resistance value in comparison to their as deposited counterparts. This is the opposite effect that was seen in the films produced with a 400°C deposition temperature as their resistance increases following annealing.

6.5.5 Film Cross Sections by SEM

Very little difference is observed between the annealed and the as deposited films produced. The NMO films however appear to maintain good adhesion with the alumina substrate.

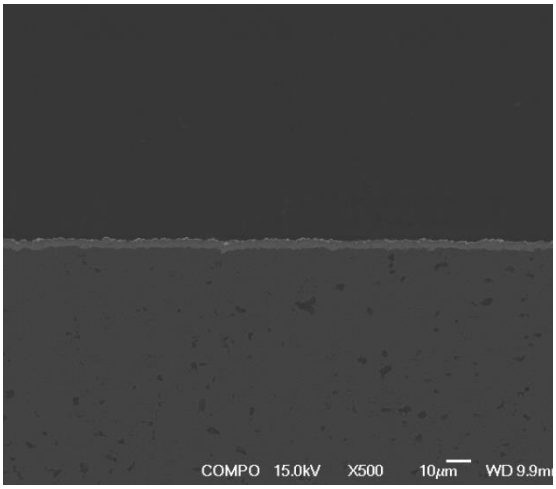

550°C 50 mTorr Annealed

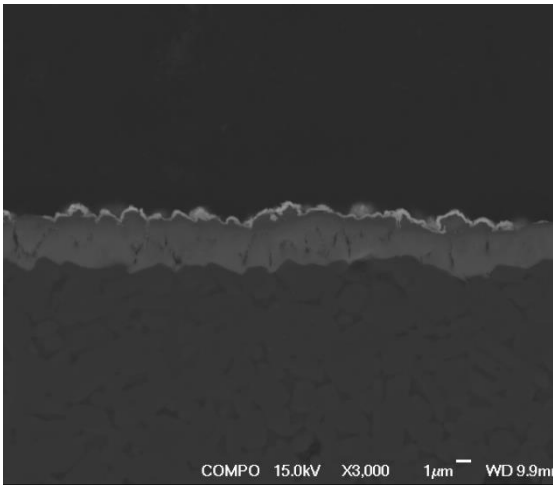

550°C 250 mTorr Annealed

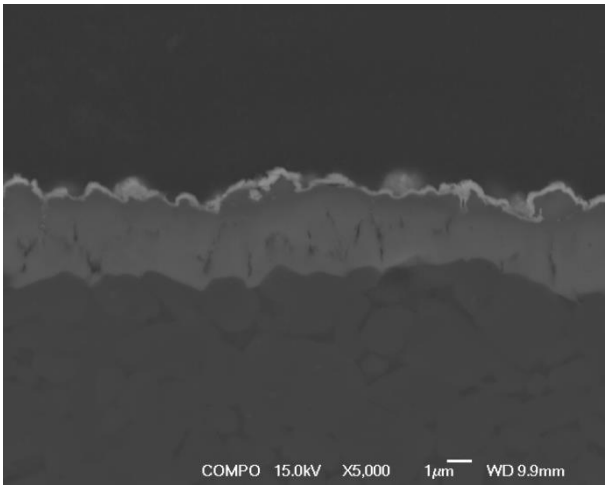

550°C 50 mTorr Annealed

Figure 6.48. SEM Micrograph cross section of NMO films grown at 550°C and 50 mTorr O_2 and annealed (Jeol 7000F)

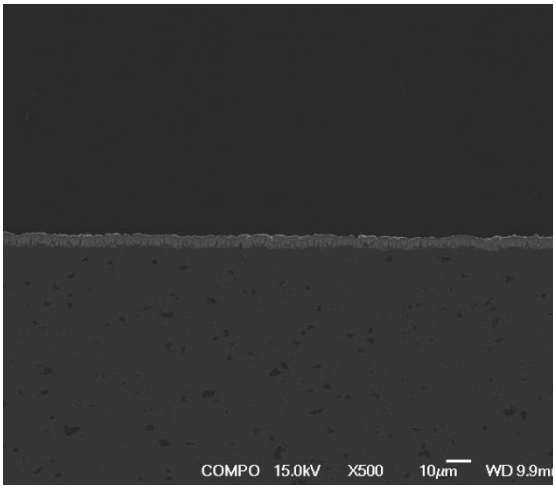

550°C 150 mTorr Annealed

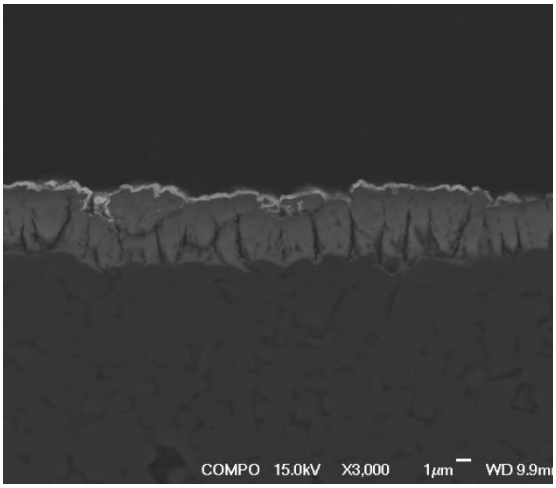

550°C 150 mTorr Annealed

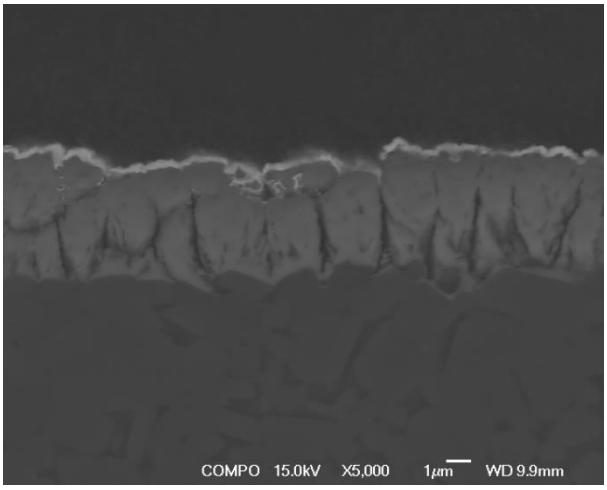

550°C 150 mTorr Annealed

Figure 6.49. SEM Micrograph cross section of NMO films grown at 550°C and 150 mTorr O_2 and annealed (Jeol 7000F)

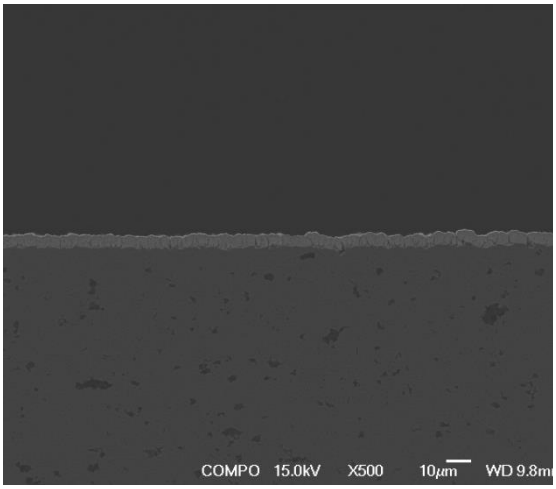

550°C 250 mTorr Annealed

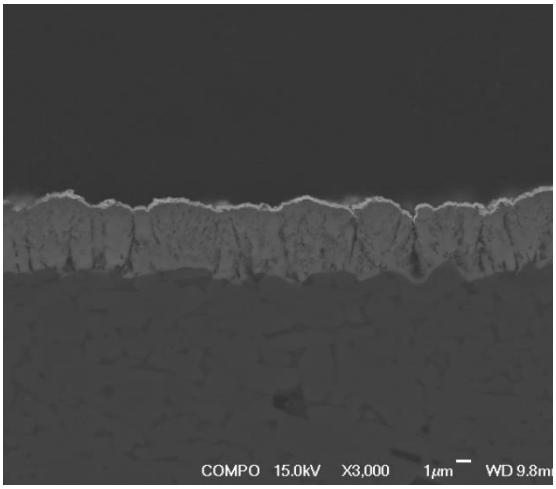

550°C 250 mTorr Annealed

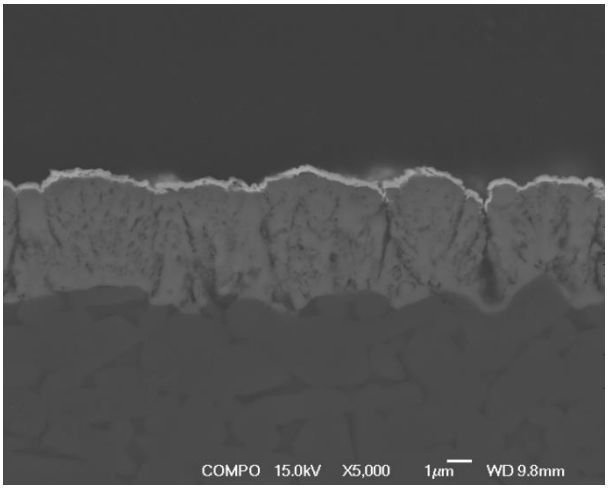

550°C 250 mTorr Annealed

Figure 6.50. SEM Micrograph cross section of NMO films grown at 550°C and 250 mTorr O_2 and annealed (Jeol 7000F)

6.5.6 Thickness Measurements

The table below shows the thickness values measured for the films produced at 550°C substrate temperature and at different O_2 pressures.

Table 6.11. Average film thickness determination for films produced at 550°C and increasing O_2 pressure and annealed in oxygen

550°C 50mTorr Annealed					
Measurement Position	1	2	3	4	5
Thickness	2.60	2.34	2.73	2.34	2.40
Mean (μm)	2.48 ± 0.16				

550°C 150mTorr Annealed					
Measurement Position	1	2	3	4	5
Thickness	1.67	2.20	2.54	2.26	2.13
Mean (μm)	2.16 ± 0.28				

550°C 250mTorr Annealed					
Measurement Position	1	2	3	4	5
Thickness	4.27	3.10	1.93	1.67	0.80
Mean (μm)	2.36 ± 1.21				

6.5.7 Resistivity

The log resistivity of all the films decreased linearly with increasing temperature, confirming that the films have NTC characteristics. The annealed films do not follow the same pattern as the as deposited films and in fact the order of their resistance switches over after annealing. Reasons for this may be because the annealed films are duplicates of the as deposited as opposed to the as deposited films themselves that have been annealed. As the films have been deposited on fairly rough substrates the film's thickness is difficult to determine. This will inevitably lead to errors and problems with reproducibility, which is seen here. Further investigation into repeatability will be discussed in Chapter 7.

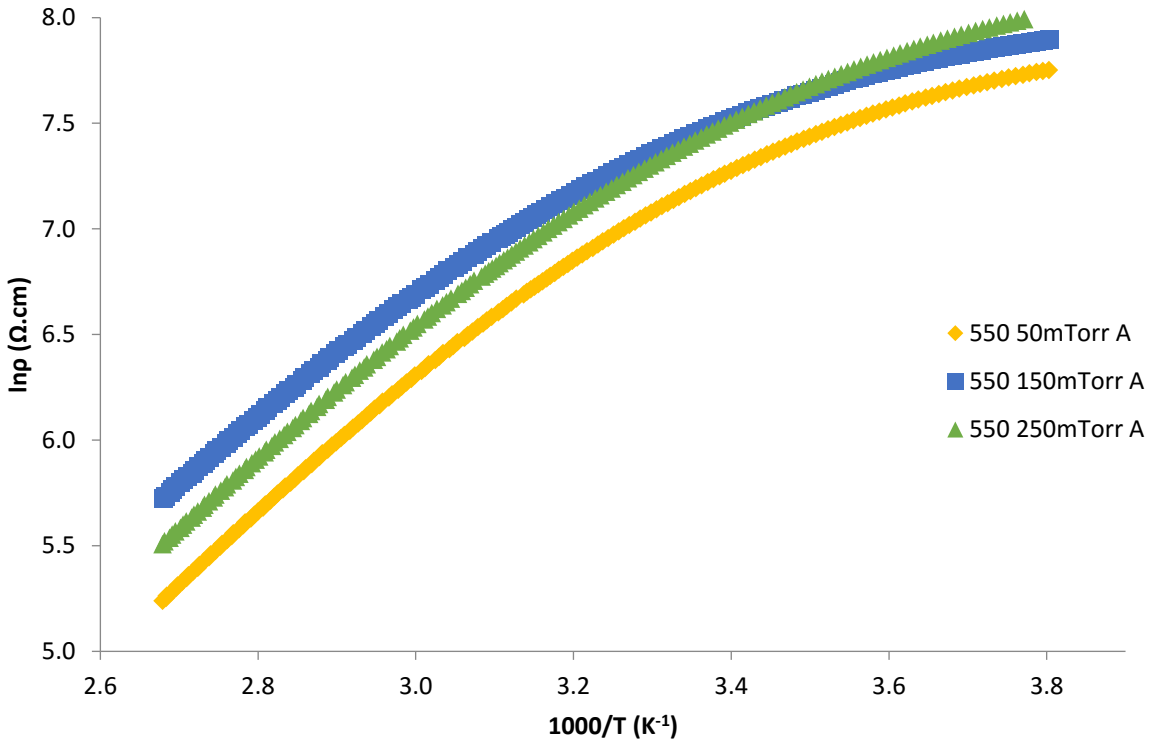

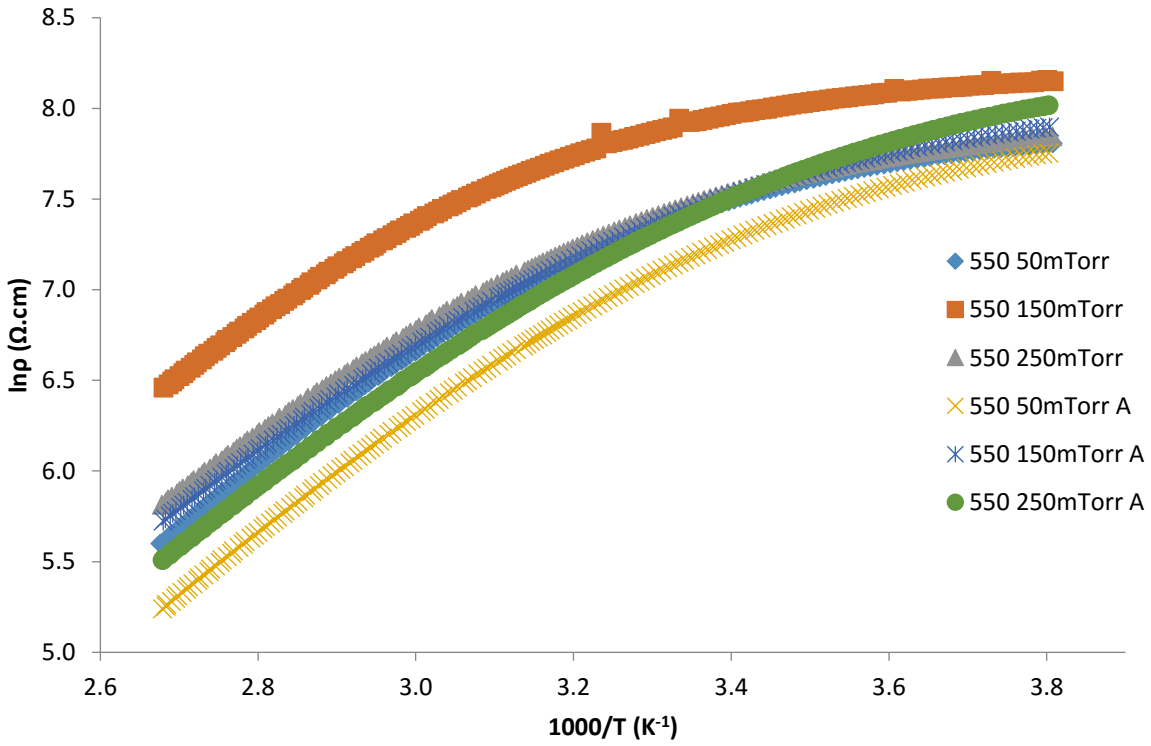

Figure 6.51. lnρ vs. reciprocal temperature of as deposited and annealed films produced at 550°C substrate temperature and varying oxygen pressures

With an increase of oxygen pressure, a decrease in the B value is noticed suggesting the thermistors sensitivity decreases. The activation energies decrease with an increase of oxygen pressure and resistivity.

Table 6.12. Thermistor measured and calculated electrical parameters

Substrate Temperature (°C)	O_2 Pressure (mTorr)	25°C Resistivity (Ω.cm)	85°C Resistivity (Ω.cm)	Thermistor constant β Value (K)	Activation Energy (eV)
550	50	1.04E+03	2.19E+02	2782.16	0.2580
550	150	1.30E+03	2.93E+02	2647.51	0.2163
550	250	1.37E+03	2.71E+02	2886.94	0.2106

When compared with their as deposited counterparts the β values and activation energies appear to be quite similar to each other. Therefore, the sensitivity of the thermistors is not affected much by the annealing process, which may be because the films have been deposited at the higher substrate temperature of 550°C becoming subject to pre-annealing. There is no clear trend seen in these parameters.

6.5.8 Discussion and Comparison of the Annealed Films Produced at 550°C with the As - Deposited Films Produced at 550°C and the Annealed Films Produced at 400°C

Following annealing the films produced at 550°C substrate temperature experience a decrease in their resistivity values. This is a marked difference when compared to the films produced at 400°C where following annealing their resistivity increases in value. Higher resistivity values are observed in the films produced at 550°C in comparison to the 400°C.

No clear trend is seen in the β values or activation energies in all the films fabricated at 550°C, in contrast to the films produced at a substrate temperature of 400°C. Where there is a decrease in these values with an increase of oxygen pressure.

More NMO spinel peaks are also observed in the XRD patterns of the 550°C films indicating they are more crystalline in comparison to the 400°C films. This is also observed in the SEM micrographs where the 550°C have a more crystalline appearance. These may the reasons why the 550°C have higher resistivity values than the 400°C films.

6.6 Discussion and Conclusions

In this chapter thin films have been produced using the new set of conditions, 1.5 J/cm^2 laser fluence, an increase of laser pulses from 24,000 to 36,000 laser pulses and a decrease in the target to substrate distance from 50 mm to 40 mm. The substrate temperatures used were 400°C and 550°C and the oxygen pressure was varied from 50 to 250 mTorr.

All films were measured by XRD, SEM and had their electrical properties measured by a four wire resistance technique.

All films displayed the NMO spinel structure after deposition and annealing. An increase in oxygen pressure in the as deposited films deposited at 400°C led to an increase to the number of NMO peaks that were observed and an increase in their intensity, perhaps indicating an increase in grain size. It was also noticed that with an increase of O_2 pressure there was a decrease in the intensity of the Mn_2O_3 secondary phase. With a deposition temperature of 550°C a different pattern is observed with a decrease in the number of NMO peaks observed with an increase in the oxygen pressure and an increase in the amount of Mn_2O_3 secondary phase peaks. There were more NMO peaks observed in the films deposited at 550°C in comparison to the films deposited at 400°C substrate temperature, this in agreement with the films produced by G. Ji et al [10].

The resistivity of the thin films deposited at a substrate temperature of 400°C showed a decrease in resistivity with an increase of O_2 pressure. It was suggested this happened due to a change in the Mn valence states and / or the available oxygen vacancies or a change in the

inversion parameter. Also a decrease in the sensitivity of the NMO thin films (β value) occurred with an increase in the oxygen pressure. In film's produced at a substrate temperature of 550°C and 150 mTorr O_2 pressure have the highest resistivity. Also it is noticed that the thermistor sensitivity in these conditions were lower than those produced at 50 and 250 mTorr O_2 pressure and their activation energies were higher. This is in contrast to the films produced by Basu et al. [4] where with an increase in oxygen pressure would lead to similar resistivity values to films that were annealed in O_2. These changes in the films produced in this project suggest that temperature is having a greater effect on the films resistivity.

The thickness measurements errors indicate that the mean thickness of the films were not entirely accurate. This will have an effect on the film's resistivity as these mean thicknesses required to be inputted in the equation that is used to determine the films resistivity.

The effects of annealing on the resistivity of the films resulted in an increase in resistivity in the films deposited at a substrate temperature of 400°C, while for the films deposited at 550°C the resistivity decreased following annealing. In general, the literature suggests that annealing will lead to a decrease in the resistivity as suggested by literature [1, 2, 4, 11] as well as an increase in crystallinity. The amount of NMO spinel peaks observed in the XRD patterns are greater in the films deposited at 550°C which is also agreement with G. Li et al [10] who suggested this was due to the increased amount of thermal energy available during deposition.

Another reason for the films produced at higher temperature to have a higher resistivity is their increased porosity and cracking observed in SEM micrographs which is also in agreement with M. Lee et al [12].

References

1. Ryu, J., et al., *Highly Dense and Nanograined $NiMn_2O_4$ Negative Temperature coefficient Thermistor Thick Films Fabricated by Aerosol-Deposition.* Journal of the American Ceramic Society, 2009. **92**(12): p. 3084-3087.
2. Ma, C.J., et al., *Preparation and characterization of $Ni_{0.6}Mn_{2.4}O_4$ NTC ceramics by solid-state coordination reaction.* Journal of Materials Science-Materials in Electronics, 2013. **24**(12): p. 5183-5188.
3. de Gyorgyfalva, G. and I.M. Reaney, *Decomposition of $NiMn_2O_4$ spinel: an NTC thermistor material.* Journal of the European Ceramic Society, 2001. **21**(10-11): p. 2145-2148.
4. Basu, A., A.W. Brinkman, and R. Schmidt, *Effect of oxygen partial pressure on the NTCR characteristics of sputtered $Ni_xMn_{3-x}O_{4+delta}$ thin films.* Journal of the European Ceramic Society, 2004. **24**(6): p. 1247-1250.
5. Jadhav, R.N. and V. Puri, *Influence of copper substitution on structural, electrical and dielectric properties of $Ni_{((1-x))}Cu_{(x)}Mn_{(2)}O_{(4)}$ (0 <= x <= 1) ceramics.* Journal of Alloys and Compounds, 2010. **507**(1): p. 151-156.
6. Bruker, *Eva Software*.
7. Brabers, V.A.M. and J. Terhell, *Electrical-conductivity and cation valencies in nickel manganite.* Physica Status Solidi a-Applied Research, 1982. **69**(1): p. 325-332.
8. Kukuruznyak, D.A., et al., *Preparation and properties of thermistor thin-films by metal organic decomposition.* Thin Solid Films, 2001. **385**(1-2): p. 89-95.
9. Schmidt, R., *Production and performance of thin and thick film NTCR thermistors based on $NiMn_{(2)}O_{(4)}$ +*, 2003, University of Durham: Durham.
10. Ji, G., et al., *Low-temperature (< 300 degrees C) growth and characterization of single-100 -oriented Mn-Co-Ni-O thin films.* Materials Letters, 2013. **107**: p. 103-106.
11. Parlak, M., et al., *Effect of heat treatment on nickel manganite thin film thermistors deposited by electron beam evaporation.* Thin Solid Films, 1999. **345**(2): p. 307-311.
12. Lee, M. and M. Yoo, *Detectivity of thin-film NTC thermal sensors.* Sensors and Actuators a-Physical, 2002. **96**(2-3): p. 97-104.

Chapter 7

The Standardisation of Deposition Conditions to Improve the Reproducibility of the $NiMn_2O_4$ Thin Films

7.1. Introduction

In the previous chapter the effect of changing the deposition conditions (substrate temperature and oxygen pressure) was investigated. It was discovered that an increase in the substrate temperature during deposition had a big effect on the behaviour of the films, including higher resistivity values and a change in the order of most resistance with a change in oxygen pressure. There were also changes in the films crystallinity with a higher substrate deposition temperature as more peaks were observed which may explain the changes in behaviour of the films. Also the appearance of the films changed with an increase of pores and visible cracks evident in the films produced at 550°C, these are less dense than the films produced at 400°C which may contribute to their higher resistivity.

In this chapter the reproducibility of the films resistivity and thermistor characteristics will be discussed for all sets of preparation conditions, as well as their structure morphology and

thickness. The variability of the films properties was determined to see if the differences observed for the different deposition conditions were due to the deposition parameters or more random changes.

For each set of deposition conditions, a series of films were produced and then characterised and compared with each other to measure their reproducibility.

7.2. Film Repeatability and Reproducibility

7.2.1. XRD

All films produced were characterised by XRD. The results showed good reproducibility with similar patterns being obtained for each film deposited under the same conditions. An example of reproducibility is shown in the XRD patterns in Figure 7.1.

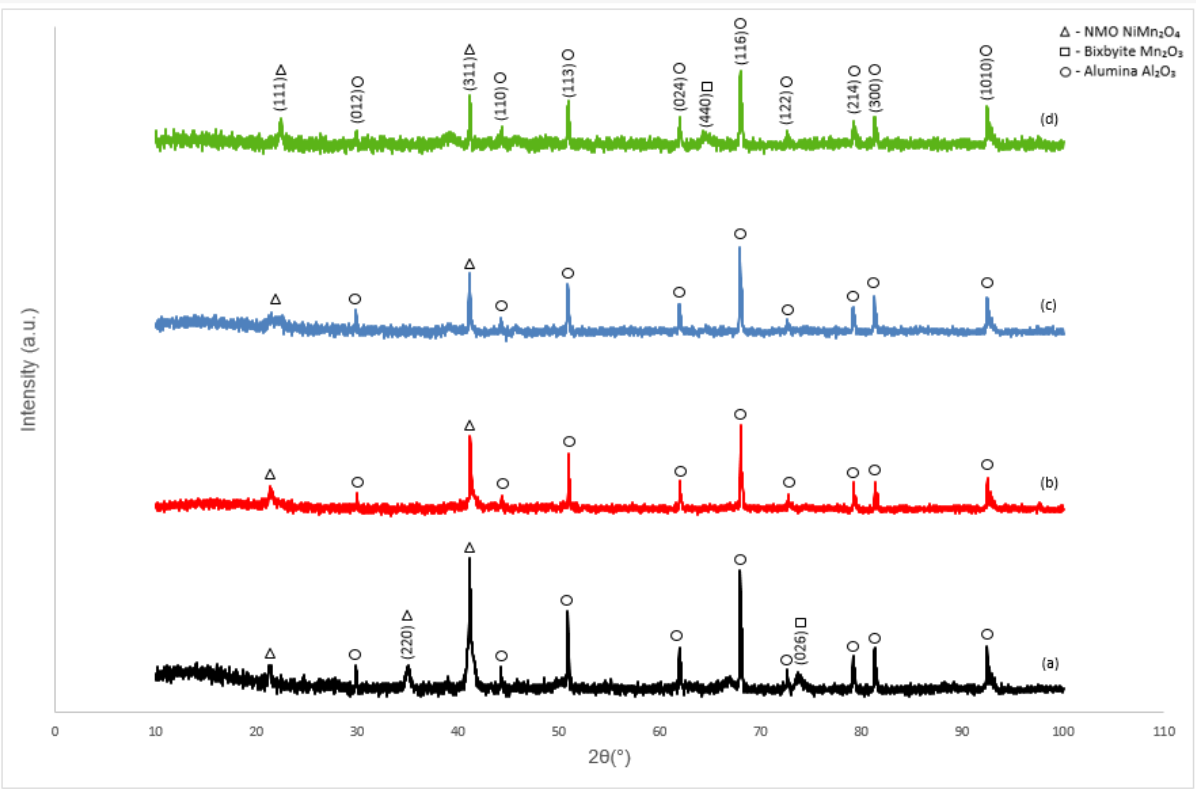

Figure 7.1. XRD patterns of films produced at 400°C and 50 mTorr of O_2 pressure (a) original data (b) repeat 1 (c) repeat 2 (d) repeat 3

The majority of the observed peaks could be attributed to either NMO or the alumina substrate which were in agreement with the reference spectra obtained from the JCPDS database, which allowed for unequivocal identification (Al_2O_3 PDF no. 01-073-1512 and NMO PDF no. 04-008-6982). For some films a few peaks were also attributed to a secondary phase identified as Mn_2O_3 (indicated by a '□' in the XRD traces) (Mn_2O_3 PDF no. 01-089-2809), although no systematic reason for this could be found. The XRD data for the thin films and target material were analysed using Eva software with the background subtracted using this software.

The XRD data shows that the structure of the films produced using any set of the deposition parameters investigated, was largely reproducible, with only a few minor differences observed. Any additional peaks could be attributed to either NMO or Mn_2O_3.

7.2.2. Microstructure

The microstructures of all of the films were measured by SEM to investigate the consistency of the microstructure from run to run. An example is presented in Figure 7.2, showing the microstructure of films produced at 400°C and 50 mTorr.

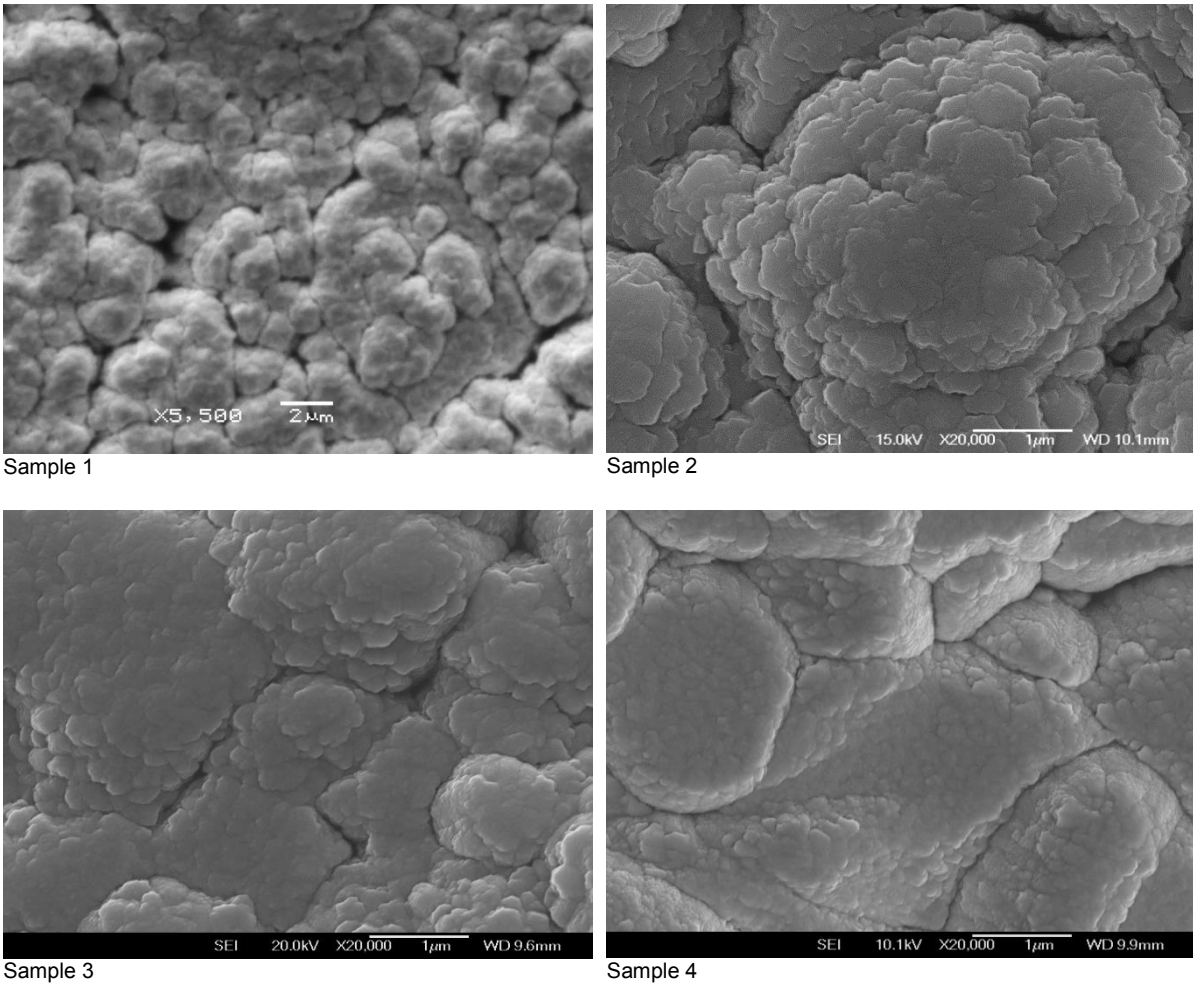

Sample 1 Sample 2

Sample 3 Sample 4

Figure 7.2. SEM surface micrographs of NMO films produced at 400°C and 50 mTorr

All the films produced despite their deposition conditions appear to have a granular structure with little porosity. However the films appear to be more dense with few holes and pores in comparison to films produced by screen printing [1]. The appearance of the films are reproducible for all conditions, with intergranular cracks larger in the annealed films in

comparison to the as deposited films. All the films produced at 550°C had a more crystalline appearance in comparison to the films produced at 400°C.

7.2.3. Film Cross Sections by SEM

Each set of repeats had their cross sections measured to see if it was possible to repeat the film's thickness, a set of complete repeats is given in Figure 7.3.

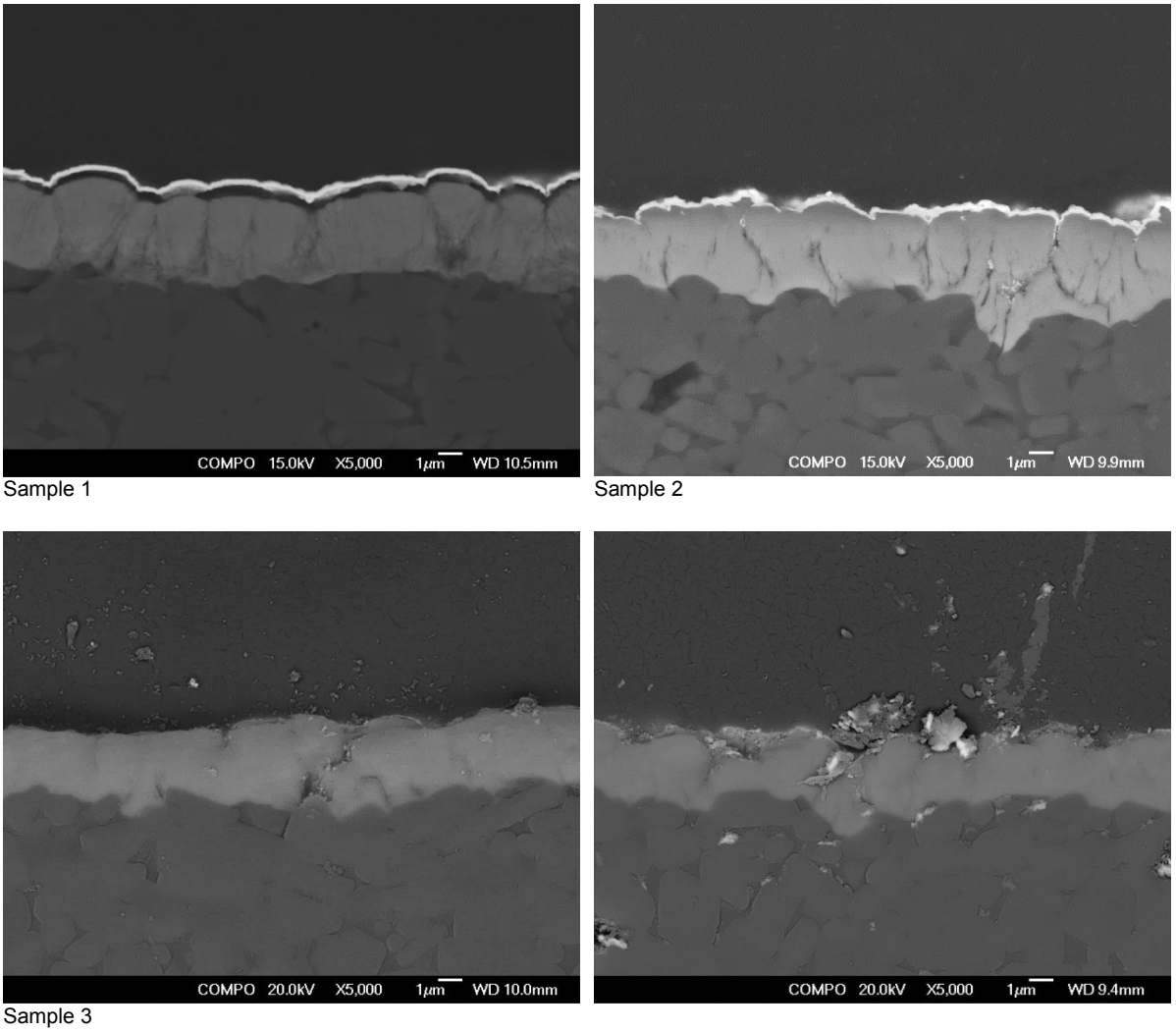

Figure 7.3. SEM Micrographs of cross-sections of NMO films grown at 400°C and 50 mTorr O_2 (Jeol 7000F)

Film thickness measurements for all the as deposited films produced at 400°C and 550°C at different O_2 pressures are given in the table below.

Table 7.1. Mean thickness measurement of repeated films produced at 400°C and 550°C substrate temperature and different oxygen pressures

Substrate Temperate (°C)	Oxygen pressure (mTorr)	Annealed	Mean thickness measurement (µm)			
			Original	Repeat 1	Repeat 2	Repeat 3
400	50	No	2.58	2.65	2.47	2.61
400	150	No	3.10	3.21	2.45	2.85
400	250	No	2.85	3.32	3.33	2.90
550	50	No	3.13	3.35	2.61	2.73
550	150	No	3.32	3.41	3.29	2.91
550	250	No	2.81	3.20	3.64	2.40
400	50	Yes	3.40	2.50	2.84	2.74
400	150	Yes	3.10	2.73	3.67	2.87
400	250	Yes	3.30	3.43	3.86	2.50
550	50	Yes	2.75	2.89	2.36	2.43
550	150	Yes	3.26	3.21	2.93	3.40
550	250	Yes	3.86	4.01	4.11	2.87

Table 7.1 shows the mean thickness measurements of the films produced under different conditions. As can be seen there is no consistency with the measurements, and this is primarily due to the substrate roughness leading to variation in the thickness of the deposited films. This is not ideal as it will lead to errors and problems with reproducibility. The films range of thicknesses were between 2.36 – 4.11 µm, therefore some films are over 1 µm in thickness difference. For most sample sets the difference in thickness tend to be less than 1µm with the exception of the sets produced at 400°C 250 mTorr annealed and 550°C 250 mTorr both as

deposited and annealed. These films will most likely have the least reproducibility because of this. These changes in thickness will have an effect on the resistivity values as they need to be included in the resistivity equation as shown in Chapter 2. The most significant effect on the thickness measurement is from sample to sample due to constant variation in the film thickness shown in the cross sections. Therefore, it is impossible to gain an accurate film thickness measurement due to this problem.

The use of polished substrates is likely to alleviate these problems and lead to better reproducibility. There will still however be variation in the thickness from the centre to the edge of the films, as there is a higher deposition rate in the centre of the plume during the PLD process, this will be evidently especially in larger 10 × 10 mm films. With a polished substrate the number of laser pulses during deposition can allow the user to determine the film thickness each time as achieved by V.S Dang [2] using 5 × 5 mm substrates depositing YBCO using PLD used in this project.

7.2.4. Resistivity

Each set of film repeats had their resistivity measured to see if it was possible to reproduce the same resistivity values and thermistor characteristics.

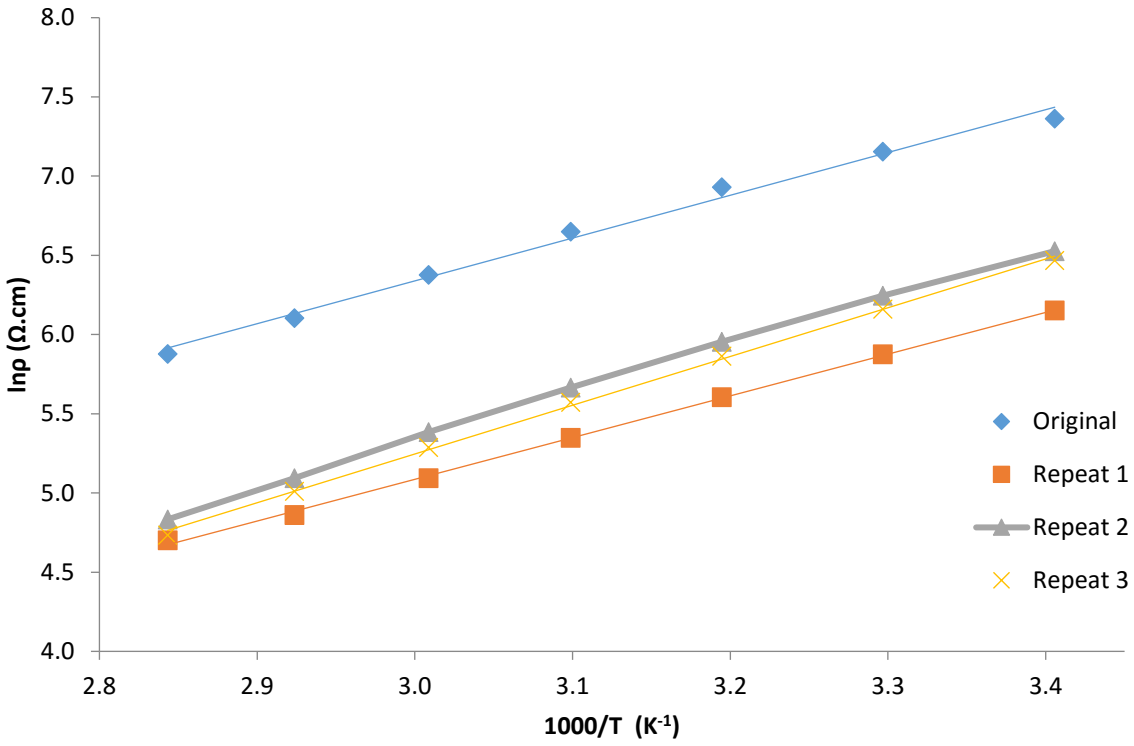

Figure 7.4. Lnρ vs 1000/T graph of NMO films grown at 400°C at 50 mTorr of O_2 pressure

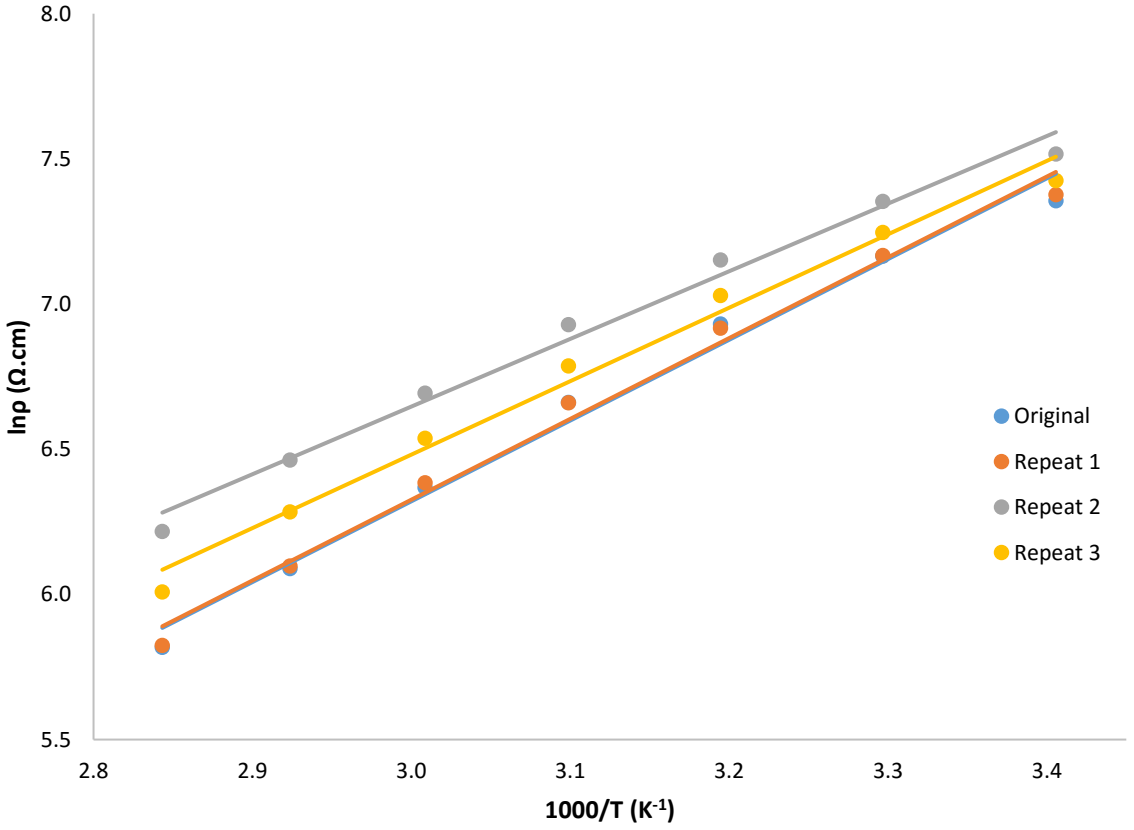

Figure 7.5. Lnρ vs 1000/T graph of NMO films grown at 550°C at 50 mTorr of O_2 pressure

A comparison between the original set of data and the repeats has been made and is shown in the graphs above. There appears to be fairly good reproducibility however it is not perfect, which will be an issue when producing devices, as an exact resistance would need to be known. This is therefore likely to effect the β value as well which is an important parameter that is taken into consideration when selecting a thermistor in industry.

The resistance values for the films produced at 400°C and 50 mTorr of O_2 pressure are given in the table below.

Table 7.2. Resistance of films produced at 400°C substrate temperature and 50 mTorr of O_2 pressure measured at different temperatures

	Resistance (Ω)			
Temperature (°C)	Sample 1	Sample 2	Sample 3	Sample 4
25	2.35×10^6	1.68×10^6	3.02×10^6	2.26×10^6
35	1.77×10^6	1.23×10^6	2.29×10^6	1.70×10^6
45	1.33×10^6	8.96×10^5	1.68×10^6	1.28×10^6
55	9.92×10^5	6.53×10^5	1.27×10^6	9.55×10^5
65	7.48×10^5	4.75×10^5	9.73×10^5	7.08×10^5
75	5.60×10^5	3.56×10^5	7.25×10^5	5.31×10^5
85	4.32×10^5	2.67×10^5	5.42×10^5	4.18×10^5

Table 7.2 shows the resistance of different samples measured at different temperatures produced using the same deposition conditions. There is a lot of variation in the measured resistances despite them being measured at the same temperatures, it should be noted that the variation of the films thickness also changes for each sample. It is therefore possible that these changes in their thickness are having an effect on the film's resistance. As this cannot be controlled due to the alumina substrate roughness, the reproducibility of the films will be poor.

7.2.5. Thermistor Characteristics Repeatability

The table below shows the full range of samples produced with their repeats and their measured electrical properties.

Table 7.3. Thermistor measured and calculated electrical parameters for the original and repeat set of films

Set of films	Substrate Temperature (°C)	O_2 Pressure (mTorr)	Annealed	25°C Resistivity (Ω.cm)	85°C Resistivity (Ω.cm)	Thermistor constant β Value (K)	Activation Energy (eV)
Original	400	50	No	7.45E+02	1.34E+02	3053.72	0.2631
	400	150	No	4.29E+02	9.55E+01	2671.72	0.2302
	400	250	No	4.70E+02	1.10E+02	2583.52	0.2226
Repeat 1	400	50	No	7.79E+02	1.45E+02	2994.01	0.2580
	400	150	No	8.38E+02	2.05E+02	2509.91	0.2163
	400	250	No	1.38E+03	3.49E+02	2443.34	0.2106
Repeat 2	400	50	No	6.13E+02	1.11E+02	3044.89	0.2624
	400	150	No	4.24E+02	8.53E+01	2851.18	0.2457
	400	250	No	5.26E+02	1.10E+02	2779.35	0.2395
Repeat 3	400	50	No	6.06E+02	1.11E+02	3013.47	0.2597
	400	150	No	4.61E+02	9.17E+01	2873.52	0.2476
	400	250	No	5.31E+02	1.08E+02	2826.23	0.2435
Original	400	50	Yes	1.14E+03	2.36E+02	2796.84	0.2410
	400	150	Yes	1.74E+03	4.67E+02	2343.97	0.2020
	400	250	Yes	1.81E+03	5.42E+02	2142.62	0.1846
Repeat 1	400	50	Yes	7.45E+02	1.34E+02	3053.72	0.2631
	400	150	Yes	4.29E+02	9.55E+01	2671.72	0.2302
	400	250	Yes	4.70E+02	1.10E+02	2583.52	0.2226
Repeat 2	400	50	Yes	1.15E+03	2.41E+02	2779.65	0.2395
	400	150	Yes	1.72E+03	4.46E+02	2397.06	0.2066
	400	250	Yes	1.58E+03	4.31E+02	2312.36	0.1993
Repeat 3	400	50	Yes	1.14E+03	2.17E+02	2962.58	0.2553
	400	150	Yes	1.77E+03	4.11E+02	2601.62	0.2242
	400	250	Yes	1.80E+03	4.52E+02	2460.22	0.2120
Original	550	50	No	1.60E+03	3.39E+02	2761.59	0.2380
	550	150	No	2.50E+03	8.25E+02	1910.38	0.1646

	550	250	No	1.10E+03	2.48E+02	2653.31	0.2286
Repeat 1	550	50	No	1.57E+03	3.36E+02	2736.68	0.2358
	550	150	No	1.90E+03	5.09E+02	2343.90	0.2020
	550	250	No	1.40E+03	2.76E+02	2887.48	0.2488
Repeat 2	550	50	No	1.89E+03	4.70E+02	2476.45	0.2134
	550	150	No	2.10E+03	6.57E+02	2071.17	0.1785
	550	250	No	1.52E+03	4.13E+02	2312.36	0.1993
Repeat 3	550	50	No	1.92E+03	4.65E+02	2519.53	0.2171
	550	150	No	2.50E+03	8.25E+02	1974.33	0.1701
	550	250	No	1.70E+03	4.68E+02	2297.28	0.1980
Original	550	50	Yes	1.04E+03	2.19E+02	2782.16	0.2397
	550	150	Yes	1.30E+03	2.93E+02	2647.51	0.2281
	550	250	Yes	1.37E+03	2.71E+02	2886.94	0.2488
Repeat 1	550	50	Yes	1.30E+03	2.46E+02	2963.73	0.2554
	550	150	Yes	1.83E+03	4.46E+02	2509.46	0.2162
	550	250	Yes	1.50E+03	2.98E+02	2875.02	0.2477
Repeat 2	550	50	Yes	1.04E+03	2.16E+02	2803.08	0.2416
	550	150	Yes	1.80E+03	4.35E+02	2524.80	0.2176
	550	250	Yes	1.26E+03	2.68E+02	2757.53	0.2376
Repeat 3	550	50	Yes	1.27E+03	2.65E+02	2782.83	0.2398
	550	150	Yes	1.75E+03	4.42E+02	2445.40	0.2107
	550	250	Yes	1.60E+03	3.48E+02	2719.17	0.2343

The resistivity measurements of each sample at 25°C and 85°C are presented in Table 7.3 using the 4 wire resistance measurement technique as described in Chapter 4. The β value and the activation energy for each sample is also presented in the table which are calculated using the equations given in Chapter 4. The original samples given in the table are the samples which are presented in Chapter 6.

For each of the different parameters that were measured (the resistivity, β value and activation energy) in each set of films the range is quite similar, suggesting that it is possible for there to be good reproducibility in these films. The β values for example are all very similar, and as this parameter is used to describe the sensitivity and hence the behaviour of the films, it is good indication of reproducibility.

The resistivity values, β values and activation energies of the films produced in this project in general are smaller than those presented in literature. The main difference with the films produced in this project and those in the literature is the use of a rough alumina substrate.

In the films produced at 400°C with an increase of oxygen pressure, a decrease in the β value is noticed suggesting the thermistors sensitivity decreases. The activation energies also decrease with an increase of oxygen pressure.

There appears to be no clear pattern seen in the β value or activation energy in the film's produced at 550°C as their values increase and then decrease with an increase of O_2 pressure.

The variation in the films thickness can sometimes be as high as 1 μm for the same set of films, this will have a huge effect as this measurement is required for the determination of the films resistivity. The results reflect this as seen in their differences between the different samples with the same deposition set. There are other possible reasons such as the presence of many pores and cracks in the films due to the films bring deposited unevenly. All of these will contribute to the poor reproducibility of the films produced in this project.

7.3. Conclusions

In this chapter the reproducibility of the films produced was tested by doing a series of repeats and comparing them to each other. Each set of films were analysed by XRD to determine if there was any change in crystallinity which may be used to explain any anomalies or changes in trends. When analysed there appeared to be good reproducibility in the crystallinity of the films, therefore any changes in the measured resistances could not be attributed to differences in crystallinity. All peaks that were measured could be attributed to material that is present in the NMO bulk target, therefore there was no contamination present in any of the films which could explain any differences in resistance measurements.

The microstructure is consistent throughout each repeat, with the film clearly following the alumina substrates microstructure. The only real difference noticed in microstructure can be seen when the films are either annealed or deposited at a higher substrate temperature, where the grains will adopt a more crystalline appearance and there is an increase in the amount of pores and cracking.

A comparison of the cross sections under SEM shows similar appearance in comparison to repeats, and the film is seen to adhere well to the alumina substrate following its profile well. This may be the cause for the appearance of cracks in the films, due to the alumina substrates roughness. This led to the variation in the film thickness meaning only an average film thickness could be calculated. The relationship between the film thickness and the resistivity means there will be errors as it is not possible to accurately obtain a correct film thickness, as this value is required for the determination of the resistivity. This may also explain the variation in the film thicknesses in the repeats of the material.

References

1. Schmidt, R., et al., *Screen printing of co-precipitated $NiMn_2O_{4+delta}$ for production of NTCR thermistors.* Journal of the European Ceramic Society, 2003. **23**(10): p. 1549-1558.
2. Dang, V.-S., *Nanotechnology of pinning centres in high temperature superconducting $YBa_2Cu_3O_7$ films*, in *Metallurgy and Materials*2011, University of Birmingham. p. 329.

Chapter 8

Conclusions and Future Work

8.1 Summary and Conclusions

The major conclusions of this project has demonstrated that it is possible to deposit thin films of NMO with a granular structure using PLD onto alumina substrates. It has been shown that these films have NTC properties and have been successfully observed in the as deposited and annealed films.

An in depth analysis of the starting materials NiO, Mn_2O_3 and calcined NMO was required so that a good comparison could be made against the thin films produced using the sintered NMO target material. This data was presented in Chapter 5 of the thesis alongside the examination of the sintered NMO target material.

The biggest obstacle that had to be overcome in Chapter 4 was the determination of the most appropriate resistance measurement technique for both the film and sintered bulk target. Due to the highly insulating nature of NMO it proved quite difficult to determine a technique that would be suitable for its measurement. Several methods failed such as a through thickness measurement and the four point probe method, where the NMO material proved to be too insulating because of contact resistance when trying to get reliable result. It was determined that it was necessary to apply electrodes along the edge of the material and by use of the four wire resistance measurement technique to ensure an accurate measurement of the resistance could be achieved.

Once an accurate measurement of resistance could be determined initial thin films were deposited onto alumina substrates provided by the sponsoring company Amphenol. When the initial thin films were analysed by XRD it was noticed that there was a decrease in the amount of NMO peaks that were present in their X ray diffraction patterns in comparison to the bulk NMO target. The XRD analysis showed there was a change in the preferred orientation and crystallinity in the thin films, which is likely to have an effect on the electrical properties of the material.

Despite the success of determining the presence of an NMO film on the alumina substrate problems arose when attempting to determine the films thickness. Due to the roughness of the commercial substrate provided it was impossible to determine an accurate film measurement. One of the aims of the project as given in in Chapter 3 was to investigate the use of different substrates and their suitability for deposition of NMO. Films were then deposited onto highly polished substrates of STO and Si to see if a film thickness could be accurately measured. Here it was determined that the films being produced were too thin to be measured (< 100 nm) on the rough alumina substrate. It was deemed necessary to then change the PLD conditions to allow for an increase in the film thickness. Due to the commercial aspect of the project it was

encouraged to continue to deposit on the films on the alumina substrates as opposed to the highly polished Si and STO substrates, therefore no further studies were conducted using these substrates as it was clear an NTC film could be produced using the alumina substrates.

With an increase in the film's thickness a huge difference was noticed in these films, XRD patterns when compared to initial films produced. Less NMO peaks were evident in the films produced using the new conditions and an increase in the amount of secondary phase Mn_2O_3 peaks.

With these new deposition conditions to produce a more suitable thicker film, the effect of changing the substrate temperature and oxygen pressure on the film's properties was to be investigated. All the films analysed displayed the spinel structure and a preferred orientation following deposition in comparison to the bulk target. Effects of increasing the oxygen pressure in the as deposited films produced at a substrate temperature of 400 °C showed an increase in the amount of NMO peaks available and an increase in their intensity, it was suggested the increase in intensity was due to grain growth. There was also a decrease in the amount of Mn_2O_3 peaks available and in their intensity. An opposite effect was noticed in films produced at a substrate temperature of 550°C.

Resistivity measurements showed a clear trend whereby the resistivity would increase with an increase of oxygen pressure in films produced at a substrate temperature of 400°C, it was suggested this was due to a change in the Mn valance states and or the available oxygen vacancies or a change in the inversion parameter. In films produced at a higher substrate temperature of 550°C the resistivity would decrease with an increase of oxygen pressure. However, despite the different pattern, all the films produced at this temperature had resistivity's higher than those at 400°C. The β values and activation energies of the films fabricated at 400°C decreased with an increase of oxygen pressure, showing a clear trend as these are determined from a slope and not absolute values. However, with the films fabricated

at a substrate temperature of 550°C there was no clear trend shown, as all the films that were produced at an oxygen pressure of 150 mTorr had the highest β values and the lowest activation energy.

With the increased substrate temperature of 550°C the SEM micrographs showed the films had more predominate cracks, which may be one reason why these films were more resistive. The appearance of cracks was also observed in their cross sections.

The aim to produced NTC thin films of NMO was met as shown by these investigations, it was also shown that these film's resistivity can be manipulated by the changing of their deposition conditions. To show that these results are correct and that the films can be reproduced the next aim of the project was to produce sets of the same films and to measure their characteristics.

The reproducibility of the films was measured by producing repeat sets of films and comparing them to each other. XRD analysis was carried out on each set of films to determine the repeatability of the crystallinity of the films. The analysis proved that there was good reproducibility present on all repeat set of films, it was therefore deemed that any changes in the films resistivity would not be due to any changes made in the films crystallinity. All of the peaks measured in the films could be attributed to the NMO system, so therefore there was no contamination present in the films which could cause any changes in the films behaviour.

Microstructure analysis showed consistency throughout each repeat, with dense films being produced that clearly followed the microstructure of the alumina substrate. A change in substrate temperature and further heat treatment by annealing led to changes in the grain microstructure, giving them a more crystalline appearance which is in agreement with previous reports.

Cross sectional measurements show the films have a similar appearance to each other, indicating good reproducibility. The films also follow the substrate pattern well suggesting all

films had good adherence with the substrate. However due to the roughness of the substrate it was too difficult to determine an accurate thickness measurement of the films as variation in the thickness can sometimes be as high as 1 μm. Therefore, only average film thicknesses could be determined which may have possibly led to some errors and problems with reproducibility as this value is used for the determination of the resistivity.

However regardless of the difficulties in measuring the thin films thickness the resistivities of the films could still be seen to follow a pattern. Therefore, the reproducibility of these films was good as the repeats followed the same pattern as the original set of films measured.

It was concluded that the changes in resistances were due to the sample alone and the deposition conditions used to produce them.

It is therefore possible to tailor thin films of NMO using PLD to get thermistor which could be used as commercial thermistors. However, more work needs to be done to allow for exact resistance values to be duplicated each time. Way to achieve this are outlined in the future work section in this chapter.

8.2 Future Work

It is recommended further research to be conducted in the following areas which is based on what was observed in the experimentations and results obtained in this investigation.

The films deposited in this project were deposited on rough commercial alumina substrates; this affected the film's microstructure and its thickness causing an uneven film to be produced. It is recommended that a polished alumina substrate should be used to allow for more accurate thickness measurements to be taken and to compare if any differences between films produced on a polished substrate and an unpolished substrate are seen in the resistance values. Also it would be interesting if the use of a polished substrate would improve the reproducibility of the films.

The effect of changing the substrate temperature to 300°C and how this affects the thermistor characteristics of the films would help confirm if a trend is being seen. If the resistivity decreases with a decrease in substrate temperature then a confirmation of the effect of decreasing the substrate temperature will be known. Also if the crystallisation of the films either improves or not, it would also confirm what the effect of decreasing substrate temperature has on the crystallinity of the films.

An investigation into the laser frequency could be conducted to see if lowering the frequency to allow more time for the film to settle improves the microstructure and hence create a denser film allowing for improvements in the electrical characteristics of the material in terms of reproducibility.

An in depth study into changing the oxygen pressure and how it affects the plume and hence the deposition could be conducted. This will show whether there is a particular shape of plume which improves the thermistor properties of the films or improves the microstructure of the films.

Further investigation into the resistivity of the material by the use of impedance spectroscopy could give a more detailed picture into the resistivity characteristics of the NMO material.

EBSD measurements is possible for the NMO material, more research into how to get a good EBSD map for the NMO material will allow for a comparison to be made of the texture of the sintered NMO bulk target material and a NMO thin film. Using a polished substrate will allow for EBSD measurement to be conducted on the thin film from the film's surface.

The effect of aging on the films, how the resistivity changes over time should be investigated as it is known that most aging occurs within the first 24 hrs or week in this material. Investigating if different deposition conditions have any effect on the aging process would be highly beneficial for the production of devices.

APPENDIX

Al_2O_3 JCPDS Card 01-073-1512 (Co Radiation)

H	K	L	2THETA	D-VALUE	MULT	INTENSITY
0	1	2	29.86	3.4740	6	559.1
1	0	4	41.15	2.5467	6	1000.0
1	1	0	44.27	2.3753	6	430.8
0	0	6	48.92	2.1617	2	12.4
1	1	3	50.93	2.0818	6	457.4
1	1	-3	50.93	2.0818	6	457.4
2	0	2	54.32	1.9608	6	5.5
0	2	4	62.03	1.7370	6	488.3
1	1	6	68.09	1.5987	6	376.2
1	1	-6	68.09	1.5987	6	376.2
2	1	1	70.86	1.5439	6	14.0
1	2	-1	70.86	1.5439	6	14.0
1	2	2	72.58	1.5121	6	9.2
2	1	-2	72.58	1.5121	6	9.2
0	1	8	72.79	1.5084	6	106.2
1	2	-4	79.34	1.4021	6	187.6
2	1	4	79.34	1.4021	6	187.6
3	0	0	81.48	1.3714	6	519.2
2	1	-5	84.30	1.3337	6	7.1
1	2	5	84.30	1.3337	6	7.1
2	0	8	89.32	1.2733	6	25.7
1	0	10	92.69	1.2370	6	150.9
1	1	9	93.17	1.2321	6	43.3
1	1	-9	93.17	1.2321	6	43.3
1	2	-7	97.42	1.1911	6	4.6
2	1	7	97.42	1.1911	6	4.6
2	2	0	97.81	1.1876	6	65.2
0	3	6	101.23	1.1580	6	1.5
3	0	6	101.23	1.1580	6	1.5
2	2	-3	102.80	1.1452	6	26.8
2	2	3	102.80	1.1452	6	26.8
3	1	-1	103.89	1.1366	6	1.7
1	3	1	103.89	1.1366	6	1.7
1	3	-2	105.58	1.1238	6	19.5
3	1	2	105.58	1.1238	6	19.5
2	1	-8	105.79	1.1222	6	26.8
1	2	8	105.79	1.1222	6	26.8
0	2	10	109.32	1.0971	6	78.9
0	0	12	111.80	1.0809	2	12.0
1	3	4	112.51	1.0763	6	58.5
3	1	-4	112.51	1.0763	6	58.5
3	1	5	117.94	1.0445	6	1.6
1	3	-5	117.94	1.0445	6	1.6
2	2	-6	118.60	1.0409	6	104.6
2	2	6	118.60	1.0409	6	104.6
0	4	2	123.54	1.0158	6	35.2
2	1	10	127.94	0.9960	6	96.1
1	1	12	130.94	0.9838	6	15.8
4	0	4	131.82	0.9804	6	41.4
3	1	-7	134.20	0.9716	6	1.7
1	3	7	134.20	0.9716	6	1.7

Al_2O_3 JCPDS Card 01-073-1512 (Cu Radiation)

H	K	L	2THETA	D-VALUE	MULT	INTENSITY
0	1	2	25.64	3.4740	6	548.5
1	0	4	35.24	2.5467	6	1000.0
1	1	0	37.88	2.3753	6	433.1
0	0	6	41.78	2.1617	2	12.6
1	1	3	43.47	2.0818	6	464.8
1	1	-3	43.47	2.0818	6	464.8
2	0	2	46.30	1.9608	6	5.6
0	2	4	52.69	1.7370	6	500.9
1	1	6	57.66	1.5987	6	384.4
1	1	-6	57.66	1.5987	6	384.4
2	1	1	59.91	1.5439	6	14.3
1	2	-1	59.91	1.5439	6	14.3
1	2	2	61.30	1.5121	6	9.3
2	1	-2	61.30	1.5121	6	9.3
0	1	8	61.47	1.5084	6	107.5
1	2	-4	66.71	1.4021	6	184.9
2	1	4	66.71	1.4021	6	184.9
3	0	0	68.41	1.3714	6	505.7
2	1	-5	70.62	1.3337	6	6.8
1	2	5	70.62	1.3337	6	6.8
2	0	8	74.52	1.2733	6	23.5
1	0	10	77.10	1.2370	6	133.5
1	1	9	77.46	1.2321	6	38.1
1	1	-9	77.46	1.2321	6	38.1
1	2	-7	80.66	1.1911	6	3.9
2	1	7	80.66	1.1911	6	3.9
2	2	0	80.95	1.1876	6	54.3
0	3	6	83.48	1.1580	6	1.2
3	0	6	83.48	1.1580	6	1.2
2	2	-3	84.62	1.1452	6	20.8
2	2	3	84.62	1.1452	6	20.8
3	1	-1	85.41	1.1366	6	1.3
1	3	1	85.41	1.1366	6	1.3
1	3	-2	86.63	1.1238	6	14.5
3	1	2	86.63	1.1238	6	14.5
2	1	-8	86.78	1.1222	6	19.9
1	2	8	86.78	1.1222	6	19.9
0	2	10	89.28	1.0971	6	55.4
0	0	12	91.00	1.0809	2	8.1
1	3	4	91.49	1.0763	6	38.9
3	1	-4	91.49	1.0763	6	38.9
3	1	5	95.14	1.0445	6	0.9
1	3	-5	95.14	1.0445	6	0.9
2	2	-6	95.57	1.0409	6	62.4
2	2	6	95.57	1.0409	6	62.4
0	4	2	98.73	1.0158	6	19.2
2	1	10	101.43	0.9960	6	48.1
1	1	12	103.18	0.9838	6	7.4
4	0	4	103.69	0.9804	6	19.1
3	1	-7	105.02	0.9716	6	0.8
1	3	7	105.02	0.9716	6	0.8
3	2	1	109.96	0.9413	6	2.5
2	3	-1	109.96	0.9413	6	2.5
1	2	11	110.27	0.9395	6	1.7
2	3	2	111.25	0.9340	6	0.2

3	2	-2	111.25	0.9340	6	0.2
3	1	8	111.41	0.9331	6	25.2
1	3	-8	111.41	0.9331	6	25.2
2	2	-9	114.52	0.9165	6	10.5
2	2	9	114.52	0.9165	6	10.5
2	3	-4	116.57	0.9062	6	59.0
3	2	4	116.57	0.9062	6	59.0
0	1	14	117.07	0.9038	6	42.9
1	4	0	118.34	0.8978	6	31.2
4	1	0	118.34	0.8978	6	31.2
2	3	5	120.72	0.8869	6	2.4
3	2	-5	120.72	0.8869	6	2.4
4	1	-3	122.57	0.8790	6	8.7
4	1	3	122.57	0.8790	6	8.7
1	4	-3	122.57	0.8790	6	8.7
1	4	3	122.57	0.8790	6	8.7
0	4	8	125.15	0.8685	6	36.4
1	3	10	128.27	0.8567	6	64.6
0	3	12	130.50	0.8489	6	12.8
3	0	12	130.50	0.8489	6	12.8
2	0	14	131.73	0.8447	6	65.8
3	2	7	132.88	0.8410	6	2.6
2	3	-7	132.88	0.8410	6	2.6
2	1	13	133.28	0.8397	6	1.8
4	1	6	136.81	0.8291	6	47.5
4	1	-6	136.81	0.8291	6	47.5
1	4	6	136.81	0.8291	6	47.5
1	4	-6	136.81	0.8291	6	47.5

Mn_2O_3 JCPDS Card 01-089-2809 (Co Radiation)

H	K	L	2THETA	D-VALUE	MULT	INTENSITY
2	0	0	21.91	4.7100	6	30.6
2	1	1	26.92	3.8457	24	153.4
2	2	0	31.18	3.3305	12	0.1
2	2	2	38.43	2.7193	8	1000.0
2	3	1	41.65	2.5176	24	1.0
3	2	1	41.65	2.5176	24	2.8
4	0	0	44.67	2.3550	6	170.8
4	1	1	47.54	2.2203	24	28.6
2	4	0	50.29	2.1064	12	2.0
4	2	0	50.29	2.1064	12	12.4
3	3	2	52.93	2.0084	24	93.7
4	2	2	55.48	1.9228	24	10.1
3	4	1	57.95	1.8474	24	58.7
4	3	1	57.95	1.8474	24	61.4
2	5	1	62.72	1.7198	24	6.8
5	2	1	62.72	1.7198	24	23.4
4	4	0	65.02	1.6652	12	387.4
4	3	3	67.28	1.6155	24	12.9
4	4	2	69.51	1.5700	24	3.4
6	0	0	69.51	1.5700	6	1.2
3	5	2	71.70	1.5281	24	7.3
6	1	1	71.70	1.5281	24	37.6
5	3	2	71.70	1.5281	24	11.7
2	6	0	73.87	1.4894	12	5.1
6	2	0	73.87	1.4894	12	6.8
4	5	1	76.01	1.4535	24	24.6
5	4	1	76.01	1.4535	24	27.8
6	2	2	78.13	1.4201	24	224.0
6	3	1	80.24	1.3889	24	28.7
3	6	1	80.24	1.3889	24	22.8
4	4	4	82.33	1.3597	8	34.9
4	5	3	84.42	1.3322	24	6.9
5	4	3	84.42	1.3322	24	5.2
6	4	0	86.49	1.3063	12	19.3
4	6	0	86.49	1.3063	12	4.9
6	3	3	88.56	1.2819	24	6.9
7	2	1	88.56	1.2819	24	4.2
5	5	2	88.56	1.2819	24	0.6
2	7	1	88.56	1.2819	24	21.1
6	4	2	90.63	1.2588	24	1.9
4	6	2	90.63	1.2588	24	14.8
5	6	1	96.85	1.1963	24	4.1
7	3	2	96.85	1.1963	24	2.1
3	7	2	96.85	1.1963	24	0.2
6	5	1	96.85	1.1963	24	10.1
8	0	0	98.94	1.1775	6	42.2
7	4	1	101.04	1.1595	24	5.1
4	7	1	101.04	1.1595	24	4.9
8	1	1	101.04	1.1595	24	20.0
5	5	4	101.04	1.1595	24	4.1
2	8	0	103.16	1.1423	12	14.6
6	4	4	103.16	1.1423	24	1.8
8	2	0	103.16	1.1423	12	5.4
5	6	3	105.29	1.1259	24	17.1
6	5	3	105.29	1.1259	24	12.1

6	6	0	107.45	1.1102	12	0.1
8	2	2	107.45	1.1102	24	17.5
8	3	1	109.63	1.0951	24	8.8
7	4	3	109.63	1.0951	24	10.9
4	7	3	109.63	1.0951	24	10.8
3	8	1	109.63	1.0951	24	8.9
6	6	2	111.85	1.0805	24	77.9
7	5	2	114.09	1.0666	24	0.1
5	7	2	114.09	1.0666	24	2.0
8	4	0	116.38	1.0532	12	28.8
4	8	0	116.38	1.0532	12	28.8
8	3	3	118.71	1.0403	24	16.7
8	4	2	121.10	1.0278	24	6.7
4	8	2	121.10	1.0278	24	11.9
7	6	1	123.55	1.0158	24	15.4
6	7	1	123.55	1.0158	24	4.3
9	2	1	123.55	1.0158	24	0.1
2	9	1	123.55	1.0158	24	6.5
6	5	5	123.55	1.0158	24	26.1
6	6	4	126.07	1.0042	24	2.9
7	5	4	128.67	0.9930	24	14.1
5	7	4	128.67	0.9930	24	12.3
8	5	1	128.67	0.9930	24	9.5
5	8	1	128.67	0.9930	24	7.9
6	7	3	134.19	0.9716	24	37.6
9	3	2	134.19	0.9716	24	0.1
3	9	2	134.19	0.9716	24	4.2
7	6	3	134.19	0.9716	24	20.2
8	4	4	137.15	0.9614	24	90.4

Mn_2O_3 JCPDS Card 01-089-2809 (Cu Radiation)

H	K	L	2THETA	D-VALUE	MULT	INTENSITY
2	0	0	18.84	4.7100	6	29.8
2	1	1	23.13	3.8457	24	150.5
2	2	0	26.77	3.3305	12	0.1
2	2	2	32.94	2.7193	8	1000.0
2	3	1	35.66	2.5176	24	1.0
3	2	1	35.66	2.5176	24	2.8
4	0	0	38.22	2.3550	6	172.6
4	1	1	40.63	2.2203	24	29.1
2	4	0	42.94	2.1064	12	2.1
4	2	0	42.94	2.1064	12	12.6
3	3	2	45.14	2.0084	24	95.9
4	2	2	47.27	1.9228	24	10.4
3	4	1	49.33	1.8474	24	60.4
4	3	1	49.33	1.8474	24	63.2
2	5	1	53.26	1.7198	24	7.0
5	2	1	53.26	1.7198	24	24.1
4	4	0	55.15	1.6652	12	398.9
4	3	3	57.00	1.6155	24	13.3
4	4	2	58.82	1.5700	24	3.4
6	0	0	58.82	1.5700	6	1.2
3	5	2	60.59	1.5281	24	7.4
6	1	1	60.59	1.5281	24	38.4
5	3	2	60.59	1.5281	24	12.0
2	6	0	62.34	1.4894	12	5.2
6	2	0	62.34	1.4894	12	6.9
4	5	1	64.06	1.4535	24	24.7
5	4	1	64.06	1.4535	24	27.9
6	2	2	65.75	1.4201	24	223.3
6	3	1	67.43	1.3889	24	28.3
3	6	1	67.43	1.3889	24	22.5
4	4	4	69.08	1.3597	8	34.0
4	5	3	70.71	1.3322	24	6.6
5	4	3	70.71	1.3322	24	5.0
6	4	0	72.33	1.3063	12	18.2
4	6	0	72.33	1.3063	12	4.6
6	3	3	73.94	1.2819	24	6.4
7	2	1	73.94	1.2819	24	3.8
5	5	2	73.94	1.2819	24	0.5
2	7	1	73.94	1.2819	24	19.6
6	4	2	75.53	1.2588	24	1.8
4	6	2	75.53	1.2588	24	13.5
5	6	1	80.24	1.1963	24	3.4
7	3	2	80.24	1.1963	24	1.7
3	7	2	80.24	1.1963	24	0.1
6	5	1	80.24	1.1963	24	8.5
8	0	0	81.79	1.1775	6	34.8
7	4	1	83.34	1.1595	24	4.1
4	7	1	83.34	1.1595	24	3.9
8	1	1	83.34	1.1595	24	16.0
5	5	4	83.34	1.1595	24	3.3
2	8	0	84.88	1.1423	12	11.3
6	4	4	84.88	1.1423	24	1.4
8	2	0	84.88	1.1423	12	4.2
5	6	3	86.42	1.1259	24	12.9
6	5	3	86.42	1.1259	24	9.1

6	6	0	87.96	1.1102	12	0.1
8	2	2	87.96	1.1102	24	12.7
8	3	1	89.50	1.0951	24	6.2
7	4	3	89.50	1.0951	24	7.7
4	7	3	89.50	1.0951	24	7.6
3	8	1	89.50	1.0951	24	6.2
6	6	2	91.03	1.0805	24	52.6
7	5	2	92.57	1.0666	24	0.1
5	7	2	92.57	1.0666	24	1.3
8	4	0	94.10	1.0532	12	18.0
4	8	0	94.10	1.0532	12	18.0
8	3	3	95.64	1.0403	24	10.0
8	4	2	97.19	1.0278	24	3.8
4	8	2	97.19	1.0278	24	6.8
7	6	1	98.74	1.0158	24	8.4
6	7	1	98.74	1.0158	24	2.4
9	2	1	98.74	1.0158	24	0.0
2	9	1	98.74	1.0158	24	3.6
6	5	5	98.74	1.0158	24	14.3
6	6	4	100.29	1.0042	24	1.5
7	5	4	101.86	0.9930	24	7.0
5	7	4	101.86	0.9930	24	6.1
8	5	1	101.86	0.9930	24	4.7
5	8	1	101.86	0.9930	24	3.9
6	7	3	105.02	0.9716	24	16.6
9	3	2	105.02	0.9716	24	0.0
3	9	2	105.02	0.9716	24	1.8
7	6	3	105.02	0.9716	24	8.9
8	4	4	106.61	0.9614	24	37.4
8	5	3	108.22	0.9516	24	9.2
5	8	3	108.22	0.9516	24	10.4
4	9	1	108.22	0.9516	24	2.8
9	4	1	108.22	0.9516	24	1.9
6	8	0	109.84	0.9420	12	8.3
10	0	0	109.84	0.9420	6	4.4
8	6	0	109.84	0.9420	12	2.2
7	7	2	111.48	0.9327	24	6.3
10	1	1	111.48	0.9327	24	2.1
8	6	2	113.14	0.9237	24	24.3
6	8	2	113.14	0.9237	24	2.2
2	10	0	113.14	0.9237	12	8.3
10	2	0	113.14	0.9237	12	7.1
9	4	3	114.82	0.9150	24	7.1
4	9	3	114.82	0.9150	24	5.5
10	2	2	116.53	0.9064	24	35.6
6	6	6	116.53	0.9064	8	7.3
10	3	1	118.25	0.8982	24	5.3
3	10	1	118.25	0.8982	24	6.2
9	5	2	118.25	0.8982	24	1.0
7	6	5	118.25	0.8982	24	5.6
6	7	5	118.25	0.8982	24	8.1
5	9	2	118.25	0.8982	24	4.1
8	5	5	121.80	0.8823	24	11.0
7	8	1	121.80	0.8823	24	9.5
7	7	4	121.80	0.8823	24	3.1
8	7	1	121.80	0.8823	24	9.0
8	6	4	123.62	0.8746	24	0.6
6	8	4	123.62	0.8746	24	27.9

10	4	0	123.62	0.8746	12	12.8
4	10	0	123.62	0.8746	12	5.0
6	9	1	125.49	0.8672	24	5.7
9	6	1	125.49	0.8672	24	17.2
10	3	3	125.49	0.8672	24	6.8
10	4	2	127.40	0.8599	24	9.3
4	10	2	127.40	0.8599	24	27.5
7	8	3	129.35	0.8528	24	6.0
9	5	4	129.35	0.8528	24	6.9
5	9	4	129.35	0.8528	24	7.9
8	7	3	129.35	0.8528	24	6.6
5	10	1	133.45	0.8392	24	16.3
11	2	1	133.45	0.8392	24	3.4
2	11	1	133.45	0.8392	24	0.3
9	6	3	133.45	0.8392	24	3.9
6	9	3	133.45	0.8392	24	11.7
10	5	1	133.45	0.8392	24	10.1
8	8	0	135.60	0.8326	12	11.7

$NiMn_2O_4$ JCPDS Card 01-071-0852 (Co Radiation)

H	K	L	2THETA	D-VALUE	MULT	INTENSITY
1	1	1	21.27	4.8497	8	180.7
2	2	0	35.08	2.9698	12	308.8
3	1	1	41.39	2.5327	24	1000.0
2	2	2	43.32	2.4249	8	101.4
4	0	0	50.45	2.1000	6	207.0
3	3	1	55.35	1.9271	24	1.5
4	2	2	62.93	1.7146	24	82.3
5	1	1	67.23	1.6166	24	297.1
3	3	3	67.23	1.6166	8	43.1
4	4	0	74.13	1.4849	12	384.9
5	3	1	78.15	1.4199	48	17.9
4	4	2	79.48	1.4000	24	0.6
6	2	0	84.73	1.3282	24	27.1
5	3	3	88.64	1.2810	24	88.6
6	2	2	89.94	1.2663	24	52.2
4	4	4	95.15	1.2124	8	27.0
5	5	1	99.09	1.1762	24	12.4
7	1	1	99.09	1.1762	24	0.4
6	4	2	105.75	1.1225	48	49.1
5	5	3	109.85	1.0936	24	79.3
7	3	1	109.85	1.0936	48	85.9
8	0	0	116.94	1.0500	6	69.6
7	3	3	121.41	1.0262	24	0.2
6	4	4	122.95	1.0186	24	0.2
6	6	0	129.40	0.9899	12	16.7
8	2	2	129.40	0.9899	24	22.7
7	5	1	134.66	0.9699	48	133.9
5	5	5	134.66	0.9699	8	39.1
6	6	2	136.52	0.9635	24	55.2

$NiMn_2O_4$ JCPDS Card 01-071-0852 (Cu Radiation)

H	K	L	2THETA	D-VALUE	MULT	INTENSITY
1	1	1	18.29	4.8497	8	175.1
2	2	0	30.09	2.9698	12	305.4
3	1	1	35.44	2.5327	24	1000.0
2	2	2	37.07	2.4249	8	101.7
4	0	0	43.07	2.1000	6	210.1
3	3	1	47.16	1.9271	24	1.5
4	2	2	53.44	1.7146	24	84.3
5	1	1	56.96	1.6166	24	303.8
3	3	3	56.96	1.6166	8	44.0
4	4	0	62.55	1.4849	12	387.7
5	3	1	65.77	1.4199	48	17.7
4	4	2	66.82	1.4000	24	0.6
6	2	0	70.96	1.3282	24	25.8
5	3	3	74.00	1.2810	24	81.6
6	2	2	75.00	1.2663	24	47.6
4	4	4	78.96	1.2124	8	23.2
5	5	1	81.90	1.1762	24	10.2
7	1	1	81.90	1.1762	24	0.4
6	4	2	86.75	1.1225	48	36.5
5	5	3	89.65	1.0936	24	55.1
7	3	1	89.65	1.0936	48	59.7
8	0	0	94.48	1.0500	6	42.8
7	3	3	97.39	1.0262	24	0.1
6	4	4	98.36	1.0186	24	0.1
6	6	0	102.29	0.9899	12	8.1
8	2	2	102.29	0.9899	24	11.0
7	5	1	105.27	0.9699	48	58.2
5	5	5	105.27	0.9699	8	17.0
6	6	2	106.27	0.9635	24	23.0
8	4	0	110.34	0.9391	24	26.5
7	5	3	113.46	0.9220	48	0.9
9	1	1	113.46	0.9220	24	4.7
8	4	2	114.52	0.9165	48	0.8
6	6	4	118.84	0.8954	24	5.7
9	3	1	122.20	0.8806	48	75.0
8	4	4	128.11	0.8573	24	127.8
9	3	3	131.89	0.8442	24	2.6
7	7	1	131.89	0.8442	24	0.0
7	5	5	131.89	0.8442	24	1.2
10	2	0	138.75	0.8237	24	14.2
8	6	2	138.75	0.8237	48	19.8

NiO JCPDS Card 47-1049 (Co Radiation)

H	K	L	2THETA	D-VALUE	MULT	INTENSITY
1	1	1	43.66	2.4066	8	786.6
2	0	0	50.86	2.0842	6	1000.0
2	2	0	74.79	1.4738	12	518.1
3	1	1	90.81	1.2568	24	263.0
2	2	2	96.11	1.2033	8	169.1
4	0	0	118.37	1.0421	6	104.3
3	3	1	138.75	0.9563	24	247.5

NiO JCPDS Card 47-1049 (Cu Radiation)

H	K	L	2THETA	D-VALUE	MULT	INTENSITY
1	1	1	18.40	4.8227	8	0.5
2	0	0	21.27	4.1766	6	0.0
2	2	0	30.26	2.9533	12	0.0
3	1	1	35.65	2.5186	24	0.5
2	2	2	37.29	2.4114	8	762.9
4	0	0	43.33	2.0883	6	1000.0
3	3	1	47.44	1.9164	24	0.4
4	2	0	48.75	1.8678	24	0.0
4	2	2	53.76	1.7051	24	0.0
5	1	1	57.31	1.6076	24	0.0
3	3	3	57.31	1.6076	8	0.1
4	4	0	62.94	1.4767	12	552.0
5	3	1	66.18	1.4119	48	0.1
4	4	2	67.25	1.3922	24	0.0
6	0	0	67.25	1.3922	6	0.0
6	2	0	71.42	1.3208	24	0.0
5	3	3	74.48	1.2739	24	0.0
6	2	2	75.49	1.2593	24	265.5
4	4	4	79.49	1.2057	8	163.7
5	5	1	82.46	1.1697	24	0.0
7	1	1	82.46	1.1697	24	0.1
6	4	0	83.44	1.1584	24	0.0
6	4	2	87.36	1.1162	48	0.0
5	5	3	90.29	1.0875	24	0.0
7	3	1	90.29	1.0875	48	0.1
8	0	0	95.17	1.0441	6	76.4
7	3	3	98.12	1.0205	24	0.1
8	2	0	99.11	1.0130	24	0.0
6	4	4	99.11	1.0130	24	0.0
6	6	0	103.09	0.9844	12	0.0
8	2	2	103.09	0.9844	24	0.0
7	5	1	106.11	0.9645	48	0.0
5	5	5	106.11	0.9645	8	0.0
6	6	2	107.13	0.9582	24	126.3
8	4	0	111.27	0.9339	24	255.4
7	5	3	114.45	0.9169	48	0.1
9	1	1	114.45	0.9169	24	0.0
8	4	2	115.52	0.9114	48	0.0
6	6	4	119.93	0.8905	24	0.0
9	3	1	123.37	0.8757	48	0.0
8	4	4	129.44	0.8525	24	281.0
9	3	3	133.34	0.8395	24	0.0
7	7	1	133.34	0.8395	24	0.1
7	5	5	133.34	0.8395	24	0.0
10	0	0	134.70	0.8353	6	0.0
8	6	0	134.70	0.8353	24	0.0